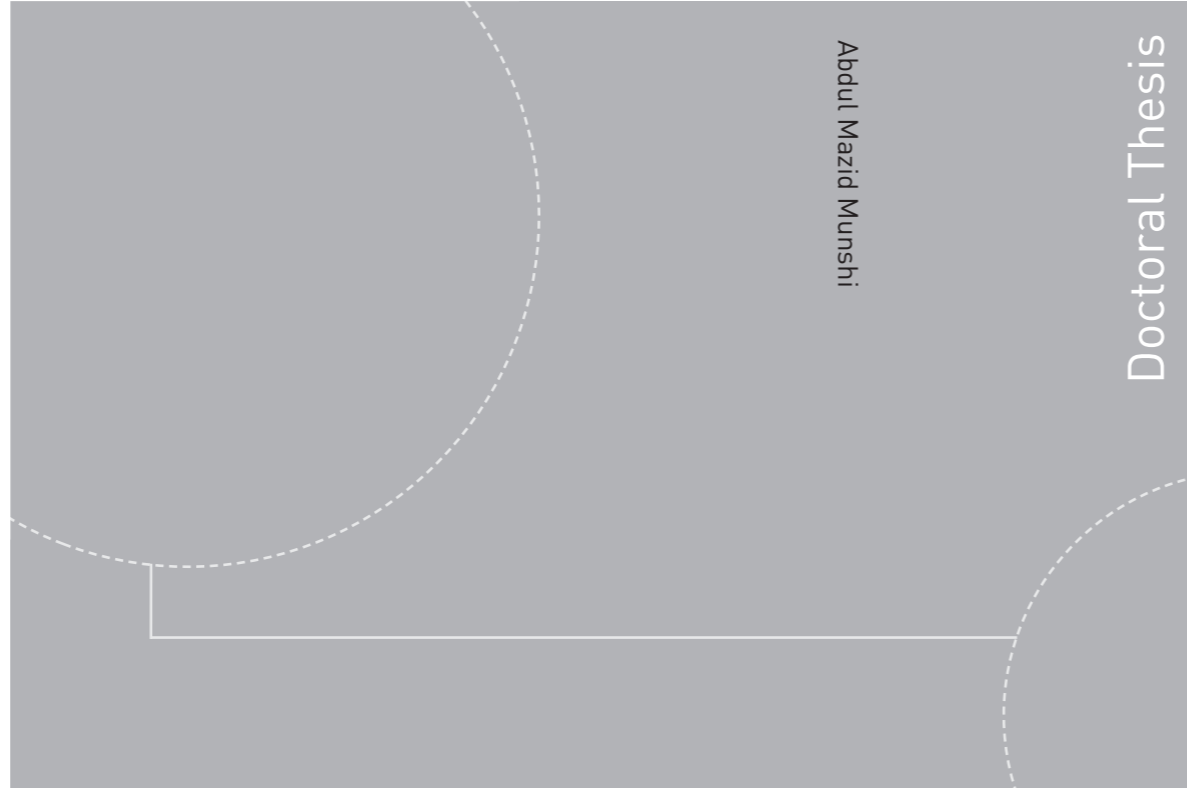


ISBN 978-82-326-0254-4 (printed version)  
ISBN 978-82-326-0255-1 (electronic version)  
ISSN 1503-8181



Doctoral theses at NTNU, 2014:166

**NTNU**  
Norwegian University of Science and Technology  
Faculty of Information Technology,  
Mathematics and Electrical Engineering  
Department of Electronics and Telecommunications



Doctoral theses at NTNU, 2014:166

Abdul Mazid Munshi

## Epitaxial Growth of Self-Catalyzed GaAs Nanowires by Molecular Beam Epitaxy

Abdul Mazid Munshi

# Epitaxial Growth of Self-Catalyzed GaAs Nanowires by Molecular Beam Epitaxy

Thesis for the degree of Philosophiae Doctor

Trondheim, May 2014

Norwegian University of Science and Technology  
Faculty of Information Technology,  
Mathematics and Electrical Engineering  
Department of Electronics and Telecommunications



**NTNU – Trondheim**  
Norwegian University of  
Science and Technology

**NTNU**

Norwegian University of Science and Technology

Thesis for the degree of Philosophiae Doctor

Faculty of Information Technology,  
Mathematics and Electrical Engineering  
Department of Electronics and  
Telecommunications

© Abdul Mazid Munshi

ISBN 978-82-326-0254-4 (printed version)

ISBN 978-82-326-0255-1 (electronic version)

ISSN 1503-8181

Doctoral theses at NTNU, 2014:166



Printed by Skipnes Kommunikasjon as

# Abstract

This thesis deals with the growth of GaAs nanowires (NWs) by molecular beam epitaxy (MBE) using vapor-liquid-solid method on various substrates including GaAs(111)B, Si(111) and graphene. The growth of the NWs on GaAs substrates was carried out by Au-catalyzed technique, whereas the growths on Si and graphene substrates were carried out using self-catalyzed technique that has been the main focus of this thesis. The long-term goal of this work was to produce p-n radial junction GaAs NWs for solar cell applications.

Necessary conditions were established for obtaining vertical self-catalyzed GaAs NWs on Si(111), which is reproducible from run-to-run. One of the major issues in these NWs grown by both Au- and self-catalyzed techniques is their crystal structure. The Au-catalyzed GaAs NWs usually adopt a wurtzite (WZ) crystal phase, whereas the self-catalyzed NWs a zinc blende (ZB) phase. However, in both the cases the NWs contain stacking faults, rotational twins or/and a mixed crystal phase. The ZB and WZ phases show different optical properties, and one phase might be favored over other for certain applications. Therefore the crystal phase was controlled within single NWs by tuning the V/III ratio and introducing GaAsSb inserts. The change of the crystal phases was correlated with the change in the contact angle of the Ga droplet.

Since the discovery of graphene, an ultra-thin two-dimensional material, the research on graphene has become an active field in recent years due to its remarkable properties including excellent electrical and thermal conductivities, mechanical strength and flexibility, and optical transparency. By growing the semiconductor NWs on graphene, a completely new hybrid system can be envisioned where the unique properties of both NWs and graphene can be utilized. Therefore we established a method for the growth of semiconductor NWs on graphene by demonstrating epitaxial growth of vertical GaAs and InAs NWs on different graphitic substrates.

Core-shell heterostructure, doping, optical properties, and position controlled growth of self-catalyzed GaAs NWs were investigated. Growth of GaAs/GaAsSb core-shell NWs where the Sb content was tuned from about 10% - 70% was studied. The effect of growth temperature and the Sb flux on the morphology of GaAsSb shell was investigated. In addition, by utilizing the core-shell geometry where the shell copies the crystal phase of the core, WZ phase of GaAsSb was demonstrated. Successful p-type doping of GaAs core using Be as dopant, and n-type doping of GaAs shell using Si and Te as dopants were achieved. To investigate the optical properties, GaAs/AlGaAs core-shell NWs were grown with different V/III ratios during the core growth. The NWs grown with high V/III ratio, despite containing a higher density of twinned ZB and WZ GaAs with SFs, were found to have superior optical quality as compared to the NWs grown with low V/III ratio that contain pure ZB GaAs. The observed V/III ratio dependent optical quality was correlated to the intrinsic defects such as As vacancies ( $V_{As}$ ) and Ga anti-sites ( $Ga_{As}$ ). Finally, position controlled growth was demonstrated on Si(111) using nanoimprint lithography. After optimizing different growth parameters, uniform GaAs NWs with a yield of about 80% was obtained. Achieving GaAs NWs with core-shell geometry and a high uniformity on Si over a large scale is an important step forward for fabricating optoelectronic devices including radial junction NW solar cells, lasers, and light emitting diodes on Si.



# Journal papers

## Included in this thesis:

- I. **Controlling crystal phases in GaAs nanowires grown by Au-assisted molecular beam epitaxy**  
D. L. Dheeraj, A. M. Munshi, M. Scheffler, A. T. J. van Helvoort, H. Weman, and B. O. Fimland, *Nanotechnology* **24** (2013) 015601.  
*I took part in the morphological characterization, discussion of the results and in the writing process.*
  
- II. **Crystal phase engineering in self-catalyzed GaAs and GaAs/GaAsSb nanowires grown on Si(111)**  
A. M. Munshi, D. L. Dheeraj, J. Todorovic, A. T. J. van Helvoort, H. Weman, and B. O. Fimland, *Journal of Crystal Growth* **372** (2013) 163.  
*I was the primary investigator of the project, including design of the experiment and the nanowire growth, morphological and most of the structural characterizations, interpretation of the results, and wrote the manuscript.*
  
- III. **Vertically aligned GaAs nanowires on graphite and few-layer graphene: generic model and epitaxial growth**  
A. M. Munshi, D. L. Dheeraj, V. T. Fauske, D. C. Kim, A. T. J. van Helvoort, B. O. Fimland, and H. Weman, *Nano Letters* **12** (2012) 4570.  
*I carried out approximately half of the nanowire growth experiments and morphological characterizations, participated actively in the analysis of the results and in the writing process.*
  
- IV. **Self-catalyzed MBE grown GaAs/GaAs<sub>x</sub>Sb<sub>1-x</sub> core-shell nanowires in ZB and WZ crystal structures**  
S. G. Ghalamestani, A. M. Munshi, D. L. Dheeraj, B. O. Fimland, H. Weman, and K. A. Dick, *Nanotechnology* **24** (2013) 405601.  
*I was responsible for the nanowire growth, participated in the design of the experiment and in the interpretation of the results.*
  
- V. **Comparison of Be-doped GaAs nanowires grown by Au- and Ga-assisted molecular beam epitaxy**

D. L. Dheeraj, A. M. Munshi, O. M. Christoffersen, D. C. Kim, G. Signorello, H. Riel, A. T. J. van Helvoort, H. Weman, and B. O. Fimland, *Journal of Crystal Growth* **378** (2013) 532.

*I participated in the nanowire growth, design of the experiment, morphological and structural characterizations, and discussion of the results.*

**VI. Position-controlled uniform GaAs nanowires on silicon using nanoimprint lithography**

A. M. Munshi, D. L. Dheeraj, V. T. Fauske, D. C. Kim, J. Huh, J. F. Reinertsen, L. Ahtapodov, K. D. Lee, B. Heidari, A. T. J. van Helvoort, B. O. Fimland, and H. Weman, *Nano Letters* **14** (2014) 960.

*I was the primary investigator of the project, including design of the experiment and the nanowire growth, morphological characterizations, interpretation of the results, and wrote the manuscript.*

**Not included in this thesis:**

**VII. Limitations of self-catalytic growth in controlling diameter of GaAs nanowires on Si substrates**

A. M. Munshi, D. L. Dheeraj, V. T. Fauske, A. T. J. van Helvoort, B. O. Fimland, and H. Weman, *In preparation.*

**VIII. Effect of intrinsic defects on the optical properties of self-catalyzed GaAs nanowires**

L. Ahtapodov<sup>§</sup>, A. M. Munshi<sup>§</sup>, S. Gulla, J. S. Nilsen, D. L. Dheeraj, A. T. J. van Helvoort, B. O. Fimland, and H. Weman, *In preparation.*

*§L. Ahtapodov and A. M. Munshi contributed equally to this work and co-wrote the manuscript.*

**IX. Compositional characterization of GaAs/GaAsSb nanowires by quantitative HAADF-STEM**

H. Kauko, T. Grieb, R. Bjørge, M. Schowalter, A. M. Munshi, H. Weman, A. Rosenauer, A. T. J. van Helvoort, *Micron* **44** (2013) 254.

**X. Advances in semiconductor nanowire growth on graphene**

A. M. Munshi and H. Weman, *Physica Status Solidi RRL* **7** (2013) 713.

- XI. Near-surface reduction of antimony during the growth of GaAsSb and GaAs/GaAsSb nanowires**  
H. Kauko, B. O. Fimland, T. Grieb, A. M. Munshi, K. Muller, A. Rosenauer, and A. T. J. van Helvoort, *In preparation*.
- XII. In-situ electrical and structural characterization of individual GaAs nanowires**  
V. T. Fauske, D. C. Kim, A. M. Munshi, D. L. Dheeraj, B. O. Fimland, H. Weman and A. T. J. van Helvoort, *Submitted to EMAG proceeding* (2013).
- XIII. Rectifying single GaAsSb nanowire devices based on self-induced compositional gradients**  
J. Huh, H. Yun, D. C. Kim, A. M. Munshi, D. L. Dheeraj, H. Kauko, A. T. J. van Helvoort, S. W. Lee, B. O. Fimland, and H. Weman, *Submitted to Nature Communications* (April, 2014) under review.
- XIV. Compositional analysis of GaAs/AlGaAs heterostructures using quantitative scanning transmission electron microscopy**  
H. Kauko, C. L. Zheng, Y. Zhu, S. Glanvill, C. Dwyer, A. M. Munshi, B. O. Fimland, A. T. J. van Helvoort, and J. Etheridge, *Applied Physics Letters* **103** (2013) 232111.





# Acknowledgements

I would like to thank my supervisor Helge Weman for his support throughout the entire tenure of this PhD project. His valuable suggestions during the experiments and useful feedback in the writing process are greatly acknowledged. I also would like to thank him for his encouragement to carry out independent research. His leadership quality is equally commendable. Without his guidance and suggestion this thesis work would not have been succeeded.

I would also like to extend my gratitude to my co-supervisor Bjørn-Ove Finland. I am grateful to him for giving me the opportunity to use MBE machine unlimitedly and for sharing his many MBE related fundamental concepts that immensely helped me in understanding many growth related problems. I would also like to thank him for giving important feedback and for careful reading on my manuscripts.

I also thank Ton van Helvoort for giving me the opportunity to work on TEM, his assistance with its operation, and the data interpretation. His quick and important feedback and comments on the manuscripts, posters and presentations are greatly acknowledged.

I am immensely grateful to Dheeraj Dasa for his help from the beginning of this PhD project. Starting from the MBE operation to SEM and TEM, I have learned almost everything from him. I thank him for giving me many important information regarding MBE and answering with patience to all of my questions. His help during the MBE growth, data analysis, as well as in the writing process was very helpful.

I would also like to thank Dong Chul Kim for helping me with the cleanroom processes and assisting me in the NanoLab. His knowledge and the passion for work are totally inspiring.

I am thankful to Vidar Fauske for his assistance with the cross-sectional TEM analysis, and helping me to understand many crystallography and structure related topics. I am also thankful to Jelena Todorovic and Hanne Kauko for helping me with TEM.

I would like to thank Lyubomir Ahtapodov and Johannes Reinertsen for their support with PL spectroscopy. I am grateful to them for sharing and explaining many PL related issues.

I am grateful to Saroj Kumar Patra, Tron Arne Nilsen for helping me with the MBE operation as well as for sharing their knowledge on MBE. I am also thankful to all the MBE users especially Dheeraj, Tron, Saroj, Geir Myrvågnes, Renato Bugge and Maryam Gholami for their cooperation and friendly nature which created a pleasant working atmosphere in the MBE Lab.

I am also thankful to Sepideh Gorji Ghalamestani and Kimberly Dick Thelander from Lund University, Sweden for the collaborative work and for many useful discussions.

I am grateful to Gaurav Sharma and Sverre Pettersen, Espen Rogstad, Bjørn Soleim, and Yingda Yu for their technical support with the MBE, instruments in the NanoLab, TEM, and SEM, respectively.

I am also thankful to all the nanowire group members specially Junghwan Huh, Cheng Guan Lim, Dingding Ren, and the Master students for their help and discussions.

*Abdul Mazid Munshi*  
*March 2014*  
*Trondheim, Norway*

# List of abbreviations

|              |  |
|--------------|--|
| <b>BF</b>    | Bright-field                                     |
| <b>BFM</b>   | Beam flux monitor                                |
| <b>CBE</b>   | Chemical beam epitaxy                            |
| <b>DF</b>    | Dark-field                                       |
| <b>EBL</b>   | Electron beam lithography                        |
| <b>EDX</b>   | Energy dispersive x-ray                          |
| <b>FI</b>    | Flux interruption                                |
| <b>HAADF</b> | High-angle annular dark-field                    |
| <b>HRTEM</b> | High-resolution transmission electron microscopy |
| <b>NW</b>    | Nanowire   |
| <b>MBE</b>   | Molecular beam epitaxy                           |
| <b>ML</b>    | Monolayer  |
| <b>MOVPE</b> | Metal-organic vapor phase epitaxy                |
| <b>NIL</b>   | Nanoimprint lithography                          |
| <b>PL</b>    | Photoluminescence                                |
| <b>RHEED</b> | Reflection high energy electron diffraction      |
| <b>SEM</b>   | Scanning electron microscopy                     |
| <b>SF</b>    | Stacking fault                                   |
| <b>STEM</b>  | Scanning transmission electron microscopy        |
| <b>TEM</b>   | Transmission electron microscopy                 |
| <b>TPL</b>   | Triple-phase-line                                |
| <b>UHV</b>   | Ultra-high vacuum                                |
| <b>vdWE</b>  | van der Waals epitaxy                            |
| <b>VLS</b>   | Vapor-liquid-solid                               |
| <b>VS</b>    | Vapor-solid                                      |
| <b>VSS</b>   | Vapor-solid-solid                                |
| <b>WZ</b>    | Wurtzite   |
| <b>ZB</b>    | Zinc blende                                      |



# Table of contents

| <b>Contents</b>                       | <b>Page</b> |
|---------------------------------------|-------------|
| <b>Abstract</b> .....                 | <b>i</b>    |
| <b>Journal papers</b> .....           | <b>iii</b>  |
| Included in this thesis:.....         | <b>iii</b>  |
| Not included in this thesis:.....     | <b>iv</b>   |
| <b>Acknowledgements</b> .....         | <b>vii</b>  |
| <b>List of abbreviations</b> .....    | <b>ix</b>   |
| <b>Table of contents</b> .....        | <b>xi</b>   |
| <b>1 Introduction</b> .....           | <b>1</b>    |
| <b>2 NW growth mechanisms</b> .....   | <b>9</b>    |
| 2.1 Au-catalyzed growth.....          | 10          |
| 2.2 Self-catalyzed growth.....        | 11          |
| <b>3 Experimental methods</b> .....   | <b>13</b>   |
| 3.1 Molecular beam epitaxy.....       | 13          |
| 3.2 Characterization .....            | 16          |
| 3.2.1 RHEED .....                     | 16          |
| 3.2.2 Other techniques.....           | 17          |
| <b>4 Growth optimization</b> .....    | <b>19</b>   |
| 4.1 Self-catalyzed NWs on Si.....     | 19          |
| 4.2 Crystal defects in NWs.....       | 21          |
| 4.2.1 Point defects .....             | 22          |
| 4.2.2 Extended defects .....          | 22          |
| 4.3 NW growth on graphene.....        | 28          |
| 4.4 Core-shell NW growth .....        | 31          |
| 4.4.1 GaAs/AlGaAs core-shell NW.....  | 32          |
| 4.4.2 GaAs/GaAsSb core-shell NW ..... | 35          |
| 4.5 Doping .....                      | 36          |
| 4.6 Optical properties .....          | 38          |
| 4.7 Position controlled growth.....   | 41          |

|          |  |            |
|----------|--|------------|
| <b>5</b> | <b>Summary and outlook</b> .....   | <b>45</b>  |
| 5.1      | Summary.....   | 45         |
| 5.2      | Outlook.....   | 47         |
| <b>6</b> | <b>Papers</b> .....  | <b>51</b>  |
| 6.1      | Paper I: Controlling crystal phases in GaAs nanowires grown by Au-assisted molecular beam epitaxy.....                                 | 53         |
| 6.2      | Paper II: Crystal phase engineering in self-catalyzed GaAs and GaAs/GaAsSb nanowires grown on Si(111) .....                            | 63         |
| 6.3      | Paper III: Vertically aligned GaAs nanowires on graphite and few-layer graphene: generic model and epitaxial growth.....               | 73         |
| 6.4      | Paper IV: Self-catalyzed MBE grown GaAs/GaAs <sub>x</sub> Sb <sub>1-x</sub> core-shell nanowires in ZB and WZ crystal structures ..... | 95         |
| 6.5      | Paper V: Comparison of Be-doped GaAs nanowires grown by Au- and Ga-assisted molecular beam epitaxy .....                               | 105        |
| 6.6      | Paper VI: Position-controlled uniform GaAs nanowires on silicon using nanoimprint lithography .....                                    | 113        |
| <b>7</b> | <b>References</b> .....  | <b>133</b> |

# 1 Introduction

With the ever increasing global power consumption and the concern over global warming, there is an urgent need for the utilization of renewable energy resources. For this purpose, solar cells that convert solar energy into electricity have been explored for a long time [1]. Crystalline silicon solar cells that belong to the category of first generation technology, are the most common solar cells with 80-90% share of today's solar cell market [2]. Commercial silicon solar cells with efficiency above 20% are available today [2]. However, the high cost per kWh of the first generation solar cells limits their use as an alternative energy source. To reduce the cost, second generation solar cells based on thin films emerged [3]. The reduction of cost mainly stems from the use of low cost materials, reduced material usage and manufacturing with high throughput. However, due to high non-radiative recombination losses, the efficiencies of the second generation cells are lower than the first generation silicon cells [4]. To increase the efficiency, multi-junction solar cells where a broad range of the solar spectrum can be used to create charge carriers were invented and referred as third generation solar cells [5]. Using various III-V semiconductors in a four-junction tandem cell, a world record efficiency of 44.7% has been achieved recently under a concentration of 297 suns [6].

Despite being an abundant green energy source, widespread use of electric power produced by solar cells is limited due to either the high cost of high quality crystalline materials or low power conversion efficiency. Some strategies in the third generation solar cells to address these issues are to use intermediate-band cells based mainly on quantum dots [7-9], hot carrier cells [10] and spectrum conversion cells [11, 12]. A comprehensive review on these different types of third generation solar cells can be found in Ref. [13]. Recently, various nanostructured materials are being actively used to produce low cost and high efficiency solar cells [14]. Of these, semiconductor nanowires (NWs) due to their unique electronic and optical properties are being investigated extensively [15-17]. Apart from solar cells, semiconductor NWs have also great potential as building blocks in various other novel electronic and optoelectronic devices [18-21].

NWs, due to their small diameter, can relax strain in the lateral direction allowing defect-free heteroepitaxial growth [22, 23]. By utilizing the unique geometry of the NWs, the challenges regarding the integration of III-V semiconductors with existing Si technology can be overcome in spite of the lattice mismatch and difference in the thermal expansion coefficients. Therefore by epitaxially growing III-V NWs on Si, the superior optoelectronic



properties of the III-Vs can be merged with the mature Si-based electronics. Moreover, heterostructures in NWs can be formed in radial, axial or in both directions [21].

Another advantage of NW arrays is the reduced reflection of incident light even when no antireflection coatings are used. In particular, a tapered NW array that will result in a continuously graded refractive index would be ideal for increasing light absorption over a broad range of wavelengths [24]. The increased absorption of light in the NWs has also been investigated by implementing the light trapping effect. Two different light incident directions can be considered; parallel (Figure 1.1a) and perpendicular (Figure 1.1b) to the NW axis. Waveguide modes propagating along the NW are activated when light incident direction is parallel to the NW axis (Figure 1.1a), whereas radially confined optical resonances or leaky-mode resonances take place when light incident direction is perpendicular to the NW axis (Figure 1.1b) [25, 26]. Both the waveguide modes and the leaky-mode resonances are dependent on the diameter of the NWs, wavelength of light and effective refractive index of the medium. Apart from these waveguide modes, multiple scattering of light in the NW arrays also contributes to the light trapping effect for increasing the absorption [27]. Moreover, due to a low filling fraction of the NWs in the NW-based solar cells, the cost of the materials reduces when compared to planar thin film structures, especially for the III-V semiconductors [28, 29].

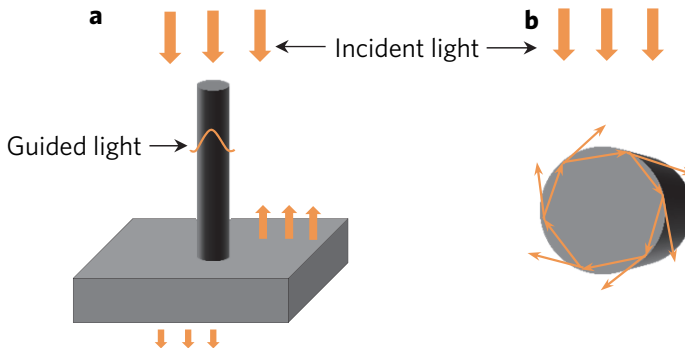


**Figure 1.1. Two different optical modes generated in a NW upon incidence of light. (a)** Axially guided optical modes are excited when the direction of incident light is along the NW axis [25]. **(b)** Radially confined leaky-modes are excited when the direction of incident light is perpendicular to the NW axis [26].

NW heterostructures with both radial and axial p-n junctions are promising for solar cells applications. In the case of radial p-n junction, a unique advantage in the solar cell performance can be realized as compared to the conventional thin film solar cells. For thin film solar cells, light absorption and charge carrier collection take place along the same direction (Figure 1.2a).

Therefore cell thickness cannot be increased to enhance light absorption without reducing the carrier collection due to a higher carrier recombination. This means the thin film solar cells suffer from a geometrical constraint. On the other hand, for NW array solar cells the light incidence and absorption take place along the axial direction, whereas the charge carriers are collected along the radial direction (Figure 1.2b). Therefore the length of the NW can be increased for optimum absorption without affecting the carrier collection efficiency. This effect was first studied theoretically by Kayes et al., showing that coaxial NWs having a radial p-n junction with the NW axis parallel to the light direction provide large improvement of carrier collection and overall efficiency relative to the conventional planar p-n junction solar cell [30].

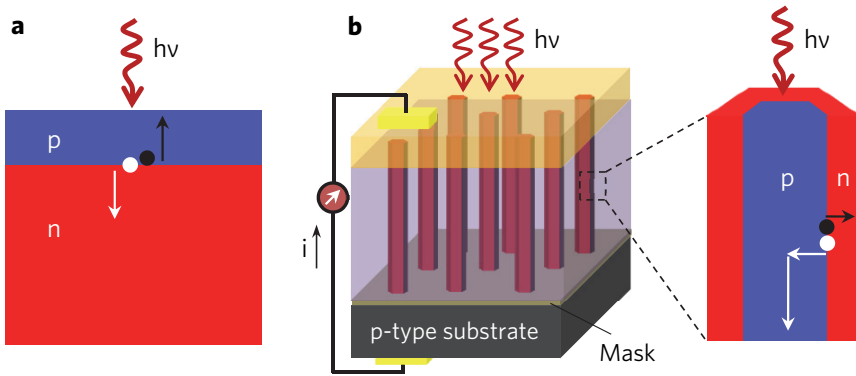


**Figure 1.2. Comparison between conventional planar p-n junction and NW-based radial p-n junction solar cells. (a)** Planar p-n junction where the light absorption and charge carrier separation directions are the same. **(b)** NW-based radial p-n junction where light absorption is along the axial direction and carrier separation is along the radial direction [30].

The above mentioned unique advantage cannot be realized in the case of axial p-n junction NW array solar cells. Instead, tandem solar cells can be fabricated consisting of segments with the bandgap decreasing from top to bottom of the NW and the segments connected in series via tunnel diodes. Such NW tandem solar cells can absorb different parts of the solar spectrum and hence increase the solar cell efficiency [31].

Due to the above mentioned unique properties of the NWs, both radial and axial junctions are promising candidates for future photovoltaic devices. Radial p-i-n GaAs NW array [32] and axial p-i-n InP NW array solar cells have already been reported with promising energy conversion efficiencies [33].

The aim of this thesis project was to study the growth of GaAs NWs by MBE for the application in radial junction NW solar cells. In the initial stage of this thesis work, GaAs NWs were grown by the Au-assisted technique on

GaAs(111)B substrates. Soon it was realized that self-catalyzed NW growth would be advantageous in various aspects as compared to the Au-catalyzed growth. The first issue is due to the potential contamination of the Au atoms. Incorporation of Au atoms during the Au-catalyzed growth of InAs [34], GaAs [35] and Si [36] NWs have been shown experimentally. However, the impact or the influence of this possible Au incorporation on the electrical and optical properties of the NWs is still debated. Nevertheless, the introduction of any foreign metals in the MBE growth chamber or their incorporation in the grown structures, as well as for their subsequent device processing is always undesirable. On the contrary, the self-catalyzed GaAs NW growth uses Ga that is itself one of the elements of the grown material as the catalyst, leaving no question of incorporation of any foreign elements. The second issue is regarding the formation of a core-shell NW geometry. For the growth of core-shell NWs, especially by MBE, an unwanted axial growth of the shell material during the shell growth is a well-known issue. This problem could potentially be solved by ex-situ etching of the Au catalyst after the core growth. However, in such process the sample needs to be taken out from the growth chamber, and will be exposed to the atmosphere and to the etching solution, deteriorating surface quality of the NWs. In addition, the remnant from the chemical solution on the sample might not be compatible to maintain the degree of cleanliness of the growth chamber. On the other hand in self-catalyzed growth, the Ga droplet can be consumed in-situ under an As flux after the core has been grown. As there are no catalyst droplets left at the top of the NWs, the shell growth will result in a radial growth without any axial growth. The third issue is related to the growth of position controlled NWs. For position controlled NW growth, the growth temperature should be high enough in order to avoid any parasitic crystal growth on the oxide mask. The usual growth temperature regime for MBE grown Au-catalyzed GaAs NWs is probably below that range. On the other hand, self-catalyzed growth of GaAs NWs usually takes place at temperatures above 600 °C which is sufficient to avoid the parasitic crystal growth on the oxide.

Therefore the Ga-assisted or self-catalyzed technique was adapted for the NW growth at NTNU in 2010 and was used throughout this PhD thesis project. In 2010, mainly GaAs(111)B substrates were used for the self-catalyzed NW growth in the literature [37]. However, due to the high-cost of III-V substrates, other alternatives were necessary to be adapted, and a natural choice was to investigate the use of Si(111) substrates. Due to the small diameter of the NWs, the issues related to the lattice mismatch and thermal expansion coefficients are expected to be less critical during NW growth as compared to planar thin film growth. At that time, reports on the growth of self-catalyzed GaAs NWs on Si(111) were scarce [38, 39]. Therefore

part of the goals of this thesis was to understand the NW growth mechanism on Si substrates. For NW-based solar cells, the orientation on the NWs on the substrate, the morphological and structural uniformity, doping control, formation of core-shell structure, good optical quality, as well as a site controlled growth of the NWs are important. By optimizing the Si substrate preparation method and tuning the growth condition, highly reproducible growth of GaAs NWs with almost 100% vertical alignment were obtained. In addition, the density and the diameter of the NWs were found to be dependent on the doping level of the Si substrates.

Most III-V semiconductors, except the nitrides, adopt a cubic zinc blende (ZB) crystal phase under normal growth conditions. Other polytypes such as hexagonal wurtzite (WZ) can be obtained under special conditions for example, under high pressure. The bandgap value of the WZ phase is different (usually larger) than the ZB phase [40-42]. Also, the indirect bandgap III-V semiconductors, such as GaP and AlAs become direct bandgap in the WZ phase. Therefore, if the WZ phase can be obtained under normal growth conditions, it could be very useful for various device applications. Interestingly, it has been observed that MBE grown Au-assisted III-V NWs often adopt the WZ crystal phase, while the self-catalyzed NWs usually adopt the ZB phase. However, due to a very low energy difference for the formation of ZB and WZ phase, they usually contain defects such as stacking faults and twins. Since these structural defects might affect the device functionalities [43-46], it is necessary to have a good control on the crystal phase of the NW. Therefore a study was focused on controlling the crystal phases of the GaAs NWs by tuning the basic growth parameters, such as V/III flux ratio and growth rate, both in Au-assisted and self-catalyzed GaAs NWs, which are reported in Paper I and II, respectively. These findings can be used to make crystal phase heterostructures in a single NW.

In parallel with this, a separate study was performed to investigate the growth of III-V semiconductor NWs epitaxially on graphene. Due to graphene's remarkable properties, including excellent electrical conductivity, optical transparency, and mechanical strength and flexibility, it could act as an excellent electrode material [47, 48]. A hybrid structure, by epitaxially growing semiconductor NWs on graphene, has the potential to provide a new avenue for the development of future advanced NW-based flexible electronic and optoelectronic devices [49]. In pursuit of this goal, an extensive study was carried out to grow GaAs and InAs NWs on graphite and few-layer graphene. The result of this study is summarized in Paper III. The GaAs NW/graphene hybrid holds great potential for future low-cost, flexible solar cells [50, 51].

NWs provide a great opportunity to form heterostructures in axial, radial or in both directions. In the case of an axial heterostructure, one can either change the composition or the crystal phase of the material, whereas in the case of the radial heterostructure, i.e. core-shell, the heterostructure can only be compositional as the shell tends to copy the crystal phase of the core. Interestingly, a change in the composition could also lead to a change in the crystal phase of the material. For example, only a small amount of Sb in GaAs(Sb) is sufficient to change the crystal phase from a WZ GaAs NW core to ZB GaAs(Sb). In addition, by changing the amount of Sb, the bandgap of GaAsSb can be changed to the near infrared, covering the important telecommunication bands 1.3 and 1.55  $\mu\text{m}$ . Moreover, type-II band alignment between GaAs and GaAsSb could be interesting for solar cell applications due to spatial separation of electrons and holes [52-54]. Therefore the effect of various growth parameters on the morphology of GaAsSb shells in self-catalyzed GaAs/GaAsSb core-shell NWs was studied where the Sb content in the shell was tuned in a wide range. In addition, the core-shell geometry in GaAs/GaAsSb core-shell NWs was utilized to explore the WZ phase of GaAsSb. First, the GaAs core was grown in both ZB and WZ phases by using the method reported in Paper II. Subsequently, the GaAsSb shell was grown which copies the crystal phase of the GaAs core. The result of this study is reported in Paper IV.

After the successful growth of NWs on different substrates and making different heterostructures, a study on doping of the NWs was carried out. In this study, the effect of beryllium (Be) dopants on the growth of the NWs as well as on their electrical characteristic was investigated for both Au-assisted and self-catalyzed GaAs NWs. Parts of this study is reported in Paper V.

As the ultimate goal of this PhD thesis project was to produce p-n radial junction NW solar cells, the immediate study after the successful p-doping of core was to investigate n-doping of the radial NW shell. This study was divided into two parts. The first part was dedicated to the optimization of the growth condition to produce a conformal and uniform shell (GaAs or AlGaAs) around the GaAs core. The second part constituted the doping study of the shell using Si or tellurium (Te) as the n-dopants. During this time, an independent report was published in the literature addressing a similar issue [55].

Despite the great potential of the self-catalyzed technique to grow GaAs NWs and the successful demonstration of crystal phase engineering, formation of core-shell geometry and doping, it was however found that the NWs have a poor optical quality. The NWs show weak (i.e. low brightness, only emit at low temperatures) photoluminescence intensity from the GaAs core. The main

PL emission peak was also observed to be centered well below the GaAs free exciton energy reported in the literature [56]. In order to solve this problem, a study comprised of optimization of the NW growth conditions was carried out in order to improve the optical properties. It was concluded that part of the problems are related to intrinsic defects, such as anti-sites and vacancies, which has remained unnoticed in the case of NWs. During the time of this work, a separate theoretical study addressing a similar problem was reported in the literature [57]. By a subsequent suitable design of the NW growth parameters (different V/III ratios), it is now possible to reduce the concentration of such intrinsic defects in the NWs grown with a high V/III ratio. This has led to a clear improvement in the optical quality of the NWs that is similar to published reports in the literature from other groups. The detailed analysis of the results from this study is under process and the manuscript is under preparation (Paper VIII), however not included in this thesis.

When the self-catalyzed NWs are grown on a Si substrate with an unpatterned oxide, the NWs are distributed in a random manner. The surrounding, and hence the growth kinetics is different for each NW in this situation, resulting in NWs with different physical properties. In addition, a two-dimensional parasitic GaAs crystal growth takes place in-between the NWs. However, a reliable device application of a single or as-grown NW array would require NWs with almost identical characteristics and no parasitic crystal growth. For this purpose, position controlled NW growth was also attempted. Here, a layer of SiO<sub>2</sub> on the Si substrates was used as the mask. In the early stage, electron-beam lithography (EBL) was used to make patterns with different oxide hole sizes and pitches. Later, to make the process more cost-effective and for wafer-scale patterning, nanoimprint lithography (NIL) was used. By systematically tuning the growth parameters, the yield of vertical NWs was improved to about 80%. A summary of this study is reported in Paper VI. After achieving the position controlled NW growth, p-i-n junction core-shell NWs were grown on the NIL patterned Si substrates. Subsequently, NW solar cell devices were fabricated on these as-grown NWs and device characteristics were studied. However, as the results from these solar cells are pre-mature, they are not included in this thesis.

The organization of this thesis is as follows: Chapter 2 describes the NW growth techniques, including catalyst-assisted, self-catalyzed and catalyst-free techniques. In Chapter 3, the experimental techniques used to grow and characterize the NWs in this study are briefly explained. Chapter 4 describes the results from the optimization processes including the growth of self-catalyzed GaAs NWs on silicon and graphene substrates, morphological and

structural features of the NWs, formation of core-shell structure, doping, and position-controlled growth. In Chapter 5 a summary and outlook of the work is presented. In Chapter 6 of this thesis, selected published papers during the course of this PhD work are included.

## 2 NW growth mechanisms

The most popular mechanism to grow semiconductor NWs by the bottom-up approach is to use the vapor-liquid-solid (VLS) method. The VLS method was first used by Wagner and Ellis back in 1964 to grow Si whiskers using chemical vapor deposition (CVD) [58]. The name VLS originated from the coexistence of three phases at the growth front, namely vapor-phase precursor, liquid-phase metal catalyst (alloy) and solid-phase NW. In the work of Wagner and Ellis, they grew Si microwires on Si(111) substrates using Au as the catalyst. In 1965, Holonyak Jr. et al. extended this VLS method to III-V compound semiconductors by demonstrating the growth of GaP microwires [59]. In the early 90s, extensive and pioneering work was done by Hiruma et al. on the VLS growth of III-V NWs using metal-organic vapor phase epitaxy (MOVPE) [60, 61]. Along with the growth of regular ZB crystal phase, they demonstrated the possibility of other polytypes such as WZ in the case of InAs NWs [62]. The NWs are preferred to grow along the [111] direction in the case of ZB phase and along the [0001] in the case of WZ. Subsequently, the Au-catalyzed VLS method was successfully used to grow III-V NWs by other techniques, including molecular beam epitaxy (MBE) [63, 64] and chemical beam epitaxy (CBE) [65, 66].

Apart from the Au-catalyzed VLS technique, a gold-free technique called self-catalyzed VLS technique has also been used extensively to grow III-V NWs in recent years. This self-catalyzed technique was first used for the growth of GaP crystals by Ellis et al. back in 1968 [67]. After about more than three decades, the self-catalyzed growth was again employed by Fontcuberta i Morral et al., who grew GaAs NWs on GaAs(111)B substrates by MBE [37]. The main interesting aspects that attracted the NW community are that the self-catalyzed technique is gold-free as well as more advantageous in forming core-shell NW geometry when compared to the Au-catalyzed technique. Later, this technique has also been demonstrated in MBE growth of GaAsSb [68, 69], InAs [70], InAsSb [71] NWs, CBE growth of GaAs [72], InGaAs [73], InSb [74] NWs, and MOCVD growth of GaAs [75, 76], GaAsP [77], InP [78, 79], InPSb [80], and InSb [81] NWs.

An alternative of the VLS technique to grow NWs is to use a catalyst-free technique. In this case, neither any external metal catalyst nor any group III element is needed for the NW growth. The one-dimensional growth is mainly related to the surface energy and facet-dependent growth. The catalyst-free technique has been heavily explored for MOVPE growth of III-V NWs, including GaAs, GaP, InAs and InP [82]. Recently, this technique has also



been extended to MBE growth of GaAs [83], InAs [84-87], InGaAs [88, 89], and InAsP [90] NWs.

In the following, the basic mechanisms for Au-catalyzed and self-catalyzed VLS NW growth techniques are discussed together with a brief outline of the work that has been done on various material systems in the literature.

## 2.1 Au-catalyzed growth

Among all the catalyst-assisted techniques, the Au-catalyzed one is the most used for the NW growth in almost all the material and the growth systems. Figure 2.1 shows a schematic illustration of the Au-assisted growth technique. A gold thin film or nanoparticle is deposited on the substrate (Figure 2.1a). The substrate is then heated to an elevated temperature in presence/absence of the precursor supplied in the form of chemical complexes (MOVPE) or molecular beams (MBE). At this stage Au forms a liquid alloy with the supplied materials or with one of the constituents from the substrate (Figure 2.1b). With continuous supply of the material vapor, more and more materials are accommodated in the liquid droplet and supersaturation takes place. With further supply, the materials in the droplet start to precipitate at the liquid-solid interface, resulting in the initiation of the NW growth (Figure 2.1c). There have been some reports where the metal catalyst that favors the unidimensional growth was reported to be in a solid phase, and the method was referred to as vapor-solid-solid (VSS) [91], which is however debated [64]. In any case, the phase of the catalyst is not important for a NW growth to take place. What is important for the NW growth is that there is a preferential nucleation at the interface between the catalyst and the crystalline solid [92].

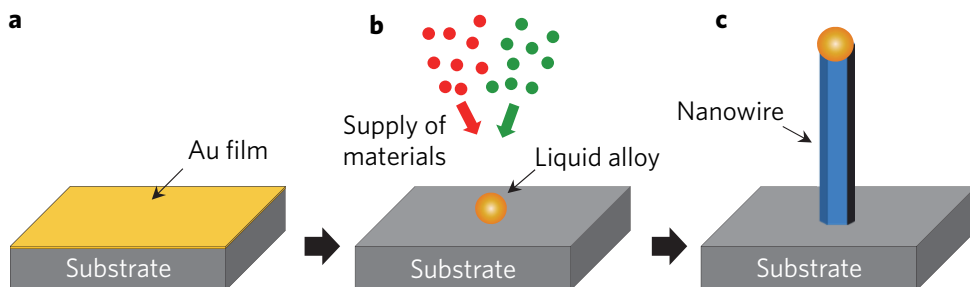


**Figure 2.1. Schematic illustration of the Au-catalyzed NW growth technique.** (a) Deposition of Au film or Au nanoparticle on the substrate. (b) Annealing the substrate with/without the material vapors, forming a liquid alloy droplet. (c) Supersaturation and precipitation of the materials at the liquid-solid interface with continuous supply of the material vapor, resulting in the growth of a NW under the droplet.

Most of the initial works on the Au-catalyzed III-V NWs grown by MOVPE were performed by Samuelson's group in Sweden [65, 93, 94]. Later, the Au-catalyzed technique was employed in the MBE system to grow the III-V NWs. During this time, much theoretical works on the NW growth kinetics were done mostly by V. G. Dubrovskii et al and F. Glas et al [95-98]. They addressed some of the basic mechanisms especially the diffusion induced NW growth by MBE [95] that explains the dependence of the NW growth rate on the NW radius [96], and occurrence of different crystal structures in the NWs [97, 98].

## 2.2 Self-catalyzed growth

In recent years, it was found that the external metal catalyst could incorporate in the NWs during growth. For instance, Au atoms were detected in Au-catalyzed Si [36], InAs [99] and GaAs [35] NWs, which could be detrimental to the optical and electrical properties. The problem can be tackled by instead using a self-catalyzed technique to grow these NWs. This self-catalyzed technique was first employed by Fontcuberta i Morral et al. to grow GaAs NWs using MBE [37] as schematically illustrated in Figure 2.2 for a III-V semiconductor. First, a substrate covered with native or thin deposited oxide that may contain some pinholes is chosen (Figure 2.2a). The substrate is then heated up to a suitable temperature and material vapors are supplied. At this stage, the group-III atoms accumulate in the pre-existing or newly formed pinholes, resulting in the formation of group-III droplets on the substrate (Figure 2.2b). Now, similar to the Au-catalyzed technique, with continuous supply of the vapors, materials supersaturate in the droplet and precipitate as a solid NW (Figure 2.2c).

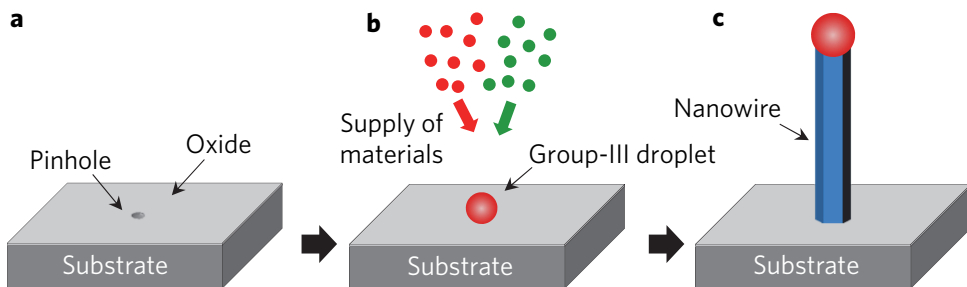


**Figure 2.2. Schematic illustration of the self-catalyzed NW growth technique.** (a) Native oxide covered substrate with nanoscale pinhole. (b) Formation of group-III droplet upon supply of the material vapor. (c) Supersaturation and precipitation of the materials at the liquid-solid interface with continuous supply of the material vapor, resulting in the growth of a NW under the droplet.



## 3 Experimental methods

In this section, the experimental growth technique used to grow the NWs and associated techniques used for their characterizations are briefly discussed.

### 3.1 Molecular beam epitaxy

MBE is a technique widely used for growing epitaxial structures of semiconductors, metals or insulators. The growth is carried out in an ultra-high vacuum condition, with a base pressure of about  $10^{-10}$  Torr, which minimizes the incorporation of impurities from the ambient into the grown structures. Extremely high quality materials are evaporated or sublimated from the effusion cells and are supplied in the form of atoms or molecules. Due to the high vacuum condition, the vaporized particles reach the substrate in the form of atomic or molecular beams without interacting with each other. The growth rates of the epitaxial layers which can be as low as a few Å/s, are controlled by adjusting the temperature of the effusion cells. By using a shutter in front of the effusion cells, the fluxes can be turned on and off abruptly, ensuring abrupt heterointerfaces in a multilayer structure. An additional advantage due to the high vacuum condition is that the epitaxial growth process can be monitored using in-situ characterization techniques such as reflection high-energy electron diffraction (RHEED).

The NW growth in this study was carried out in a Varian Gen II Modular MBE system at NTNU. The main components of the growth chamber are schematically illustrated in Figure 3.1. There are a total of 8 cells installed, as shown in Figure 3.2. This MBE system can be used to grow III-V semiconductors containing Al, Ga, In, As and Sb with Si, Te and Be as the dopants.

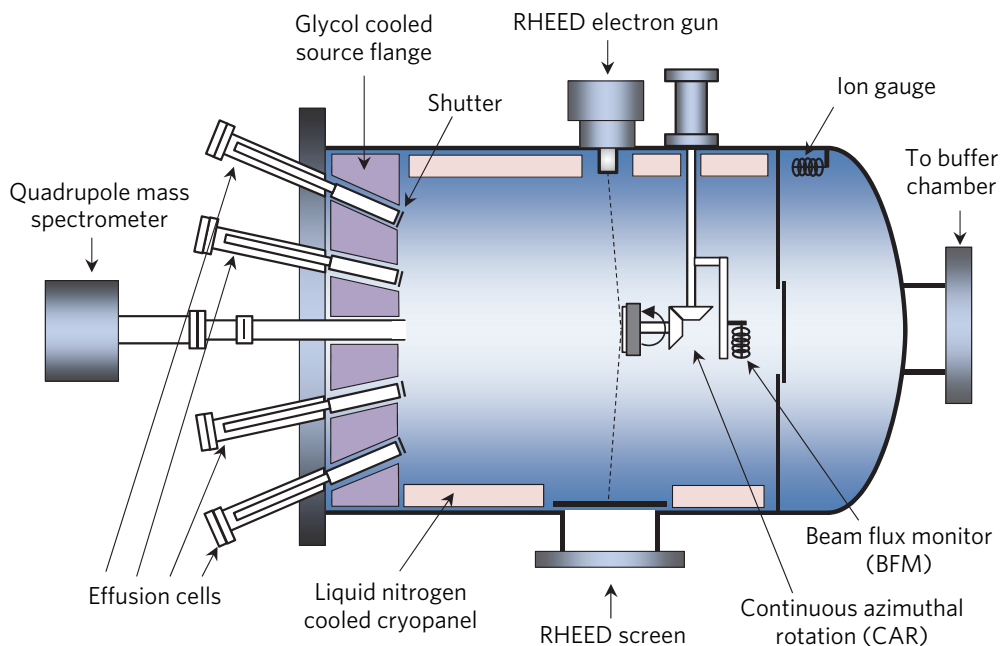


**Figure 3.1. Schematic diagram of the MBE system used in this study.** Four out of the eight effusion cells, RHEED gun, RHEED screen, substrate assembly (CAR), BFM, and other important parts of the growth chamber are indicated in the figure.

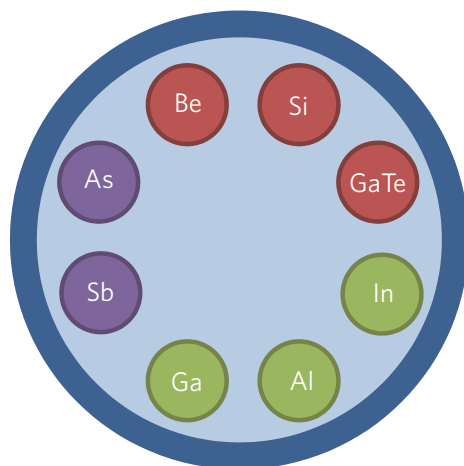


**Figure 3.2. Source materials in the Varian Gen II Modular MBE system at NTNU used in this study.** Schematic drawing of the position of three group III (Ga, Al and In), two group V (As and Sb), and three dopants (Be, Si and GaTe) sources.

In epitaxial thin film growth, monocrystalline material growth takes place on a monocrystalline substrate. If the grown film consists of the same material as that of the substrate, the growth is called homoepitaxy (Figure 3.3a). In the case of heteroepitaxy, the grown film and the substrate are of different materials. Although the heteroepitaxial growth is the most interesting to exploit in order to combine properties of different materials, it is however challenging. The main challenges in the heteroepitaxy are due to the differences in lattice constants and thermal expansion coefficients of the two materials. During the growth of a material with different lattice constant than the substrate, the grown film adopts the same lattice constant in the lateral direction as that of the substrate, up to a certain thickness, resulting in a pseudomorphic growth (Figure 3.3b). However, as the thickness increases, the strain energy in the film increases. After a critical thickness, the strain energy becomes so high that the film undergoes a plastic relaxation by introducing a defect (misfit dislocation) by missing or introducing a half-plane at the heterointerface (Figure 3.3c). Threading dislocations also generated with the misfit dislocations and extends to the bulk. In addition, due to the differences in the thermal expansion coefficients, the film undergoes strain during the cooling down from the growth to ambient temperature, leading to either bending of the substrate or formation of cracks in the grown film [100].

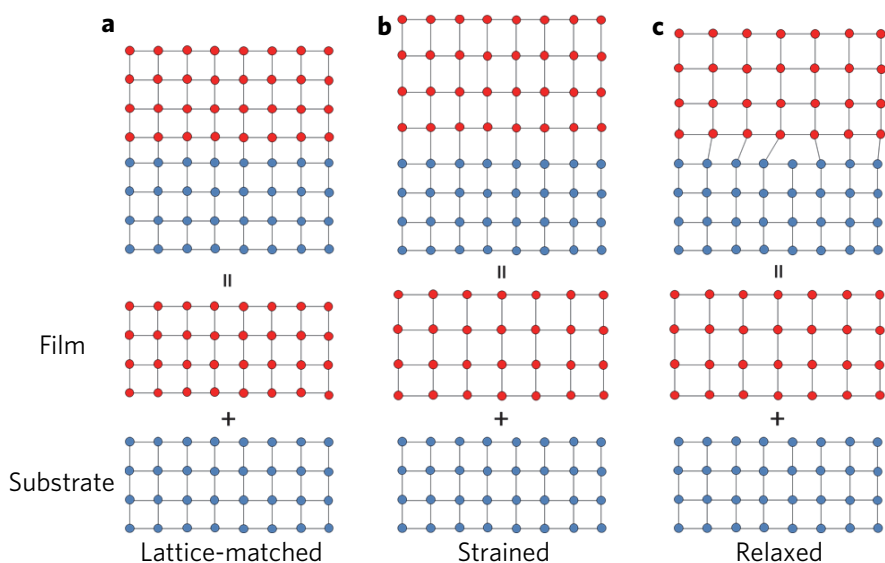


**Figure 3.3. Schematic representation of epitaxial growth.** Illustrations of (a) lattice-matched, (b) strained, and (c) relaxed (misfit dislocation) heteroepitaxial structures. Lattice-matched heteroepitaxy is structurally equivalent to homoepitaxy [100].

## 3.2 Characterization

The characterization techniques used in this study are briefly stated in the following sections.

### 3.2.1 RHEED

The characterization tool that is available in MBE during growth is RHEED. It can be used for growth rate calibration, to monitor oxide removal from the substrate surface, make temperature calibration of the substrate, and study surface reconstruction. An electron beam with energy in the range 2-15 keV strikes the sample at an angle of 1-2° which makes it to be surface sensitive. From the specular reflection and diffraction patterns that form on a phosphor screen, the crystallographic information of the surface can be obtained.

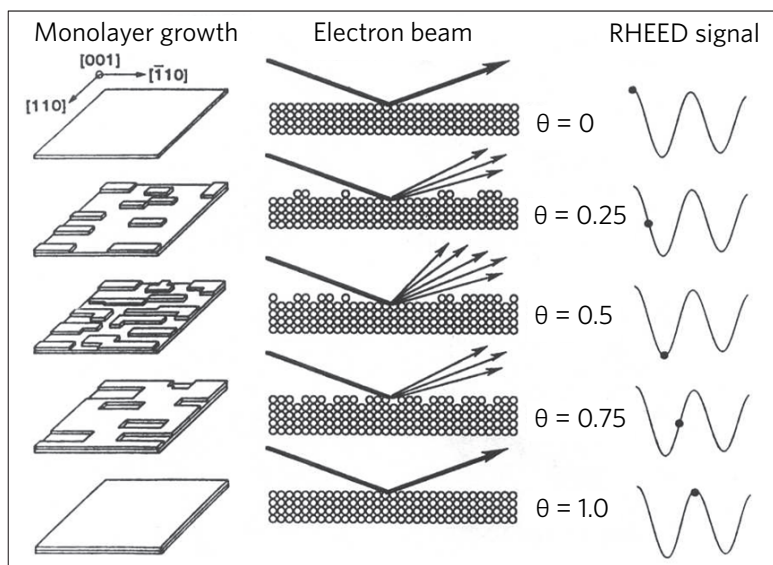


**Figure 3.4. Growth rate calibration by RHEED.** Representation of the formation of a single complete monolayer with the corresponding oscillation in the RHEED intensity signal. The fractional layer coverage is represented by  $\theta$  [100].

For thin film growth, RHEED is used both in static and dynamic modes. In the dynamic mode, the growth rate can be measured directly using the RHEED intensity oscillations. For a layer by layer growth mode, the intensity oscillations are illustrated in Figure 3.4. At the initial stage, the surface is smooth which gives a bright specular spot. As the growth proceeds, the surface becomes rough due the formation of islands, and specular spot

intensity dims. The intensity increases again when the islands coalesce, completing formation of one monolayer. The specular spot intensity continues to oscillate as the film grows. By measuring the periodicity of these intensity oscillations, growth rates of group III materials can be calibrated.

In the case of the static mode, RHEED can be used to study the reconstruction of surfaces. To minimize the energy, the atoms at the surface rearrange into a structure with a symmetry that differs from that of the bulk solid, i.e. a surface reconstruction takes place. The surface reconstruction is sensitive to the temperature. Therefore, by studying the surface reconstruction, the temperature of the surface can be calibrated.

For the NW growth study, RHEED can be used to study the incubation time and the crystal structure of the NW. The electron beam transmits through the NW and produces a diffraction pattern on the RHEED screen. Figure 3.3 shows a typical example of the diffraction pattern during the growth of WZ and ZB GaAs NWs.

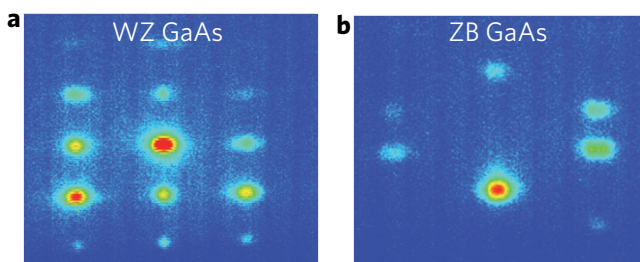


**Figure 3.3. RHEED pattern during GaAs NW growth.** Diffraction pattern during the growth of (a) WZ and (b) ZB GaAs NWs. The direction of the incident beam was along  $\langle 110 \rangle$  direction.

### 3.2.2 Other techniques

**Scanning electron microscopy:** The morphological features of the NWs were studied by Zeiss Supra 55 and Zeiss Ultra 55 scanning electron microscopes (SEM). A Hitachi S-5500 scanning transmission electron microscope (STEM) in the scanning mode was also used. An acceleration voltage in the range of 5-15 keV was used for the secondary electron imaging.

**Transmission electron microscopy:** For the structural characterization, a Phillips CM30 transmission electron microscope (TEM) was routinely used for quick feedback. Bright-field (BF), dark-field (DF), high-resolution imaging (HRTEM) and selected area electron diffraction (SAED) patterns were used to analyze the crystal structures of the NWs. In addition, JEOL 2010F and 2100



TEMs were also used by other colleagues for the results in Papers II, III and VI. All the TEMs were operated at a voltage of 200 keV. For the collaborative work with Lund (Paper IV), a JEOL 3000F TEM operated at 300 kV was used. To determine the chemical composition and the shell thickness in grown core-shell NWs, energy dispersive x-ray (EDX) analysis and high-angle annular dark-field scanning transmission electron microscopy (HAADF STEM) were used.

**Photoluminescence:** The optical properties of the NWs were investigated by micro-photoluminescence ( $\mu$ -PL) spectroscopy. Room and low temperature PL, time-resolved, temperature and power dependent  $\mu$ -PL measurements were used to access the optical quality of the NWs, in order to investigate how it is affected by the crystal structure and possible crystal defects.

## 4 Growth optimization

This chapter focuses on the work undertaken to optimize the NWs for solar cell applications. This include the optimization of NW morphology, reducing the structural defects, extending the range of substrates that can be used for NW growth, doping control, improving optical properties, growth of core-shell and positioned controlled NWs. Since most of the work was focused on the self-catalyzed NWs, the discussion is focused on the different growth optimization processes using the self-catalyzed technique.

### 4.1 Self-catalyzed NWs on Si

The main motivation for the growth of self-catalyzed GaAs NWs is that it is a gold-free growth technique. In this thesis project, Si(111) substrates were chosen instead of GaAs(111)B that were used for the Au-catalyzed growth in the NW group at NTNU, as well as for the self-catalyzed growth in the literature [37, 52]. One of the main challenges was to obtain vertical GaAs NWs on Si(111) substrates. As shown in Figure 4.1a, when the NWs are grown on as-received native oxide covered p-Si(111) substrates (lightly doped, resistivity: 1-50  $\Omega$  cm), apart from the vertical NWs, a substantial number of tilted NWs were also obtained. To reduce the number of tilted NWs, growth parameters such as V/III ratio and growth temperature were varied. An increasing V/III ratio was found to reduce the number of tilted NWs to some extent, although it could not be completely avoided. This increase in vertical NWs with a high V/III ratio could be associated with the reduction of the three-dimensional multiple order twinning [101]. On the other hand, no noticeable change in the yield of vertical NWs was found with the change in the growth temperature.

A more straightforward method to obtain vertical GaAs NWs was found by pre-treating the Si substrates prior to the NW growth. The Si(111) substrates were etched in 5% hydrofluoric acid (HF) for 1 min, rinsed in deionized water and dried by blowing nitrogen. The substrates were then kept in a flow-bench for a few days to form a fresh native oxide. Figure 4.1b shows a SEM image of the GaAs NW grown on such Si(111) substrate with the same growth condition as for the sample in Figure 4.1a. It can be seen that almost 100% yield of vertical NWs were obtained. It was also found that a change of the growth parameters did not influence the yield of the vertical NWs. Due to the growth of vertical NWs with the growth parameters, it was possible to investigate the influence of various growth conditions on the morphological or structural properties of the NWs.

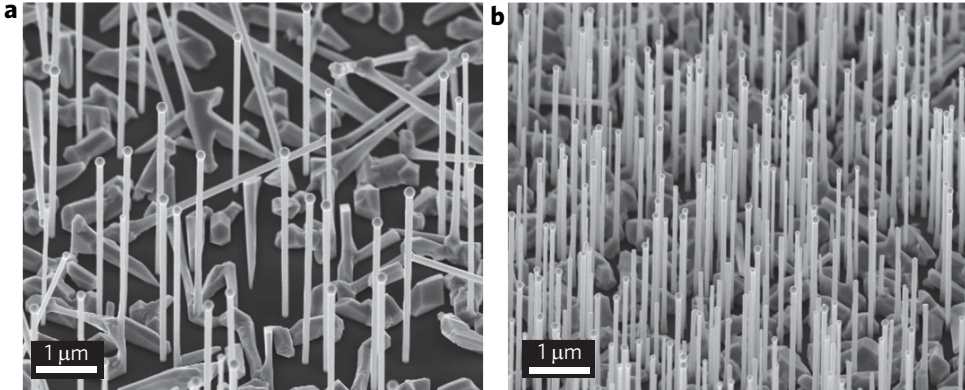


**Figure 4.1. SEM images of self-catalyzed GaAs NWs on Si(111).** (a) NWs grown on an as-received native oxide covered p-Si(111) substrate. (b) NWs grown on a fresh native oxide covered p-Si(111) substrate.

An important issue in this study was the reproducibility of the NW growth, which is necessary to correlate the properties of the NWs from one run to next. If the Si substrates were directly loaded in to the MBE after treating with HF, resulted in either NWs with variations in the density and morphology or an unsuccessful NW growth. On the other hand, highly reproducible NWs were obtained if the substrates were kept in the flow-bench for a few days. This result indicates that the presence of a thin oxide layer helps the formation of NWs. The tilted NWs in the case of the as-received native oxide could be related to a different composition or thickness compared to those of the fresh native oxide.

Another challenge was to have a control on the density of the NWs. Although a high density of NWs might be required for certain applications, it has a few drawbacks as well. For solar cell applications, a maximum solar cell efficiency requires a considerably larger GaAs NW core diameter than that usually obtained by the self-catalyzed technique [29]. Thicker NWs can be accomplished by either controlling the diameter of the Ga particle or by growing a radial shell around the NW core, forming a homo-structured core-shell geometry. Due to the inclined molecular beam axes in the MBE chamber, a shadowing effect from the neighboring NWs play a role on the NW growth kinetics in the case of highly dense NWs once the NW exceeds a certain length [102]. In the case of the core-shell NW structure, this effect often results in an inverse tapering of the NW morphology and thereby a non-uniform shell thickness. This effect can be reduced by lowering the density of NWs.

The density of GaAs NWs was lowered by growing the NWs on heavily doped Si substrates (resistivity:  $<0.005 \text{ } \Omega \text{ cm}$ ). Figure 4.2 shows SEM images of GaAs NWs grown on lightly and heavily doped Si substrates, with the same growth condition and same pre-treatment, as for the samples in Figure 4.1b. A significant difference in the density of NWs grown on the two different substrates was observed. The density of NWs on the lightly and heavily doped substrates was estimated to be  $\sim 7 \times 10^8$  and  $4 \times 10^7$  NWs/cm<sup>2</sup>, respectively. The observed difference in the NW density of at least one order of magnitude can be understood from the dependence of the native oxide thickness on the doping density of the Si substrates. The oxide thickness is known to be lower on lightly doped substrates as compared to that on heavily doped substrates [103]. It is believed that in the case of a thinner oxide, the number density of pinholes in the oxide would be higher than in the case of a thicker oxide. The presence of a higher number of pinholes essentially act as a collection center for the Ga adatoms and eventually results in a higher density of NWs on the lightly doped substrates as compared to the heavily doped substrates. Therefore by selecting the substrates with different doping levels, the density of NWs can be altered if required. In addition, the diameter of the NWs on heavily doped substrates ( $\sim 115 \text{ nm}$ ) is found to be larger than that on lightly doped substrates ( $\sim 75 \text{ nm}$ ) for a growth duration of 20 min. This dependence of the NW diameter on the substrate doping is again attributed to the thickness of the native oxide [104], which has been reported previously [105].

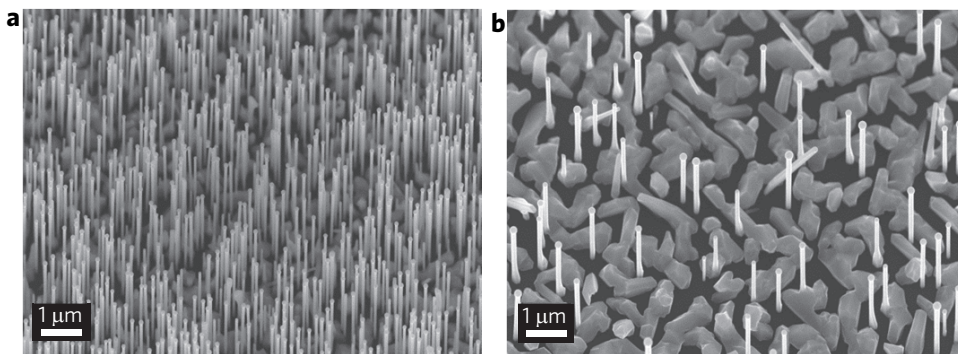


**Figure 4.2. SEM images of self-catalyzed GaAs NWs.** (a) GaAs NWs grown on a lightly doped p-type Si(111) substrate. (b) GaAs NWs grown on a heavily doped p-type Si(111) substrate.

## 4.2 Crystal defects in NWs

The properties of NWs are directly associated with the presence of defects. The occurrence and distribution of the defects may be influenced by the

synthesis process and the growth parameters of the NWs. The defects can be categorized into mainly two types: point defects and extended defects.

### 4.2.1 Point defects

Any deviation from stoichiometry leads to the formation of native point defects in the NWs. The point defects include vacancies, interstitials and antisites. As in the case of thin films, these native point defects affect the physical properties of the NWs. Therefore, it is necessary to optimize the growth conditions in order to control or minimize the point defects. More discussion about on point defects is presented in Chapter 4.6.

### 4.2.2 Extended defects

The most commonly observed extended defect in the NWs is the irregularity in the stacking of atomic planes. A periodic irregularity of the atomic stacking leads to the formation of polytypes in the NWs. It has been observed that the III-V semiconductors can often adopt a different crystal phase than in bulk when grown as NWs. For instance, GaP, GaAs, InP and InAs were found to change their crystal phase from ZB in bulk to WZ in Au-catalyzed NWs grown by MOVPE [62, 106]. In the case of Au-catalyzed MBE, the GaAs NWs usually adopt the WZ phase [64, 97, 107], whereas the self-catalyzed GaAs NWs are usually ZB [108-110]. These two crystal phases are believed to have different properties. For example, theoretical calculations predicted different bandgaps and band offsets [40, 41]. Experimental results showed the bandgap of WZ phase is larger than that of ZB for GaAs [111-113], as well as for other material systems [114, 115]. However for GaAs, contrary reports showing a smaller bandgap of the WZ phase than the ZB phase are also available [112, 116, 117]. In addition to the differences in the bandgap, the linear polarization of the PL emission was found to be strongly dependent on the crystal phase of the NWs. The PL emission from a ZB NW was reported to be polarized along the NW axis, while from a WZ NW the emission is perpendicular to the NW axis [118, 119]. Issues regarding the exact bandgap of WZ GaAs, band offset at the ZB-WZ interface, effective masses of carriers, etc. are still debated.

Due to a small difference in the cohesive energy between these two crystal phases [120], the NWs often suffer from structural irregularities. As the NWs grow in the  $\langle 111 \rangle$  and  $\langle 0001 \rangle$  directions in case of ZB and WZ GaAs, respectively, the stacking sequence of the Ga and As atoms can be represented as in Figure 4.3. In the ZB phase the sequence is ABCABC... (Figure 4.3a),

while in the WZ phase it is ABABAB... (Figure 4.3b), where A, B and C each represents one bilayer with vertically stacked Ga and As atoms.

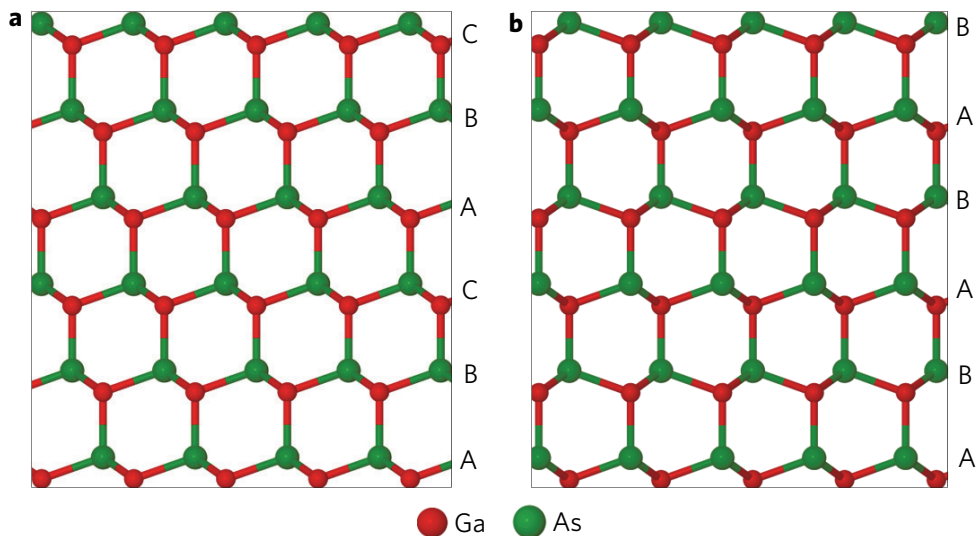


**Figure 4.3. GaAs crystal phases.** Schematic illustrations of atomic arrangements in (a) ZB and (b) WZ crystal phases. Both models are seen along the  $\langle 110 \rangle$  direction.

Commonly observed defects in the ZB and WZ phases are rotational twins and stacking faults (SFs), respectively. A rotational twin occurs in the ZB structure when the stacking changes from ABCABC... to ABCACBA ..., where A is called the twin plane. Here the ZB segment above the twin plane is rotated by  $60^\circ$  around the  $\langle 111 \rangle$  growth axis. In the WZ structure, SFs are local interruptions in the regular stacking after which the stacking continues in the same manner. This can be represented as ABABCACA or ABABCABAB, where C is the faulty placed bilayer. In some reports, a rotational twin in ZB is considered as a minimally thin WZ segment CAC, whereas a SF in WZ as a minimally thin ZB segment ABCC [121]. However in other reports, it has been argued that the sequence should be repeated at least for four bilayers, i.e. CACA and ABCCA before they can be considered as WZ and ZB segments, respectively [106]. Nevertheless, these structural defects or the mixed ZB-WZ structures can be unwanted as they have reported to influence the optical and transport properties of the NWs [43, 122]. In order to avoid these problems as well as to address the issues related to their fundamental properties, it is important to understand the origin of different crystal phases and to have control on their formation in the NWs.

The WZ crystal structure formation in the MBE grown Au-catalyzed GaAs NWs was first theoretically explained by Glas et al. [97]. Later, this

explanation was further elaborated by Dubrovskii et al. and other different groups, and was applied to explain the crystal structure formation in various materials and growth systems [98, 123]. The nucleation based theory predicts that the nucleation can occur either at the liquid-solid interface (C) or at the vapor-liquid-solid interface i.e. at the triple phase line (TPL), as shown in Figure 4.4. The C nucleation favors a ZB phase whereas the TPL nucleation

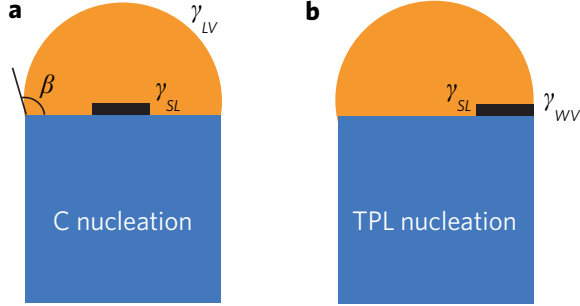


**Figure 4.4.** (a) Nucleation at the center of the NW-liquid interface. (b) Nucleation at the TPL eliminating one solid-liquid interface in panel **a**, and creating a NW-vapor interface.

favors WZ phase. Now the TPL nucleation will take place if the following condition is satisfied.

$$\Delta\gamma = \gamma_{WV} - \gamma_{SL} - \gamma_{LV} \sin \beta < 0,$$

where  $\gamma_{WV}$ ,  $\gamma_{SL}$  and  $\gamma_{LV}$  are the NW-vapor, solid-liquid and liquid-vapor interface energies, respectively, and  $\beta$  is the contact angle of the droplet. Now, considering  $\gamma_{WV} = 1.3 \text{ J/m}^2$ ,  $\gamma_{SL} = 0.59 \text{ J/m}^2$ ,  $\gamma_{LV} = 1.0 \text{ J/m}^2$  for 40% Ga in the Au-Ga alloy [124], and  $\beta \approx 110^\circ$  in the case of Au-catalyzed MBE grown GaAs NWs, it can be shown that the above conditions are satisfied. This means a TPL nucleation is favored, resulting in the formation of a WZ structure. However in the case of self-catalyzed GaAs NWs, due to the low surface energy ( $\gamma_{LV} \approx 0.67 \text{ J/m}^2$  at typical growth temperature) and larger contact angle ( $\beta \approx 130^\circ$ ) of the Ga droplet [108], the above condition does not hold, resulting in a central nucleation favoring a ZB structure.

It was shown that Au-catalyzed GaAs NWs can be grown in the ZB structure by increasing the content of Ga in the Au-Ga alloy droplet. In this study it was found that a high V/III ratio favors a WZ structure whereas a low V/III ratio favors ZB structure in MBE grown Au-catalyzed GaAs NWs. The low V/III ratio changes the growth mode from Au-catalyzed to pseudo Ga-catalyzed, thereby resulting in a ZB phase. These results where a control of the crystal phase of Au-catalyzed GaAs NWs was achieved are reported in

Paper I. This result was further supported by the finding of Soda et al. who observed an uncontrolled change of the crystal phase from WZ to ZB in Au-catalyzed MBE grown GaAs NWs [125].

Here it should be noted that in all the above theoretical studies, the cross-section of the NW was considered as cylindrical [97, 98, 123]. However, in all the experimental studies the NW cross-section was found to be hexagonal. Krogstrup et al. first took into account the hexagonal shape of the NW cross-section, and showed that the droplet shape will change as a function of its relative volume [126]. The change in the droplet shape has a huge impact on the nucleation statistics. In this theory, the NW growth is divided into two regimes: 1) the droplet stays only on the top (111) NW surface without touching the edge of the NW top-facet, and 2) the droplet spreads to the NW side-facets and wets the NW sidewalls. Here, the important parameters that will affect the nucleation probability are: the fraction of the TPL in contact with the edge of the NW top-facet ( $\chi$ ), and the contact angle of the droplet ( $\beta$ ), as illustrated in Figure 4.5.

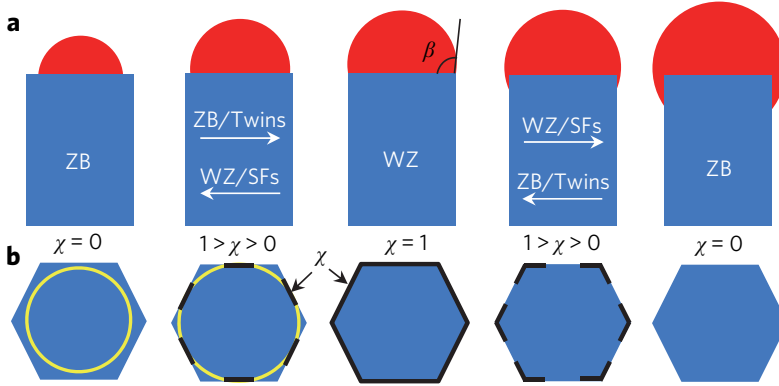


**Figure 4.5. Schematic illustration of the crystal phase evolution as a function of  $\chi$  and  $\beta$ .** (a) Side-view and (b) top-view of the Ga droplet and NW top-facet showing the change in  $\chi$  with the change in  $\beta$ . The resulting change in the crystal phase of the NW is indicated.

An experimental demonstration is shown in Figure 4.6 for a self-catalyzed GaAs NW where the Ga droplet was consumed into the NW. Before the beginning of the consumption process, the droplet was completely wetting the NW sidewall ( $\chi = 0$ ), resulting in only central nucleation and the formation of the ZB phase [108, 127]. As the consumption starts, the contact angle shrinks and part of the TPL is in contact with the edge of the NW top-facet ( $1 > \chi > 0$ ) which increase the probability for TPL nucleation. With further consumption of the droplet,  $\chi$  approaches gradually to 1. This results in a transition of the crystal phase from twinned ZB to WZ with SFs, and eventually pure WZ. With the continuation of the shrinkage of the droplet



volume, the droplet sits solely on the (111) NW top-facet ( $\chi = 0$ ), resulting in a ZB phase through a transition region as indicated in Figure 4.6.

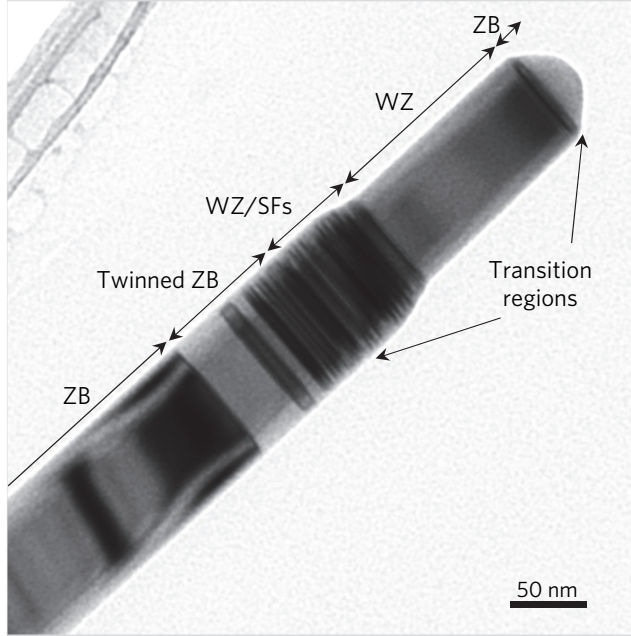
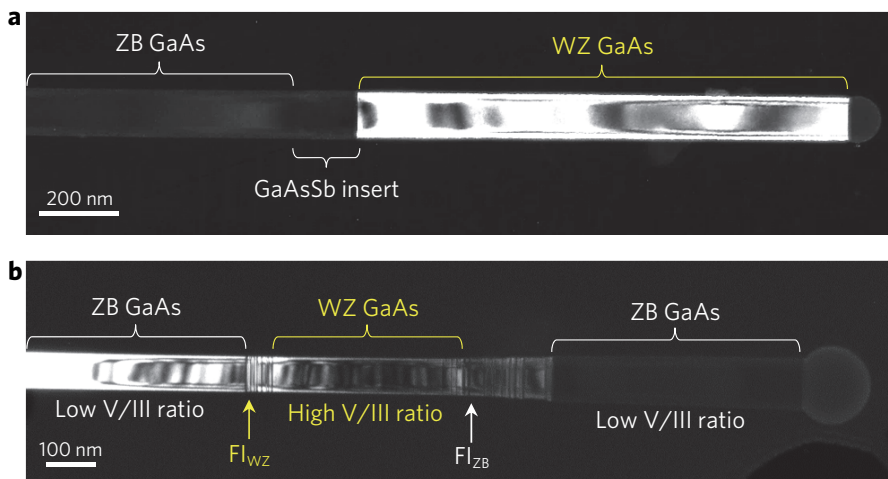


**Figure 4.6. Crystal phase change in self-catalyzed GaAs NW.** BF TEM image of a GaAs NW tip where the Ga droplet was consumed in presence of an As flux.

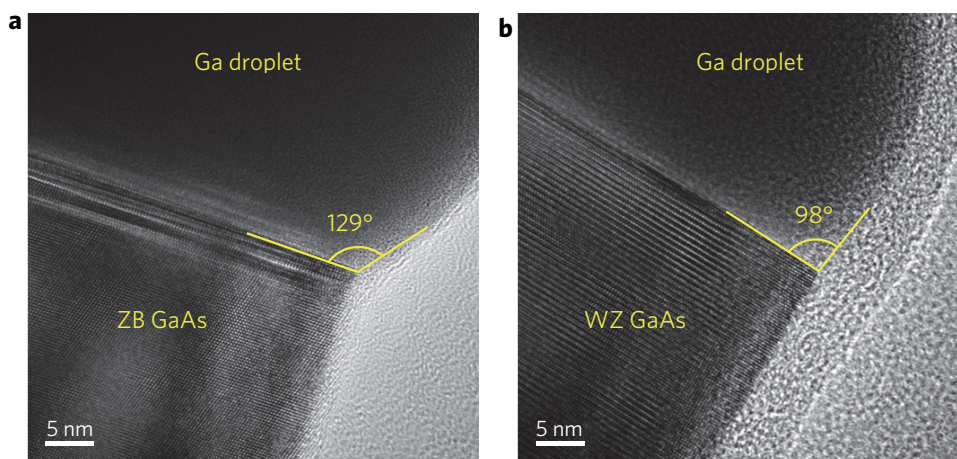
This phenomenon was utilized to engineer the crystal phase of self-catalyzed GaAs NWs using two different techniques; a) using a GaAsSb insert, and b) by changing the V/III ratio and using a flux interruption (FI). As an example, Figure 4.7a shows a self-catalyzed GaAs NW with an axial GaAsSb insert. The GaAs segment below the insert is ZB, whereas the segment after is pure WZ which results from a change in the contact angle during the growth of the insert. Therefore the use of a GaAsSb insert is a very straightforward technique to obtain pure WZ GaAs in self-catalyzed GaAs NWs.

Figure 4.7b shows a control of the crystal phase in a self-catalyzed GaAs NW using FIs and by changing the V/III ratio. The bottom part of the NW is as usual ZB ( $\chi = 0$ ), after which a  $FI_{WZ}$  was used where the Ga flux was closed and the As flux was kept open. Here the Ga droplet started to consume which decreased the contact angle. When the growth was resumed, the condition  $\chi = 1$  is satisfied, resulting in a TPL nucleation forming a WZ phase. After that a second  $FI_{ZB}$  was introduced where the As flux was closed and the Ga flux was kept open to increase the contact angle by Ga refilling.

Then the growth was continued with a low V/III ratio, the  $\chi = 0$  condition resulting in the formation of the ZB phase.



**Figure 4.7. Crystal phase engineering in self-catalyzed GaAs NWs.** (a) DF TEM image of a GaAs NW with an axial GaAsSb insert. GaAs is ZB below the insert and WZ above. (b) DF TEM image of a GaAs NW grown with different V/III ratios and FIs.  $FI_{WZ}$  and  $FI_{ZB}$  are FIs to obtain WZ and ZB phases, respectively.



**Figure 4.8. HRTEM image of ZB and WZ self-catalyzed GaAs NWs.** (a) ZB GaAs NW grown with a low V/III ratio and a large contact angle. (b) WZ GaAs NW grown with a high V/III ratio and a small contact angle. Images acquired by J. Todorovic.

The change in the crystal phase by changing the droplet contact angle can clearly be seen in Figure 4.8. The high-resolution (HR) TEM images show that a contact angle of about  $129^\circ$  favors the ZB phase, whereas a contact angle of about  $98^\circ$  favors the WZ phase in the self-catalyzed GaAs NWs. The details of

this crystal phase engineering in self-catalyzed GaAs and GaAs/GaAsSb NWs is reported in paper II. The crystal phase change in self-catalyzed GaAs NWs by modifying the Ga droplet contact angle has also been reported in the literature [70, 128, 129].

### 4.3 NW growth on graphene

For the epitaxial growth of semiconductor NWs, the common practice is to use a rigid crystalline semiconductor substrate. The use of these conventional substrates like GaAs and Si are necessary as they hold immediate applications to the existing technology. However, the rigidness and opacity of these substrates might not be suitable for flexible and transparent device applications. Moreover, the NWs that are the active materials of the device are only a few  $\mu\text{m}$  long, whereas the substrates are typically 100s of  $\mu\text{m}$  thick and therefore might also not be so cost effective. One potential alternative of these conventional substrates that could address these issues is graphene, a two-dimensional one-atom-thick crystal made of carbon. Due to its unique material characteristics including high electrical [130] and thermal [131] conductivities, optical transparency [132], and mechanical flexibility and strength [133], graphene is a potential candidate for next-generation transparent, foldable and stretchable device applications [134-136].

In recent years, there has been great improvement on the synthesis of high quality graphene using various methods, including chemical vapor deposition (CVD) grown graphene on different metal foils [137-145], and synthesis of epitaxial graphene on SiC substrates [146-149]. Moreover, recent low-cost roll-to-roll [150, 151] and large-area [146, 152] synthesis methods have reduced the cost of graphene. The improvement in the transfer process of graphene from the growth substrate to an arbitrary substrate has made it possible to obtain clean and high quality graphene in larger areas [153-155]. By using graphene as a substrate for the epitaxial growth of semiconductor NWs a new class of hybrid semiconductor/graphene material system can be developed. In such hybrid systems, the NW will act as the active device material whereas graphene will act as a flexible electrode enabling various electronic and optoelectronic devices, such as flexible light emitting diodes (LEDs), displays [156-158] and solar cells [159-161].

In graphene the carbon atoms are bonded with  $sp^2$ -hybridization [162, 163]. The carbon atoms are arranged in a regular hexagonal honeycomb lattice structure as shown in Figure 4.9. The absence of dangling bonds at its surface makes graphene chemically inert to any foreign atoms, which result in

challenges in growing three-dimensional semiconductor materials by conventional epitaxy. An alternative method to circumvent this problem is to use van der Waals epitaxy (vdWE) [164]. Due to the different bonding mechanism in vdWE, compared to conventional epitaxy with strong chemical bonding, the grown materials do not need to be lattice matched with the graphitic substrate and no strain induced interfacial defects are to be expected. Due to the increasing interest of using graphene as a substrate material for epitaxial growth, recent density functional calculations have been employed to investigate the adsorption sites and adsorption energies of different atoms and molecules on the graphene surface [165, 166]. These theoretical calculations predict the plausibility of also conventional epitaxy i.e. non-vdWE (based on a covalent or ionic binding mechanism) for growing different materials on graphitic surfaces. Based on this growth mechanism, in the following, different atomic arrangements of the semiconductor atoms on graphene are discussed for a successful non-vdWE growth to take place.

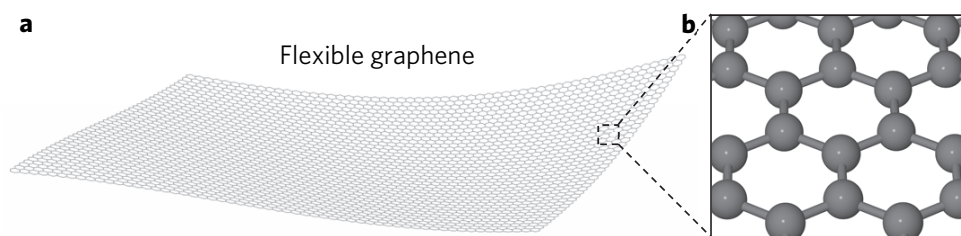


**Figure 4.9. Schematic drawing of graphene.** (a) Flexible graphene. (b) Magnified view of graphene showing the hexagonal carbon rings.

The epitaxial growth of vertical NWs on graphene can be understood considering the different adsorption sites of semiconductor atoms on the graphene surface. As shown in Figure 4.10, the sites can be identified as 1) above the center of the hexagonal carbon rings (H-site), 2) above the bridge between the carbon atoms (B-site), and 3) above the top of a carbon atom (T-site). With this model, different atomic arrangements with hexagonal symmetry, on the (111) plane for ZB and (0001) plane for WZ semiconductor, can be obtained on the graphene surface. These atomic arrangements will result in different lattice matching conditions of the semiconductor with graphene. The degree of lattice mismatch resulting from different atomic arrangements is obtained for most of the conventional semiconductors as is reported in paper III.

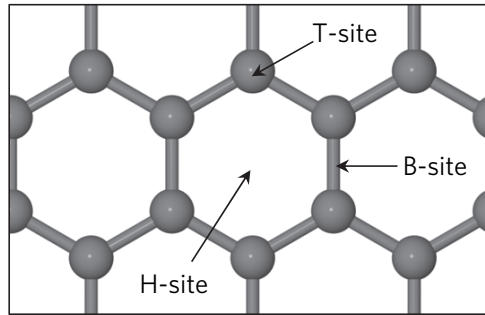


**Figure 4.10. Adsorption sites of semiconductor atoms on graphene.** H-site: center of the carbon ring; B-site: bridge between the carbon atoms; T-site: on top of the carbon atom.

The growth of self-catalyzed GaAs NWs was explored on different graphitic substrates in this thesis. Three different types of substrates were used, namely 1) Kish graphite, 2) exfoliated CVD graphene on SiO<sub>2</sub>/Si and 3) epitaxial graphene on SiC. For the NW growth, initially a growth temperature above 600 °C was used, similar to that on Si substrates. Although vertically aligned GaAs NWs were successfully achieved, their density was very low. This low density of NWs was ascribed to the non-wetting nature of the Ga droplets that form at the early stage of the growth on the graphitic surface. The density of NWs was found to increase by reducing the growth temperature to 500-540 °C (Figure 4.11a). However, the low growth temperature also increased the formation of parasitic GaAs crystal that eventually covered the substrate with increasing growth durations (Figure 4.11b). Both of these issues were partly solved by adapting a two-temperature growth technique. Here the NWs were nucleated at a low substrate temperature, whereas the NW growth was continued at a higher temperature (Figure 4.11c).

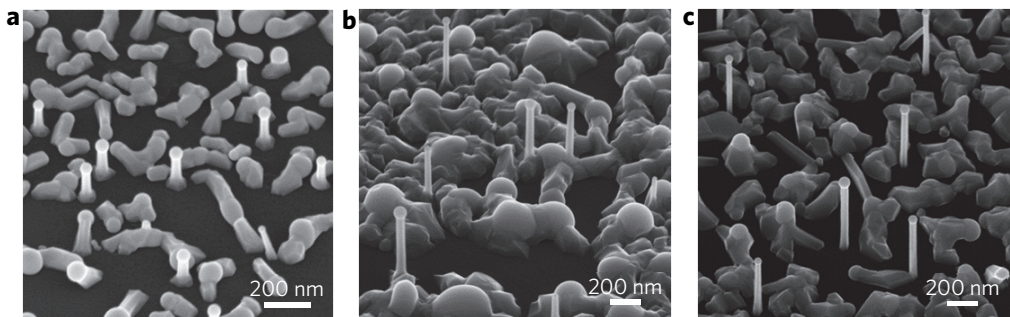


**Figure 4.11. Self-catalyzed GaAs NW growth on graphitic substrates.** GaAs NW growth at low temperature for (a) 2 min and (b) 10 min. (c) GaAs NW growth using a two-temperature technique. Nucleation of the NWs was achieved at low temperature (540 °C) for 10 s followed by the NW growth at high temperature (610 °C) for 5 min.

Apart from the demonstration of the growth of vertical GaAs NWs, the graphitic substrates have also been used to grow InAs NWs. Kish graphite as well as fresh native oxide covered Si(111) substrates were loaded in the MBE for the NW growth. In both substrates, vertically aligned InAs NWs were successfully achieved, as shown in Figure 4.12. In contrast to the GaAs NWs, the density of InAs NWs on the graphitic substrate was found to be higher. The absence of any catalyst droplet at the tip of the InAs NWs indicates that the NWs were grown by a catalyst-free mechanism. The catalyst-free growths of InAs as well as InGaAs NWs on graphitic substrates have also been reported by Hong et al. and Mohseni et al. using MOCVD [51, 167-169]. These successful growths of III-V NWs on different graphitic substrates open up for the development of new hybrid system where the unique properties of both NWs and graphene can be utilized for fabricating various novel devices.

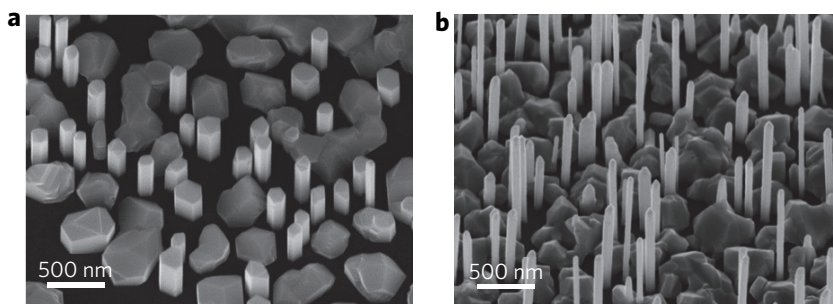


**Figure 4.12. InAs NW growth on graphitic and Si(111) substrates.** Catalyst-free InAs NW growth on (a) Kish graphite and (b) Si(111) substrates.

## 4.4 Core-shell NW growth

Among others, the growth of conformal NW shells is one of the main advantages of the self-catalyzed technique. In the case of Au-catalyzed MBE, due of the presence of the Au catalyst, an unwanted axial growth of the shell material takes place during the shell growth. In contrast, the Ga catalyst droplet can be consumed into the NW to terminate the axial growth, as shown in Figure 4.6 to terminate the axial growth. Subsequently, the growth is resumed forming a perfect core-shell geometry using the vapor-solid (VS) growth.

#### 4.4.1 GaAs/AlGaAs core-shell NW

It is well-known that the GaAs surface is prone to contain surface states which cause a deterioration of its optical properties. This problem becomes severe in the case of NWs because of their huge surface to volume ratio. To passivate the bare GaAs core, a larger bandgap material such as AlGaAs shell is epitaxially grown which protects the core from surface recombination. The shell growth can be carried out either at the same growth temperature as that for the core (600-640 °C), or at a lower temperature (~460 °C), depending on the requirement of the targeted applications. For a radial junction core-shell NW solar cell, a p-doped core and an n-doped shell are required. In the studies done during the PhD thesis project, Be was used as the p-dopant while either Si or Te was used as the n-dopants. An efficient and successful n-doping of the GaAs shell using Si or Te require a lower substrate temperature than that of the p-doped core. On the other hand for growing an undoped or p-doped shell, the growth temperature can be as high as for the core. In both cases, optimized V/III ratios are necessary for obtaining a uniform shell.

To see the effect of the As flux on the AlGaAs shell morphology, two GaAs NW samples were grown at a substrate temperature of 640 °C with a Ga growth rate of 0.7 ML/s and an As<sub>4</sub> flux of  $5.5 \times 10^{-6}$  Torr. After growing the GaAs core, the Ga droplet was solidified to terminate the axial growth. For the growth of the AlGaAs shell in the first sample, an Al rate of 0.3 ML/s was used, with other parameters same as that of the core (Figure 4.13a). In the second sample, only the As<sub>4</sub> flux was increased to  $1.3 \times 10^{-5}$  Torr during the shell growth (Figure 4.13b). In the first sample, it was seen that for some

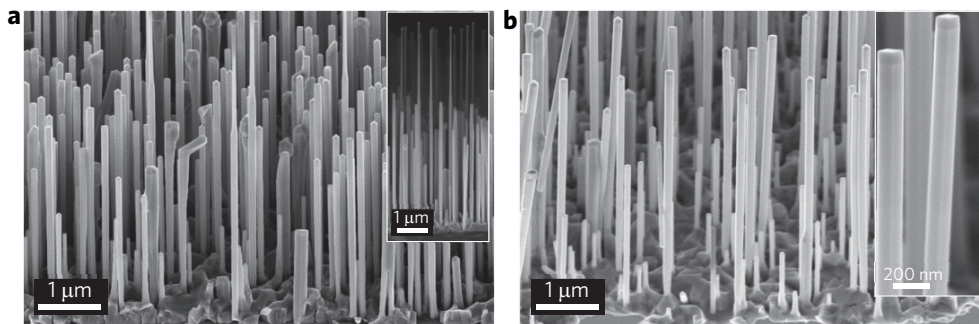


**Figure 4.13.** Effect of As flux on the shell morphology in self-catalyzed GaAs/AlGaAs core-shell NWs. AlGaAs shell grown with Ga rate = 0.7 ML/s, Al rate = 0.3 ML/s at 640 °C and with an As<sub>4</sub> flux of (a)  $5.5 \times 10^{-6}$  Torr and (b)  $1.3 \times 10^{-5}$  Torr. Inset in panel a is a side-view SEM image showing resumption of the VLS growth of the shell material during the shell growth. Inset in panel b is a magnified view SEM image showing the uniform shell morphology.

of the NWs the VLS growth resumed. Due to a low V/III ratio, a droplet of group III elements formed on the (111) top-facet of the GaAs core that resulted in the resumption of the VLS growth [170]. On the contrary in the second sample, a droplet could not be formed due to the use of a high V/III ratio. Here only the VS growth took place resulting in a uniform core-shell NW. This result shows that uniform shells can be obtained at high substrate temperature using a high V/III ratio in self-catalyzed core-shell NWs.

Now to see the effect of the growth temperature on the shell morphology, two GaAs/AlGaAs core-shell NW samples were grown. The shell growth temperature was reduced from 640 °C to 550 °C (Figure 4.14a) and 460 °C (Figure 4.14b), keeping all the other parameters the same as that of Figure 4.13b. It is evident that as the growth temperature was reduced to 550 °C, the morphology became anti-tapered (Figure 4.14a). The anti-tapering increased and a strange tip morphology appeared with a further reduction of the growth temperature to 460 °C (Figure 4.14b).

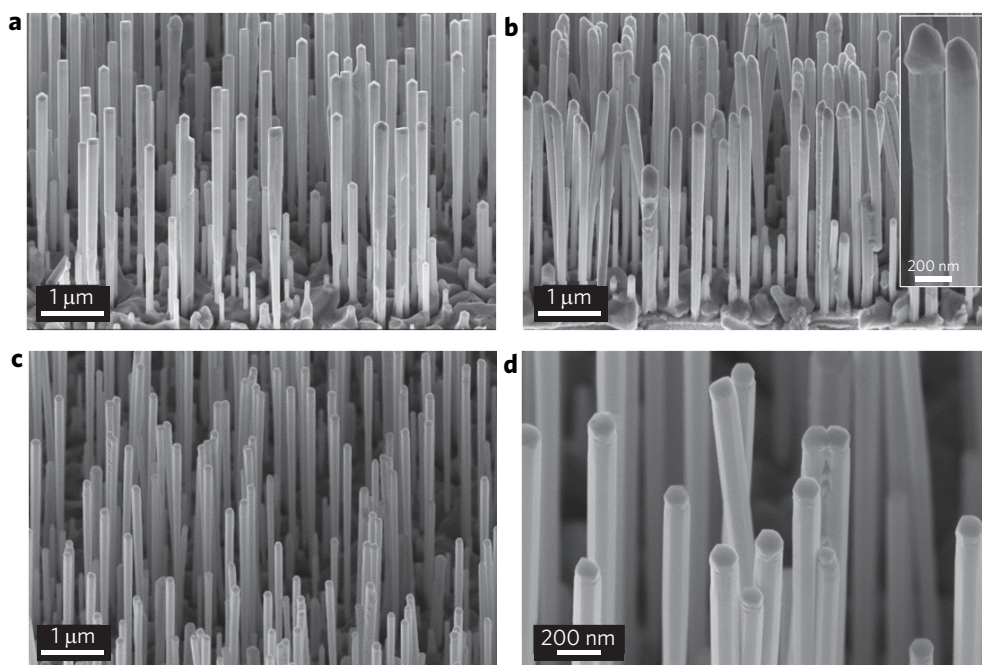


**Figure 4.14. Effect of the growth temperature and the group III rate on the shell morphology.** AlGaAs shell grown with Ga rate = 0.7 ML/s, Al rate = 0.3 ML/s,  $As_4 = 1.3 \times 10^{-5}$  Torr at growth temperatures (a) 550 °C and (b) 460 °C. Magnified view in the inset of panel b shows anti-tapered morphology with strange tip shape. (c) AlGaAs shell grown with Ga rate = 0.1 ML/s, Al rate = 0.1 ML/s,  $As_4 = 1.3 \times 10^{-5}$  Torr at growth temperatures 460 °C. (d) Magnified view of the NWs in panel c showing uniform shell morphology.



This problem was solved by reducing the group III growth rates, as shown in Figure 4.14c,d. Using a Ga rate of 0.1 ML/s and an Al rate of 0.1 ML/s, a uniform shell morphology was obtained. The observed change in the shell morphology can be explained in the following. With the decrease of the growth temperature the diffusion length of the group III adatoms decreases. This decrease is more prominent when a high growth rate is used. Due to the inclined molecular flux in the MBE, the sidewalls of NWs suffer from a shadowing effect due to the closely spaced neighboring NWs. The tip of the NWs collects more adatoms as compared to the bottom part due to this shadowing effect. When a high growth rate is used, the diffusion length of the adatoms is reduced so that they get incorporated at the tip area before they can migrate to the bottom part of the NW, resulting in either anti-tapered or a strange tip shaped morphology. As the growth rate is reduced, the diffusion length of the adatoms becomes sufficient enough to diffuse from the tip to the bottom part of the NW, resulting in a uniform shell morphology. Therefore it was concluded that a low growth rate and a high V/III ratio are essential to grow uniform shells at low temperature.

Different NW tip morphology can be observed for shell grown at high and low temperatures, as shown in Figure 4.15. After growing the GaAs NW core and solidifying the Ga droplet, AlGaAs shells were grown at 640 and 460 °C. High temperature shell growth results in a NW tip with three inclined {110} facets (Figure 4.15a), whereas no such well-defined facets at the NW tip can be observed when the shell was grown at low temperature (Figure 4.15b). This difference in the tip morphology can be attributed to the temperature dependent growth rates on different facets. At a high growth temperature, the growth rates on {110} facets are slow resulting in larger developed facets at the NW tip.

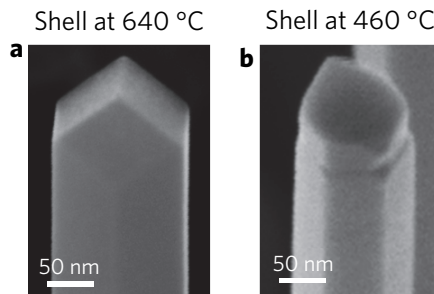


**Figure 4.15. Effect of shell growth temperature on the tip morphology.** (a) AlGaAs shell grown at high temperature (640 °C), resulting in a NW tip with three {110} facets. (b) AlGaAs shell grown at low temperature (460 °C) resulting in a rough NW tip.

#### 4.4.2 GaAs/GaAsSb core-shell NW

Formation of GaAs/GaAsSb core-shell geometry in ZB NWs was investigated by varying the growth temperature, Sb flux and the shell growth durations. The Sb composition was varied from ~10-70% in the shell. The effect of the shell growth temperature and the Sb flux on the shell morphology, is shown in Figure 4.16. Shells grown below 550 °C with an Sb flux of  $1.1 \times 10^{-6}$  Torr, have a rough morphology similar to that shown in Figure 4.16a, whereas those grown above 550 °C have a homogeneous morphology similar to the NWs shown in Figure 4.16b. Similar homogeneous shell morphology below 550 °C can also be achieved by lowering the Sb flux to  $1.1 \times 10^{-6}$  Torr, as shown in Figure 4.16c. Therefore the inhomogeneous rough shell morphology is attributed only to the Sb content in the shell. Strain induced island growth mode is activated for higher Sb content, resulting in a rough shell morphology.

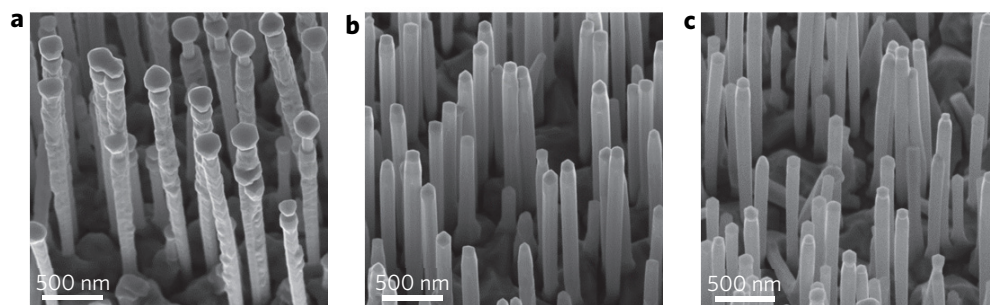


**Figure 4.16. GaAs/GaAsSb core-shell NWs.** GaAsSb shell grown with an  $\text{Sb}_2$  flux of  $1.1 \times 10^{-6}$  Torr at (a) 470 °C and (b) 570 °C. (c) GaAsSb shell grown with an  $\text{Sb}_2$  flux of  $2 \times 10^{-7}$  Torr at 470 °C. Images acquired by S. G. Ghalamestani.

In addition, utilizing the core-shell geometry the WZ phase of GaAsSb, which normally adopts a ZB phase, was also demonstrated. A WZ GaAs core was first grown using a GaAsSb insert, where GaAs is ZB below the insert and WZ above, as described in Figure 4.7a (Paper II). Subsequently, a GaAsSb shell was grown which copies the crystal structure of the core resulting in ZB and WZ GaAsSb. Moreover, a slower GaAsSb shell growth rate was observed on the WZ GaAs segment than on the ZB segment, which is attributed to the lower surface energy of the WZ facets as compared to the ZB facets [171]. The results of the GaAs/GaAsSb core-shell study are reported in Paper IV.

## 4.5 Doping

In this thesis project, p-type doping of GaAs NWs was studied using Be as the p-dopant. The nominal planar doping concentration was varied by changing the effusion cell temperature. Self-catalyzed GaAs NWs were grown at 630 °C for 40 min with a Ga rate = 0.7 ML/s, As<sub>4</sub> flux =  $5.5 \times 10^{-6}$  Torr, and with Be cell temperatures of 990, 1025, 1075, and 1125 °C, as shown in Figure 4.17. The estimated nominal doping concentrations for these temperatures are roughly between  $1.5 \times 10^{18}$  cm<sup>-3</sup> and  $3.5 \times 10^{19}$  cm<sup>-3</sup> in planar GaAs layers.

In the NWs grown with  $T_{\text{Be}} = 990$  °C (Figure 4.17a), no change in the morphology of the Be-doped NWs can be observed as compared to undoped GaAs NWs. With an increase in the Be cell temperature, some of the Ga droplets started to consume terminating the VLS growth (Figure 4.17b,c). With the Be cell temperature at 1125 °C, all the Ga droplets are consumed (Figure 4.17d). This result indicates that under a high Be flux, the self-catalyzed growth cannot be sustained. The consumption of the Ga droplet is likely to be related to the reduction of the diffusion length of Ga adatoms that migrate from the substrate. To confirm this claim, one additional sample was grown by increasing the Be cell temperature to 1165 °C keeping all other parameters same as in Figure 4.17. It was observed that the NWs in this

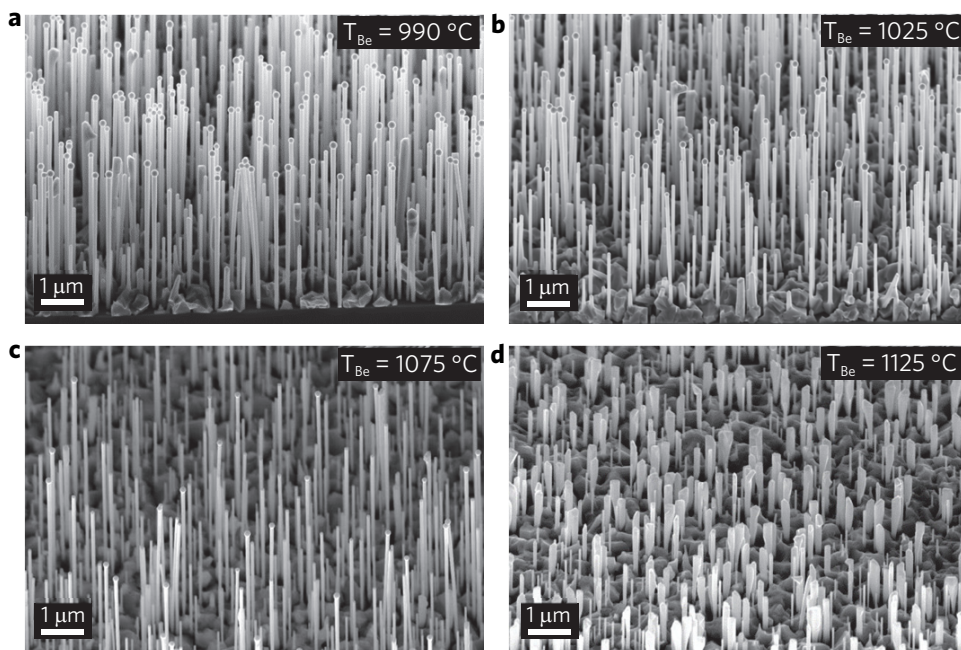


**Figure 4.17. Effect of Be cell temperature on the growth of self-catalyzed GaAs NWs.** Be-doped self-catalyzed GaAs NWs grown with Be effusion cell temperatures of (a) 990 °C, (b) 1025 °C, (c) 1075 °C and (d) 1125 °C.

are even shorter than the NWs grown with  $T_{\text{Be}} = 1125$  °C. In addition, a clear monotonic increase in the two-dimensional parasitic crystal growth on the substrate with the increase in the Be concentration was observed. This indicates that an increase in the Be concentration reduces the diffusion length of Ga adatoms. Hilde et al. reported a similar increase in the parasitic crystals, and the NWs were reported to be kinked and tapered with the increase in the Be concentration [172].

The structural and electrical characteristics of the NWs grown with  $T_{\text{Be}} = 990$  and  $1025$  °C are reported in Paper V and are compared with Au-catalyzed GaAs NWs grown with similar doping concentrations ( $T_{\text{Be}}=990$  and  $1025$  °C). This study shows that p-doping of the GaAs core can be obtained consistently and effectively in the case of self-catalyzed NWs in contrast to Au-catalyzed NWs. The doping incorporation path in the case of VLS grown NWs is usually considered to be via the catalyst droplet. So the observed difference in the doping of the self- and Au-catalyzed GaAs NWs might be due to the difference in the catalyst composition. However, another dopant incorporation path can be diffusion of Be atoms from the sidewall of the NW to the core. Since the self-catalyzed NWs were grown at higher temperature ( $\sim 630$  °C) than the Au-catalyzed NWs ( $\sim 510$  °C) the diffusion would only be prominent only in the former case, giving rise to the higher doping. Indeed, during the same time as this study, a report by Casadei et al. was published which showed that the Be incorporation in the GaAs NWs is mainly via diffusion from the sidewall to the core [173].

After achieving p-type GaAs core, study was carried out to obtain n-type GaAs shell using either Si or Te as the dopants. For this purpose, intrinsic GaAs NW core was grown on Si(111). Subsequently, after consuming the Ga droplet, n-GaAs radial shell was grown on  $\{110\}$  side-facets of the NW core. Electrical characterization was carried out by two-probe contacts after breaking off the NWs from the substrates. Successful n-type doping of the GaAs shell was achieved when the shell was grown at low temperature ( $\sim 460$  °C) and with a high V/III ratio. Due to the amphoteric nature of Si in GaAs, a low growth temperature and a high V/III ratio (i.e. As-rich condition) are essential for incorporating Si on Ga-sites in order to act as a donor. These conditions have previously been shown to be optimum for a successful n-doping of GaAs NW shell using Si [174]. Dimakis et al. have recently reported a detailed study using Si as the n-type dopant of the GaAs shell [55]. By using Raman spectroscopy and electrical characterization it was shown that high donor concentration could be achieved for shell grown at low temperature ( $\sim 440$  °C) and with high V/III ratio [55]. For shell grown at higher temperature ( $\sim 490$  °C) or with low V/III ratio, Si incorporates both as donor

and acceptor, increasing its amphoteric nature. On the other hand, for Te-doping process in planar GaAs is known to be difficult to control [175]. Te tends to accumulate on the surface by segregation and forms a stable surface compound presumably GaTe, resulting in non-uniform doping profile. For the planar growth, this problem had been solved by reducing the growth temperature below  $\sim 530$  °C [176]. Indeed for the GaAs shell growth in this study, a low temperature growth together with a high V/III ratio resulted in a successful n-type doping of GaAs using Te. The achievement core-shell NWs with p-type GaAs core and n-type GaAs shell is essential for the realization of NW devices, in particular radial junction NW solar cells.

## 4.6 Optical properties

The optical properties of the self-catalyzed GaAs NWs were studied by photoluminescence (PL) spectroscopy. As no foreign metal catalysts are used for the growth, the self-catalyzed GaAs NWs are believed to have a superior optical quality as compared to the catalyst-assisted, e.g. Au-catalyzed NWs. Breuer et al. compared the optical quality of MBE grown Au- and self-catalyzed GaAs NWs [56]. In that study, the self-catalyzed NWs in fact were reported to have brighter PL intensity, as well as longer PL lifetime, compared to the Au-catalyzed NWs.

To investigate the optical quality of self-catalyzed GaAs NWs in this study, the NWs were passivated by an AlGaAs shell and a GaAs cap as schematically represented in Figure 4.18a. Figure 4.18b shows a cross-sectional

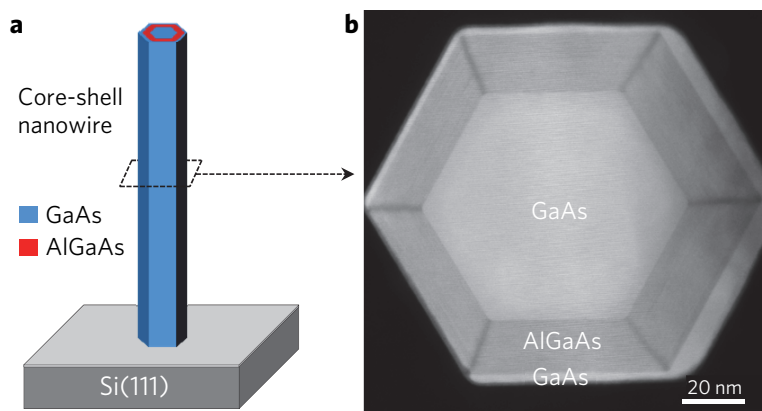


**Figure 4.18.** (a) Schematic representation of an as-grown self-catalyzed GaAs NW passivated by an AlGaAs shell and a GaAs cap. (b) Cross-section HAADF STEM image of a GaAs/AlGaAs/GaAs core-shell NW. Image acquired by H. Kauko [177].

HAADF STEM image of a representative GaAs/AlGaAs core-shell NW encapsulated by a GaAs cap. The GaAs core, AlGaAs and GaAs cap are clearly visible due to their compositional contrast (Al-rich regions appear darker than Ga-rich regions). In addition, Al-rich bands at the corners of the six hexagonal  $\{110\}$  sidewall facets could be observed [177]. Such Al-rich bands have previously been observed for both Au- [178-181] and self-catalyzed [182, 183] GaAs/AlGaAs core-shell NWs as well as Au-catalyzed GaAs/AlInP core-shell NWs [184, 185], indicating that the elemental enrichment is a universal phenomenon. These phenomena are in agreement with the self-ordering of nanostructures on non-planar surfaces observed by Biasiol et al. and have been associated with the difference in the chemical potential and adatoms diffusivity on  $\{110\}$  and  $\{112\}$  type surfaces [186-188].

While characterizing the optical properties, surprisingly the GaAs/AlGaAs core-shell NWs were found to have poor optical quality with low PL intensity with no free-exciton peak at cryogenic temperature. A series of studies were carried out that included growth of NWs by varying different growth conditions such as the Ga rate and As flux. This was followed by detailed structural characterization and optical characterizations. From this study, it was found that it is mainly the V/III ratio which determines the optical quality of the NWs. It was found that NWs which are grown with a high V/III ratio, show an optical quality that is similar to results reported in the literature [56, 109].

To understand the origin of this observation, the case of GaAs thin films grown by MBE can be considered. Thin film growth takes place in an As-rich environment in order to avoid the formation of Ga droplets on the substrate. In addition, due to the high vapor pressure of As, the growth temperature is usually kept below 600 °C to reduce their desorption from the substrate. Although such growth temperature and As overpressure are necessary, it often act as a source of intrinsic defects in the GaAs layer. For example, some of the Ga lattice sites could remain vacant creating Ga vacancies ( $V_{\text{Ga}}$ ), or some Ga-sites could be occupied by an As atom creating As antisites ( $\text{As}_{\text{Ga}}$ ).

On the contrary, self-catalyzed GaAs NWs using MBE are grown under a different environment and mechanism (VLS) than that in the case for the GaAs thin film. For NWs a unidirectional growth is carried out under a Ga catalyst droplet in a Ga-rich condition. Moreover, the growth temperature is usually kept above 600 °C. The high growth temperature is necessary in order to enhance the diffusion of Ga adatoms that diffuse from the substrate along the NW sidewall to the droplet. However, a high temperature results in an increased desorption of As due to its high vapor pressure. Therefore due to this As-deficient growth condition, this can result in a deviation from the

stoichiometry in the GaAs NWs, where some of the As lattice sites can either be remained unoccupied or be replaced by a Ga atom creating an As vacancy ( $V_{As}$ ) or a Ga antisite ( $Ga_{As}$ ), respectively. Recently Du et al. have theoretically studied, the effects of such intrinsic defects in VLS grown GaAs NWs [57]. However, no experimental study has yet been reported considering the effect of point defects on the optical properties of NWs.

In this study, a correlated PL-TEM method was used for the direct correlation of the structural and optical properties of the same individual NWs [189]. Three GaAs/AlGaAs core-shell NW batches that were grown with V/III ratios of 17.4, 23.8 and 30.1 were chosen for a detailed study. The V/III ratios were changed by changing the  $As_4$  flux during the core growth and all other parameters such as Ga rate and temperature were kept constant. This indicates that any changes on the structural and optical properties will stem only from the GaAs core grown with different V/III ratios. With a V/III ratio of 17.4, the bottom part of the NW is apparently pure ZB, whereas few twin defects started to appear as the NW grows longer. For the NWs grown with a V/III ratio of 23.8, the crystal phase is still ZB but with an increase in the number of twin defects. By further increasing the V/III ratio to 30.1, the twin defects in the NW also increased and in addition small WZ sections have started to appear. The observed change in the crystal phase and the structural defects in the NWs with the V/III ratio can be explained in terms of the change in the chemical potential and the shape of the Ga droplet, as explained in Chapter 4.2. At a low V/III ratio, the chemical potential of the droplet is low which results in a slow nucleation and a low growth rate of the NW.

The average growth rates of the NWs were found to be increasing linearly with the V/III ratio. This linear increase of the growth rate with V/III ratio, i.e. with  $As_4$  flux clearly indicates that the NW growth is in the As-limited regime. Due to this, the GaAs core growth durations were adjusted to obtain an approximately similar NW length as shown in Figure 4.19.

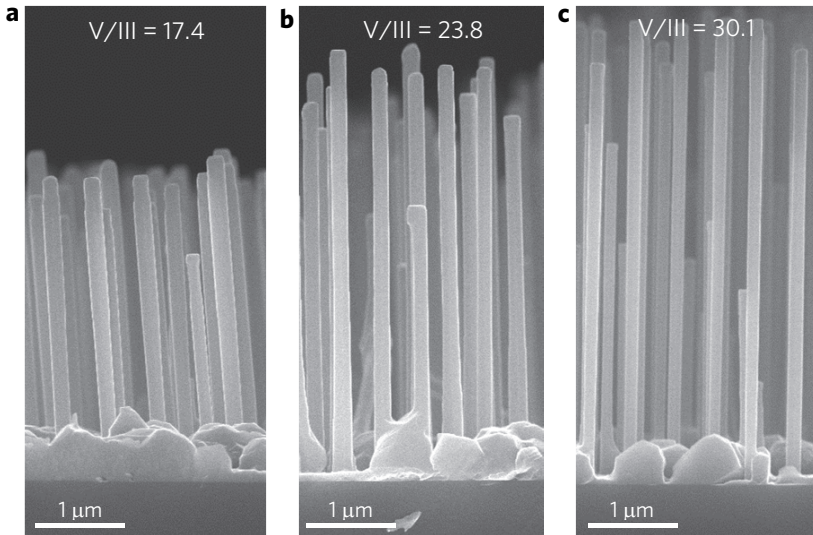


**Figure 4.19. SEM image of GaAs/AlGaAs core-shell NWs.** Side-view SEM images of core-shell NWs grown with V/III ratios of (a) 17.4, (b) 23.8, and (c) 30.1. The GaAs core growth durations were 30, 25 and 20 min in panels a, b and c, respectively.

It is often assumed that self-catalyzed GaAs NWs with pure ZB phase are superior in optical quality as compared to those containing twin defects or SFs. The results from the correlated PL-TEM study clearly contradicts this, showing that it is unlikely to obtain pure ZB self-catalyzed GaAs NWs with a high optical quality due to the presence of the intrinsic defects. A high V/III ratio is necessary in order to reduce the concentration of the intrinsic defects and achieve a high optical quality. However, the NWs will then contain a high density of twin defects in the ZB part and/or small WZ inclusions with SFs. In fact, the existing reports on self-catalyzed GaAs NWs in the literature either do not comment on the crystal phase [56], or the NWs contain crystal defects (twins or SFs) as observed in this study [109, 190]. However, as the full analysis of the results from this optical property optimization study is under process (Paper VIII, in preparation), it is not included in this thesis.

## 4.7 Position controlled growth

Usually, self-catalyzed NWs are grown on a native oxide covered Si substrate without any pre-patterning of the substrate. Due the variations in the substrate preparation method or in the growth conditions, the density of NWs can vary from sample to sample or within the same sample. In addition, as the NWs are randomly positioned on the substrate, each NW can have a different local growth environment due to the neighboring NWs. These will result in a



variation in the morphology, crystal structure, and the physical properties of the NWs. Moreover, a two-dimensional parasitic GaAs crystal growth takes in-between the NWs. Therefore it is necessary to have control on the density and position of the NWs, and to avoid the parasitic crystal growth. For this purpose, electron beam lithography (EBL) and nanoimprint lithography (NIL) were used to pre-pattern the substrates. The EBL can be used to make patterns with the flexibility in hole sizes and pitch values. However, since the process involves high-cost and is unable to efficiently produce large-area patterning, EBL cannot be used for wafer-scale production. The viable alternative would be to use NIL which is a simpler and relatively inexpensive technique, and is capable of patterning masks on wafer-scale substrates with high throughput.

To achieve vertical single NW growth in each hole opening, it is necessary to study the effect of the growth parameters on their yield. For this purpose, thermal SiO<sub>2</sub> was grown on Si(111) wafers. Using NIL, nanohole arrays with hexagonal symmetry were fabricated on these wafers. A hole size of 100 nm and an interhole distance (pitch) of 1 μm were chosen. A SEM image of such hole patterned Si substrate is shown in Figure 4.20.

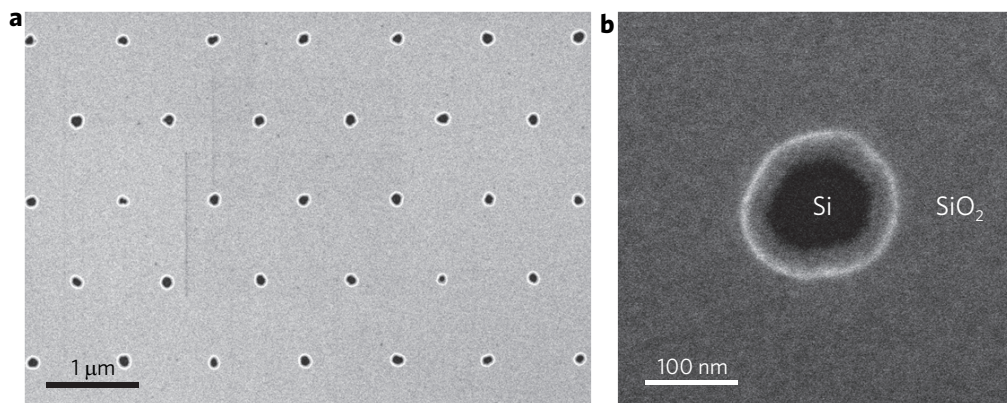


**Figure 4.20. NIL patterned Si substrate.** (a) Top-view SEM image of a NIL patterned nanohole array with hexagonal symmetry on a thermally grown SiO<sub>2</sub> covered Si(111) substrate. (b) Magnified view of an oxide hole on Si substrate.

To optimize the yield of vertical NWs on the NIL patterned Si substrate, a series of growth experiments were carried out. The effects of the growth parameters including the Ga pre-deposition time, Ga flux, As flux, growth temperature, and annealing treatment before the NW growth were studied. Figure 4.21 shows SEM images of the Ga droplet formation and the NW growth for the conditions that produce a yield of vertical NWs of about 80%.

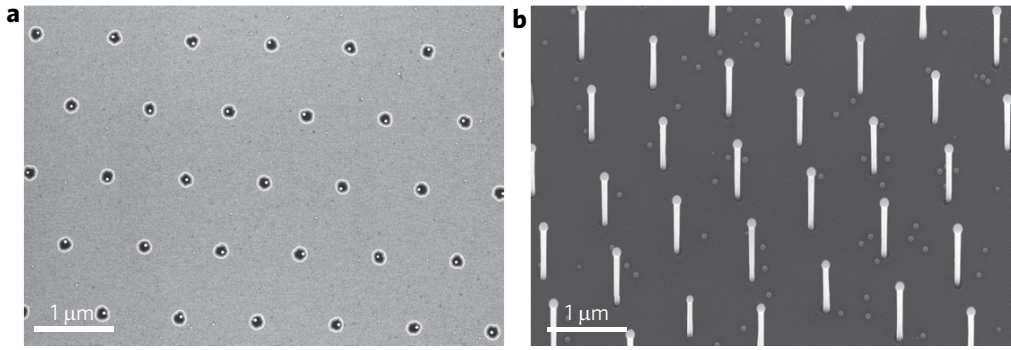


**Figure 4.21. Position controlled NW growth.** (a) Top-view SEM image of Ga droplets in the oxide holes. (b) 20° tilted-view SEM image of position controlled GaAs NWs on NIL patterned Si substrate.

In addition, to study the evolution of diameter and length of the NWs, positioned GaAs NWs were grown with two different arsenic species (i.e.  $\text{As}_2$  and  $\text{As}_4$ ) and at different temperatures. Figure 4.22a shows a plot of diameter and length of the GaAs NWs grown for 1, 5, 10, 15 and 30 min with  $\text{As}_2$  at 630 °C. It can be seen that diameter and length both are increasing with growth time, indicating a radial growth during the axial growth of the NW. Similar trend was observed when the NW are grown with  $\text{As}_4$  and at higher temperature (640 °C), suggesting an unavoidable radial growth. From this observation, it was concluded that for a NW device based on an axial p-n junction, this presented growth technique can be problematic due the simultaneous formation of a radial p-n junction. The structural characterization of the GaAs NW/Si substrate interface was accessed by cross-sectional TEM.

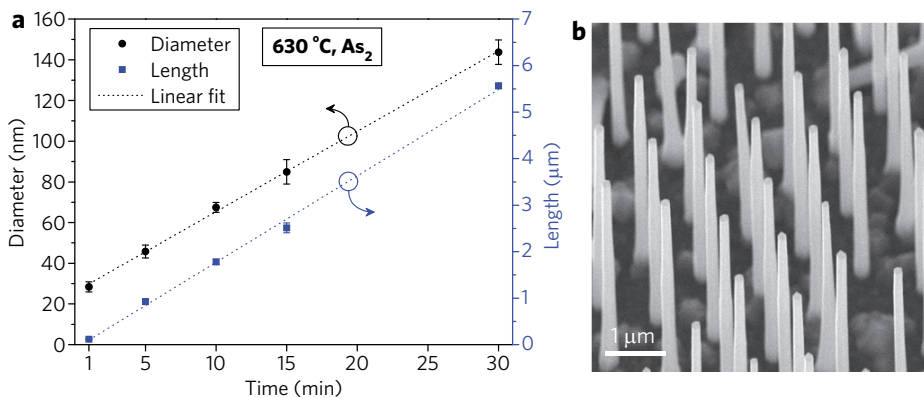


**Figure 4.22. (a)** Plot of diameter and length of GaAs NWs with growth time. (b) 30° tilted-view SEM image of GaAs/AlGaAs core-shell NWs on NIL patterned Si substrates.

The patterned Si substrates have also been used for growing core-shell NWs. Figure 4.22b shows GaAs NWs passivated by AlGaAs shell and GaAs cap. The PL characterization of these GaAs/AlGaAs core-shell NWs revealed good optical quality. The results from this position controlled growth on NIL patterned substrates are summarized in Paper VI. Finally, radial p-i-n junction GaAs NWs were grown on the NIL patterned p-Si(111) substrates for solar cell application. However, preliminary results from these NW solar cells show a very low the efficiency, suggesting the requirement of further optimization of the growth and device process parameters.

# 5 Summary and outlook

## 5.1 Summary

The goal of this thesis work was to develop the growth of GaAs NWs using MBE and finally to make NW array solar cells based on a radial p-i-n junction. Most of the challenges and problems encountered during this project have been solved to some degree. The thesis work began with the MBE growth of Au-catalyzed GaAs NWs on GaAs(111)B substrates that already was going on in the NW group at NTNU. However, due to some issues with the Au-catalyzed growth such as, (i) the Au incorporation issue in the NWs during growth, (ii) the formation of an unwanted axial segment during the shell growth in core-shell NWs, and (iii) difficulties in position controlled growth, the self-catalyzed growth technique was adapted.

The self-catalyzed growth was carried out on Si(111) and graphene substrates. Growth on as-received native oxide covered Si substrates resulted in both tilted as well as vertical GaAs NWs, whereas only vertically aligned NWs were obtained after treating the substrates in a HF acid. To achieve reproducible NW growth, a fresh native oxide formed by keeping the HF treated substrate in flow bench was found to be necessary. The density of NWs on unpatterned substrates could be varied by more than one order of magnitude by selecting substrates with different level of doping; high density on lightly-doped and low density on heavily-doped substrates, and was ascribed to the native oxide thickness and density of pinholes.

Control on the GaAs crystal phases of both Au- and self-catalyzed GaAs NWs was achieved. In both cases, high V/III ratios favor the WZ phase, whereas low V/III ratios favor the ZB phase. These findings were used to obtain crystal phase heterostructures within a single NW [Papers I and II].

Growth of vertical self-catalyzed GaAs NWs on different graphitic substrates, including Kish graphite, epitaxial graphene on SiC, and exfoliated graphene, is demonstrated. Using the usual high temperature growth condition similar to that used on Si, the densities of both NWs and parasitic crystals were found to be low. The density of NWs was increased by reducing the growth temperature, which however also increased the parasitic crystals. By employing a two-temperature growth procedure, a low-temperature nucleation step followed by a high-temperature growth step, it was possible to increase the density of NWs without increasing the parasitic crystals. A model is proposed for the epitaxial growth by taking into account the different adsorption sites (H, B and T) of the semiconductor atoms on the graphene

surface. Different atomic arrangements result in different lattice mismatch of the semiconductor with graphene. A relatively large lattice mismatch (6.3%) of GaAs with graphene and a non-wetting nature of the Ga droplet on the graphene surface can explain the low density of GaAs NWs. Catalyst-free growth of vertical InAs NWs on graphitic substrates shows a higher density compared to GaAs NWs. The higher density of InAs NWs can be associated to the close lattice matching condition (0.42%) of InAs with graphene. The experimental results and the proposed model show the possibility of epitaxial growth of a broad range of semiconductor NWs on graphene [Paper III].

Growth of GaAs/GaAsSb core-shell NWs is demonstrated with an Sb concentration of up to 70%, covering the miscibility gap. Both ZB and WZ phase of the GaAsSb shell are realized through the crystal phase engineering of the GaAs core. An inhomogeneous rough shell morphology stemming from the strain induced island growth was obtained for a high Sb content, whereas a uniform shell over a broad range of growth temperatures was achieved for a relatively low Sb content. The GaAs/GaAsSb core-shell NWs can be a potential candidate in applications such as solar cells due to their type-II band offset. In addition, the WZ GaAsSb shell in the GaAs/GaAsSb core-shell NWs provides a possibility for investigating the properties of the WZ phase of GaAsSb [Paper IV].

Doping of self-catalyzed GaAs NW cores and GaAs NW shells was investigated using Be as the p-type and Si and Te as the n-type dopants. In addition, a comparative study of Be-doping in self- and Au-catalyzed GaAs NWs was carried out. Electrical characterization revealed more effective p-doping in the case of the self-catalyzed NWs in contrast to that of Au-catalyzed NWs. The successful doping in the case of self-catalyzed NWs is most likely results from the increased diffusion of the dopant atoms from the sidewalls to the core of the NWs due to the high growth temperature (630 °C), as compared to the lower growth temperature (510 °C) for Au-catalyzed NWs that were grown at a lower temperature (510 °C) [Paper V]. These results also indicate that the predominant Be dopant incorporation path is the diffusion from the NW sidewalls rather than through the Ga catalyst. This result supports the finding of Casadei et al. [173]. At a higher Be flux, the growth of self-catalyzed NWs ceases and the growth of two-dimensional parasitic crystals increases, which was attributed to a Be flux-induced reduction of the diffusion length of the Ga adatoms [172]. For successful n-type doping of the GaAs shell using Si or Te as dopants, a low growth temperature together with a high V/III ratio are found to be essential [55, 174]. A controlled p-doping of the GaAs core and n-doping of the GaAs shell is important for realizing p-n radial junction NW-based solar cells [29].

Attempts were made to optimize the optical quality of self-catalyzed GaAs NWs. It was found that GaAs NWs grown with a high V/III ratio consist of twinned ZB as well as WZ inclusions have a superior optical quality as compared to the NWs grown with a low V/III ratio which consist of mainly ZB segments. The V/III ratio-dependent optical quality is attributed to the presence of intrinsic point defects such as As vacancies and Ga anti-sites in the NWs due to the Ga-rich and high temperature growth conditions [57]. These results indicate that pure ZB self-catalyzed GaAs NWs grown with a high Ga flux (low V/III ratio) will not have a high optical quality. Therefore it was concluded that the intrinsic point defects, rather than extended structural defects such as rotational twins and stacking faults, determine the optical quality of self-catalyzed NWs. This finding has important implications for NW-based devices that require a high radiative recombination intensity and/or long radiative lifetime, e.g. LEDs [191-193], lasers [194, 195] and solar cells [29, 32, 134].

In paper VI, position controlled growth of vertical GaAs NWs on p-Si(111) was demonstrated using nanoimprint lithography. In this study, the influence of various growth parameters on the yield of vertical GaAs NWs was investigated in detail. Optimized Ga predeposition time and V/III ratio were found to be necessary for obtaining a high yield of vertical NWs. A concurrent radial growth during the axial growth was found to be unavoidable. This indicates that self-catalyzed NWs grown by MBE are more suitable for radial than axial p-n junction devices. In addition, position-controlled GaAs/AlGaAs core-shell NWs were demonstrated with a high optical quality at room temperature, which is important for optoelectronic devices. Finally, position-controlled growth of p-i-n core-shell GaAs NWs on p-Si(111) substrates was achieved. Preliminary results show a photovoltaic effect, however, with a very low solar cell efficiency ( $\sim 0.3\%$ ). Further work is necessary to improve the device performance by optimizing the thickness and resistivity of the doped layers and using surface passivation layers, e.g. AlGaAs. It should be noted that lightly doped Si(111) substrates were used in this study. Therefore, the low efficiency can also be associated with the resistive substrate (resistivity: 1-50  $\Omega$  cm) to where the bottom electrode was contacted. Therefore the efficiency is expected to be enhanced by growing the NW arrays on a heavily doped substrate.

## 5.2 Outlook

**Yield of position-controlled vertical NWs.** With the present growth optimization, a yield of vertical NWs of about 80% was achieved. The effect of

the hole patterning process should be studied for further improvement of the yield. For example, the hole sizes should be made more uniform by optimizing the nanoimprinting process and/or by adapting a dry etching instead of a wet etching process.

**Influence of pitch on the NW growth.** Due to the unavailability of NIL stamps with different geometry and pitch, neither its effect on the yield nor on the growth kinetics could be studied. Such studies should be carried out using EBL patterned substrates.

**Optical quality of the GaAs/AlGaAs core-shell NWs.** To further improve the optical quality of the GaAs/AlGaAs core-shell NWs, the following studies could be carried out:

a) For the GaAs core:

- Further increasing the V/III ratio during the core growth.
- Annealing the GaAs core in an As vapor. This can possibly reduce the density of  $V_{As}$  and  $Ga_{As}$  and hence improve the optical quality of the NWs [57].

b) For the AlGaAs shell:

- Recent studies [180] have reported that the quality of the GaAs/AlGaAs interface has a large impact on the PL lifetime from the GaAs core. In a MOCVD system, AlGaAs shells grown at a high temperature and a low growth rate, result in interdiffusion of Ga-Al atoms at the interface. This causes a graded GaAs/AlGaAs interface and/or an increase of impurity diffusion, resulting in a reduction of the PL lifetime from the GaAs core. Although the shell growth temperatures in MBE are lower compared to that in MOCVD, it would be interesting to make a study also in MBE by varying the shell growth temperature and growth rate, for example by using two growth temperatures, 630 °C (high) and 460 °C (low), and using different group-III growth rates (e.g. at 1, 3 and 5 ML/s while keeping the Al content and shell thickness constant).
- The effect of the Al content in the  $Al_xGa_{1-x}As$  shell on the PL lifetime from the GaAs core could be studied. Recently, the effect of strain from the AlGaAs shell on the GaAs core was studied. Increasing the Al content as well the thickness of the AlGaAs shell were reported to red-shift the PL peak from the GaAs core [196, 197]. Therefore, a separate study should be carried out for MBE grown NWs by varying the Al content and the shell thickness. In most of the GaAs/AlGaAs core-shell NWs studied in this PhD thesis project, the nominal Al content was 30-40% and the shell thickness about 30 nm [177].

**Density of vertical GaAs NWs on graphene.** To increase the density of vertical GaAs NWs grown on graphene, the following strategies could be followed:

- a) Nitrogen doped graphene:
  - To increase the chemical reactivity of graphene, N can be incorporated as a substitutional impurity [198]. N not only moves the Fermi level but also changes the electronic structure of graphene.
- b) Plasma treatment:
  - Study the influence of plasma treatment of graphene on the nucleation of NWs.

**Position controlled NW growth on patterned graphene.** The achieved process for positioned-controlled growth on Si(111) should also be targeted for NW growth on graphene as this is essential for reproducibility and further device developments. Thus a suitable oxide mask has to be found that sticks and can be selectively patterned using EBL or NIL. A crucial step in such developments is to understand the nucleation of NWs on graphene. Subsequently, optimization of the position-controlled growth on patterned graphene substrates needs to be carried out.

**Refinement of growth conditions for improved device performance.** To improve the device performance of the p-i-n core-shell GaAs NWs, further refinement of the growth conditions are required.

- a) GaAs core (p-doping):
  - Study the influence of  $As_2$  and  $As_4$  on the Be-doping of the p-type GaAs NW core.
- b) GaAs shell (p-doping):
  - The effect of the growth temperature for Be-doping of the GaAs shell should be further studied. To minimize the 2D growth on the oxide mask, the p-shell was grown at 630 °C. However, usually a lower growth temperature is used in the literature [67]. Moreover, the optical quality of radial GaAs shell grown on the side-facets of NWs at low temperature in GaAs/AlGaAs multi-quantum well structures, was reported to have a superior optical quality as compared to those grown at high temperature [190, 199]. Therefore the effect of Be-doped GaAs shells grown at 460 °C on the optical quality should be further studied.
- c) Passivation layer:
  - The efficiency of the solar cell has been reported to improve by using a passivation layer [32, 200]. Holm et al. fabricated solar cells from broken GaAsP NWs that were grown on Si substrates [200]. By using an InGaP passivation layer on the GaAsP NWs, the efficiency of the best cell was



reported to improve by 50%, from 6.8% in unpassivated NWs to 10.2% in passivated NWs. Similarly, Mariani et al. used the InGaP passivation layer on GaAs NW array grown on GaAs substrates [32]. The overall solar cell efficiency of the as-grown NW arrays were reported to increase from 1.02% for the unpassivated NWs to 6.63% for the passivated NWs. Due to the high surface-to-volume ratio in NWs and a high density of surface states in GaAs, such improvement in the efficiency is also expected in the present study. Therefore a study should be carried out by passivating the p-i-n GaAs core-shell NWs with a heavily n-doped AlGaAs shell (as P is not available in the MBE system at NTNU).

d) Substrate:

- One of the reasons for the low efficiency could be related to the doping level of the substrates used in this study. Due to the unavailability of heavily doped p-type patterned substrates at the time, lightly doped (resistivity: 1-50  $\Omega$  cm) substrates were used for the NW growth. Therefore, NW growth should be carried out on heavily doped patterned substrates. The high conductivity of such substrate in contact with the p-GaAs core and the bottom electrode is expected to improve the device performance.

## **6 Papers**



**6.1 Paper I: Controlling crystal phases in GaAs nanowires grown by Au-assisted molecular beam epitaxy**

*Nanotechnology* **24** (2013) 015601



# Controlling crystal phases in GaAs nanowires grown by Au-assisted molecular beam epitaxy

D L Dheeraj<sup>1</sup>, A M Munshi<sup>1</sup>, M Scheffler<sup>2</sup>, A T J van Helvoort<sup>2</sup>,  
H Weman<sup>1</sup> and B O Fimland<sup>1</sup>

<sup>1</sup> Department of Electronics and Telecommunications, Norwegian University of Science and Technology, NO-7491 Trondheim, Norway

<sup>2</sup> Department of Physics, Norwegian University of Science and Technology, NO-7491 Trondheim, Norway

E-mail: [bjorn.fimland@iet.ntnu.no](mailto:bjorn.fimland@iet.ntnu.no)

Received 25 July 2012, in final form 4 October 2012

Published 5 December 2012

Online at [stacks.iop.org/Nano/24/015601](http://stacks.iop.org/Nano/24/015601)

## Abstract

Control of the crystal phases of GaAs nanowires (NWs) is essential to eliminate the formation of stacking faults which deteriorate the optical and electronic properties of the NWs. In addition, the ability to control the crystal phase of NWs provides an opportunity to engineer the band gap without changing the crystal material. We show that the crystal phase of GaAs NWs grown on GaAs(111)B substrates by molecular beam epitaxy using the Au-assisted vapor–liquid–solid growth mechanism can be tuned between wurtzite (WZ) and zinc blende (ZB) by changing the V/III flux ratio. As an example we demonstrate the realization of WZ GaAs NWs with a ZB GaAs insert that has been grown without changing the substrate temperature.

(Some figures may appear in colour only in the online journal)

## 1. Introduction

It has been a challenge to control the crystal phase in Au-assisted growth of III–V nanowires (NWs) due to the fact that most III–V NWs, like for example GaAs and InP, normally adapt a wurtzite (WZ) crystal phase with stacking faults (SFs) rather than the zinc blende (ZB) phase found in their bulk form [1, 2]. The prevailing lattice defect in WZ NWs can be seen as a local change in the ABAB... stacking sequence in WZ to the ABCABC... stacking sequence in ZB. SFs in NWs are normally considered to be a detrimental problem for both the optical and electronic properties of NWs, and therefore the usual goal is to minimize their occurrence. In addition, by mastering how to control the crystal phase of NWs, band gap engineering without changing the crystal material becomes possible, which will enable a new degree of freedom in designing heterostructured semiconductor devices [3–5].

The band gap of WZ GaAs has been reported to differ from the band gap of ZB GaAs. However, in the reported

theoretical as well as experimental claims, the difference between the two band gaps varies between  $-20$  meV and  $+30$  meV [5–7]. Despite the variation in the measured band gap of WZ GaAs, the predicted type-II band alignment at the interface between WZ and ZB GaAs makes such structures interesting for various optoelectronic applications [6, 8, 9]. In addition, it has recently been found that the crystal phase influences the linear polarization of photoluminescence emitted from GaAs NWs [10]. Thus, numerous benefits can be obtained by tuning the crystal phase of NWs if the growth challenges in the control of the crystal phase of NWs can be surmounted.

Several theoretical models and experimental observations have been presented to understand and accomplish the control of the crystal phase of NWs. Theoretical models suggest that the crystal phase of NWs mainly depends on the difference in chemical potential between the Au–Ga–As liquid catalyst particle and the III–V solid (supersaturation;  $\Delta\mu$ ), and the diameter of NWs [11, 12]. It has been shown that for a NW with given diameter, there is a critical supersaturation for

every III–V material, below which the phase adapts to the ZB crystalline phase and to WZ above [12]. The fluctuation in the supersaturation level to below and above the critical supersaturation leads to the formation of SFs [13]. Recently, it has been shown that the low solubility of As (<1%) in the Au catalyst particle makes the supersaturation more sensitive to the As concentration than the Ga concentration [14, 15].

The growth parameters influencing the crystal phase of NWs grown either by metal organic vapor phase epitaxy (MOVPE) or molecular beam epitaxy (MBE) have been found to be the growth rate of NWs [16], the substrate temperature [17, 18], and the V/III flux ratio [17, 19]. The possibility of controlling the crystal phase of NWs has also been demonstrated by using techniques such as two-temperature growth [20], pulsed growth [21], and the introduction of foreign elements such as Zn [22], In [23], or Sb [24] which are not necessarily incorporated into the NW. In most cases, it has been explained that tuning these growth parameters adjusts the supersaturation levels of the group III adatoms in the Au catalyst particle and hence affects the crystal phase of the NWs. However, Paiman *et al* [25] emphasized that understanding the influence of the group V supersaturation levels in addition to the group III elements is required for a full understanding of the crystallization of NWs with different crystal phases.

Joyce *et al* [17] optimized the growth conditions (substrate temperature and V/III flux ratio) to obtain both pure WZ and pure ZB III–V NWs by MOVPE. The approach chosen by Joyce *et al* to determine the optimum growth conditions was to grow samples for different combinations of substrate temperature and V/III ratio [17]. Also, Dick *et al* [26] exploited the possibility of tuning the supersaturation levels by using growth interruptions, which allowed them to grow InAs based NW crystal phase superlattices by MOVPE. However, their determined growth parameters cannot be directly adapted for the growth of NWs grown by MBE since the influence of growth parameters on crystal phase of NWs varies from MOVPE to MBE [27].

To the best of our knowledge, there are only two reports on the growth of [111]B-oriented ZB GaAs NWs grown on GaAs(111)B substrates by Au-assisted MBE, either grown at higher substrate temperatures (630 °C) yielding NWs with rather complex geometries [28], or as uncontrolled inclusions of short ZB segments in WZ NWs grown at 540 °C [29]. In this work, we determine the growth parameters influencing the crystal phase of GaAs NWs grown by Au-assisted MBE. The understanding of the influence of growth parameters on the crystal phase of NWs enabled us to demonstrate the growth of WZ GaAs NWs with a controllable length of a ZB GaAs insert by Au-assisted MBE.

## 2. Experimental details

GaAs NWs were grown on GaAs(111)B substrates in a Varian Gen II Modular MBE system equipped with a Ga dual filament cell, an Sb valved cracker cell, and an As valved cracker cell, allowing us to fix the proportion of dimers and tetramers. In the present study, the major species of arsenic

and antimony were As<sub>4</sub> and Sb<sub>2</sub>, respectively. The substrate surface was first deoxidized at 620 °C, as measured with a pyrometer, and then a 60 nm thick GaAs film was grown under growth conditions that produced an atomically flat surface. The GaAs buffer layer was transferred to an electron-beam evaporation system for Au deposition. An approximately 6 Å thick Au film was deposited on the sample surface as measured by a quartz crystal thickness monitor. The sample was then loaded into the MBE system again for the NW growth. Under an As<sub>4</sub> flux of  $6 \times 10^{-6}$  Torr, the substrate temperature was increased to 540 °C for GaAs NW growth. At this stage, Au particles alloyed with the Ga from the substrate, forming Au–Ga liquid particles. GaAs NW growth was initiated by opening the shutter of the Ga effusion cell. The temperature of the Ga effusion cell was preset to yield a nominal planar GaAs growth rate of 0.7 monolayer (ML) per second ( $4 \times 10^{-7}$  Torr) resulting in a V/III beam equivalent pressure ratio (i.e. 'global' V/III ratio) of 15. To form GaAsSb NW inserts, the Sb valve and shutter were also opened to supply an Sb<sub>2</sub> flux of  $6 \times 10^{-7}$  Torr. Growth of GaAs NWs was always terminated by shutting down the Ga and As fluxes simultaneously and immediately ramping down the substrate to room temperature. The growth conditions used for NWs as described above is hereafter called 'standard growth conditions' (SGC).

All the NW samples mentioned in this work were grown at a substrate temperature of 540 °C. There were three sets of samples grown for this study, as schematically depicted in figure 1. The first set of GaAs NW samples were grown under SGC mentioned above, for a duration of 20, 25, and 35 min, to study the formation of SFs. The second set consists of only one NW sample, which was grown to study the influence of the V/III flux ratio on the crystal phase of NWs. The third set of NW samples was grown by a two-step process as shown in figure 1. During the first step, GaAs NWs were grown under the SGC for 15 min. During the second step, GaAs NW growth was continued under the growth conditions required to obtain GaAs NWs with a SF-free WZ crystal phase, GaAs NWs with a long segment of ZB crystal phase, and WZ GaAs NWs with a ~250 nm long ZB GaAs insert. The WZ GaAs NWs with a ZB GaAs insert (of the third set) have an additional radial AlGaAs shell to suppress the surface states in order to make them useful for photoluminescence characterization [30]. However, the additional AlGaAs shell does not affect the present crystal phase study. The optical characterization of these core–shell NWs will be published elsewhere. The purpose of growing the GaAs NWs in sets II and III by a two-step process under different V/III flux ratios was to obtain rod-shaped NWs. GaAs NW growth with lower or higher V/III flux ratios in a one-step process leads to the formation of conical-shaped and tilted NWs, respectively.

Morphological characterization of the NWs was performed in a Zeiss Ultra field emission scanning electron microscope (FE-SEM) operating at 5 kV. For characterization with transmission electron microscopy (TEM), the NWs were removed from the substrate by immersing a cleaved portion of the substrate in ethanol and sonicating it for 3 min. A small volume of the NW suspension was left to dry onto either a

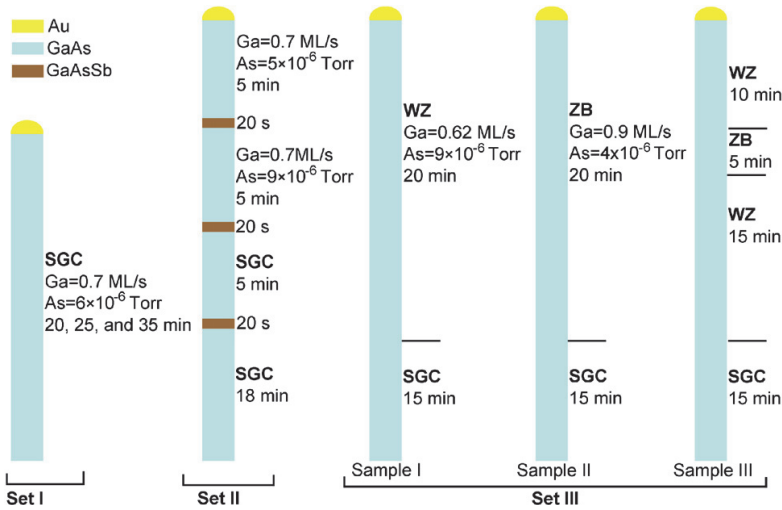


**Figure 1.** Schematic drawing depicting three different sets of samples grown by Au-assisted MBE. SGC: ‘standard growth conditions’. WZ: ‘wurtzite growth conditions’. ZB: ‘zinc blende growth conditions’.

full or a lacey carbon film supported by a 300-mesh Cu TEM grid. The NWs were analyzed in a Philips CM30 and a JEOL 2010F TEM, both operating at 200 kV.

### 3. Results and discussion

TEM characterization performed on approximately 50 NWs obtained from the first set of samples with GaAs NWs grown for 25 min confirmed that the NWs adopt a mainly WZ crystalline phase with a variation in the density of SFs for the given growth parameters (SGC). These NWs, with diameters ( $d$ ) ranging from 20 to 80 nm, have been classified into four different types (A, B, C, or D), depending on the distribution in the density of the SFs (see figure 2). Type A NWs have no SFs and usually have a thick diameter;  $d > 55$  nm. Type B NWs ( $30 \text{ nm} < d < 55 \text{ nm}$ ) are free of SFs up to a certain length along the NW growth direction, after which the NWs exhibit a WZ crystal phase with SFs. Type C NWs (small diameter ( $30 \text{ nm} < d < 40 \text{ nm}$ ) and medium length ( $l$ ) ( $1 \mu\text{m} < l < 2 \mu\text{m}$ )) have very few SFs randomly along the NW. Type D NWs ( $d < 30 \text{ nm}$ ) have a high density of SFs. These observations illustrate that the density of SFs in GaAs NWs is dependent on the NW diameter for these growth conditions (SGC). It is known from previous work that thinner NWs usually grow faster and thicker NWs usually grow slower when using Au-assisted MBE [31]. Based on this fact and the observations made here, i.e. thicker NWs ( $d > 55 \text{ nm}$ ) have a very low density of SFs and thinner NWs ( $d < 30 \text{ nm}$ ) have a high density of SFs, this seems to indicate that the density of SFs depends on the growth rate of the NW, where higher growth rates give rise to more SFs.

This is further corroborated by the observation that the type B NWs (figure 2(b)) are SF-free up to a certain length, above which SFs appear, since the growth rate usually

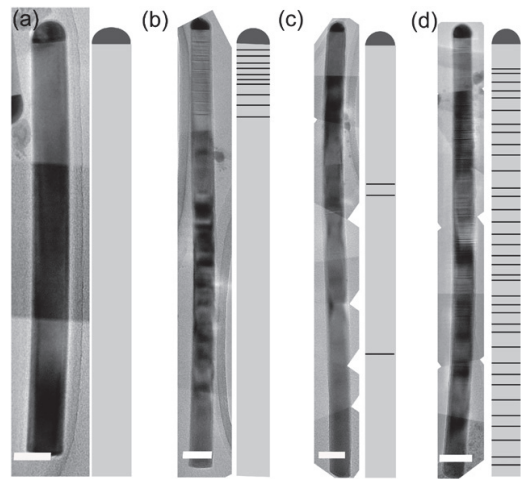


**Figure 2.** TEM images and corresponding schematic diagrams of four different types of Au-assisted WZ GaAs NWs observed in the first set of samples, as described in the text. (a) Type A NWs with no SFs. (b) Type B NWs with SFs forming above a certain critical length. (c) Type C NWs with occasional SFs. (d) Type D NWs with a high density of SFs throughout the NW. The scale bars in the images are 50 nm.

increases with the length of the NW up to a certain point [32]. Figures 3(a)–(c) show TEM images of NWs grown for 20, 25, and 35 min, respectively. These TEM images depict that the NWs are SF-free up to a certain critical length, after which SFs appear. The critical length has been indicated by an arrow in figures 3(a)–(c). The electron diffraction patterns obtained from above and below the critical length are shown in figures 3(d) and (e), respectively. Figure 3(f)



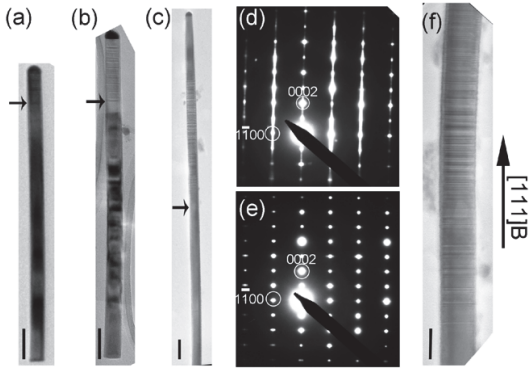


**Figure 3.** TEM images of GaAs NWs grown for (a) 20, (b) 25, and (c) 35 min. The critical length at which the SFs appeared is indicated by arrows. The diffraction patterns obtained (d) above and (e) below the critical length of the NW shown in (c). (f) HRTEM image obtained from the portion just above the critical length of the NW shown in (c), depicting the increase in the density of SFs with extended ZB GaAs segments, when moving along the [111]B growth direction of the NW. The scale bars in (a)–(c) and (f) are 100 and 50 nm, respectively.

shows the high resolution TEM (HRTEM) image of the upper part (above the critical length) of the NW shown in figure 3(c). Figure 3(f) shows that above the critical length of the NW, the density of SFs gradually increases and the NW adapts a predominantly ZB crystal phase with a high density of rotational twins. However, the density of SFs in this particular NW reduces again after some further length and eventually adopts a WZ crystal phase free of SFs. This reduction in SFs can be observed in figure 3(c). After a systematic TEM investigation, it was found that the density of SFs, which increases gradually after the critical length, either continues until the Au catalyst/NW interface with some variation (increase/decrease) in their density, or terminates after some length.

We have previously reported that the growth rate of the NW also changes with the length of the NW for Au-assisted MBE [32]. The increase in the growth rate of NWs was previously explained to be the effect of the inclined molecular beam axis in the MBE growth chamber [32]. Due to the inclined molecular beam axis, the number of Ga adatoms impinging on the NW sidewall and diffusing to the Au particle increases with the length of the NW, and hence the growth rate (assuming group III-limited growth conditions). We also found that the growth rate of a NW increases only until the shadowing from neighboring NWs becomes effective, after which the growth rate either remains the same or decreases, depending on the length of the NW relative to the lengths of neighboring NWs. Hence, under these growth conditions (SGC), the formation of SFs after a certain critical length observed here seems to be related to the increase in the growth rate of the NWs.

In addition, due to the inclined molecular beam axis in the MBE chamber, the number of As adatoms impinging on the NW sidewall and diffusing to the Au particle might

also be changing with increase in the length of the NW, influencing the growth rate of the NW. The growth rate of the NW in the simplest form above a NW length where diffusion from the substrate can be ignored can be calculated by the material impinging directly on the Au particle plus the material impinging on the sidewalls of the NW and diffusing to the Au particle. The axial growth rate  $\frac{\Delta L}{\Delta t}$  of the NW under Ga-limited and As-limited growth conditions is given by equations (1) and (2), respectively:

$$\pi \left(\frac{d}{2}\right)^2 \frac{\Delta L}{\Delta t} = k_1^{\text{Ga}} \pi \left(\frac{d}{2}\right)^2 + k_2^{\text{Ga}} d L_c^{\text{Ga}} \quad (1)$$

$$\pi \left(\frac{d}{2}\right)^2 \frac{\Delta L}{\Delta t} = k_1^{\text{As}} \pi \left(\frac{d}{2}\right)^2 + k_2^{\text{As}} d L_c^{\text{As}} \quad (2)$$

where  $d$  is the diameter of the Au particle,  $\frac{\Delta L}{\Delta t}$  is the change in length of the NW with respect to time,  $k_1^{\text{Ga(As)}}$  is a coefficient related to the rate of incorporation of Ga (As) into the Au particle that has impinged directly on the Au particle,  $k_2^{\text{Ga(As)}}$  is a coefficient related to the incorporation rate of Ga (As) into the Au particle that has impinged on the NW sidewall and diffused to it, and  $L_c^{\text{Ga(As)}}$  indicates the length of the NW below the Au particle on which the material impinged that contributes to the NW growth. The first term on the right hand side of equations (1) and (2) indicates the portion of the material that impinged directly on the Au particle that contributes to the NW growth. The second term on the right hand side of equations (1) and (2) indicates the portion of the material that impinged on the sidewalls of the NW and diffused to the Au particle and that eventually contributed to the NW growth. In case of Ga-limited growth conditions, the contribution of the second term to the NW growth becomes predominant as the length of the NW increases. Since the diffusion length of As adatoms is much shorter than that of Ga adatoms, it is quite plausible (depending on NW density and shadowing) that the increase in the rate of As adatoms reaching the Au particle saturates at some point as the NW get longer while the rate of Ga adatoms reaching the Au particle continues to increase. Hence the effective V/III ratio at the Au particle would decrease with increase in the growth rate of the NW as it becomes longer and at some point favor growth of SFs and ZB segments.

According to the model proposed by Glas [12, 14], a decrease (increase) in the As flux or V/III ratio leads to a decrease (increase) in  $\Delta\mu$  that favors the ZB (WZ) crystal phase. Our suggested decrease in the effective V/III flux ratio at the Au particle with increase in the length of the NW, due to the inclined molecular beam axis in MBE and shorter diffusion length of As adatoms as compared to Ga adatoms, would lead to a decrease in  $\Delta\mu$  and thus cause formation of SFs above some critical length of the NW. In addition, it is possible to explain the results shown in figure 2, that the density of SFs varies between NWs with different diameters. Under the SGC used in this study, thicker NWs ( $d > 55$  nm) have no SFs, and thinner NWs ( $d < 30$  nm) have a high density of SFs. It is known that thinner NWs grow faster, as can also be calculated from equation (1). Due to the

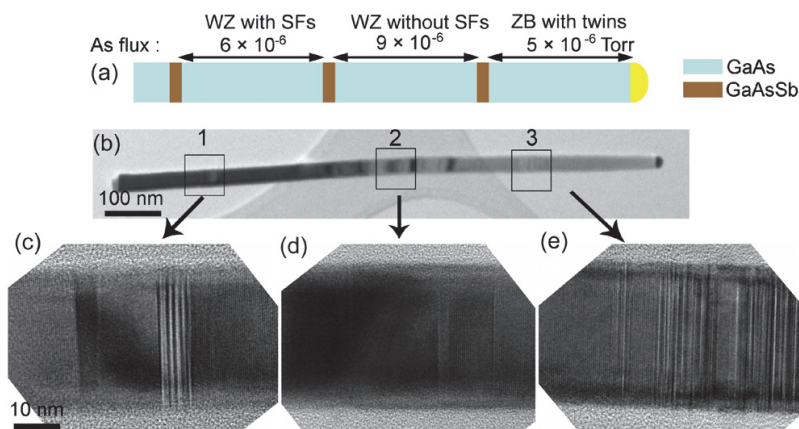


**Figure 4.** (a) Schematic diagram of the GaAs NW segment with three ZB GaAsSb inserts. The As flux is changed after the growth of every GaAsSb insert. (b) TEM image of a typical GaAs NW segment with three GaAsSb inserts enclosed in boxes and numbered as 1, 2, and 3 in (b) are shown in (c)–(e), respectively. The GaAs NW segment between the first and second GaAsSb insert tends to exhibit the WZ phase with few SFs. The GaAs NW segment between the second and third insert exhibits the WZ crystalline phase with a lower SF density than the GaAs NW segment between the first and second insert. The GaAs NW segment grown after the third insert is predominantly ZB with a high density of twin defects and SFs.

diffusion length of the As adatoms being shorter than for Ga adatoms, this faster growth rate (as explained above) leads to a lower V/III atomic ratio at the Au particle in thinner NWs than what is required to obtain SF-free WZ GaAs NWs. The decrease in the effective V/III ratio at the Au particle explains the formation of SFs in thinner NWs with a diameter of Au particles less than 30 nm.

To study the influence of the global V/III flux ratio on the crystal phase of GaAs NWs, GaAs NWs with three ZB GaAsSb insertions were grown, as shown schematically in figure 4(a) (and set II in figure 1). This method of exploiting the GaAsSb inserts as markers provides an opportunity to investigate the effect of the global V/III flux ratio on the density of SFs within a single NW. Figure 4(b) depicts a typical bright field TEM image of a GaAs NW grown at different V/III flux ratios varied after each GaAsSb insert. The GaAsSb inserts, due to their ZB crystalline phase in contrast to the WZ crystalline phase normally adapted by GaAs NWs, can easily be identified by TEM [24]. The GaAsSb inserts have been marked by squares in figure 4(b), and the corresponding HRTEM images are shown in figures 4(c)–(e). The GaAs NW segment grown under an As flux of  $6 \times 10^{-6}$  Torr between the first and second GaAsSb insert exhibits WZ crystalline phase with few SFs. The GaAs NW segment grown under an As flux of  $9 \times 10^{-6}$  Torr between the second and third GaAsSb insert exhibits a WZ crystalline phase with much fewer SFs than the GaAs NW segment grown under an As flux of  $6 \times 10^{-6}$  Torr. The GaAs NW segments grown under an As flux of  $5 \times 10^{-6}$  Torr after the third GaAsSb insert exhibit predominantly a ZB crystal phase with a high density of twin defects. However, a variation in the density of SFs (twin defects) from one NW to another under these V/III ratios was also observed and found to be dependent on the growth rate of the GaAs NW segment, where the WZ (ZB) segment with a lower growth rate exhibits a lower density of

SFs (higher density of twin defects). These results suggest that the crystal phase of GaAs NWs is dependent on the V/III flux ratio and the growth rate of NWs, i.e. the GaAs NWs tend to adopt a WZ crystal phase under high V/III flux ratios and low growth rates, whereas they tend to adopt a ZB crystal phase under low V/III flux ratios and high growth rates.

These findings were used to grow the three samples of set III, depicted in figure 1, i.e. GaAs NWs with a WZ crystal phase, a ZB phase, and a WZ GaAs NW with a ZB GaAs insert. Figures 5(a) and (b) show the 45°-tilted view SEM images of GaAs NWs grown under the growth conditions in order to obtain the WZ and ZB crystal phases, respectively. As can be observed in figure 5(a), the diameter at the tip of WZ GaAs NWs is equal to the diameter of the Au catalyst particle. However, the diameter of the NW tip is smaller than the diameter of the rest of the NW. This can be attributed to the radial GaAs growth (on the sidewalls of the NWs) that occurred during the axial growth of the GaAs NW. On the other hand, the diameter of the catalyst particle is much larger than the diameter of the NW tips in the case of ZB GaAs NWs, as can be observed in figure 5(b). The contact angle of the catalyst particle measured with respect to the NW top surface is between 115 and 125°, as compared to ~90° usually observed in case of WZ GaAs NWs. By investigating the catalyst particle using TEM (shown in figure 5(c)), it was found that the catalyst particle has segregated into two different compositional phases, where an inner Au–Ga alloy particle is enclosed within an outer amorphous Ga phase.

Another interesting observation, noticed from figure 6, is that whereas the length of the WZ GaAs NWs decreases with increasing NW diameter, the length of the ZB GaAs NWs increases with increasing diameter up to a certain diameter (~60 nm), above which the length of the NWs is approximately the same independent of the NW diameter. This dependence of the length of WZ GaAs NWs on their

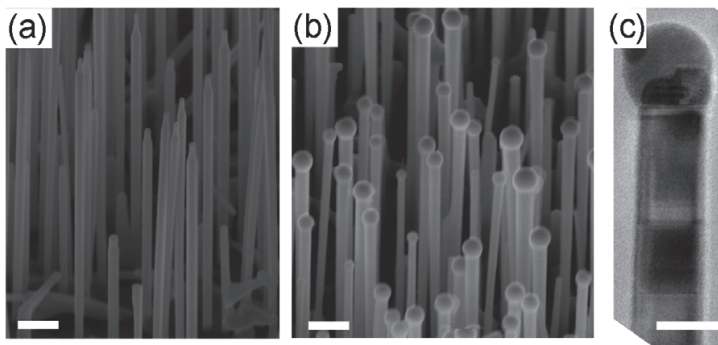


**Figure 5.** 45° tilted view SEM image of Au-assisted GaAs NWs aimed to grow (a) in the WZ crystal phase and (b) in the ZB crystal phase. (c) TEM image depicting the top part of a ZB GaAs NW with a few twin defects, and the catalyst particle. It can be noticed from (b) and (c) that the catalyst particle and catalyst contact angle are much larger when a ZB GaAs crystal phase is grown compared to when a WZ crystal phase is grown (a). The presence of a small particle within the large catalyst particle can be noticed in (c), where the small particle is identified to be an Au–Ga alloy enclosed within an amorphous Ga phase. The scale bars in the SEM images and the TEM image are 200 and 50 nm, respectively.

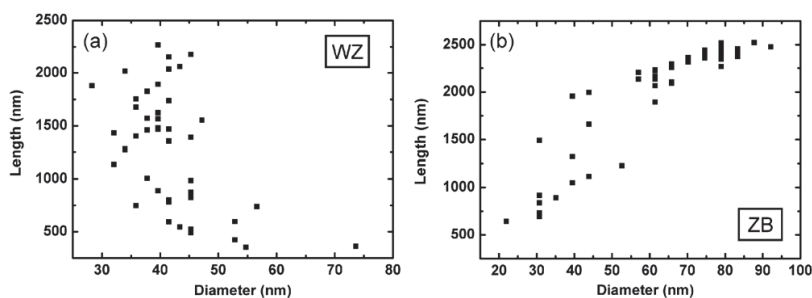


**Figure 6.** Length versus diameter dependence of (a) the WZ and (b) the ZB GaAs NWs. The lengths of the WZ GaAs NWs follow the conventional dependence on the diameter of the NWs, i.e. the length of the NWs decreases with increasing diameter of the NWs. The length of the ZB GaAs NWs increases with increasing diameter of the NWs up to ~60 nm, above which the length of the NWs remain approximately the same irrespective of their diameter.

diameter has been well explained by Dubrovskii and Sibirev to be dependent on the diffusion of group III adatoms along the substrate surface and the sidewall of the NW to the Au particle [31]. The growth mechanism under such growth conditions can be called diffusion-limited growth, as the growth rate of the NW is defined by the diffusion rate of the Ga adatoms to the Au particle. On the other hand, for the ZB GaAs NWs grown under a low V/III flux ratio, the catalyst particle is rich in Ga, as shown in figure 5(c), indicating that the growth conditions are group V-limited. After a certain NW length, we would expect the growth rate of the NWs to be defined by equation (2), where the first term is expected to be dominant due to the short diffusion length of As adatoms, resulting in a growth rate of the NWs independent of diameter. This is in agreement with our observation only for NWs with diameters above 60 nm and does not explain the diameter dependent growth rate for thinner NWs, and therefore further investigation is needed.

TEM characterization of GaAs NWs grown at a lower Ga flux and a higher V/III ratio revealed that the NWs were of high optical quality and predominantly WZ crystalline phase

with very few SFs [33]. As explained by Glas *et al* [14], decreasing the Ga flux and increasing the As flux leads to higher  $\Delta\mu$ , favoring a WZ crystal phase in the GaAs NWs. Although using growth conditions with higher V/III ratios than used in this report, lead to the growth of SF-free WZ GaAs NWs, it was observed that an increasing As flux leads to an increase in the radial growth rate of the NW, due to the reduced diffusion length of the Ga adatoms under higher As flux. Therefore, it was necessary to use suitable growth conditions at which both the radial growth rate and the density of SFs are low.

GaAs NWs with a ZB crystalline phase were obtained at a higher Ga flux and a lower V/III ratio. As depicted in figure 5(c), the catalyst particles that assisted the growth of GaAs NWs under a low V/III ratio exhibiting a ZB crystal phase are rich in Ga. In addition, the contact angle of the catalyst particle is in the range of 115–125°, which is larger than the 90° observed in the NWs grown under higher V/III ratios to obtain WZ GaAs NWs. These observations are similar to the results reported by Cirlin *et al* [34], who grew GaAs NWs by a Ga-assisted MBE technique, which usually

adapt ZB crystal phase [34–36]. According to Glas *et al*, it can be argued that the lower As flux used to grow Ga-assisted GaAs NWs leads to a lower  $\Delta\mu$  (explained above) which favors the formation of a ZB crystal phase [14]. However, there have been arguments that other factors such as the liquid–vapor interfacial energy ( $\gamma_{LV}$ ) and the contact angle ( $\beta$ ) of the catalyst particle play a more important role than the supersaturation in defining the crystal phase of the NW [34, 37, 38]. The triple phase line (TPL) is a line at which the surface of the nucleus is in contact with all the three phases (material vapor, liquid catalyst, and solid NW) [12]. The nucleus formed away from the TPL favors a ZB crystal phase because of its lower SF energy compared to the formation of WZ nuclei. As described by Glas *et al* [12], the nucleation at TPL is favored when the following condition is satisfied:

$$\Delta\gamma = \gamma_{LV} - \gamma_{IL} - \gamma_{LV} \sin \beta < 0 \quad (3)$$

where  $\gamma_{LV}$  is the lateral interface energy between nucleus and vapor and  $\gamma_{IL}$  is the lateral interface energy between nucleus and liquid. As can be calculated from equation (3), either the decrease in  $\gamma_{LV}$  or the increase in  $\beta$  ( $>90^\circ$ ) favors the nucleation away from the TPL, favoring a ZB phase. In fact,  $\gamma_{LV}$  of the Ga particle is lower ( $0.675 \text{ J m}^{-2}$  at  $540^\circ\text{C}$ ) than that of the Au–Ga particle ( $1.0 \text{ J m}^{-2}$  for 40% Ga concentration) [34]. This indicates that the larger contact angle of the catalyst particle and the lower surface energy of the Ga particle can also be one of the reasons favoring the formation of a ZB crystal phase in GaAs NWs grown under a low V/III ratio. However, it is not obvious whether it is  $\Delta\mu$ ,  $\gamma_{LV}$  or the contact angle of the catalyst particle that play the predominant role in controlling the crystal phase of NWs grown under the growth conditions used in this study, and more experimental and theoretical studies are essential to understand their impact in determining the crystal phase of NWs.

Finally, we have demonstrated the growth of WZ GaAs NW with a ZB GaAs insert which is important for both fundamental studies and device applications. Figure 7(a) shows the dark field TEM image of a typical WZ GaAs NW with a ZB GaAs insert. The dark field image was obtained by using a  $1\bar{1}00$  diffraction spot so that the WZ GaAs NW appears bright and the ZB GaAs insert dark. Figures 7(b)–(d) show the electron diffraction pattern images of the WZ GaAs NW above the ZB GaAs insert, the ZB GaAs insert, and the WZ GaAs NW below the ZB GaAs insert, respectively. As can be seen from figure 7(a), the transitions between different crystal phases exhibit a few SFs and twins, and thus further optimization of the growth parameters is needed to perfect these hetero-crystalline GaAs interfaces.

#### 4. Conclusion

We have found that the effective V/III flux ratio at the Au particle plays an important role in controlling the crystal phase of Au-assisted GaAs NWs grown by MBE. It was observed that the density of the SFs change with increase in the length of the WZ GaAs NWs, which we attribute to the increase in the growth rate with NW length and thus

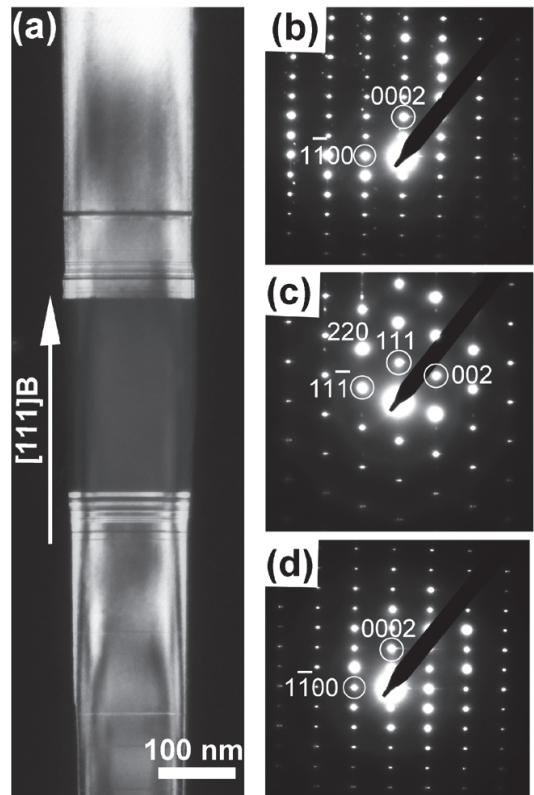


**Figure 7.** (a) Dark field TEM image of a typical WZ/ZB/WZ GaAs axial hetero-crystalline structured NW enclosed in a radial AlGaAs shell. The dark field TEM was obtained by using the  $1\bar{1}00$  diffraction spot. Electron diffraction patterns obtained from (b) the WZ GaAs NW above the ZB GaAs NW insert, (c) the ZB GaAs NW insert, and (d) the WZ GaAs NW below the ZB GaAs NW insert. SFs and twins can be seen in the WZ GaAs NW around the hetero-crystalline interfaces.

the variation of the effective V/III ratio at the Au particle that are plausibly caused due to the inclined molecular beam axis in the MBE growth chamber. This study also revealed that diameter dependent SF formation is due to the diameter dependent growth rate of NWs which influences the local V/III ratio at the Au particle. We have shown that the composition of the catalyst particle assisting the NW growth can be changed from a Au- to a Ga-rich particle by decreasing the V/III ratio, favoring the formation of GaAs NWs with a ZB crystal phase. Finally, the growth of WZ GaAs NWs with a ZB GaAs insert was demonstrated with a change in the V/III ratio and the Ga flux while the substrate temperature remained the same.

#### Acknowledgments

This work was partially supported by ‘RENERGI’ program (grant no. 190871) of the Research Council of Norway, and the NANORDSUN consortium (grant no. 10048) funded from

the 'Top-level Research Initiative' of the Nordic Innovation Centre (NICe), Norway.

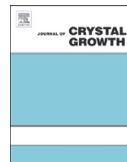
## References

- [1] Harmand J C, Patriarche G, Pere-Laperne N, Merat-Combes M N, Travers L and Glas F 2005 *Appl. Phys. Lett.* **87** 203101
- [2] Plante M C and LaPierre R R 2006 *J. Cryst. Growth* **286** 394
- [3] Bao J, Bell D C, Capasso F, Wagner J B, Mårtensson T, Trägårdh J and Samuelson L 2008 *Nano Lett.* **8** 836
- [4] Akopian N, Patriarche G, Liu L, Harmand J C and Zwiller V 2010 *Nano Lett.* **10** 1198
- [5] Hoang T B, Moses A F, Zhou H L, Dheeraj D L, Fimland B O and Weman H 2009 *Appl. Phys. Lett.* **94** 133105
- [6] Heiss M *et al* 2011 *Phys. Rev. B* **83** 045303
- [7] Ketterer B, Heiss M, Livrozet M J, Rudolph A, Reiger E and Fontcuberta i Morral A 2011 *Phys. Rev. B* **83** 125307
- [8] Murayama M and Nakayama T 1994 *Phys. Rev. B* **49** 4710
- [9] De A and Pryor C E 2010 *Phys. Rev. B* **81** 155210
- [10] Hoang T B, Moses A F, Ahtapodov L, Zhou H, Dheeraj D L, van Helvoort A T J, Fimland B O and Weman H 2010 *Nano Lett.* **10** 2927
- [11] Dubrovskii V G, Sibirev N V, Harmand J C and Glas F 2008 *Phys. Rev. B* **78** 235301
- [12] Glas F, Harmand J-C and Patriarche G 2007 *Phys. Rev. Lett.* **99** 146101
- [13] Cornet D M, Mazzetti V G M and LaPierre R R 2007 *Appl. Phys. Lett.* **90** 013116
- [14] Glas F 2010 *J. Appl. Phys.* **108** 073506
- [15] Glas F, Harmand J-C and Patriarche G 2010 *Phys. Rev. Lett.* **104** 133501
- [16] Joyce H J *et al* 2009 *Nano Lett.* **9** 695
- [17] Joyce H J, Wong-Leung J, Gao Q, Tan H H and Jagadish C 2010 *Nano Lett.* **10** 908
- [18] Plante M C and LaPierre R R 2008 *Nanotechnology* **19** 495603
- [19] Joyce H J *et al* 2008 *Adv. Funct. Mater.* **18** 3794
- [20] Joyce H J, Gao Q, Tan H H, Jagadish C, Kim Y, Zhang X, Guo Y and Zou J 2007 *Nano Lett.* **7** 921
- [21] Johansson J, Karlsson L S, Dick K A, Bolinsson J, Wacaser B A, Deppert K and Samuelson L 2008 *J. Cryst. Growth* **310** 5102
- [22] Algra R E, Verheijen M A, Borgström M T, Feiner L-F, Immink G, van Enckevort W J P, Vlieg E and Bakkers E P A M 2008 *Nature* **456** 369
- [23] Johansson J, Karlsson L S, Dick K A, Bolinsson J, Wacaser B A, Deppert K and Samuelson L 2009 *Cryst. Growth Des.* **9** 766
- [24] Dheeraj D L, Patriarche G, Zhou H, Hoang T B, Moses A F, Grönsberg S, van Helvoort A T J, Fimland B O and Weman H 2008 *Nano Lett.* **8** 4459
- [25] Paiman S *et al* 2009 *Nanotechnology* **20** 225606
- [26] Dick K A, Thelander C, Samuelson L and Caroff P 2010 *Nano Lett.* **10** 3494
- [27] Dick K A 2008 *Prog. Cryst. Growth Charact. Mater.* **54** 138
- [28] Dubrovskii V G *et al* 2009 *Phys. Rev. B* **80** 205305
- [29] Soda M, Rudolph A, Schuh D, Zweck J, Bougeard D and Reiger E 2012 *Phys. Rev. B* **85** 245450
- [30] Zhou H L, Hoang T B, Dheeraj D L, van Helvoort A T J, Liu L, Harmand J C, Fimland B O and Weman H 2009 *Nanotechnology* **20** 415701
- [31] Dubrovskii V G and Sibirev N V 2007 *J. Cryst. Growth* **304** 504
- [32] Dheeraj D L, Patriarche G, Zhou H, Harmand J C, Weman H and Fimland B O 2009 *J. Cryst. Growth* **311** 1847
- [33] Ahtapodov L, Todorovic J, Olk P, Mjåland T, Slåttnes P, Dheeraj D L, van Helvoort A T J, Fimland B-O and Weman H 2012 *Nano Lett.* *submitted*
- [34] Cirlin G E *et al* 2010 *Phys. Rev. B* **82** 035302
- [35] Plissard S, Dick K A, Wallart X and Caroff P 2010 *Appl. Phys. Lett.* **96** 121901
- [36] Colombo C, Spirkoska D, Frimmer M, Abstreiter G and Fontcuberta i Morral A 2008 *Phys. Rev. B* **77** 155326
- [37] Algra R E, Verheijen M A, Feiner L-F, Immink G G W, van Enckevort W J P, Vlieg E and Bakkers E P A M 2011 *Nano Lett.* **11** 1259
- [38] Wallentin J, Ek M, Wallenberg L R, Samuelson L, Deppert K and Borgström M T 2010 *Nano Lett.* **10** 4807

**6.2 Paper II: Crystal phase engineering in self-catalyzed GaAs and GaAs/GaAsSb nanowires grown on Si(111)**

*Journal of Crystal Growth* **372** (2013) 163





## Crystal phase engineering in self-catalyzed GaAs and GaAs/GaAsSb nanowires grown on Si(111)



Abdul Mazid Munshi<sup>a</sup>, Dasa L. Dheeraj<sup>a</sup>, Jelena Todorovic<sup>b</sup>, Antonius T.J. van Helvoort<sup>b</sup>, Helge Weman<sup>a</sup>, Bjørn-Ove Fimland<sup>a,\*</sup>

<sup>a</sup> Department of Electronics and Telecommunications, Norwegian University of Science and Technology, NO-7491, Trondheim, Norway

<sup>b</sup> Department of Physics, Norwegian University of Science and Technology, NO-7491, Trondheim, Norway

### ARTICLE INFO

#### Article history:

Received 13 December 2012

Received in revised form

26 February 2013

Accepted 3 March 2013

Communicated by K. Deppert

Available online 22 March 2013

#### Keywords:

A1. Crystal structure

A1. Nanowires

A3. Contact angle

A3. Molecular beam epitaxy

A3. Self-catalyzed

B2. Semiconducting gallium arsenide

### ABSTRACT

Accomplishing control of the crystal phases in III–V semiconductor nanowires (NWs) is important for applications in future advanced nano-devices. In this work, we report on the growth of both zinc blende (ZB) and wurtzite (WZ) GaAs in self-catalyzed GaAs and GaAs/GaAsSb axial heterostructured NWs on Si (111) substrates by the vapor–liquid–solid technique using molecular beam epitaxy. The self-catalyzed GaAs NWs usually adopt the ZB phase. However, by growing GaAs NWs with short GaAsSb axial inserts, the crystal phase of GaAs can be changed from ZB below the GaAsSb insert, to WZ above. This crystal phase change in GaAs can be explained in terms of a change in the contact angle of the Ga droplet which changes the fraction of the triple-phase-line in contact with the edge of the NW top facet and therefore affects the probability of nucleation for ZB and WZ phases. In addition, by growing ZB GaAs after the insert using a flux interruption, we demonstrate the growth of all combinations of crystal phases of the GaAs segments on both sides of the GaAsSb insert. This understanding has also enabled us to achieve the growth of WZ phase in GaAs NWs as well as a ZB–WZ–ZB GaAs NW heterostructure, by changing the Ga droplet contact angle, without growing a GaAsSb insert. The contact angle was controlled by introducing different flux interruptions and tuning the V/III flux ratio.

© 2013 Elsevier B.V. All rights reserved.

### 1. Introduction

III–V semiconductor nanowires (NWs) have received an increasing attention in the last few years due to their interesting fundamental properties as well as for their potential in future nano-device applications [1]. In addition, because of their small diameters, the III–V NWs can be epitaxially grown on Si substrates aiding the integration of the superior optoelectronic properties of III–Vs with the matured Si technology [2]. One of the most extensively studied techniques to grow NWs is exploiting the vapor–liquid–solid (VLS) mechanism [3] by using mostly Au as a catalyst. It has been observed that these III–V NWs often adopt different crystal phases. For example, Au-catalyzed GaAs NWs grown by metal–organic vapor phase epitaxy (MOVPE) [4–6] are usually zinc blende (ZB) phase in bulk, whereas in the case of molecular beam epitaxy (MBE) [7–11] they adopt wurtzite (WZ) phase. The availability of ZB and WZ crystal phases is of major interest for various fundamental and applied reasons as they can display different optical [12–14] and transport properties.

Control on both the ZB and WZ GaAs crystal phases in the same NW grown by using the Au-assisted VLS mechanism have been demonstrated in few cases [15–17]. However, it has been pointed out that Au might not be an ideal catalyst for subsequent device applications. The main concern is that Au may get incorporated into the NWs [18], which could create deep level traps acting as non-radiative recombination centers detrimental to the electrical and optical properties of the NWs [19]. This concern is, however, debated and Au-assisted NWs of good optical properties have been demonstrated by MBE [20]. As an alternative to the Au-assisted technique, a self-catalyzed (also called Ga-assisted) technique has been successfully demonstrated recently for MBE grown GaAs NWs on different substrates, including GaAs, Si as well as graphene [21–26].

Due to the differences in the growth parameters and the used catalyst particle, the GaAs NWs usually adopt a different crystal structure in the self-catalyzed technique than in the Au-assisted technique. Previously, it has been shown that the self-catalyzed GaAs NWs grown by MBE usually adopt the ZB crystal phase [27,28] in contrast to the MBE grown Au-assisted GaAs NWs. The controlled growth of GaAs NWs with both WZ and ZB phases by using self-catalyzed MBE is considered a challenging task. Short WZ inclusions in a self-catalyzed ZB GaAs NW were demonstrated in few cases where the WZ formation was explained in terms

\* Corresponding author.

E-mail address: [bjorn.fimland@ntnu.no](mailto:bjorn.fimland@ntnu.no) (B.-O. Fimland).



of V/III flux ratio, size and supersaturation of Ga droplet [29,30], and shift of the triple-phase-line (TPL) [31]. TPL is the line where the Ga liquid droplet is in contact with both vapor and solid phases. Long WZ segments in a ZB GaAs NW were also demonstrated [32], but no explanation was provided for the formation of WZ GaAs. To achieve control on the growth of GaAs NWs with different crystal phases, it is necessary to understand the growth conditions under which the nucleation of ZB and WZ phase prevails. Achieving such control on the crystal phases is necessary in order to design hetero-crystalline heterostructures for various device applications.

In this work, we investigate the effect of Ga droplet contact angle on the crystal phases of GaAs NWs grown on p-type Si(111) substrates using self-catalyzed MBE technique. By growing GaAs/GaAsSb axial heterostructures, we demonstrate a straightforward method for forming long pure WZ GaAs segments. Alternatively, the WZ segments were also achieved without using the GaAsSb insert by using flux interruption (FI) to modify the Ga droplet contact angle, and by tuning the V/III flux ratio. Our results demonstrate that the crystal phase can be engineered, and to some extent control the occurrence of structural defects such as stacking faults (SFs), through controlled modification of the Ga droplet contact angle.

## 2. Experimental details

A solid source Varian Gen II Modular MBE system equipped with a Veeco dual filament Ga source and Veeco valved crackers with As and Sb, allowing adjustment of the proportion of dimers and tetramers, was used for the growth of the NWs. The major As and Sb species used were  $As_4$  and  $Sb_2$ , respectively. Fresh native oxide covered p-Si(111) substrates were loaded into the MBE system for the NW growth. The substrate temperature during growth was measured with a pyrometer. The GaAs NW growth was initiated by opening the Ga and As shutters, and As valve, simultaneously. The temperature of the Ga source was preset to achieve a nominal planar growth rate of  $0.7 \text{ ML s}^{-1}$  (beam equivalent pressure  $3.3 \times 10^{-7} \text{ Torr}$ ) on a GaAs(001) substrate as calibrated by reflection high-energy electron diffraction. During the growth the substrate was rotated with 5 rpm. A schematic drawing depicting all the samples grown in this study can be seen in Fig. 1.

Firstly, self-catalyzed GaAs NWs were grown at a growth temperature of  $620^\circ\text{C}$  (sample A, Fig. 1) for a duration of 25 min. The valve position of As was set to produce a beam equivalent pressure of  $4.2 \times 10^{-6} \text{ Torr}$ , optimized to achieve homogenous and

non-tapered NW morphology (V/III–12.7). The NW growths in all the samples used in this study were terminated by simultaneously closing the As valve, and Ga and As shutters, and immediately ramping down the substrate temperature, in order to preserve the contact angle of the Ga droplet.

Secondly, five GaAs/GaAsSb axial heterostructured NW samples (samples B–F; see Fig. 1) were grown. The growth conditions for the GaAs segments before the GaAsSb inserts in samples B–E were the same as mentioned above for sample A except for the growth duration. The GaAsSb inserts were grown for 1 min with an Sb flux of  $1.1 \times 10^{-6} \text{ Torr}$  in all the samples containing GaAsSb inserts. For sample B, the GaAs NW segment was grown for a duration of 20 min followed by the growth of a GaAsSb insert for 1 min. The NW growth was stopped immediately after growing the insert. For samples C and D, in addition to the growth of the GaAs NW segment and the GaAsSb insert as in sample B, a GaAs NW segment was also grown for 5 and 15 min, respectively. These samples were grown to investigate if there is any change in NW side-facets and crystal phase of the GaAs segment grown after the GaAsSb insert. To investigate the effect of the insert further, four GaAsSb inserts were grown (for 1 min) in between five GaAs segments, each grown for the duration of 10 min (sample E, Fig. 1). Sample F was grown at slightly higher temperature ( $640^\circ\text{C}$ ) than the previous samples. Since the growth temperature was  $20^\circ\text{C}$  higher for this sample, the As flux was set to  $5.5 \times 10^{-6} \text{ Torr}$  (V/III–16.6) to achieve a similar homogenous, non-tapered NW morphology as in samples A–E. After growing a GaAs NW segment for 20 min and GaAsSb for 1 min, a  $Fl_{ZB}$  was introduced where all the fluxes were closed for 1 min followed by opening only the Ga shutter for 45 s intended to increase the Ga droplet contact angle. Up to the  $Fl_{ZB}$ , the same nominal planar growth rate of  $0.7 \text{ ML s}^{-1}$  was used as for earlier samples. After the  $Fl_{ZB}$  a GaAs segment was grown for 5 min with an optimized decreased As flux ( $4.8 \times 10^{-6} \text{ Torr}$ ) and an increased Ga flux ( $4.2 \times 10^{-7} \text{ Torr}$ ) equivalent to a nominal planar growth rate of  $0.9 \text{ ML s}^{-1}$  (V/III–11.4).

Thirdly, GaAs NWs (sample G, Fig. 1) without any GaAsSb insert were grown by a two-step growth procedure. The conditions for the growth of the lower GaAs segment were the same as used for the lower GaAs NW segment in sample F except that growth time was reduced to 15 min. Then a  $Fl_{WZ}$  (different from that used in sample F) was used where the As flux was increased to  $9 \times 10^{-6} \text{ Torr}$  and the Ga shutter was closed for 30 s to decrease the Ga droplet contact angle. After this  $Fl_{WZ}$ , a 15 min growth of GaAs was initiated by opening the Ga shutter and reducing the As flux to  $7 \times 10^{-6} \text{ Torr}$  (V/III–21.2) simultaneously.

Finally, a ZB–WZ–ZB GaAs heterostructured NW sample was grown (sample H, Fig. 1). The lower GaAs segment was grown by

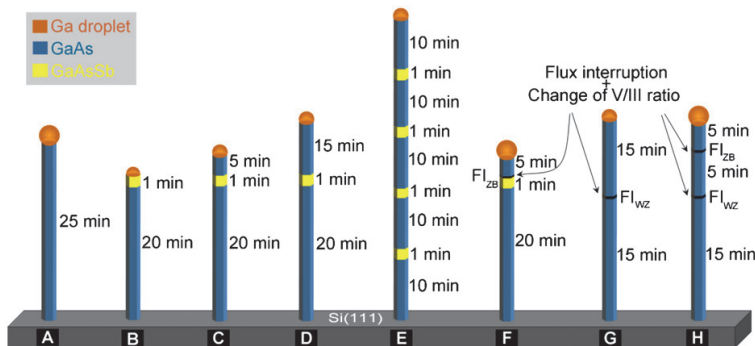


Fig. 1. Description of the NW samples. Schematic drawing depicting the different MBE grown self-catalyzed GaAs and GaAs/GaAsSb NW samples synthesized and studied in this work. Flux interruptions  $Fl_{ZB}$  and  $Fl_{WZ}$  are used to achieve ZB and WZ GaAs phases, respectively.

using the same growth conditions as for the lower GaAs segment in sample F or G, followed by a  $\text{Fl}_{\text{WZ}}$  and WZ segment (as in sample G but for 5 min). To grow the top ZB segment, a  $\text{Fl}_{\text{ZB}}$  was introduced, followed by the growth of ZB GaAs for 5 min (as in sample F).

The morphological features of the NWs were characterized by a Zeiss Ultra field emission scanning electron microscope (SEM) operated at 10 kV. The structural properties of the NWs were analyzed by Phillips CM30 (LaB<sub>6</sub>) and JEOL 2010F transmission electron microscopes (TEM), both operated at 200 kV. For the TEM study, a part of the center of the NW sample was scribed by a fine diamond scribe and a small droplet of isopropyl alcohol (IPA) was put on it. Subsequently, the NWs were transferred onto a full or holey carbon film supported by a 300 mesh Cu TEM grid by gently sliding it on the top of the IPA covered scribed NW sample.

### 3. Results and discussion

Fig. 2(a–d) shows representative SEM images of the NWs from samples A, B, D and F, respectively. Close to 100% of the NWs from all the samples are vertically aligned with the Si substrate and have a rod-shaped morphology without any substantial tapering. The catalyst droplet is visible on the top of the NWs, indicating that the growth was Ga self-catalyzed. Sample A is a reference GaAs NW sample used to compare with NWs grown under other conditions. Samples B, D and F are GaAs NWs with short GaAsSb inserts. In this study, we focus on the change in the contact angle of the Ga droplet with the change in the growth conditions. The contact angle of the Ga droplet in the GaAs NWs from reference sample A was found to be ~130 deg, as shown in Fig. 2(a). In the case of sample B, where the growth was stopped after growing the GaAsSb insert on top of the GaAs segment, the contact angle was found to be in the range of 85–95 deg (Fig. 2(b)), which is significantly smaller as compared to the contact angle for the reference NWs in sample A. For NWs in sample D (and sample C) where a GaAs NW segment was also grown after the GaAsSb insert, the contact angle is found to have an intermediate value of ~95 deg, as can be seen in Fig. 2(c), except for a small number of NWs where the contact angle is found to be considerably larger (~115 deg). In sample F (Fig. 2(d)), where the GaAs segment above the GaAsSb insert was grown after a  $\text{Fl}_{\text{ZB}}$  and with a decreased V/III flux ratio, the contact angle was found to be similar (~130 deg) to that of the reference NWs in sample A.

Crystal phase formation and structural defects in the grown NWs were studied using TEM. The crystal phases are confirmed by electron diffraction and high-resolution (HR) TEM. The observed structural characteristics of the GaAs NWs from all the samples are summarized in Table 1.

Fig. 3 shows dark-field TEM images of the NWs from sample D, E and F taken along a  $\langle 1\bar{1}0 \rangle$  zone axis. The NWs from sample A have ZB crystal phase with a few rotational twins along the NW length (not shown). In all the NW samples with the GaAsSb inserts (Fig. 3(a–d)), the GaAs segment below the first insert has always ZB phase (inset in Fig. 3(a)) with at most a few twin defects as was observed in sample A. The GaAsSb inserts are always ZB. However, the GaAs segments above the GaAsSb inserts are found mostly to have pure WZ phase with the few exceptions being WZ with SFs. It was found that the presence or the absence of SFs in the WZ GaAs segment after the GaAsSb insert depends on the Ga droplet contact angle. For relatively smaller contact angles, ~95 deg, the GaAs segment is pure WZ (Fig. 3(a), inset), whereas for relatively larger contact angles, ~115 deg, the WZ segment has many SFs as depicted in Fig. 3(b). This can also be seen by the presence or absence of stripes in the corresponding electron diffraction patterns (inset in Fig. 3(b)). Fig. 3(c) shows the dark-field TEM image

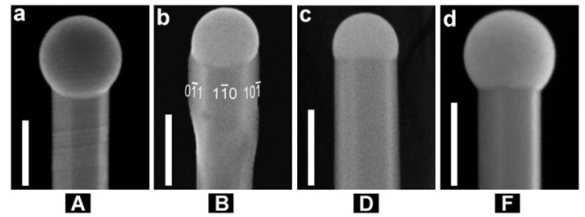


Fig. 2. SEM characterization of NWs. SEM images of representative NWs from (a) sample A, (b) sample B, (c) sample D and (d) sample F depicting the variation in shape and contact angle of the Ga droplet. Scale bars are 100 nm.

Table 1

Summary of the structural characteristics of the GaAs NW segments for different samples.

| Sample | Growth strategy   | Lower GaAs                | Upper GaAs      | Contact angle (deg) |
|--------|---|---------------------------|-----------------|---------------------|
| A      | –   | ZB                        | ZB              | 130                 |
| B      | Insert  | ZB                        | –               | 90                  |
| C      | Insert  | ZB                        | WZ              | 95                  |
| D      | Insert  | ZB                        | WZ              | 95                  |
| E      | Inserts   | ZB                        | WZ/SFs          | 115                 |
| F      | Insert + $\text{Fl}_{\text{ZB}}$ + V/III                          | ZB                        | WZ              | 95                  |
| G      | $\text{Fl}_{\text{WZ}}$ + V/III                                   | ZB                        | ZB              | 130                 |
|        |   |                           | WZ              | 98                  |
|        |   |                           | WZ/SFs          | 115                 |
|        |   |                           | ZB/twins        | 129                 |
| H      | $\text{Fl}_{\text{WZ}}$ + V/III & $\text{Fl}_{\text{ZB}}$ + V/III | ZB (lower)<br>WZ (middle) | ZB (upper)<br>– | 130<br>–            |

of a NW from sample E with four GaAsSb inserts. The TEM study revealed that only the lowest GaAs segment is ZB, and all the other GaAs segments are WZ. This confirms that the crystal phase of the GaAs segments after the GaAsSb inserts always adopts WZ phase, irrespective of the height position of the GaAsSb insert. In an earlier report, we performed compositional analysis on the GaAsSb inserts by energy dispersive X-ray spectroscopy and quantitative high-angle annular dark-field scanning TEM on this sample [33], where we have no indication that Sb is incorporated into WZ GaAs segment above an insert. Our observation also supports the previous finding by Xu et al. that even a small content of Sb is sufficient for forming the ZB phase [34]. We conclude that the formation of pure WZ GaAs segment after the insert is related to the decrease in the droplet contact angle. However, if a  $\text{Fl}_{\text{ZB}}$  (sample F) is introduced to increase the droplet contact angle and followed by a reduced V/III flux ratio during the growth of the GaAs segment after the insert, the GaAs segment eventually adopts a ZB phase after the insert (Fig. 3(d)). The Ga droplet contact angle for this NW is ~130 deg which is similar to that of the NWs in reference sample A. These NWs have an extended transition region immediately after the GaAsSb insert where the GaAs segment has a WZ phase with a very high density of SFs (red arrows in Fig. 3(d)) followed by twinned ZB (yellow arrows in Fig. 3(d)) and eventually pure ZB. A longer  $\text{Fl}_{\text{ZB}}$  time (with just Ga flux before further growth) can reduce the length of the transition region. It is to be noted that we have demonstrated heterostructures with the GaAs segments on each side of the insert both having WZ phase (Fig. 3(c)), both having ZB phase (Fig. 3(d)), and with one having ZB phase and one having WZ phase (Fig. 3(a) and (b)).

For these NWs the side-facets of the ZB GaAs segments, ZB GaAsSb inserts and WZ GaAs segments were identified. The ZB GaAs segments have  $\{1\bar{1}0\}$  side-facets as has previously been observed for ZB GaAs NWs grown by the self-catalyzed MBE

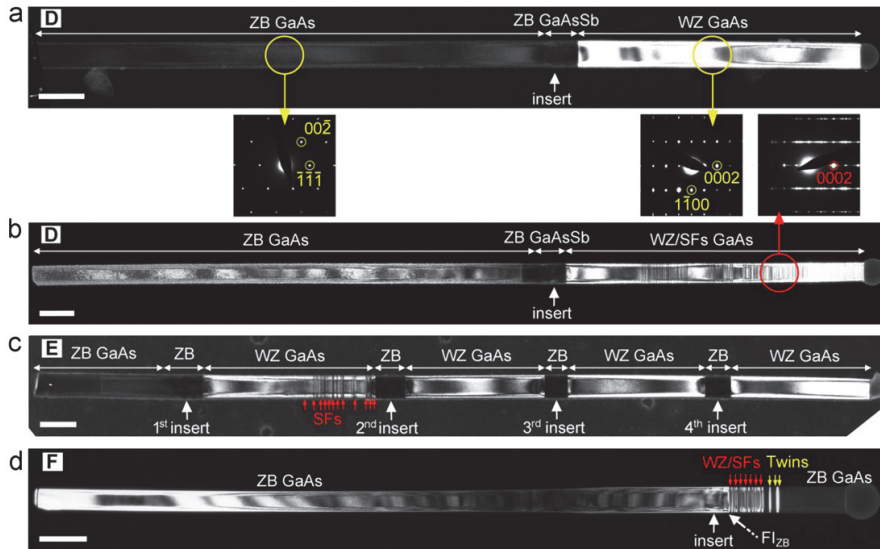


**Fig. 3.** TEM characterization of GaAs/GaAsSb heterostructured NWs from samples D–F. (a, b) Dark-field TEM images of NWs from sample D with one GaAsSb insert showing that the GaAs segment below the insert is pure ZB whereas above the insert it is (a) pure WZ or (b) WZ with SFs. Insets show electron diffraction patterns from the marked regions in (a) and (b). (c) Dark-field TEM image of NW from sample E with four GaAsSb inserts showing that the GaAs segment below the first insert is ZB and that all the other GaAs segments are WZ. The liquid Ga droplet has deformed in this NW during the TEM sample preparation process. (d) Dark-field TEM image of NW from sample F with one GaAsSb insert where the  $FI_{ZB}$  was introduced to make the GaAs segment ZB after the insert. The GaAs segments below and above the insert are now both ZB. However, the GaAs segment above the insert has an extended transition region. In all the samples, the GaAsSb inserts are ZB and therefore no contrast can be seen between the insert and the ZB GaAs segment, except when there are rotational twins. Scale bars are 200 nm. (For interpretation of the references to color in this figure, the reader is referred to the web version of this article.)

technique. The ZB GaAsSb inserts also have the same  $\{1\bar{1}0\}$  side-facets as shown in Fig. 2(b). The GaAs segment after the GaAsSb insert, which was found to have a WZ crystal phase, also exhibit the same facet orientations. To be specific, the WZ GaAs segment has  $\{11\bar{2}0\}$  side-facets. Therefore we conclude that the crystal phase (ZB to WZ) or composition change (GaAs to GaAsSb to GaAs) is not altering the side-facet orientation of the NW, in contrast to the 30 deg rotation observed for other systems [34,35].

To study the impact of the droplet contact angle on the crystal phase of NWs without the GaAsSb insert, but with a  $FI_{WZ}$  and subsequent growth with an increased V/III flux ratio, NWs from sample G were also studied by TEM. Depending on the Ga droplet contact angle and GaAs crystal phase, the NWs from this batch can be categorized into three different types. Most of the NWs are found to be of type-I (smaller contact angle), and only a few of type-II (intermediate contact angle) and type-III (larger contact angle). In order to establish a complete picture of the crystal phase dependence on the contact angle, bright-field TEM images of one NW from each type are depicted in Fig. 4(a–c). In all three types of NWs, the lower GaAs segment has pure ZB phase, as in the samples presented before. The blue dashed arrows in Fig. 4(a–c) indicate the position where the  $FI_{WZ}$  was introduced. The upper part of the GaAs NW, after the  $FI_{WZ}$  point, was grown with an increased V/III ratio. As can be seen in Fig. 4, the upper GaAs segment of a type-I NW is WZ with a low density of SFs (Fig. 4(a)), that of a type-II NW is WZ with a high density of SFs (Fig. 4(b)) and that of a type-III NW is ZB with twins (Fig. 4(c)). The SFs are indicated by red arrows in Fig. 4(a) and (b). Fig. 4(d–f) shows HRTEM images of the GaAs tip part of the corresponding NWs in Fig. 4(a–c), respectively. The contact angles of the Ga droplets are indicated. These results also suggest a correlation of the GaAs NW crystal phase with the Ga droplet contact angle. A similar dependence of the crystal phase on the catalyst droplet contact angle

was reported for MOVPE grown Zn-doped Au-catalyzed InP NWs by Wallentin et al. [36].

Finally, GaAs ZB–WZ–ZB axial heterostructured NWs were grown (sample H) to demonstrate that phase tuning with just different FI approaches within the same single NW can be achieved. A representative dark-field TEM image of such NW is depicted in Fig. 5a. The growth conditions and the  $FI_{WZ}$  and  $FI_{ZB}$  are the same as used for samples F and G, in order to achieve the desired respective crystal phases. Electron diffraction patterns in Fig. 5(b) and (c) confirm that the middle part of the NW is pure WZ and the top part is pure ZB. It has to be noted that the ZB to WZ transition region follows the sequence ZB–ZB/twins–WZ/SFs–WZ, whereas the transition region from WZ to ZB follows the sequence WZ–WZ/SFs–ZB/twins–ZB, which correspond to the observations for the NWs in samples G and F, respectively. The Ga droplet contact angle is found to be  $\sim 130$  deg and is in the same range as for the NWs with upper ZB segment below the Ga droplet, which confirms that larger contact angle favors ZB formation.

The presented results confirm that the GaAs NWs and ZB GaAsSb inserts grown by self-catalyzed MBE adopt a ZB crystal phase under normal growth conditions as reported in previous studies [11,22,23,27]. The observed change in the crystal phase from ZB to WZ in the GaAs segment grown above the GaAsSb insert was unexpected. The results obtained in this study suggest a direct relation between the crystal phase of the GaAs NW segment and the Ga droplet contact angle. With the increase in the contact angle, the crystal phase of the GaAs NW changes from pure WZ to WZ with SFs to twinned ZB to pure ZB, and vice versa for a decreasing contact angle. We anticipate that the growth of the GaAsSb insert or the introduction of the FIs is a simple strategy to alter the contact angle of the Ga droplet and this holds the key for realizing the crystal phase engineering in self-catalyzed GaAs and heterostructured GaAs/GaAsSb NWs grown by MBE.

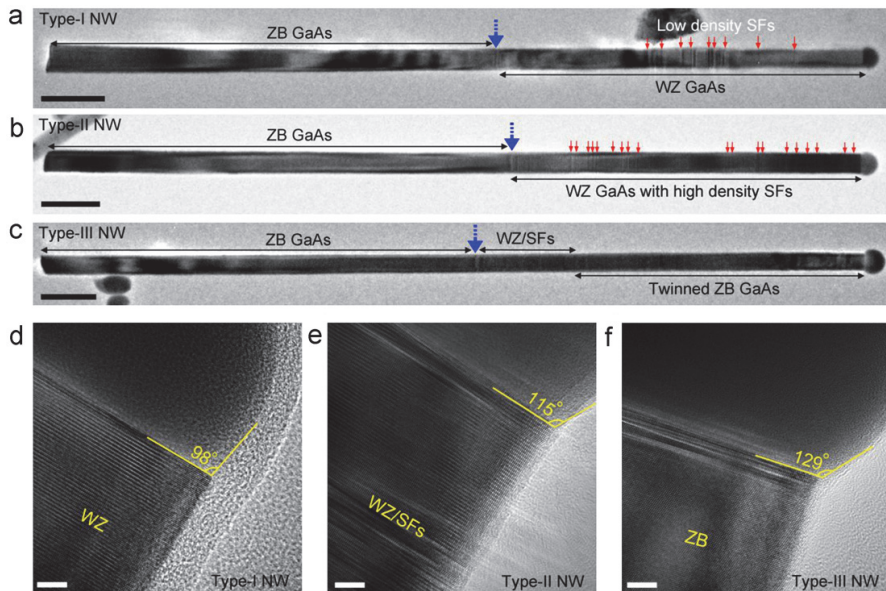


**Fig. 4.** TEM characterization of GaAs NWs from sample G. (a–c) Bright-field TEM images of three different types of GaAs NWs from sample G. The blue dashed arrows are positioned where the  $\text{Fl}_{\text{WZ}}$  was introduced followed by the GaAs growth with an increased V/III flux ratio. The GaAs NW adopts a ZB crystal phase for all types of NWs before the growth condition is changed. After the growth condition is changed, the GaAs NW adopts a WZ crystal phase with a low density of SFs (red arrows) in the type-I NW (a), a WZ phase with a high density of SFs (red arrows) in the type-II NW (b) and a twinned ZB phase in the type-III NW (c). (d–f) HRTEM images of the NWs in (a)–(c), showing a clear dependence of the crystal phase on the Ga droplet contact angle. Scale bars in (a–c) are 200 nm and (d–f) are 5 nm. (For interpretation of the references to color in this figure legend, the reader is referred to the web version of this article.)

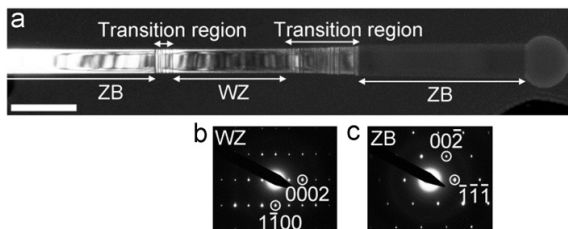


**Fig. 5.** TEM characterization of a representative GaAs NW with ZB–WZ–ZB heterostructure from sample H. (a) Dark-field TEM image indicating ZB and WZ segments. Due to the gradual change in the droplet contact angle, both the interfaces contain a transition region. Scale bar is 200 nm. (b, c) Diffraction patterns for the WZ and top ZB segments, respectively.

The effect of the Ga droplet contact angle on the crystal phase can be explained by the modified nucleation theory of Glas et al. [37], proposed by Krogstrup et al. [38]. In this theory, the impact of the Ga droplet shape or contact angle on the nucleation statistics is described by taking into account the hexagonal shape of the NW >top facet. Depending on the droplet contact angle there could be two cases, (1) contact angle > 90 deg and (2) contact angle < 90 deg. We mainly focus on the first case in this study. The NWs with hexagonal cross-sectional shape have a {111} top surface and six {1 $\bar{1}$ 0} side-facets. If the droplet volume and hence the contact angle change during the growth, the Ga droplet can then (i), spread to the NW side-facets and wet the NW sidewalls or (ii), be exactly in contact with the edge of the NW top-facet without wetting the sidewalls or (iii), stay only on the top {111} NW surface without touching the edge of the NW top-facet. For GaAs, the former two cases correspond to contact angles > 90 deg and the last one to < 90 deg. The fraction of the TPL which is in contact with the edge of the NW top-facet can be defined as a parameter  $\chi$  which is

described in Fig. 6 illustrating the resulting crystal phases depending on the different nucleation sites. The variation of the fraction  $\chi$  with increasing Ga droplet contact angle and the resulting crystal phases are depicted in Fig. 6(a–c). It should be noted that in this analysis, we considered a flat morphology of the interface between the NW top facet and the catalyst droplet, as suggested by Ramdani et al. [39], and not the truncated morphology reported for other materials systems [40,41].

When the contact angle is large (~130 deg), the droplet wets the NW sidewalls along the entire TPL and  $\chi=0$  (Fig. 6(c)). According to the model proposed by Dubrovskii et al. [42], the NW nucleation will in this case give rise to a ZB crystal phase and this is also in line with observations by Cirlin et al. [28]. If the contact angle decreases due to a decrease of the droplet volume, such that the droplet wets the NW sidewalls only along parts of the TPL, then  $1 > \chi > 0$  (Fig. 6(b)). In this case, the crystal phase will be either WZ with SFs (for  $\chi$  closer to 1) or ZB with twins (for  $\chi$  closer to 0). If the contact angle decreases further such that the entire TPL is on the edge of the top-facet i.e.  $\chi=1$  (Fig. 6(a)), then the NW nucleation results in a pure WZ crystal phase.

The Ga droplet contact angle (~130 deg) for the GaAs NWs in the reference sample A and during growth of the lower GaAs NW segments in all the other samples should correspond to  $\chi=0$ . Therefore they all adopt a ZB crystal phase, as confirmed by TEM. For samples with axial GaAsSb inserts, contact angle decreases when the insert is grown. This decrease of the contact angle during the growth of GaAsSb could be due to (i) the decrease of the droplet volume due to the increased Ga consumption with increase in the net group V flux or (ii) a change in the surface energies due to Sb [43]. However, which of these factors is dominating could not be deduced from the experimental results presented here. This decrease in contact angle can be seen in sample B (Fig. 2(b)) where the growth was stopped immediately after growing the GaAsSb insert. When the GaAs segment was

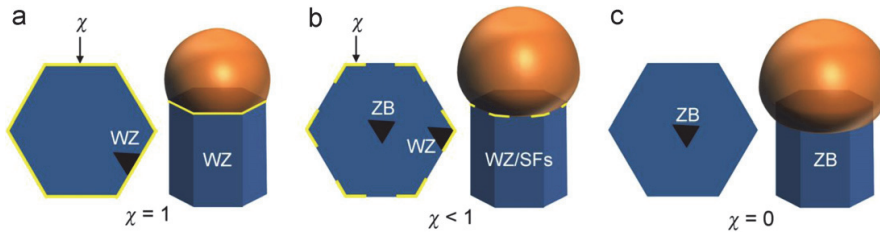


**Fig. 6.** Schematic illustration of the formation of WZ and ZB crystal phases as a function of the catalyst contact angle and  $\chi$  (yellow lines) in a VLS grown NW for contact angle  $> 90$  deg (regime II in Ref. [38]). (a) The contact angle of the Ga droplet is such that the entire TFL is in contact with the edge of the NW top-facet, which corresponds to  $\chi = 1$ . (b) The Ga droplet contact angle is larger than that in (a), which results in that the droplet wets the NW sidewalls along parts of the TFL, resulting in  $\chi < 1$ . (c) The contact angle is even larger and the droplet wets the NW sidewalls along the entire TFL making  $\chi = 0$ . WZ or ZB GaAs crystallization occurs depending on if the nucleation takes place where the TFL is in contact with the edge of the NW top-facet or not, respectively. (For interpretation of the references to color in this figure legend, the reader is referred to the web version of this article.)

grown after the GaAsSb insert, the Ga droplet shape and contact angle is such that the TPL is only in contact with the edge of the NW top-facet, i.e.  $\chi = 1$ , and hence the resulting GaAs segments for most of the NWs adopt a pure WZ crystal phase (Fig. 3(a)), contact angle  $\sim 95$  deg). This is also consistent with the observation by Ambrosini et al. [30] of a WZ phase at the tip of their NWs where the droplet contact angle looks to be in the same range as observed in our study. On the other hand, for larger contact angles ( $\sim 115$  deg) the condition  $\chi = 1$  is likely not satisfied since a fraction of the droplet may wet the NW sidewalls ( $1 > \chi > 0$ ), resulting in WZ GaAs NWs with SFs (Fig. 3(b)).

For sample F the contact angle is in a regime where  $\chi \sim 1$ , after the growth of the GaAsSb insert. However, due to the additional supply of only a Ga flux during the  $Fl_{ZB}$ , the Ga droplet volume builds up and the TPL starts spreading over the NW sidewalls which leads to the case where  $1 > \chi > 0$ . When the GaAs NW segment growth was started with an increased Ga and reduced As flux (sample F), the growth transits to a regime where  $\chi \sim 0$ . This transition is not abrupt and hence will lead to a region with a high defect density. Therefore, in sample F we observed a tendency of forming a WZ GaAs crystal phase with SFs directly after the  $Fl_{ZB}$  (when  $\chi > 0$ ) followed by a twinned ZB and pure ZB GaAs crystal phase (when  $\chi \sim 0$ ) (Fig. 3(d)).

In the case of the GaAs NWs in sample G, a two-step growth condition was used to control the contact angle of the Ga droplet without the use of a GaAsSb insert. After growing the first ZB GaAs segment, a  $Fl_{WZ}$  was introduced during which the Ga shutter was closed and the As flux was increased. During this  $Fl_{WZ}$  the Ga from the droplet starts precipitating to form GaAs NW leading to a decrease in the volume and contact angle of the droplet. However, this decrease of the Ga droplet volume is also gradual and corresponds to the case when  $1 > \chi > 0$ . Therefore, we see a transition region consisting of structural defects in all the GaAs NWs in sample G, as indicated by the blue dashed arrows in Fig. 4 (a–c). A similar type of the transition region was also observed by Yu et al. [31] and was explained by the shift of the TPL, however, without any direct correlation of the Ga droplet contact angle (i.e.  $1 > \chi > 0$  condition) with the resulting crystal phases. According to Krogstrup et al. [38], the change of the droplet contact angle with the change in the droplet volume should be considered in order to see the nucleation events of the resulting crystal phases and therefore is considered in our study. Due to the variation of NW density and hence the local surrounding of each NW, the Ga droplet contact angle was found to have a range of values and the NWs can be divided into mainly three types (type-I, II and III, Fig. (4)) of NWs. For the majority type-I NW in Fig. 4(a), the contact angle ( $\sim 98$  deg) is such that  $\chi \sim 1$  and therefore the upper GaAs segment adopt a WZ crystal phase with a low density of SFs. The contact angle in the type-II NW has an intermediate value

( $\sim 115$  deg) which corresponds to  $1 > \chi > 0$ . This therefore explains the observed WZ crystal phase with high density of SFs. The contact angle and crystal phase of the type-I and type-II NWs are similar to those of the NWs in sample D (Fig. 3(a) and (b)). For the type-III NW, the contact angle is larger ( $\sim 129$  deg) and  $\chi \sim 0$ . Here the upper part of the GaAs NW segment above the FI has a ZB crystal phase with twins. This is similar to the reference sample A or sample F in Fig. 3(d). The explanation for the formation of different crystal phases presented above is further corroborated by the observation for the ZB–WZ–ZB heterostructured GaAs NW in sample H (Fig. 5). The reduction in the Ga droplet contact angle results in the WZ phase where  $\chi \sim 1$ , whereas the increased contact angle at the top part of the NW results in the ZB phase where  $\chi \sim 0$ .

It is noteworthy that the control on the Ga droplet contact angle is very sensitive to the chosen growth conditions (FI and V/III flux ratio). Therefore, to control the contact angle, care must be taken in choosing especially the proper FI duration and the V/III flux ratio so that the Ga droplet does not totally get consumed during the two-step growth process. Since an instant change of the droplet volume during growth by a sudden change in the growth parameters (such as V/III ratio) is not to be expected, it could be very challenging to achieve an abrupt heterointerface between the two crystal phases. If the crystal phase change in pure GaAs was due to the liquid composition, a relatively sharper crystal phase heterointerface was to be expected with the sudden change of the V/III ratio. The gradual heterointerface in our GaAs NWs is in agreement with an earlier in-situ X-ray study where it was reported that the crystal phase transition takes place when the Ga droplet reaches a critical size [44]. The Ga atoms from the droplet have to be consumed partially by growing GaAs to decrease the contact angle in order to change the crystal phase from ZB to WZ. Therefore the ZB–WZ interface will likely contain twins and SFs. However, a defect-free interface from WZ to ZB could be obtained by growing GaAs segment after introducing a FI which involves opening only the Ga shutter until the droplet volume builds up and a desired contact angle is reached, which results in a pure ZB phase. Therefore, further optimization of the growth parameters is required to achieve the heterostructure interfaces with lesser defects between the different crystal phases within a single GaAs NW.

#### 4. Conclusions

In conclusion, the mechanism and the tuning of the ZB and the WZ crystal phase formation in self-catalyzed GaAs NWs grown by MBE was demonstrated by using ZB GaAsSb inserts and different FI conditions. In the case of GaAs NWs with axial GaAsSb inserts, the GaAs crystal phase and defect density above the insert was altered

by modifying the Ga droplet contact angle. The use of GaAsSb insert demonstrates a straightforward method for forming WZ phase in self-catalyzed GaAs NWs. WZ GaAs NW can also be obtained without using the GaAsSb insert by applying a FI technique and an increased V/III flux ratio. Depending on the Ga droplet contact angle, the GaAs NWs are found to adopt WZ, WZ with SFs, or ZB crystal phase. The axial ZB–WZ–ZB heterostructure NWs confirm that the crystal phase in a single self-catalyzed GaAs NW can be tuned between ZB and WZ by modifying the droplet contact angle in a controlled way.

## Acknowledgment

This work was supported by the “RENERGI” program of the Research Council of Norway under Grant no. 190871.

## References

- [1] P. Yang, R. Yan, M. Fardy, *Nano Letters* 10 (2010) 1529–1536.
- [2] T. Mårtensson, C.P.T. Svensson, B.A. Wacaser, M.W. Larsson, W. Seifert, K. Deppert, A. Gustafsson, L.R. Wallenberg, L. Samuelson, *Nano Letters* 4 (2004) 1987–1990.
- [3] R.S. Wagner, W.C. Ellis, *Applied Physics Letters* 4 (1964) 89–90.
- [4] B.J. Ohlsson, M.T. Björk, M.H. Magnusson, K. Deppert, L. Samuelson, L. R. Wallenberg, *Applied Physics Letters* 79 (2001) 3335–3337.
- [5] M.M. Borgström, K. Deppert, L. Samuelson, W. Seifert, *Journal of Crystal Growth* 260 (2004) 18–22.
- [6] H.J. Joyce, Q. Gao, H.H. Tan, C. Jagadish, Y. Kim, X. Zhang, Y. Guo, J. Zou, *Nano Letters* 7 (2007) 921–926.
- [7] V.G. Dubrovskii, G.E. Cirlin, I.P. Soshnikov, A.A. Tonkikh, N.V. Sibirev, Y. B. Samsonenko, V.M. Ustinov, *Physical Review B* 71 (2005) 205325.
- [8] J.C. Harmand, G. Patriarche, N. Pere-Laperne, M.N. Merat-Combes, L. Travers, F. Glas, *Applied Physics Letters* 87 (2005) 203101–203103.
- [9] M.C. Plante, R.R. LaPierre, *Nanotechnology* 19 (2008) 495603.
- [10] F. Jabeen, S. Rubini, F. Martelli, *Microelectronics Journal* 40 (2009) 442–445.
- [11] D.L. Dheeraj, G. Patriarche, H. Zhou, T.B. Hoang, A.F. Moses, S. Grønsberg, A.T. van Helvoort, B.-O. Fimland, H. Weman, *Nano Letters* 8 (2008) 4459–4463.
- [12] A. De, C.E. Pryor, *Physical Review B* 81 (2010) 155210.
- [13] I. Vurgaftman, J.R. Meyer, L.R. Ram-Mohan, *Journal of Applied Physics* 89 (2001) 5815–5875.
- [14] M. Heiss, S. Conesa-Boj, J. Ren, H.-H. Tseng, A. Gali, A. Rudolph, E. Uccelli, F. Peiró, J.R. Morante, D. Schuh, E. Reiger, E. Kaxiras, J. Arbiol, A. Fontcuberta i Morral, *Physical Review B* 83 (2011) 045303.
- [15] S. Lehmann, D. Jacobsson, K. Deppert, K. Dick, *Nano Research* 5 (2012) 470–476.
- [16] H.J. Joyce, J. Wong-Leung, Q. Gao, H.H. Tan, C. Jagadish, *Nano Letters* 10 (2010) 908–915.
- [17] D.L. Dheeraj, A.M. Munshi, M. Scheffler, A.T.J. van Helvoort, H. Weman, B. O. Fimland, *Nanotechnology* 24 (2013) 015601.
- [18] M. Bar-Sadan, J. Barthel, H. Shtrikman, L. Houben, *Nano Letters* 12 (2012) 2352–2356.
- [19] S. Breuer, C. Pfüller, T. Flissikowski, O. Brandt, H.T. Grahn, L. Geelhaar, H. Riechert, *Nano Letters* 11 (2011) 1276–1279.
- [20] L. Ahtapodov, J. Todorovic, P. Olk, T. Mjåland, P. Slättnes, D.L. Dheeraj, A.T.J. van Helvoort, B.-O. Fimland, H. Weman, *Nano Letters* 12 (2012) 6090–6095.
- [21] A. Fontcuberta i Morral, C. Colombo, G. Abstreiter, J. Arbiol, J.R. Morante, *Applied Physics Letters* 92 (2008) 063112–063113.
- [22] S. Plissard, K.A. Dick, X. Wallart, P. Caroff, *Applied Physics Letters* 96 (2010) 121901–121903.
- [23] F. Jabeen, V. Grillo, S. Rubini, F. Martelli, *Nanotechnology* 19 (2008) 275711.
- [24] J.H. Paek, T. Nishiwaki, M. Yamaguchi, N. Sawaki, *Physica Status Solidi (c)* 6 (2009) 1436–1440.
- [25] S. Ambrosini, M. Fanetti, V. Grillo, A. Franciosi, S. Rubini, *Journal of Applied Physics* 109 (2011) 094306–094307.
- [26] A.M. Munshi, D.L. Dheeraj, V.T. Fauske, D.-C. Kim, A.T.J. van Helvoort, B.-O. Fimland, H. Weman, *Nano Letters* 12 (2012) 4570–4576.
- [27] P. Krogstrup, R. Popovitz-Biro, E. Johnson, M.H. Madsen, J. Nygård, H. Shtrikman, *Nano Letters* 10 (2010) 4475–4482.
- [28] G.E. Cirlin, V.G. Dubrovskii, Y.B. Samsonenko, A.D. Bouravlev, K. Durose, Y. Y. Proskuryakov, B. Mendes, L. Bowen, M.A. Kaliteevski, R.A. Abram, D. Zeze, *Physical Review B* 82 (2010) 035302.
- [29] D. Spirkoska, J. Arbiol, A. Gustafsson, S. Conesa-Boj, F. Glas, I. Zardo, M. Heigoldt, M.H. Gass, A.L. Bleloch, S. Estrade, M. Kaniber, J. Rossler, F. Peiro, J.R. Morante, G. Abstreiter, L. Samuelson, A. Fontcuberta i Morral, *Physical Review B* 80 (2009) 245325.
- [30] S. Ambrosini, M. Fanetti, V. Grillo, A. Franciosi, S. Rubini, *AIP Advances* (2011) 042142.
- [31] X. Yu, H. Wang, J. Lu, J. Zhao, J. Misuraca, P. Xiong, S. von Molnár, *Nano Letters* 12 (2012) 5436–5442.
- [32] B. Ketterer, M. Heiss, E. Uccelli, J. Arbiol, A. Fontcuberta i Morral, *ACS Nano* 5 (2011) 7585–7592.
- [33] H. Kauko, T. Grieb, R. Bjørge, M. Schowalter, A.M. Munshi, H. Weman, A. Rosenauer, A.T.J. van Helvoort, *Micron* 44 (2013) 254–260.
- [34] T. Xu, K.A. Dick, S. Plissard, T.H. Nguyen, Y. Makoudi, M. Berthe, J.-P. Nys, X. Wallart, B. Grandidier, P. Caroff, *Nanotechnology* 23 (2012) 095702.
- [35] L. Lugani, D. Ercolani, F. Rossi, G. Salviati, F. Beltram, L. Sorba, *Crystal Growth and Design* 10 (2010) 4038–4042.
- [36] J. Wallentin, M. Ek, L.R. Wallenberg, L. Samuelson, K. Deppert, M.T. Borgström, *Nano Letters* 10 (2010) 4807–4812.
- [37] F. Glas, J.-C. Harmand, G. Patriarche, *Physical Review Letters* 99 (2007) 146101.
- [38] P. Krogstrup, S. Curioetto, E. Johnson, M. Aagesen, J. Nygård, D. Chatain, *Physical Review Letters* 106 (2011) 125505.
- [39] M.R. Ramdani, J.C. Harmand, F. Glas, G. Patriarche, L. Travers, *Crystal Growth & Design* 13 (2013) 91–96.
- [40] C.Y. Wen, J. Tersoff, K. Hillerich, M.C. Reuter, J.H. Park, S. Kodambaka, E. A. Stach, F.M. Ross, *Physical Review Letters* 107 (2011) 025503.
- [41] A.D. Gamalski, C. Ducati, S. Hofmann, *Journal of Physical Chemistry C* 115 (2011) 4413–4417.
- [42] V.G. Dubrovskii, G.E. Cirlin, N.V. Sibirev, F. Jabeen, J.C. Harmand, P. Werner, *Nano Letters* 11 (2011) 1247–1253.
- [43] N. Pramod, Z. Qi, C.D. Elizabeth, M.R. Joan, *Nanotechnology* 20 (2009) 025607.
- [44] P. Krogstrup, M.H. Madsen, W. Hu, M. Kozu, Y. Nakata, J. Nygård, M. Takahashi, R. Feidenhansl, *Applied Physics Letters* 100 (2012) 093103–093104.



### **6.3 Paper III: Vertically aligned GaAs nanowires on graphite and few-layer graphene: generic model and epitaxial growth**

*Nano Letters* **12** (2012) 4570





# Vertically Aligned GaAs Nanowires on Graphite and Few-Layer Graphene: Generic Model and Epitaxial Growth

A. Mazid Munshi,<sup>†</sup> Dasa L. Dheeraj,<sup>†</sup> Vidar T. Fauske,<sup>‡</sup> Dong-Chul Kim,<sup>†</sup> Antonius T. J. van Helvoort,<sup>‡</sup> Bjørn-Ove Fimland,<sup>†</sup> and Helge Weman<sup>\*,†</sup>

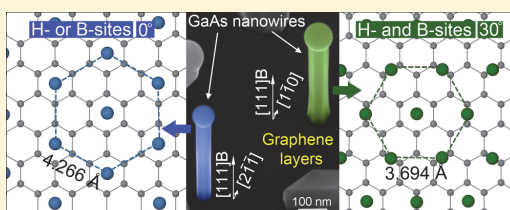
<sup>†</sup>Department of Electronics and Telecommunications, Norwegian University of Science and Technology (NTNU), NO-7491 Trondheim, Norway

<sup>‡</sup>Department of Physics, Norwegian University of Science and Technology (NTNU), NO-7491 Trondheim, Norway

## 5 Supporting Information

**ABSTRACT:** By utilizing the reduced contact area of nanowires, we show that epitaxial growth of a broad range of semiconductors on graphene can in principle be achieved. A generic atomic model is presented which describes the epitaxial growth configurations applicable to all conventional semiconductor materials. The model is experimentally verified by demonstrating the growth of vertically aligned GaAs nanowires on graphite and few-layer graphene by the self-catalyzed vapor–liquid–solid technique using molecular beam epitaxy. A two-temperature growth strategy was used to increase the nanowire density. Due to the self-catalyzed growth technique used, the nanowires were found to have a regular hexagonal cross-sectional shape, and are uniform in length and diameter. Electron microscopy studies reveal an epitaxial relationship of the grown nanowires with the underlying graphitic substrates. Two relative orientations of the nanowire side-facets were observed, which is well explained by the proposed atomic model. A prototype of a single GaAs nanowire photodetector demonstrates a high-quality material. With GaAs being a model system, as well as a very useful material for various optoelectronic applications, we anticipate this particular GaAs nanowire/graphene hybrid to be promising for flexible and low-cost solar cells.

**KEYWORDS:** Graphene, nanowire, hybrid structures, vapor–liquid–solid, molecular beam epitaxy, GaAs



Semiconductor nanowires have today advanced to a level beyond thin films with respect to design freedom, including structuring of both material composition and crystal phase in three dimensions with high spatial precision,<sup>1–6</sup> making them promising for various device applications.<sup>7,8</sup> One potential way for their fabrication that also gives a solution for further monolithic device integration is to grow the nanowires homo- or heteroepitaxially on a semiconductor substrate.<sup>9</sup> If semiconductor nanowires can be grown epitaxially on graphene films with excellent optoelectronic properties,<sup>10</sup> graphene could function as a novel low-cost, transparent (flexible) electrode for, e.g., nanowire based solar cells<sup>11,12</sup> and light emitting diodes,<sup>13</sup> as well create new types of hybrid heterostructures.

While the potential benefits are enormous, there are, however, several challenges to epitaxially combine semiconductors and graphene into a functional hybrid heterostructure. Apart from differences in lattice constants and crystal structures, growth of semiconductors on graphitic surfaces is not obvious from a chemical perspective, since most semiconductors are three-dimensional (3D) with reactive dangling bonds and the graphitic surface (graphene) is two-dimensional (2D) with no dangling bonds. The binding mechanism between such materials is often referred to as a *quasi*-van der Waals binding (3D–2D heteroepitaxy), to distinguish it from

the van der Waals binding between, e.g., the graphene layers in graphite (2D–2D homoepitaxy).<sup>14</sup> The high surface tension, caused by the lack of dangling bonds, leads to weak nucleation and clustering when semiconductor thin films are grown on graphitic surfaces.<sup>15,16</sup>

By utilizing some inherent properties of semiconductor nanowires, there is a potential to overcome the hurdles of semiconductor thin films on graphitic surfaces. There are at least three important features that make the epitaxial growth of vertical semiconductor nanowires on graphitic surfaces likely to be successful:

(1) Nanowires can accommodate much more lattice mismatch than thin films, due to very efficient elastic relaxation at the lateral free surface.<sup>17</sup>

(2) Semiconductor nanowires preferentially grow along the [111] ([0001]) crystallographic direction for cubic (hexagonal) crystals.<sup>2,3</sup> Therefore, cubic semiconductor growth takes place on the (111) plane ((0001) for hexagonal), and the nanowires will then have the same hexagonal symmetry as the (0002)-

Received: May 14, 2012

Revised: July 23, 2012

Published: August 13, 2012

oriented graphitic surface. Hence, vertical nanowires are to be expected on graphitic substrates.

(3) Graphite (including few-layer graphene) can consist of various A, B, or C stacked graphene layers at the surface.<sup>18</sup> Nanowires have much smaller cross sections compared to the grain size of different A, B, and C layers; hence, they can grow epitaxially on graphitic surfaces with different stacking. In contrast, semiconductor thin film, due to its larger size, will have to grow across the grains, and will not be in epitaxial registry across an entire surface with different A, B, and C layers.

Epitaxial growth of vertical semiconductor nanowires on graphitic surfaces (including single-layer graphene) is therefore plausible, if the nanowire nucleation phase can be induced. The growth of vertical ZnO nanostructures<sup>19,20</sup> and catalyst-free InAs nanowires<sup>21</sup> on graphitic surfaces has in fact very recently been reported.

In this work, we present a generic atomic model by which semiconductor nanowire materials can be epitaxially combined with graphene and other graphitic substrates. We experimentally demonstrate the epitaxial growth of vertical *self*-catalyzed GaAs nanowires on graphite and few-layer graphene using the widely used vapor–liquid–solid (VLS) technique<sup>22</sup> by molecular beam epitaxy (MBE).<sup>23</sup> The use of a VLS technique leads to nanowires with regular hexagonal cross sections in contrast to earlier attempts for other materials using the catalyst-free technique.<sup>19,21</sup> In addition, since the nanowires are self-catalyzed, the approach avoids any foreign elements that could affect the active semiconductor in subsequent device processing or operation.

Due to the symmetry of a cubic semiconductor in the (111) plane ((0001) plane for hexagonal), various degrees of strain with graphene result depending on which sites the semiconductor atoms take on top of graphene. As possible semiconductor adsorption sites on top of graphene, we consider (1) above the center of the hexagonal carbon rings of graphene (H-site) and (2) above the bridge between carbon atoms (B-site), as indicated in the inset of Figure 1a. Figure 1a–d shows the atomic arrangements when atoms are placed above (1) H- and B-sites (Figure 1a, b, and d) and (2) H- or B-sites (Figure 1c). There is a third possible adsorption site: above the top of a carbon atom (T-site, inset of Figure 1a). However, since the T-site is an unfavorable site for semiconductor atoms,<sup>24</sup> atomic arrangements involving T-sites will not be discussed here. In Figure 1e, the bandgap energies of the III–V semiconductors (as well as Si and ZnO) are plotted against their lattice constants. Vertical solid (dashed) colored lines depict the lattice constant of an ideal crystal that would give exact lattice match with graphene for a cubic (hexagonal) crystal with the four different atomic arrangements (Figure 1a–d) with respect to graphene. The plot visualizes the vast possibilities for epitaxial growth of vertical semiconductor nanowires on graphitic substrates. In the case of some semiconductors, the lattice mismatch with graphene is very small (e.g., ZnO and InAs) for one suggested atomic configuration. For example, for InAs, only the orientation relation as sketched in Figure 1c is expected, which has been experimentally observed.<sup>21</sup> For other semiconductors like GaAs, the lattice mismatch is quite large and the lattice constant is in between two different atomic configurations (as in Figure 1b or c), as indicated by the green and blue arrows in Figure 1e. Below, we demonstrate our experimental results

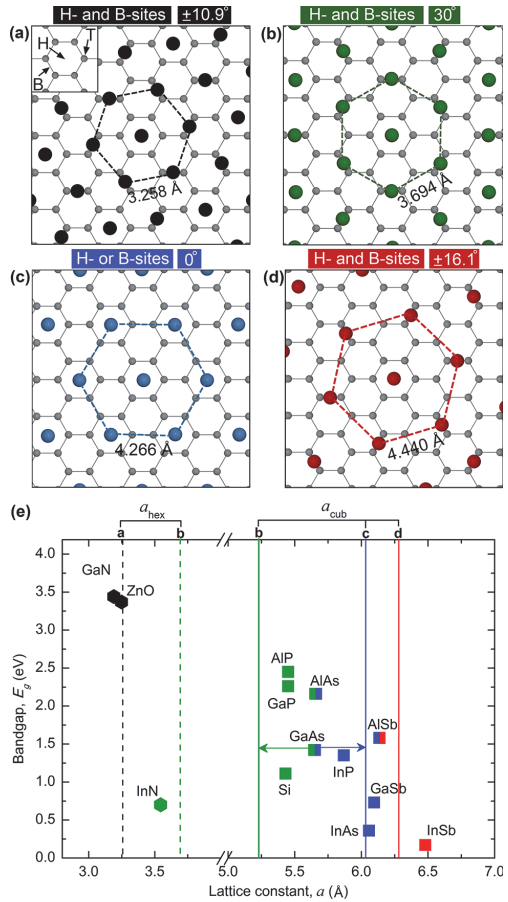


**Figure 1.** Semiconductor atoms on graphene and semiconductor bandgaps vs lattice constants as well as the lattice-matched semiconductor/graphene lattice constants. (a–d) Artificial lattice-matched arrangement of the semiconductor atoms in the (111) plane of a cubic crystal ((0001) plane for hexagonal) when the atoms are placed above (1) H- and B-sites (a, b, and d) and (2) H- or B-sites (c). Dashed lines are to guide the eye to see the hexagonal symmetry of the semiconductor atoms. The relative rotations of these hexagons for each atom arrangement are written on the top of each figure. For parts a and d, two relative orientations are possible,  $\pm 10.9^\circ$  and  $\pm 16.1^\circ$ , respectively (only the + rotations are shown in the figures). (e) Lattice constants for the lattice-matched atom arrangements in (a) (black vertical line), (b) (green vertical lines), (c) (blue vertical line), and (d) (red vertical line). Dashed and solid lines correspond to the hexagonal ( $a_{\text{hex}}$ ) and cubic ( $a_{\text{cub}} = a_{\text{hex}} \times \sqrt{2}$ ) crystal phases of these lattices, respectively. The square (■) and the hexagon (●) represent the cubic and hexagonal phases, respectively, for Si, ZnO, and III–V semiconductors. Squares (GaAs, AlAs, AlSb) with two different colors indicate that the semiconductor can adopt either of two atomic arrangements on graphene. The figure visualizes the vast possibilities for epitaxial growth of vertical semiconductor nanowires on graphitic substrates. For the case studied in this Letter, GaAs, the lattice mismatch is quite large and in between two different atomic configurations, as indicated with the blue (6.3% lattice mismatch) and green arrows (8.2% lattice mismatch).

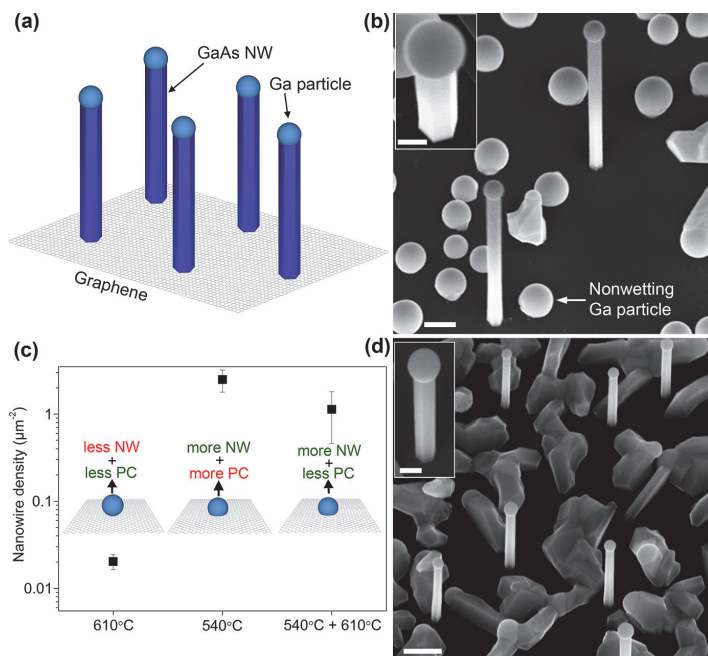


**Figure 2.** (a) Schematic drawing of self-catalyzed GaAs nanowires on a graphitic surface. (b) SEM image of nanowires grown on graphite at 610 °C for 10 min with an As flux of  $6 \times 10^{-6}$  Torr. The inset shows a near top-view image where the uniform hexagonal side-facets of the nanowire can be seen. (c) Variation in the average nanowire density with growth temperature. Insets schematically show contact angles of the Ga catalyst droplet at different temperatures. The Ga droplets have a large contact angle (nonwetting) at high temperature (610 °C), causing a very low nanowire nucleation density. At low temperature (540 °C), the contact angle is reduced and is in a regime where the nanowire nucleation is favored. In the two-temperature growth procedure, the nucleation step was done at low temperature, and subsequent growth was performed at high temperature to promote the nanowire growth over the parasitic crystal growth. NW, nanowire; PC, parasitic crystal. (d) SEM image of nanowires grown on graphite by a two-temperature growth technique where the nanowires are nucleated at 540 °C during 10 s of growth under an As flux of  $3 \times 10^{-6}$  Torr with further nanowire growth under conditions as in part b but for 5 min. In the inset, a tilted-view image of one of the nanowires shows a uniform hexagonal cross section. The scale bars are 200 nm in the main figures and 100 nm in the insets.

from the growth of GaAs nanowires on graphitic substrates that can be understood on the basis of this generic model.

Figure 2a shows a schematic drawing of vertical epitaxial GaAs nanowires grown on a graphitic surface. Figure 2b shows a tilted-view scanning electron microscopy (SEM) image of GaAs nanowires grown on graphite at 610 °C for 10 min with an As flux of  $6 \times 10^{-6}$  Torr (see Supporting Information S1 for details). The nanowires are vertically aligned and have a uniform hexagonal cross section (Figure 2b, inset). The density of the nanowires was, however, found to be low ( $\sim 0.02/\mu\text{m}^2$ ). In addition to the nanowires, a high density of spherical Ga particles with high contact angle were formed (Figure 2b), suggesting that the nonwetting behavior of Ga does not favor nanowire nucleation. By decreasing the growth temperature to 540 °C and the As flux to  $3 \times 10^{-6}$  Torr, the density was substantially increased ( $\sim 1/\mu\text{m}^2$ ), as shown in Supporting Information S2 for 2 min growth. The increased nucleation probability is ascribed to increased Ga wetting at lower temperature, resulting in a smaller contact angle. However, the density of GaAs parasitic crystals is also much higher. Coarse nanowires grew along the surface and with longer growth time coalesced. This coalescence, as well as the growth of the parasitic crystals, eventually (growth time >10 min) led to the coverage of graphite with a rough polycrystalline semi-

conductor thin film. The variation in the nanowire density, and Ga catalyst contact angle at the nucleation stage, is illustrated schematically in Figure 2c. A *two-temperature* growth procedure was applied in order to reduce the parasitic crystals, without compromising on the density of vertical nanowires. First, a low temperature *nanowire nucleation* step was made (using growth conditions as in Supporting Information S2 but for only 10 s), followed by a second high-temperature *nanowire growth* step (for 5 min with growth conditions as for nanowires in Figure 2b). Figure 2d shows a tilted-view SEM image of nanowires grown in this way. Subsequently, GaAs nanowires were grown on few-layer epitaxial graphene synthesized on a SiC substrate<sup>25</sup> without any significant difference in the final morphology and crystal phase of the nanowires (see Supporting Information S3). The salient features are that all nanowires are vertical, have a uniform hexagonal cross-sectional shape, and are aligned with the substrate with a 0 or 30° in-plane side-facet orientation. These features are signatures of an epitaxial link of the nanowires with the graphitic substrates.

To further investigate the epitaxial relationship in relation to the proposed model, the nanowire/graphitic interfaces were studied by transmission electron microscopy (TEM). Figure 3a shows a cross-sectional bright-field TEM image of a vertically aligned GaAs nanowire grown on few-layer epitaxial graphene

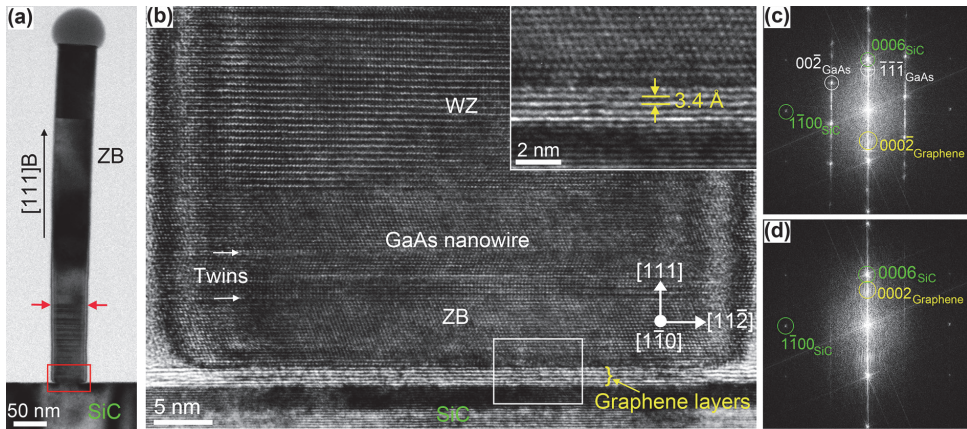


**Figure 3.** TEM images of a representative GaAs nanowire grown on few-layer epitaxial graphene synthesized on a 6H-SiC(0001) substrate. (a) Cross-sectional bright-field TEM image of the nanowire. The bottom part of the nanowire has a mixture of ZB and WZ segments with twins and stacking faults, whereas the rest of the nanowire (above the two red arrows) is nearly defect-free ZB. (b) Cross-sectional high-resolution TEM image showing the interface region of the graphene layers and the nanowire marked with a red box in part a. The inset shows a magnified high-resolution TEM image of the nanowire/graphene/SiC interface area from the area marked with a box in part b. The lattice fringes of the nanowire, the SiC, and the graphene layers separated by  $\sim 3.4$  Å can be seen. (c, d) Fast Fourier transforms from the high-resolution TEM image in part b, from the nanowire/graphene/SiC and graphene/SiC interface regions, respectively.

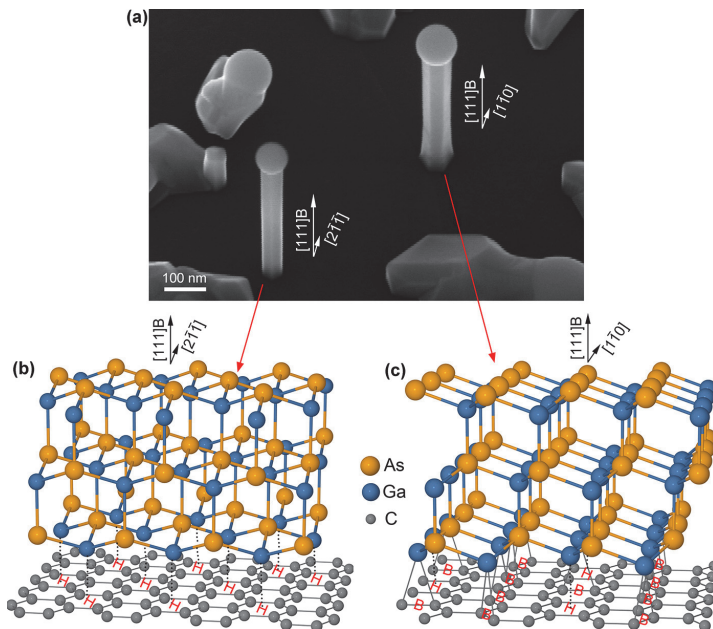


**Figure 4.** SEM image of two nearby  $30^\circ$  rotated GaAs nanowires on graphene with schematic atomic models. (a) SEM image of GaAs nanowires grown on few-layer epitaxial graphene synthesized on a 6H-SiC(0001) substrate, showing the nanowire side-facet rotation by  $30^\circ$  with respect to each other. (b and c) Side-view of the schematic atomic model for coherently strained  $[111]_B$ -oriented GaAs when Ga are adsorbed only above H-sites (b) and above both H- and B-sites (c). Both nanowires have the same  $\{1\bar{1}0\}$  side-facets, as confirmed by electron diffraction. About 2/3 (of 300) of the nanowires on the sample have the facets oriented as the nanowire to the lower left in part a, and about 1/3 have facets oriented as the nanowire to the upper right in part a. Correlation with the crystal orientation of the SiC substrate shows that the nanowire to the lower left in part a has the atomic arrangement as in Figure 1c, with a lattice mismatch of 6.3%, and the nanowire to the upper right in part a has the atomic arrangement as in Figure 1b, with a lattice mismatch of 8.2%.

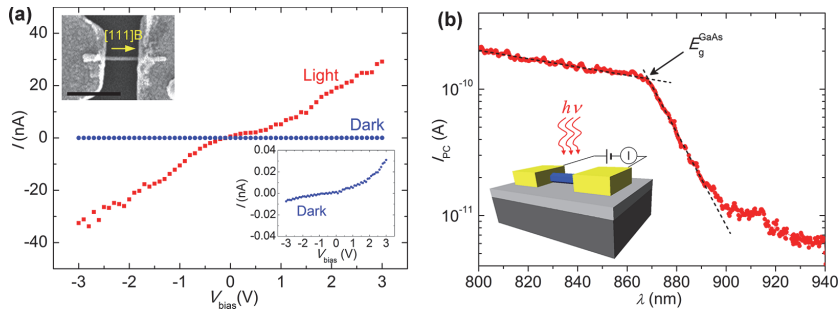


**Figure 5.** Photocurrent response of a single GaAs nanowire photodetector. (a)  $I$ - $V$  curves of a single GaAs nanowire photodetector. The blue circles are measured dark current ( $I_{\text{dark}}$ ), whereas the red squares are measured photocurrent ( $I_{\text{PC}}$ ). The photocurrent was measured using an 800 nm laser line with an estimated power density of  $\sim 2.5$  kW/cm<sup>2</sup>. The bottom inset shows the dark current with an enlarged y-axis. The top inset is a SEM image of the photodetector where a single nanowire had been dispersed from the same sample, as shown in Figure 2d. The scale bar in the inset is 500 nm. (b) Wavelength ( $\lambda$ ) dependence of the photocurrent for the nanowire at an applied bias voltage of 50 mV. From the crossing of the black dashed lines, the absorption edge was estimated to be at  $\sim 869$  nm (1.427 eV) denoted by a black arrow. The inset shows a schematic image of the fabricated nanowire photodetector.

(synthesized on a 6H-SiC(0001) substrate) using the two-temperature growth procedure (from the same sample as depicted in Supporting Information S3). Figure 3b depicts a cross-sectional high-resolution TEM image of the interface region marked with a red rectangular box in Figure 3a. The graphene layers were found to be flat without any steps and ledges underneath the nanowire. In the inset, a magnified image of the nanowire/graphene/SiC interface region is shown, where graphene layers separated by  $\sim 3.4$  Å can be seen. The fast Fourier transforms in Figure 3c,d from the nanowire/graphene/SiC and graphene/SiC interface regions, respectively, demonstrate the epitaxial relationship between the nanowire and graphene. The nanowires grew along the  $[111]_{\text{B}}$  direction and have  $\{1\bar{1}0\}$  side-facets. Misfit dislocations were not observed in the nanowires adjacent to the interface with graphene (Figure 3b). Similar observations have been made for GaAs nanowires grown on graphite (see Supporting Information S4). These results indicate that the GaAs nanowires grow epitaxially on graphitic surfaces and mainly have a zinc blende (ZB) crystal phase (above the red arrows in Figure 3a). The same crystal phase is commonly observed for self-catalyzed GaAs nanowires grown on GaAs(111)B or Si(111) substrates by MBE.<sup>26</sup> The lower part of the nanowire (below the red arrows in Figure 3a) consists of a mixture of ZB and wurtzite (WZ) segments, with twinning defects and stacking faults for both growth on few-layer graphene and graphite (see Supporting Information S4). These structural irregularities in the initial growth face are attributed to a combination of catalyst droplet shape change due to the two-temperature transition and strain relaxation in the nanowire due to the growth on a lattice-mismatched substrate.

When investigating by SEM the orientation of the side-facets of the nanowires grown on epitaxial graphene on 6H-SiC(0001), it was found that  $\sim 1/3$  of the nanowires (based on a set of 300) had facets rotated by  $30^\circ$  relative to the others (Figure 4a). Electron diffraction analysis revealed that both orientations of the nanowires have  $\{1\bar{1}0\}$  facets. For graphene on the Si-terminated side of SiC, as used here, only one phase is expected; i.e., it is without any rotational disorder.<sup>27</sup> By correlating the crystal orientation of the underlying SiC substrate, the graphene layers, and the nanowires, we verified that the smaller fraction ( $\sim 1/3$ ) of the nanowires corresponds

to the atomic arrangement given in Figure 1b (H- and B-sites) with larger lattice mismatch as discussed later in the text.

First-principle calculations have shown that the preferred adsorption sites for adatoms in groups I–III (like Ga) are above H-sites, where they bind *ionically*.<sup>28,29</sup> On the other hand, As adsorbs preferentially above B-sites, making a *covalent* binding with graphene.<sup>24,29,30</sup> Binding energies of both Ga and As with graphene are of the same order,<sup>24</sup> and irrespective of which atom binds first, GaAs (111)B can be realized in both cases. For vertical self-catalyzed GaAs nanowires on GaAs(111)B and Si(111),<sup>26</sup> Ga is always the first atomic layer.

In the case of ZB GaAs, the atoms in the (111) plane can be placed either only above H-sites (if Ga first layer), as shown in Figure 4b, or only above B-sites (if As first layer), corresponding to Figure 1c. This will result in 6.3% lattice mismatch (see Supporting Information S5). When the atoms are placed above both H- and B-sites (Figure 4c), corresponding to Figure 1b, the lattice mismatch is 8.2%. In both cases, it is expected that the first few GaAs layers will have an in-plane strain, due to the lattice mismatch with graphene. For graphite, only the top graphene layer will be strained, due to the weak van der Waals binding between various graphitic layers. Besides GaAs nanowires, also catalyst-free InAs nanowires were grown on graphite (see Supporting Information S6 for details).

Bending experiments on as-grown nanowires on graphite demonstrated failure stress slightly smaller to that for self-catalyzed GaAs nanowires grown on Si(111) (Supporting Information S7 and videos SV1 (n13018115\_si\_002.avi) for nanowire on Si and SV2 (n13018115\_si\_003.avi) for nanowire on graphite). This is in support of our view of a strong ionic/covalent binding at the nanowire/graphite interface.

Local defects in the graphitic surfaces<sup>31</sup> could play a role in the initiation and nucleation of the nanowires, for example, by trapping the Ga catalyst droplet and providing dangling bonds. Controlling the nucleation introduced by external manipulation is important for increased control of the nanowire density, reduction of parasitic crystallites, and ultimately for positioning of vertical semiconductor nanowires on graphene for device applications.

To study the optoelectronic properties of GaAs nanowires grown on graphite, single-nanowire photodetectors were

fabricated by using standard e-beam lithography and deposition of 100 nm thick Au as contact electrodes. The inset in Figure 5a is a SEM image of the device. In dark mode, a high resistance ( $R > 100 \text{ G}\Omega$ ) with an asymmetric  $I$ - $V$  curve is measured (see the bottom inset of Figure 5a). However, under laser illumination, the  $I$ - $V$  curve becomes more linear with an increase of more than 3 orders of magnitude in the current. Since an unpassivated GaAs nanowire has a surface charge trap density of  $\sim 10^{12} \text{ cm}^{-2}$ , this causes a Fermi level pinning at the nanowire surface with a surface depletion layer, which naturally results in a formation of Schottky contacts between nanowire and metal electrodes.<sup>32,33</sup> This indicates that the observed photocurrent response mainly comes from the nanowire-electrode contact region.<sup>34,35</sup>

The responsivity of the GaAs nanowire device is estimated to be  $\sim 30 \text{ mA/W}$ , which is 3 orders of magnitude larger than previously reported for a single GaAs nanowire<sup>36</sup> (see Supporting Information S1 for estimation of the responsivity). It should also be noted that the observed  $I$ - $V$  characteristics of the GaAs nanowire photodetector are similar to what we have previously observed in intrinsic GaAs nanowires grown on GaAs(111)B substrates.<sup>37</sup> This demonstrates the high purity of the MBE grown nanowires, without any apparent contamination due to the growth on graphite. The wavelength dependence of the photocurrent has a sharp drop with an absorption edge at  $\sim 869 \text{ nm}$  (Figure 5b). Although the photocurrent response is assumed to come mainly from the nanowire-electrode contact region, the exponential decrease of the photocurrent after the absorption edge is sharp in a 30 nm ( $\sim 50 \text{ meV}$ ) range, comparable to the intrinsic GaAs absorption edge.<sup>38</sup> These results convey that GaAs nanowires grown on graphite are at least of similar optoelectronic quality as the ones grown on GaAs substrates, and hence can be equally useful for nanowire optoelectronic applications.<sup>39</sup>

In conclusion, our work demonstrates that semiconductor nanowires can grow epitaxially on graphitic surfaces. A generic atomic model which explains the possible structures of the semiconductor nanowire/graphitic interfaces is presented. Experimentally, we have demonstrated that high-quality GaAs nanowire/graphene hybrid heterostructures can indeed be realized by MBE using the self-catalyzed technique. A single GaAs nanowire photodetector with a high responsivity was fabricated which demonstrates no degradation in the optoelectronic material quality, as compared to GaAs nanowires grown on GaAs substrates. The proposed heteroepitaxial growth configurations could become the basis for new types of nanowire/graphite and nanowire/graphene hybrid device systems.

## ■ ASSOCIATED CONTENT

### Supporting Information

The Supporting Information includes a description of the materials and methods (S1); GaAs nanowire growth on graphite at low temperature (S2); GaAs nanowire growth on few-layer epitaxial graphene (S3); cross-sectional TEM image of GaAs nanowires grown on graphite (S4); calculation of GaAs lattice mismatch with graphene (S5); catalyst-free InAs nanowires grown on graphite (S6); comparison of GaAs nanowire bending on graphite and on Si (S7); atomic force microscopy of graphite and epitaxial graphene (S8); as well as two videos (SV1, n13018115\_si\_002.avi; SV2, n13018115\_si\_003.avi). This material is available free of charge via the Internet at <http://pubs.acs.org>.

## ■ AUTHOR INFORMATION

### Corresponding Author

\*E-mail: helge.weman@iet.ntnu.no.

### Author Contributions

H.W. conceived and supervised the project, with the assistance from B.-O.F. D.L.D. and A.M.M. carried out the growth experiment and SEM characterization. V.T.F., A.T.J.v.H., and A.M.M. performed the TEM characterization. V.T.F. performed SEM and the FIB TEM sample preparation and the nanowire bending experiment. D.-C.K. prepared the Kish graphene sample, verified surface morphologies by AFM, fabricated the nanowire device, and carried out the photocurrent measurement. H.W. wrote the manuscript, and all authors contributed equally in analyzing the results and in the writing process.

### Notes

The authors declare no competing financial interest.

## ■ ACKNOWLEDGMENTS

We acknowledge the technical support from the staff in NTNU NanoLab and the financial support from NTNU NanoLab, NTNU Discovery, NorFab, and the Research Council of Norway (RENERGI program grant no. 190871). R. Yakimova (Linköping University, Sweden) is acknowledged for providing epitaxial graphene samples. The authors also thank T. Tybell and M. A. Dupertuis for constructive feedback on the manuscript.

## ■ REFERENCES

- (1) Bakkers, E. P. A. M.; van Dam, J. A.; De Franceschi, S.; Kouwenhoven, L. P.; Kaiser, M.; Verheijen, M.; Wondergem, H.; van der Sluis, P. *Nat. Mater.* **2004**, *3*, 769–773.
- (2) Schmidt, V.; Wittemann, J. V.; Senz, S.; Gösele, U. *Adv. Mater.* **2009**, *21*, 2681–2702.
- (3) Johansson, J.; Karlsson, L. S.; Patrik T. Svensson, C.; Martensson, T.; Wacaser, B. A.; Deppe, K.; Samuelson, L.; Seifert, W. *Nat. Mater.* **2006**, *5*, 574–580.
- (4) Dheeraj, D. L.; Patriarche, G.; Zhou, H.; Hoang, T. B.; Moses, A. F.; Grønsberg, S.; van Helvoort, A. T. J.; Fimland, B.-O.; Weman, H. *Nano Lett.* **2008**, *8*, 4459–4463.
- (5) Kodambaka, S.; Tersoff, J.; Reuter, M. C.; Ross, F. M. *Science* **2007**, *316*, 729–732.
- (6) Dick, K. A.; Thelander, C.; Samuelson, L.; Caroff, P. *Nano Lett.* **2010**, *10*, 3494–3499.
- (7) Xu, S.; Qin, Y.; Xu, C.; Wei, Y.; Yang, R.; Wang, Z. L. *Nat. Nanotechnol.* **2010**, *5*, 366–373.
- (8) Tian, B.; Cohen-Karni, T.; Qing, Q.; Duan, X.; Xie, P.; Lieber, C. M. *Science* **2010**, *329*, 830–834.
- (9) Mårtensson, T.; Carlberg, P.; Borgström, M.; Montelius, L.; Seifert, W.; Samuelson, L. *Nano Lett.* **2004**, *4*, 699–702.
- (10) Bonaccorso, F.; Sun, Z.; Hasan, T.; Ferrari, A. C. *Nat. Photonics* **2010**, *4*, 611–622.
- (11) Kelzenberg, M. D.; Boettcher, S. W.; Petykiewicz, J. A.; Turner-Evans, D. B.; Putnam, M. C.; Warren, E. L.; Spurgeon, J. M.; Briggs, R. M.; Lewis, N. S.; Atwater, H. A. *Nat. Mater.* **2010**, *9*, 239–244.
- (12) Czaban, J. A.; Thompson, D. A.; LaPierre, R. R. *Nano Lett.* **2009**, *9*, 148–154.
- (13) Chung, K.; Lee, C.-H.; Yi, G.-C. *Science* **2010**, *330*, 655–657.
- (14) Koma, A. *J. Cryst. Growth* **1999**, *201–202*, 236–241.
- (15) Johnston, W. D., Jr.; Callahan, W. M. *J. Electrochem. Soc.* **1978**, *125*, 977–983.
- (16) Bauer, E.; Poppa, H. *Thin Solid Films* **1972**, *12*, 167–185.
- (17) Glas, F. *Phys. Rev. B* **2006**, *74*, 121302.
- (18) Hass, J.; Heer, W. A. d.; Conrad, E. H. *J. Phys.: Condens. Matter* **2008**, *20*, 323202.

- (19) Kim, Y.-J.; Lee, J.-H.; Yi, G.-C. *Appl. Phys. Lett.* **2009**, *95*, 213101–213103.
- (20) Kumar, B.; Lee, K. Y.; Park, H.-K.; Chae, S. J.; Lee, Y. H.; Kim, S.-W. *ACS Nano* **2011**, *5*, 4197–4204.
- (21) Hong, Y. J.; Lee, W. H.; Wu, Y.; Ruoff, R. S.; Fukui, T. *Nano Lett.* **2012**, *12*, 1431–1436.
- (22) Wagner, R. S.; Ellis, W. C. *Appl. Phys. Lett.* **1964**, *4*, 89–90.
- (23) Weman, H.; Fimland, B. O.; Kim, D. C. U.K. patent application # 1021112.6 filed Dec 13, 2010, and PCT patent application WO 2012/080252 A1 filed Dec 13, 2011.
- (24) Nakada, K.; Ishii, A. *Solid State Commun.* **2011**, *151*, 13–16.
- (25) Tzalenchuk, A.; Lara-Avila, S.; Kalaboukhov, A.; Paolillo, S.; Syvajarvi, M.; Yakimova, R.; Kazakova, O.; Janssen, T. J. B. M.; Fal'ko, V.; Kubatkin, S. *Nat. Nanotechnol.* **2010**, *5*, 186–189.
- (26) Uccelli, E.; Arbiol, J.; Magen, C.; Krogstrup, P.; Russo-Averchi, E.; Heiss, M.; Mugny, G.; Morier-Genoud, F. o.; Nygård, J.; Morante, J. R.; Fontcuberta i Morral, A. *Nano Lett.* **2011**, *11*, 3827–3832.
- (27) Virojanadara, C.; Yakimova, R.; Zakharov, A. A.; Johansson, L. I. *J. Phys. D: Appl. Phys.* **2010**, *43*, 374010.
- (28) Chan, K. T.; Neaton, J. B.; Cohen, M. L. *Phys. Rev. B* **2008**, *77*, 235430.
- (29) Zhu, Z. H.; Lu, G. Q.; Wang, F. Y. *J. Phys. Chem. B* **2005**, *109*, 7923–7927.
- (30) Liu, X.; Wang, C. Z.; Yao, Y. X.; Lu, W. C.; Hupalo, M.; Tringides, M. C.; Ho, K. M. *Phys. Rev. B* **2011**, *83*, 235411.
- (31) Banhart, F.; Kotakoski, J.; Krasheninnikov, A. V. *ACS Nano* **2011**, *5*, 26–41.
- (32) Demichel, O.; Heiss, M.; Bleuse, J.; Mariette, H.; Fontcuberta i Morral, A. *Appl. Phys. Lett.* **2010**, *97*, 201907–201903.
- (33) Howes, M. J.; Morgan, D. V. *Gallium arsenide—Materials, devices and circuits*; John Wiley & Sons Ltd.: New York, 1985.
- (34) Maharjan, A.; Pemasiri, K.; Kumar, P.; Wade, A.; Smith, L. M.; Jackson, H. E.; Yarrison-Rice, J. M.; Kogan, A.; Paiman, S.; Gao, Q.; Tan, H. H.; Jagadish, C. *Appl. Phys. Lett.* **2009**, *94*, 193115–193113.
- (35) Gu, Y.; Kwak, E. S.; Lensch, J. L.; Allen, J. E.; Odom, T. W.; Lauhon, L. J. *Appl. Phys. Lett.* **2005**, *87*, 043111–043113.
- (36) Gallo, E. M.; Chen, G.; Currie, M.; McGuckin, T.; Prete, P.; Lovergine, N.; Nabet, B.; Spanier, J. E. *Appl. Phys. Lett.* **2011**, *98*, 241113–241113.
- (37) Kim, D. C.; Ahtapodov, L.; Boe, A. B.; Choi, J. W.; Ji, H.; Kim, G. T.; Moses, A. F.; Dheeraj, D. L.; Fimland, B. O.; Weman, H. *AIP Conf. Proc.* **2011**, *1399*, 429–430.
- (38) Blakemore, J. S. *J. Appl. Phys.* **1982**, *53*, R123–R181.
- (39) Mokkaapati, S.; Jagadish, C. *Mater. Today* **2009**, *12*, 22–32.



Supporting Information for

## Vertically Aligned GaAs Nanowires on Graphite and Few-Layer Graphene: Generic Model and Epitaxial Growth

A. Mazid Munshi<sup>†</sup>, Dasa L. Dheeraj<sup>†</sup>, Vidar T. Fauske<sup>‡</sup>, Dong-Chul Kim<sup>†</sup>, Antonius T. J. van Helvoort<sup>‡</sup>, Bjørn-Ove Fimland<sup>†</sup> and Helge Weman<sup>†\*</sup>

<sup>†</sup>*Department of Electronics and Telecommunications, Norwegian University of Science and Technology (NTNU), NO-7491 Trondheim, Norway*

<sup>‡</sup>*Department of Physics, Norwegian University of Science and Technology, NO-7491 Trondheim, Norway*

\* *To whom correspondence should be addressed. E-mail: [helge.weman@iet.ntnu.no](mailto:helge.weman@iet.ntnu.no)*

### **This PDF file includes:**

Materials and methods (S1)

Supporting materials S2 to S8

References

### **Other supporting material includes the following:**

Videos SV1 and SV2

## Table of Contents:

|   |           |
|---|-----------|
| <b>S1. Materials and Methods .....</b>  | <b>2</b>  |
| <b>S2. GaAs nanowire growth on graphite .....</b>                               | <b>3</b>  |
| <b>S3. GaAs nanowire growth on few-layer epitaxial graphene .....</b>           | <b>4</b>  |
| <b>S4. Cross-sectional TEM image of a GaAs nanowire grown on graphite .....</b> | <b>5</b>  |
| <b>S5. Calculation of GaAs lattice mismatch with graphene .....</b>             | <b>7</b>  |
| <b>S6. Catalyst-free InAs nanowires grown on graphite .....</b>                 | <b>8</b>  |
| <b>S7. Comparison of GaAs nanowire bending on graphite with on Si .....</b>     | <b>9</b>  |
| <b>S8. Atomic force microscopy of graphite and epitaxial graphene .....</b>     | <b>11</b> |

## **S1. Materials and Methods**

**Preparation of graphitic substrates.** For the growth on Kish graphite (Toshiba Ceramics Co.), the graphite was first cleaned in acetone/ethanol and then cleaved to expose the clean surface before bonding to a Si substrate using In. For the growth on few-layer graphene, epitaxial graphene synthesized on SiC was used as a substrate. Few-layer (4-5) stacked Bernal (ABA) epitaxial graphene layers (see Fig. S2) were produced on the Si-face of a nominally on-axis 6H-SiC(0001) substrate (SiCrystal AG) by Graphensic AB, Sweden. The epitaxial graphene growth was carried out under highly isothermal conditions at a temperature of 2000°C and at an ambient argon pressure of 1 atm. Surface topology of the graphitic surfaces was studied by atomic force microscopy (diMultimode V Nanoscope Veeco AFM) and is presented in the Supporting Information S8.

**Nanowire growth.** GaAs nanowires were grown on various graphitic substrates using a self-catalyzed vapor-liquid-solid growth technique. The GaAs nanowires were grown in a Varian Gen II Modular molecular beam epitaxy system equipped with a Ga dual filament cell and an As valved cracker cell. In the present study, the major species of arsenic were As<sub>4</sub>. After cleaning in acetone/ethanol, the graphitic substrates were directly loaded into the molecular beam epitaxy chamber and heated to the growth temperatures. The nanowire growth was initiated by opening the shutter of the Ga effusion cell 20 s before the As shutter. The temperature of the Ga effusion cell was pre-set to yield a nominal planar GaAs growth rate of 0.7 monolayers per second, and the valve position of the As cracker cell was adjusted to yield the required fluxes.

**Structural characterization.** The morphology of the nanowires was investigated by field-emission Zeiss Ultra55 and Supra55VP SEMs operating at 10 kV. The structural analyses were performed in Philips CM30 and JEOL 2010F TEMs, both operating at 200 kV. Specimens for cross-sectional TEM were made using a FEI Helios DualBeam focused ion

beam system with Ga<sup>2+</sup> ions in the range 5–30 kV. Initial C and Pt protection layers were electron beam deposited. An Omniprobe AutoProbe 200 lift-out finger in the DualBeam was also used for bending experiments. Nanowire facet orientation was determined by correlating SEM images of site-specific focused ion beam cross-sections with TEM diffraction patterns.

**Device fabrication and photocurrent measurement.** A tip of a cleanroom paper (tip size < ~0.5 mm) was used to remove the as-grown nanowires from the Kish graphite. After scraping the sample with the tip, the broken nanowires were transferred to the SiO<sub>2</sub>(300nm)/*p*-Si substrates. Electrode patterns for nanowire contacts were made by electron-beam lithography (Raith Elphy quantum system on a Hitachi S-4300 SEM). The exposed areas of the nanowires were etched and passivated using HCl and NH<sub>4</sub>S<sub>x</sub> solutions, respectively, before contact metallization with 100 nm Au. Photocurrent measurements were carried out using a Mitutoyo 50X, 0.65 numerical aperture objective lens. The laser power density of ~2.5 kW/cm<sup>2</sup> was estimated from the calculated spot diameter with an 800 nm laser (~1.5 μm), and a laser power of 45 μW. The responsivity was determined at a bias of 1 V, giving a photocurrent of ~10 nA. The cross-sectional area of the nanowire exposed in-between the electrodes (length ~0.35 μm, width ~40 nm) is used to calculate the responsivity. A tuneable cw Ti:sapphire laser (700–1000 nm) was used for the laser excitation. An AC technique using a lock-in amplifier with a light chopper and a current amplifier was used for the photocurrent spectroscopy. All photocurrent measurements were carried out at room temperature in vacuum (~10<sup>-5</sup> mbar).

## **S2. GaAs nanowire growth on graphite**

To check the effect of growth temperature, self-catalyzed GaAs nanowires were grown on graphite by reducing the temperature from 610 to 540 °C. This reduction in temperature leads to an increased nanowire as well as parasitic crystal density as is shown in Fig. S1 (see Fig. 2b in the Letter for comparison). In addition to the vertical nanowires growing along

[111]B direction, there are some coarse nanowires (yellow arrows in Fig. S1) which grew in random directions along the graphite surface. With increase in the growth time, the vertical nanowires grew longer, whereas the nanowires growing in other directions started to coalescence and eventually the graphitic surface was almost completely covered with parasitic crystals. To limit the parasitic crystal growth, we employed a two-temperature growth procedure, as described in the Letter, by which we achieved a higher density of vertical nanowires and less parasitic crystals.

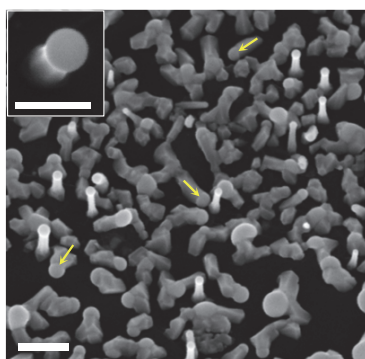


**Fig. S1.** Tilted-view scanning electron microscopy (SEM) image of self-catalyzed GaAs nanowires grown on graphite at 540 °C for 2 min with an As flux of  $3 \times 10^{-6}$  Torr. The nominal planar GaAs growth rate was 0.7 monolayers per second. Yellow arrows mark coarse nanowires growing along the graphite surface in random directions. Inset shows a near top-view magnified image of one of the nanowires. The scale bars are 200 nm in the main figure, and 100 nm in the inset.

### **S3. GaAs nanowire growth on few-layer epitaxial graphene**

GaAs nanowires were grown on few-layer epitaxial graphene synthesized on 6H-SiC(0001) with the same growth parameters as used for Kish graphite (Fig. 2d in the Letter) and is shown in Fig. S2. All the nanowires grown on few-layer graphene have similar uniform morphology and crystal phase as for those grown on graphite.

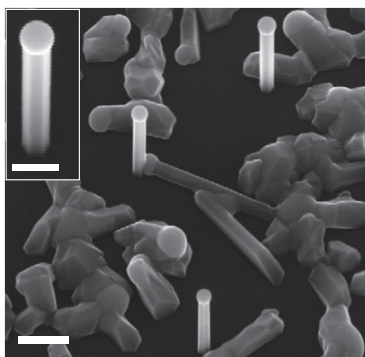


**Fig. S2.** Tilted-view SEM image of self-catalysed GaAs nanowires grown on epitaxial few-layer graphene (synthesized on a 6H-SiC(0001) substrate) using the two-temperature growth condition. Inset shows a magnified image of one of the nanowires. The scale bars are 200 nm in the main figure and 100 nm in the inset.

#### **S4. Cross-sectional TEM image of GaAs nanowire grown on graphite**

The epitaxial relationship of the GaAs nanowires grown on graphite was also investigated by studying the nanowire/graphite interface by TEM. Fig. S3a shows a cross-sectional high-resolution TEM image of the interface region of a nanowire grown on graphite. Fig. S3b depicts the fast Fourier transforms corresponding to the nanowire, nanowire/graphite interface, and graphite area, demonstrating the epitaxial relationship between the nanowire and graphite. The nanowires grew along the  $[111]_B$  direction and have  $\{1\bar{1}0\}$  side-facets. In Fig. S3c a magnified HRTEM image of the nanowire/graphite interface is shown. Fig. S3d shows a bright-field TEM image of a representative nanowire, which indicates that nanowires mainly consists of defect-free ZB crystal phase (Fig. S3e), A WZ segment, stacking faults and higher density of twinning planes are only found in the lower part of the nanowire adjacent to graphite. These structural characteristics are similar to the case when they are grown on few-layer epitaxial graphene on SiC (Fig. 3 in the Letter).

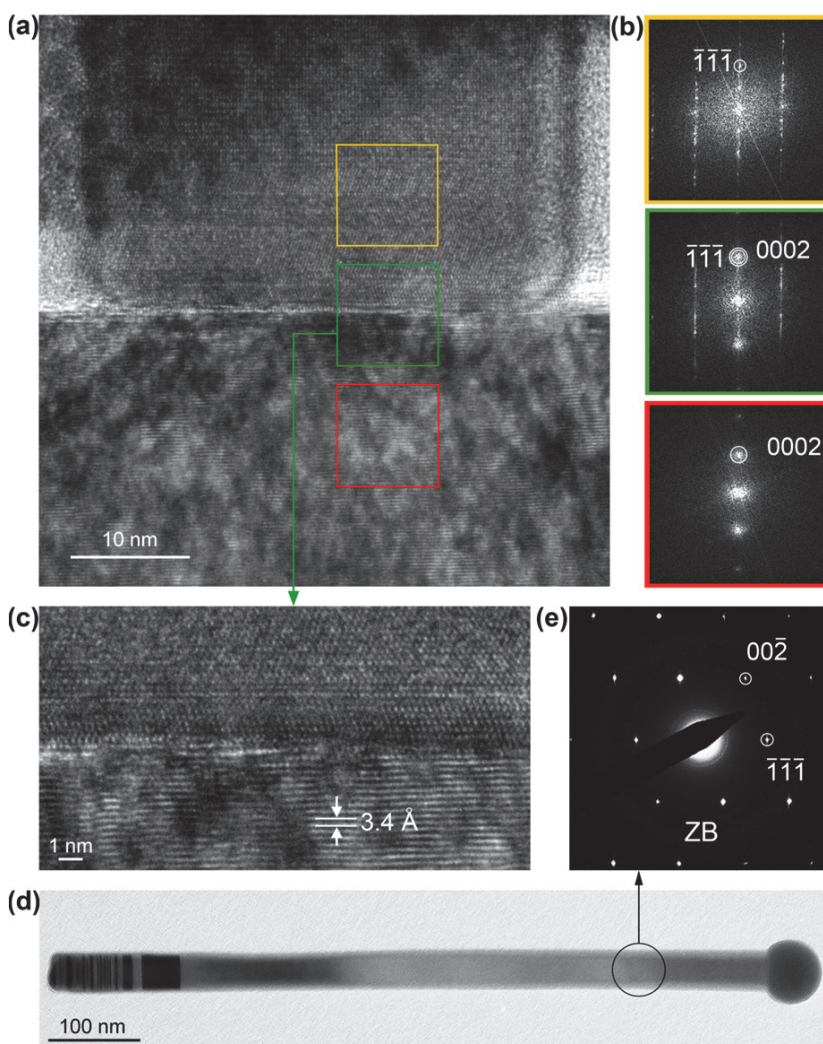


**Fig. S3.** (a) Cross-sectional high-resolution TEM image of a vertical GaAs nanowire grown on graphite (from the same sample as depicted in Fig. 2d in the Letter) showing the interface region of graphite and the vertical GaAs nanowire. To protect the nanowire during the milling process, C and Pt protection layers were used. (b) Fast Fourier transformation from the high-resolution TEM image in (a), from the nanowire (orange box), nanowire/graphite interface (green box) and graphite (red box) regions, indicating the epitaxial relationship of the nanowire with graphite. (c) Magnified high-resolution TEM image of the interface area from (a), where the lattice fringes of the GaAs nanowire and the (0002) graphitic layers separated by  $\sim 3.4$  Å can be seen. (d) Bright-field TEM image of a dispersed, representative GaAs nanowire (from the same sample as depicted in Fig. 2d in the Letter). (e) Selected area electron diffraction pattern from the top part of the nanowire in (d) shows that except for the

bottom part with higher density of stacking faults, twinning planes and a WZ segment, the nanowire has a defect-free ZB crystal phase.

### S5. Calculation of GaAs lattice mismatch with graphene

When Ga (or As) atoms are placed above H-sites, as shown in Fig. S4a, the distance between two neighbouring Ga (or As) atoms is  $4.266 \text{ \AA}$  ( $= 1.422 \text{ \AA}$  (carbon atom distance)  $\times 3$ ). For ZB (cubic) GaAs, the lattice constant is  $5.653 \text{ \AA}$ <sup>1</sup>. The lattice mismatch is then

$$\left| \frac{\frac{5.653}{\sqrt{2}} - 4.266}{4.266} \times 100\% \right| = \left| \frac{3.997 - 4.266}{4.266} \times 100\% \right| = 6.3\%$$

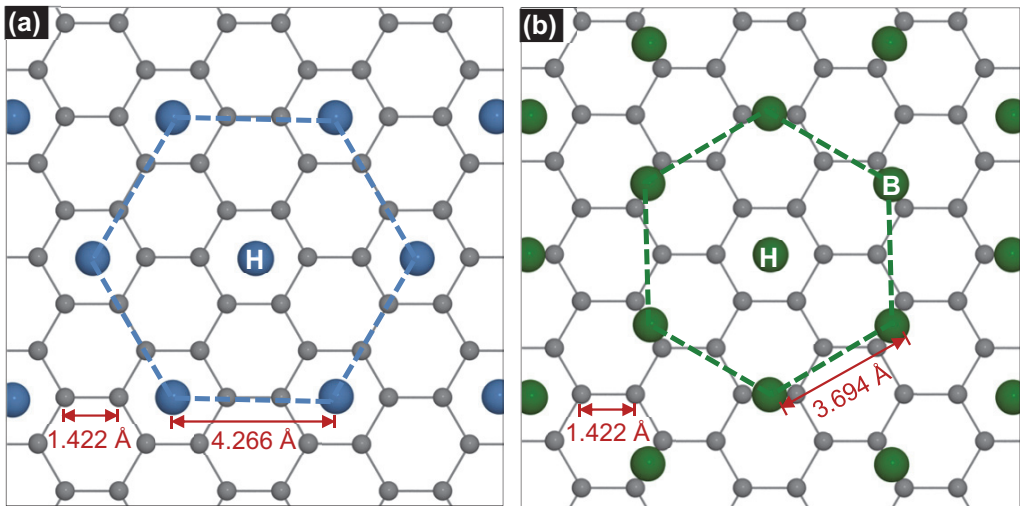


**Fig. S4.** (a), Layout of Ga (or As) atoms in the (111) plane above specific H-sites of graphene in order to be lattice-matched to graphene. For GaAs with a lattice constant of  $5.653 \text{ \AA}$ , this gives an in-plane lattice mismatch of 6.3% to graphene (exact lattice match corresponds to a ZB semiconductor with a lattice constant of  $6.033 \text{ \AA}$ ). (b), Layout of Ga (or As) atoms in the (111) plane above specific H- and B-sites of graphene in order to be lattice-matched to graphene. For GaAs this gives an 8.2% in-plane lattice mismatch between GaAs and graphene (exact lattice match corresponds to a ZB semiconductor with a lattice constant of  $5.224 \text{ \AA}$ ).

When Ga (or As) atoms are placed above both H- and B-sites as in Fig. S4b, the distance between two neighbouring Ga (As) atoms is  $1.422 \text{ \AA} \times 3 \times \sqrt{3}/2 = 3.694 \text{ \AA}$ . The lattice mismatch then becomes

$$\left| \frac{\frac{5.653}{\sqrt{2}} - 3.694}{3.694} \times 100\% \right| = \left| \frac{3.997 - 3.694}{3.694} \times 100\% \right| = 8.2\%$$

### S6. Catalyst-free InAs nanowires grown on graphite

InAs nanowires were grown on graphite. After cleaning in acetone/ethanol, the graphitic substrate was directly loaded into the molecular beam epitaxy chamber. The sample was ramped up to a growth temperature of 450 °C, and the growth was initiated by opening the In and As shutters at the same time. The In effusion cell temperature was pre-set to yield a nominal planar InAs growth rate of 0.1 monolayers per second, and the As flux was  $5 \times 10^{-6}$  Torr. The growth duration was 60 min, and growth was terminated by closing the In and As shutters simultaneously before the sample was quickly ramped down to room temperature. Fig. S5 shows a SEM image of such catalyst-free InAs nanowires grown on graphite.

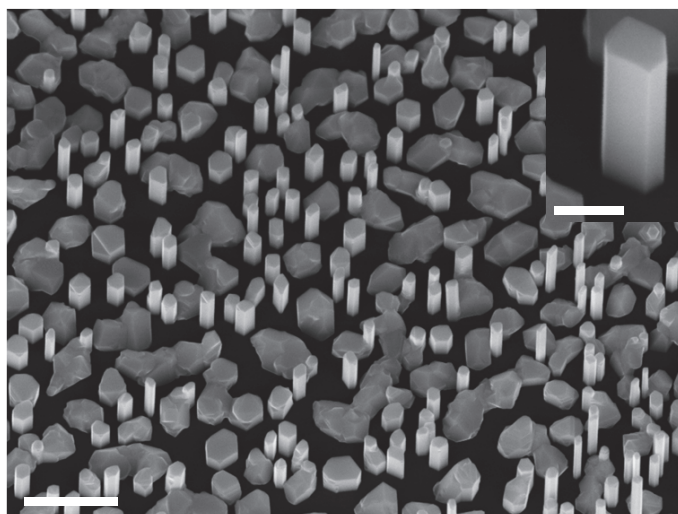


**Fig. S5.** Tilted-view SEM image of catalyst-free InAs nanowires grown on graphite. Scale bar is 1  $\mu\text{m}$ . Inset is magnified image of one of the nanowires showing an asymmetric cross-section. Scale bar in inset is 200 nm.



The nanowires are observed to have an asymmetric cross-section (inset in Fig. S5) and they have a reduced length-to-diameter ratio compared to the GaAs nanowires in the Letter. In addition, we did not observe any catalyst particle at their tip, indicating that the growth mode was catalyst-free<sup>2</sup>. The density of the nanowires was found to be higher than for the self-catalysed GaAs nanowires grown on graphitic substrates. This might be due to the much smaller lattice mismatch for InAs on a graphitic surface. The lattice mismatch when the In (or As) atoms are placed on graphene as in Fig. S4a (above H, B or T-sites) is:

$$\left| \frac{\frac{6.058}{\sqrt{2}} - 4.266}{4.266} \times 100\% \right| = \left| \frac{4.284 - 4.266}{4.266} \times 100\% \right| = 0.42\%$$

The in-plane orientation of the InAs nanowire side-facets and the InAs parasitic crystals, suggests an epitaxial relationship with the graphitic substrate.

## S7. Comparison of GaAs nanowire bending on graphite with on Si

Bending experiments were performed on as-grown GaAs nanowires by applying a lateral force with an Omniprobe AutoProbe 200 nano-manipulator. This was done *in-situ* in a FEI Helios Dual Beam focused ion beam system. The mechanical response of the nanowires was monitored directly by SEM at a 38° angle from the substrate. By comparing the response of GaAs nanowires grown on graphite with positioned GaAs nanowires grown on a Si(111) substrate<sup>3</sup>, a qualitative understanding of the bonding strength was gained. Videos of the experiments were recorded and two are included in the Supplementary materials (see Supporting Video SV1 and SV2). In Fig. S6, still-frame images from the videos are shown. The videos have been edited to highlight the bending of the nanowires by varying the playback speed.

Fig. S6a,d show the unloaded nanowires on Si and graphite, respectively. Fig. S6b,e show the same nanowires momentarily before fracture at the nanowire/substrate interface, and Fig. S6c,f

after fracture. As can be seen, the nanowires on Si accommodate a larger deflection before fracture, but the nanowire is also longer and has a larger diameter.

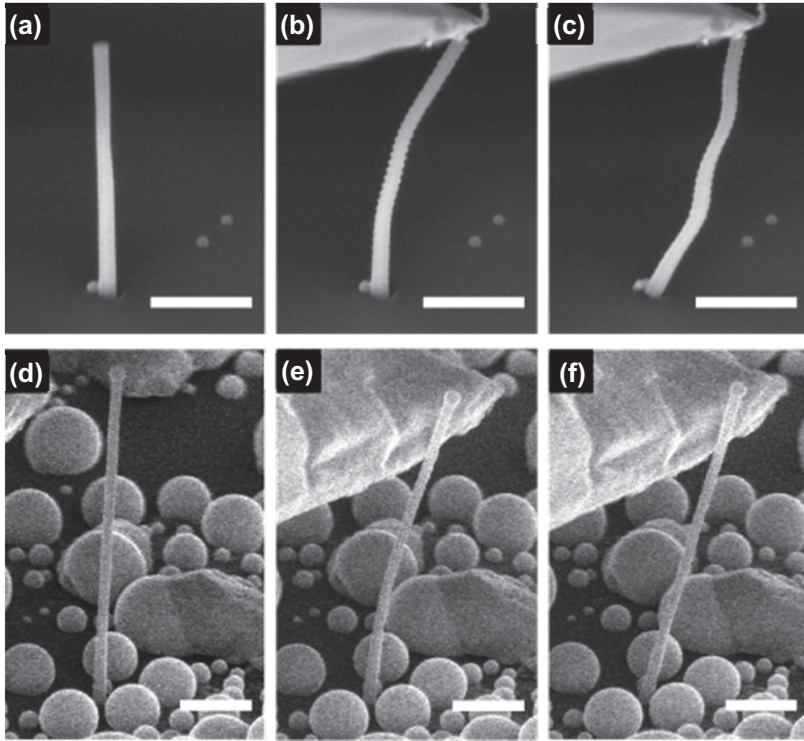


**Fig. S6.** SEM images of nanowire bending experiments. **(a-c)** Unloaded nanowire, just before, and after fracture at the nanowire/substrate interface, respectively, for the GaAs nanowire grown on Si(111). **(d-f)** Unloaded nanowire, just before, and after fracture at the nanowire/substrate interface, respectively, for the GaAs nanowire grown on graphite. Scale bars are 1  $\mu\text{m}$  for (a-c) and 500 nm for (d-f).

To compare the two systems, the simple Euler-Bernoulli beam theory<sup>4-5</sup> for cantilevers is applied as a first-order approximation, ignoring nanoscale effects. The bonding strength is compared by considering the critical tensile stress at the edge of the nanowire, just prior to fracture,

$$\sigma_{crit} = \frac{Mc}{I} \propto \frac{w_{max}}{L^2} D$$

where  $M$  is the bending moment,  $c$  is the distance of the edge from the neutral axis,  $I$  is the second moment of area,  $w_{max}$  is the deflection of the nanowire tip from its neutral position,  $L$

is the length from the substrate to the loading point, and  $D$  is the nanowire diameter. For the unloaded nanowire on Si,  $L = 2540$  nm and  $D = 173$  nm, and for the nanowire on graphite,  $L = 1840$  nm and  $D = 53$  nm. The bent nanowire on Si had a maximum deflection of 867 nm before fracture. If the same critical stress is assumed for the nanowire on graphite, a maximum deflection of 940 nm is predicted, while a deflection of 347 nm is measured. As the critical tensile stress is linearly proportional to the deflection, this means a reduction in bonding strength per unit area by a factor of 2.7 compared to nanowires grown on Si.

Comparing the critical stress on the nanowire interface for nanowires grown on Si and graphite, for 5 nanowires on each substrate, the average ratio is found to be 5.9, hence the bonds to graphite are weaker than to Si, but still of the same order of magnitude. This result is in agreement with the model proposed in the Letter, which suggests a covalent/ionic bonding for the nanowire/graphitic interface.

It should be noted that for the graphitic samples, there might exist pre-failure buckling events of the substrate, i.e. that the graphitic substrate accommodates some of the strain present at failure. This would effectively reduce the critical stress at the interface. However, by considering the angle formed by the base of the nanowire with regards to the substrate at the moment of failure (Fig. S6e), it can be concluded based on the observed angle and the formulas used that the substrate is not accommodating more than one third of the strain. The bond strength should therefore still be within an order of magnitude compared to on Si.

## **S8. Atomic force microscopy of graphite and epitaxial graphene**

The surface topology of the graphitic substrates used in this study was measured by atomic force microscope (AFM) used in tapping mode, and some examples are shown in Fig. S7.

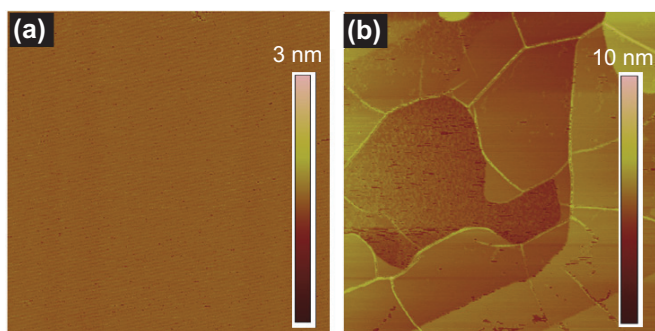


**Fig. S7.** AFM topographic images of two different graphitic substrates. The size of the images is  $2\ \mu\text{m} \times 2\ \mu\text{m}$ . The z-range height scale is shown at the right side of each image. **(a)**, Kish graphite after cleaving. **(b)**, Few-layer epitaxial graphene synthesized on a 6H-SiC(0001) substrate.

The single crystalline Kish graphite has a very flat surface after cleaving (Fig. S7a). The epitaxial graphene has a typical flat terrace-like structure normally observed in graphene synthesized on nominally on-axis 6H-SiC(0001) (Fig. S7b)<sup>6</sup>. It should be noted that this AFM topology is caused by the SiC surface itself, and is replicated to the few-layer continuous graphene that is epitaxially synthesized on top of the SiC substrate. The different single domains were found to have a 3-fold rotational symmetry meaning that there is no orientational disorder between the various ABA (Bernal) stacked graphene layers<sup>6</sup>. The terraces of the epitaxial graphene have a similar flatness as graphite, with a root-mean-square (RMS) surface roughness of less than  $1\ \text{\AA}$ .

### Supporting Videos

**Video SV1:** This SEM video (nl3018115\_si\_002.avi) is taken at 10 kV where GaAs nanowires grown on a patterned  $\text{SiO}_2/\text{Si}$  substrate are bent by a nano-manipulator as described in [S7]. The playback speed is changed during the length of the video to highlight the loading and failure parts.

**Video SV2:** This video (nl3018115\_si\_003.avi) is taken using the same conditions as Video SV1, but here the GaAs nanowires have been grown on Kish graphite. It was verified that the

nanowire was not in contact with any parasitic crystal growth prior to bending, and was situated between Ga droplets on the surface.

## References

1. Madelung, O., *Semiconductors - Basic Data*. 2nd ed.; Springer, Berlin: 1996.
2. Hertenberger, S.; Rudolph, D.; Bolte, S.; Doblinger, M.; Bichler, M.; Spirkoska, D.; Finley, J. J.; Abstreiter, G.; Koblmüller, G., *Appl. Phys. Lett.* **2011**, *98*, 123114-123113.
3. Plissard, S.; Kimberly, A. D.; Larrieu, G.; Godey, S.; Addad, A.; Wallart, X.; Caroff, P., *Nanotechnol.* **2010**, *21*, 385602.
4. Hoffmann, S.; Utke, I.; Moser, B.; Michler, J.; Christiansen, S. H.; Schmidt, V.; Senz, S.; Werner, P.; Gösele, U.; Ballif, C., *Nano Lett.* **2006**, *6*, 622-625.
5. Gere, J. M.; Timoshenko, S. P., *Mechanics of Materials*. 4th ed.; PWS Pub. Co.: Boston, 1997.
6. Virojanadara, C.; Yakimova, R.; Zakharov, A. A.; Johansson, L. I., *J. Phys. D: Appl. Phys.* **2010**, *43*, 374010.

**6.4 Paper IV: Self-catalyzed MBE grown  
GaAs/GaAs<sub>x</sub>Sb<sub>1-x</sub> core-shell nanowires in ZB and  
WZ crystal structures**

*Nanotechnology* **24** (2013) 405601



# Self-catalyzed MBE grown GaAs/GaAs<sub>x</sub>Sb<sub>1-x</sub> core-shell nanowires in ZB and WZ crystal structures

Sepideh Gorji Ghalamestani<sup>1</sup>, A Mazid Munshi<sup>2</sup>, Dasa L Dheeraj<sup>2</sup>, Bjørn-Ove Finland<sup>2</sup>, Helge Weman<sup>2</sup> and Kimberly A Dick<sup>1,3</sup>

<sup>1</sup> Solid State Physics, Lund University, PO Box 118, SE-22100 Lund, Sweden

<sup>2</sup> Department of Electronics and Telecommunications, Norwegian University of Science and Technology (NTNU), NO-7491 Trondheim, Norway

<sup>3</sup> Polymer and Materials Chemistry, Lund University, PO Box 124, SE-22100 Lund, Sweden

E-mail: [sepideh.gorji@ftf.lth.se](mailto:sepideh.gorji@ftf.lth.se)


Received 8 July 2013, in final form 15 August 2013

Published 12 September 2013

Online at [stacks.iop.org/Nano/24/405601](http://stacks.iop.org/Nano/24/405601)

## Abstract

We have investigated the growth of self-catalyzed GaAs/GaAs<sub>x</sub>Sb<sub>1-x</sub> core-shell nanowires directly on Si(111) substrates by molecular beam epitaxy. The compositions of the GaAs<sub>x</sub>Sb<sub>1-x</sub> shells are tuned in a wide range where the Sb-content is varied from 10 to ~70%, covering the miscibility gap. In addition, the GaAs<sub>x</sub>Sb<sub>1-x</sub> shells are grown on both zinc blende (ZB) and wurtzite (WZ) crystal structures. Morphological and structural characterizations of the grown nanowires indicate successful transfer of the GaAs core crystal structure to the GaAs<sub>x</sub>Sb<sub>1-x</sub> shells for both ZB and WZ nanowires, with slower shell growth rate on the WZ segments.

 Online supplementary data available from [stacks.iop.org/Nano/24/405601/mmedia](http://stacks.iop.org/Nano/24/405601/mmedia)

(Some figures may appear in colour only in the online journal)

## 1. Introduction

The growth of axial and radial heterostructure nanowires allows combination of various materials with interesting properties for both fundamental material science studies and a variety of device applications. GaAs/GaAs<sub>x</sub>Sb<sub>1-x</sub> is one of the promising material combinations, due to the tunable GaAs<sub>x</sub>Sb<sub>1-x</sub> wavelength covering the important telecommunication spectrum and their type-II band alignment suitable for numerous device applications, especially for solar cells [1, 2]. So far, there have been several reports on the axial heterostructural growth of both Au-free and Au-assisted GaAs/GaAs<sub>x</sub>Sb<sub>1-x</sub> nanowires by molecular beam epitaxy (MBE) [2–5]. Furthermore, photoluminescence (PL) properties of these nanowires and their significant dependence on the crystal structures have been extensively studied [6]. All the above mentioned studies report that GaAs<sub>x</sub>Sb<sub>1-x</sub> inserts always adopt zinc blende (ZB) crystal structure and even by adding Sb flux to GaAs nanowires with wurtzite (WZ) crystal structure, the crystal structure instantly changes

to ZB. In fact, a literature review on Sb-based nanowires indicates that they almost always prefer to grow in ZB crystal structure, partly related to their low ionicity [7]. Despite the advances made in the growth of axial heterostructure GaAs/GaAs<sub>x</sub>Sb<sub>1-x</sub> nanowires, the radial heterostructural growth of these nanowires has not been fully investigated. Therefore, employing the core-shell geometry offers a simple way to explore the WZ crystal structure of the GaAs<sub>x</sub>Sb<sub>1-x</sub> shells. In addition, GaAs<sub>x</sub>Sb<sub>1-x</sub> is known to have a large miscibility gap [8] which restricts the compositional tuning of this material. It should be mentioned that there are several bulk growth studies demonstrating that metastable GaAs<sub>x</sub>Sb<sub>1-x</sub> layers within the miscibility gap could be grown on the lattice matched substrates such as InP by using low V/III ratio and low temperatures [9–11].

We report on the successful growth of self-catalyzed GaAs/GaAs<sub>x</sub>Sb<sub>1-x</sub> core-shell nanowires directly on the Si(111) substrates by MBE. The main significance of the self-catalyzed growth approach is to avoid introducing any external material within the system such as Au and also to



prevent unwanted axial GaAs<sub>x</sub>Sb<sub>1-x</sub> growth during the shell growth. The compositions of the GaAs<sub>x</sub>Sb<sub>1-x</sub> shells were tuned and the Sb-content was varied in the range of 10 to ~70%, covering the miscibility gap. In addition, we have investigated the growth of GaAs/GaAs<sub>x</sub>Sb<sub>1-x</sub> nanowires in both ZB and WZ crystal structures, demonstrating that the core-shell geometry enables transfer of the GaAs structure to the GaAs<sub>x</sub>Sb<sub>1-x</sub> shells.

## 2. Experimental details

All the growths were performed in a Varian Gen II Modular MBE system. Solid state Ga source together with As and Sb valved crackers were employed. The use of crackers allows for adjustment of the proportion of dimers and tetramers. The nanowires were grown by using As tetramers and Sb dimers. P-type Si(111) wafers were used as substrates.

The GaAs<sub>x</sub>Sb<sub>1-x</sub> shells were grown on both ZB and WZ GaAs core nanowires. The WZ GaAs core nanowires were grown by inserting a short GaAsSb segment after the ZB GaAs core nanowire, followed by the GaAs nanowire growth (GaAs/GaAsSb/GaAs) which allows formation of the WZ GaAs nanowires [5]. All the GaAs core nanowires studied in this work (both the WZ and ZB crystal structures) were grown at 640 °C with planar equivalent GaAs growth rate of 0.7 ML s<sup>-1</sup> on GaAs(100) substrate and As flux with beam equivalent pressure of  $5.6 \times 10^{-6}$  Torr. In order to grow GaAs<sub>x</sub>Sb<sub>1-x</sub> shell around the core GaAs nanowires and to avoid axial GaAs<sub>x</sub>Sb<sub>1-x</sub> growth, after the core growth, Ga droplets were solidified under only high As flux of  $1.3 \times 10^{-5}$  Torr for 10 min. In case of ZB GaAs core nanowires, the solidification process was performed at the same temperature as the core nanowire growth (640 °C). For the GaAs/GaAsSb/GaAs core nanowires, a lower solidification temperature of 550 °C together with Sb flux of  $1.15 \times 10^{-6}$  Torr were supplied during the solidification time (10 min) to avoid GaAsSb insert decomposition and kinking issue. The GaAs<sub>x</sub>Sb<sub>1-x</sub> shell growth was done by using the same Ga and As fluxes as the core nanowires and adding various Sb fluxes from  $1.6 \times 10^{-6}$  to  $2 \times 10^{-7}$  Torr.

After the growth, nanowires were morphologically characterized in a Zeiss Ultra field emission scanning electron microscope (FE-SEM). High resolution transmission electron microscopy (HRTEM) was used to determine the crystal structure of the grown samples (TEM-JEOL 3000F operated at 300 kV). For the TEM characterization, nanowires were broken off from the substrate and transferred onto carbon-coated Cu grids. Additionally, high angle annular dark field scanning transmission electron microscopy (HAADF STEM) and x-ray energy dispersive spectroscopy (XEDS) were used to determine the chemical composition of the obtained nanowires together with the shell thickness.

## 3. Results and discussion

Figure 1(a) shows a schematic illustration of a Ga-assisted GaAs core nanowire grown directly on the Si(111) substrate, which similar to the Au-assisted growth proceeds via

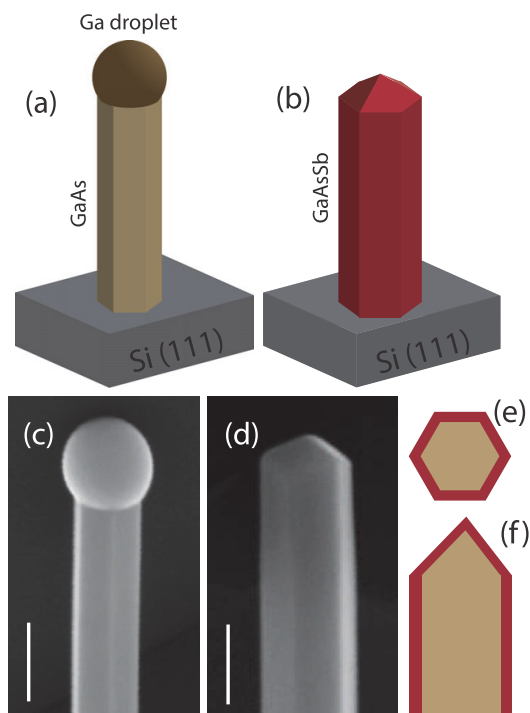


**Figure 1.** Schematic illustration of (a) a self-catalyzed GaAs core nanowire directly grown on Si(111) substrates. (b) A GaAs/GaAs<sub>x</sub>Sb<sub>1-x</sub> core-shell nanowire where GaAs<sub>x</sub>Sb<sub>1-x</sub> shell is grown after the Ga-solidification process. Magnified SEM images of (c) a self-catalyzed GaAs nanowire directly grown on the Si substrate and (d) A GaAs/GaAs<sub>x</sub>Sb<sub>1-x</sub> core-shell nanowire. The scale bar for (c) and (d) is 100 nm. Cross sectional (e) top and (f) side schematic view of the GaAs/GaAs<sub>x</sub>Sb<sub>1-x</sub> core-shell nanowires.

a vapor-liquid-solid (VLS) growth mechanism. A SEM micrograph of such a Ga-assisted GaAs nanowire is shown in figure 1(c). As mentioned in section 2, after the growth of GaAs core nanowires, the Ga droplets on top of the nanowires were solidified, and then the GaAs<sub>x</sub>Sb<sub>1-x</sub> shells were grown in a vapor-solid growth mechanism [12]. Figure 1(b) schematically illustrates a GaAs/GaAs<sub>x</sub>Sb<sub>1-x</sub> core-shell nanowire with prismatic hexagonal tip shape, and figure 1(d) shows a SEM image of such a grown nanowire. Figures 1(e) and (f) show top and side cross sectional schematic views of GaAs/GaAs<sub>x</sub>Sb<sub>1-x</sub> core-shell nanowires, respectively.

In the following, section 3.1 describes the results of the GaAs<sub>x</sub>Sb<sub>1-x</sub> shell growth with the main focuses on the composition and thickness control (on both ZB and WZ GaAs core nanowires). Section 3.2 explains the GaAs<sub>x</sub>Sb<sub>1-x</sub> shell growth results on the GaAs core nanowires in ZB and WZ crystal structures.

### 3.1. Control of GaAs<sub>x</sub>Sb<sub>1-x</sub> shell composition and thickness

In order to grow GaAs<sub>x</sub>Sb<sub>1-x</sub> shells around the GaAs core nanowires, we first studied the temperature effect on the shell

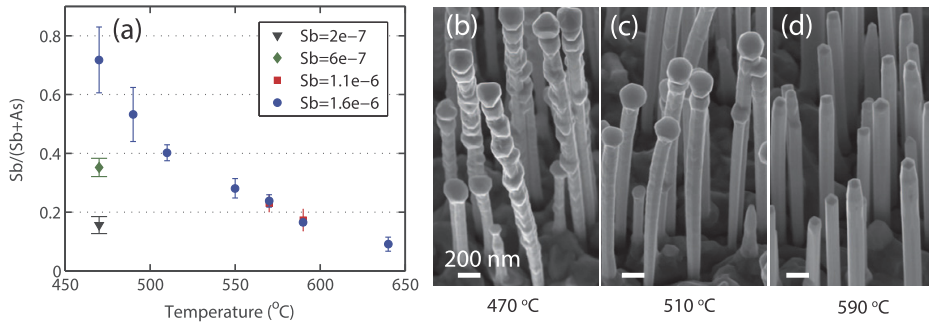


**Figure 2.** (a) The Sb composition data (calculated from XEDS analysis) for the ZB GaAs/GaAs<sub>x</sub>Sb<sub>1-x</sub> core-shell nanowires grown at different temperatures (470–640°C), averaged over 3–5 nanowires for each sample. The blue circle and red square data points (respective Sb flux of  $1.6 \times 10^{-6}$  and  $1.1 \times 10^{-6}$  Torr) indicate formation of higher Sb-content shells at lower temperatures where below the temperature of 550°C, the shell growth is inhomogeneous. The green diamond and black triangle data points (respective Sb flux of  $6 \times 10^{-7}$  and  $2 \times 10^{-7}$  Torr) indicate formation of lower Sb-content shells at lower Sb fluxes with smooth side facets, confirming that the shell morphology is only affected by strain. 30° tilted view SEM images of GaAs/GaAs<sub>x</sub>Sb<sub>1-x</sub> core-shell nanowires where the GaAs<sub>x</sub>Sb<sub>1-x</sub> shells were grown at (b) 470°C, (c) 510°C and (d) 590°C. The scale bar for (c) and (d) is 200 nm.

morphology and composition. As stated in the experimental section, all the GaAs core nanowires (both ZB and WZ) were grown at 640°C. To study the temperature effect systematically, we have grown a set of ZB samples where all the core nanowire growth conditions were kept the same and only the shell growth temperature was varied from 470 to 640°C. It should be mentioned that at higher temperatures than 640°C, the shell growth is unsuccessful, partly due to the low antimonide decomposition temperature [13]. The samples grown at different temperatures were characterized by HRTEM and their chemical compositions were determined by both radial and axial line scans as well as point and area XEDS analysis.

Figure 2(a) shows the Sb composition data for the ZB GaAs<sub>x</sub>Sb<sub>1-x</sub> shells (calculated by XEDS analysis) with respect to their growth temperatures (470–640°C). The respective blue circle, red square, green diamond, and black triangle data points correspond to the Sb flux of  $1.6 \times 10^{-6}$ ,  $1.1 \times 10^{-6}$ ,  $6 \times 10^{-7}$ , and  $2 \times 10^{-7}$  Torr, where the filled data points are the average values and the error bars represent the standard deviation from the average value. The composition results indicate that lowering the shell growth temperature enhances the Sb incorporation in the shell and hence allows formation of higher Sb-content GaAs<sub>x</sub>Sb<sub>1-x</sub> shells [14]. However, SEM inspections of the grown samples show that by lowering the temperature, the morphology of the nanowires deteriorate, and instead of flat {110}-type facets, rough side facets form.

Figures 2(b)–(d) show SEM micrographs of the ZB GaAs/GaAs<sub>x</sub>Sb<sub>1-x</sub> core-shell nanowires (with Sb flux of  $1.6 \times 10^{-6}$  Torr) grown at 470, 510, and 590°C, respectively. It should be mentioned that the nanowires grown at 550°C and higher temperatures demonstrate very similar morphology to those grown at 590°C (figure 2(d)). As shown in figures 2(b) and (c), by decreasing the temperature below 550°C the shell morphology starts to change, forming the rough side facets that indicate inhomogeneous shell growth, followed by some bending nanowires. Figure 2(b) shows the

SEM image of the nanowires grown at 470°C, demonstrating significant inhomogeneous shell growth behavior. The formation of these rough side facets at low temperatures could be related to the strain induced from the high lattice mismatch between the GaAs cores and the GaAs<sub>x</sub>Sb<sub>1-x</sub> shells, resulting in an island growth mode regime. Figure S1 of the supplementary material (available at [stacks.iop.org/Nano/24/405601/mmedia](http://stacks.iop.org/Nano/24/405601/mmedia)) shows HAADF STEM and HRTEM images of such a nanowire. The same trend was observed for another similar set of samples grown with slightly lower Sb flux of  $1.1 \times 10^{-6}$  Torr, confirming the temperature effect on the composition and morphology of the nanowires. Our finding supports a recent report where similar surface roughening and island formation were observed in GaAs/GaSb core-shell nanowires [15]. Apart from the nanowire morphology, figures 2(b)–(d) also demonstrate significant tip morphology change for samples grown with low shell temperatures (below 570°C). This is shown by the overgrown faceted tips in figures 2(b) and (c). However, in this study we only focus on the nanowire core-shell morphology and the tip morphology change is beyond the scope of this work.

We next investigated the effect of Sb flux on the morphology of the grown core-shell nanowires. This series was performed at the lowest shell temperature of 470°C since we could not increase the Sb flux further. The results of this set of samples (green diamond, black triangle together with the blue circle data point at 470°C in figure 2(a)) indicate that the morphology of the grown nanowires (figure 2(b)) could be optimized (similar to figure 2(d)) by lowering Sb flux about one order of magnitude to Sb flux of  $2 \times 10^{-7}$  Torr. This morphology improvement at the constant shell growth temperature confirms that the shell morphology is only affected by strain (i.e. Sb-content) and not the temperature. Therefore, higher temperatures seem to reduce the available Sb, perhaps by increasing desorption.

Moreover, we have studied the growth rate of GaAs<sub>x</sub>Sb<sub>1-x</sub> shells around ZB GaAs core nanowires. Figure 3

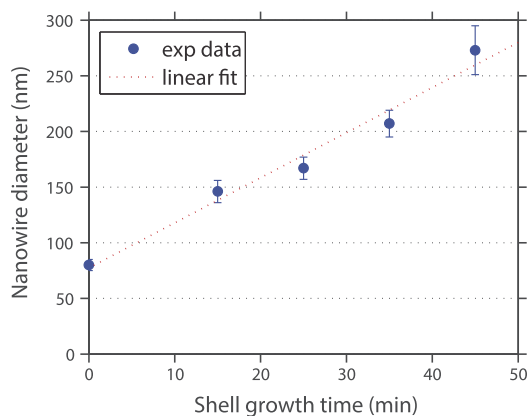


**Figure 3.** The GaAs/GaAs<sub>x</sub>Sb<sub>1-x</sub> core-shell nanowire diameter for ZB samples grown with different shell growth times (0–45 min) shown by the blue data points. The GaAs<sub>x</sub>Sb<sub>1-x</sub> shells are grown with Sb flux of  $1.6 \times 10^{-6}$  Torr at temperature of 570 °C. The measurements were done on a minimum of 12 nanowires for each sample and the error bars indicate the standard deviation from the average values. The blue experimental data points suggest a linear shell growth rate shown by the dashed red line.

shows the nanowire diameter for samples grown with different shell growth times (0–45 min) where the error bars indicate the standard deviations from the average value. As the data suggest, GaAs<sub>x</sub>Sb<sub>1-x</sub> shell growth rate follows a linear behavior, shown by dashed red line. Figure 3 suggests a quite high growth rate of  $\sim 125$  nm h<sup>-1</sup>, resulting from several processes such as the direct impingement of adatoms, their diffusion from the substrate, and contribution from the secondary adsorption process [16, 17].

### 3.2. Effect of crystal phase

HRTEM investigations on the grown ZB nanowires clearly demonstrate that the GaAs<sub>x</sub>Sb<sub>1-x</sub> shells follow the same

stacking sequence as the GaAs core nanowire, as shown for other material systems [18]. As a result, the GaAs<sub>x</sub>Sb<sub>1-x</sub> shell growth around ZB GaAs core nanowires result in the formation of ZB GaAs<sub>x</sub>Sb<sub>1-x</sub> shells. It should be noted that the same trend has been observed in other core-shell nanowire material systems such as InAs/InP and GaP/Si [19, 20].

In addition to the ZB crystal structure, the GaAs<sub>x</sub>Sb<sub>1-x</sub> shells were grown on WZ GaAs core nanowires as well. Although self-catalyzed GaAs nanowires normally adopt ZB phase, introducing a GaAsSb insert followed by shutting off Sb flux, and continuing the growth of GaAs allows the formation of WZ phase [5], as schematically shown in figure 4(a). We have used these WZ-ZB nanowires as a template to enable us to study the GaAs<sub>x</sub>Sb<sub>1-x</sub> shell growth on both ZB and WZ crystal structures within the same nanowire.

To study the GaAs<sub>x</sub>Sb<sub>1-x</sub> shell growth on the ZB-WZ GaAs nanowires, similar to the ZB GaAs nanowires, the Ga droplets were solidified after the core nanowire growth. Then, GaAs<sub>x</sub>Sb<sub>1-x</sub> shells were epitaxially grown around the GaAs/GaAsSb/GaAs core nanowires, as schematically shown in figure 4(b).

The results of our study on the GaAs/GaAsSb/GaAs core nanowires indicate that applying the same Ga-solidification condition as used for the ZB GaAs core nanowires (supplying only As flux at 640 °C) results in the decomposition of the GaAsSb inserts followed by nanowire thinning and kinking at the GaAsSb insert position. Figure 4(c) shows a SEM image of GaAs/GaAsSb/GaAs core nanowires with the same Ga-solidification condition (as compared to the ZB nanowires), resulting in GaAsSb decomposition indicated by white arrows. Therefore, to avoid this decomposition issue, Sb flux of  $1.15 \times 10^{-6}$  Torr was added during the solidification process and also the temperature was lowered to 550 °C.

By employing the improved solidification condition, GaAs<sub>x</sub>Sb<sub>1-x</sub> shells were then grown around the GaAs/GaAsSb/GaAs core nanowires. Figure 4(d) shows a SEM micrograph of such a sample with 25 min GaAs<sub>x</sub>Sb<sub>1-x</sub> shell growth at 590 °C and Sb flux of  $1.1 \times 10^{-6}$  Torr.

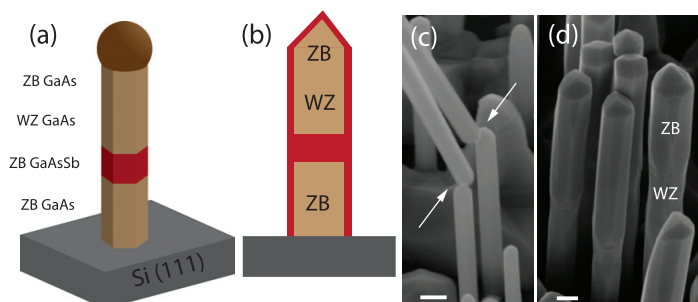


**Figure 4.** Schematic illustration of (a) self-catalyzed GaAs/GaAsSb/GaAs core nanowires grown on Si(111) substrates. (b) Side view cross section of GaAs/GaAsSb/GaAs nanowires after Ga-solidification and GaAs<sub>x</sub>Sb<sub>1-x</sub> shell growth. (c) 30° tilted view SEM image of GaAs/GaAsSb/GaAs core nanowires where Ga-solidification was performed at 640 °C without Sb flux, resulting in GaAsSb insert decomposition, shown by white arrows. The scale bar is 100 nm. (d) 30° tilted view SEM image of GaAs/GaAsSb/GaAs nanowires with optimized solidification condition covered by GaAs<sub>x</sub>Sb<sub>1-x</sub> shell grown for 25 min. The WZ segments have a visibly smaller diameter than the ZB segments, due to reduced radial growth. The scale bar is 100 nm.

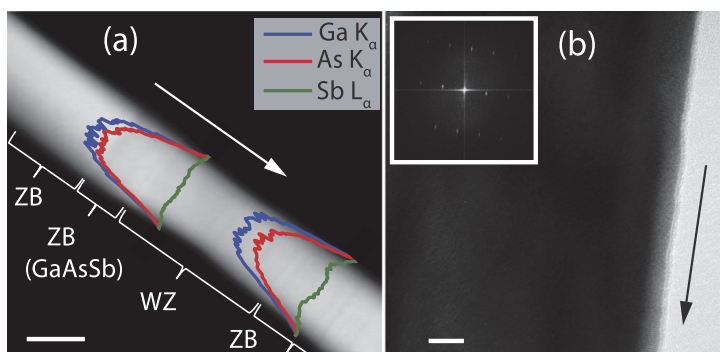


**Figure 5.** (a) HAADF STEM image of a similar nanowire (25 min shell growth) as shown in figure 4(d), demonstrating various segments along the nanowire where the white arrow shows the growth direction. The respective Ga, As and Sb signals are shown in blue, red and green colors where the shell composition is  $\text{GaAs}_{0.85}\text{Sb}_{0.15}$ . The antimony signal (green line) indicates homogeneous shell growth with slower growth rate on the WZ, compared to the ZB segment. The scale bar is 100 nm. (b) HRTEM image of the WZ segment for a sample with 15 min shell growth time, demonstrating WZ  $\text{GaAs}_x\text{Sb}_{1-x}$  shell growth. The black arrow shows the growth direction and the scale bar is 10 nm. The inset shows the fast Fourier transform taken from the  $\text{GaAs}_x\text{Sb}_{1-x}$  shell part, demonstrating the characteristic pattern of a hexagonal crystal phase.

Figure 5(a) shows a HAADF STEM image of a similar nanowire to those shown in figure 4(d), where the white arrow indicates the growth direction. As shown in figure 5(a), after the base GaAs ZB segment, a GaAsSb insert is introduced, which is followed by the formation of the GaAs WZ segment. It should be noted that after the WZ part, the crystal structure eventually changes back to ZB. The length of the GaAs WZ segment varies from 100 to 400 nm (after the GaAsSb insert) for nanowires with various diameters.

The radial XEDS line scans for both WZ and ZB segments are shown in the figure 5(a). The antimony signal (green line) indicates homogeneous shell growth on the WZ segment. Unlike the WZ segments, the shell growth is not homogeneous on the ZB segments due to the presence of polar microfacets that provide some nucleation sites. Also, the shell is thinner on the WZ, compared to the ZB segment. This is attributed to a slower  $\text{GaAs}_x\text{Sb}_{1-x}$  shell growth rate on the WZ, compared to the ZB crystal structure as shown in other material systems [19]. A lower radial growth rate for WZ nanowires than for ZB has previously been attributed to a lower surface energy for WZ facets than for ZB [19, 21, 22], consistent with theoretical calculations of common WZ and ZB side facets [23]. This slower shell growth rate explains the thicker top part of the figures 4(d) and 5(a), corresponding ZB parts. It is difficult to accurately quantify the composition of the WZ shell since it is quite thin, but the Sb-content is measured to be similar to or slightly lower than on the ZB segment.

#### 4. Conclusion

We have studied the growth of self-catalyzed  $\text{GaAs}/\text{GaAs}_x\text{Sb}_{1-x}$  core-shell nanowires directly on Si(111) substrates by MBE technique. We demonstrate that by varying the temperature and Sb flux, the composition of

the grown  $\text{GaAs}_x\text{Sb}_{1-x}$  shells is tuned in a wide range, covering the miscibility gap. However, at low temperatures (below 550 °C) and high Sb fluxes ( $\geq 1.1 \times 10^{-6}$  Torr), the high lattice mismatch between the GaAs core and  $\text{GaAs}_x\text{Sb}_{1-x}$  shells results in inhomogeneous shell growth. Furthermore,  $\text{GaAs}_x\text{Sb}_{1-x}$  shells are successfully grown on both ZB and WZ core crystal structures. The morphological characterization results indicate that the shell growth rate is lower on the WZ, compared to the ZB segment, suggesting a lower side facet surface energy.

#### Acknowledgments

This work was partially supported by the Swedish Research Council (VR), the Swedish Foundation for Strategic Research (SSF), VINNOVA, the Knut and Alice Wallenberg Foundation (KAW), and the Nanometer Structure Consortium at Lund University (nmC@LU), and partially by the 'RENERGI' program of the Research Council of Norway under Grant No. 190871.

#### References

- [1] Cao Y, Wu Z, Ni J, Bhutto W A, Li J, Li S, Huang K and Kang J 2012 *Nano-Micro Lett.* **4** 135–41
- [2] Plissard S, Dick K A, Wallart X and Caroff P 2010 *Appl. Phys. Lett.* **96** 121901
- [3] Dheeraj D L, Patriarche G, Zhou H, Hoang T B, Moses A F, Grønsberg S, van Helvoort A T J, Fimland B O and Weman H 2008 *Nano Lett.* **8** 4459–63
- [4] Dheeraj D L, Patriarche G, Zhou H, Harmand J C, Weman H and Fimland B O 2009 *J. Cryst. Growth* **311** 1847–50
- [5] Munshi A M, Dheeraj D L, Todorovic J, van Helvoort A T J, Weman H and Fimland B O 2013 *J. Cryst. Growth* **372** 163
- [6] Hoang T B, Moses A F, Ahtapodov L, Zhou H, Dheeraj D L, van Helvoort A T J, Fimland B O and Weman H 2010 *Nano Lett.* **10** 2927–33

- [7] Weman H and Dasa D L 2011 *Advances in III-V Semiconductor Nanowires and Nanodevices* ed J Li, D Wang and R R LaPierre (Bassum: Bentham Science) pp 89–104
- [8] Li J-B, Zhang W, Li Ch and Du Zh 1998 *J. Phase Equilib.* **19** 466–72
- [9] Shin J, Hsu T C, Hsu Y and Stringfellow G B 1997 *J. Cryst. Growth* **179** 1–9
- [10] Moiseev K D, Romanov V V, Voronina T I, Lagunova T S, Mikhailova M P and Yakovlev Yu P 2008 *J. Cryst. Growth* **310** 4846–9
- [11] Peter M, Herres N, Fuchs F, Winkler K, Bachem K-H and Wagner J 1999 *Appl. Phys. Lett.* **74** 410–2
- [12] Morral A F I 2011 *IEEE J. Sel. Top. Quantum Electron.* **17** 819–28
- [13] Yano M, Yokose H, Iwai Y and Inoue M 1991 *J. Cryst. Growth* **111** 609–13
- [14] Yano M, Ashida M, Kawaguchi A, Iwai Y and Inoue M 1989 *J. Vac. Sci. Technol. B* **7** 199–203
- [15] Salehzadeh O, Kavanagh K L and Watkins S P 2013 *J. Appl. Phys.* **113** 134309
- [16] Rieger T, Luysberg M, Schäers T, Grutzmacher D and Ion Lepsa M 2012 *Nano Lett.* **12** 5559–64
- [17] Ramdani M R, Harmand J C, Glas F, Patriarche G and Travers L 2013 *Cryst. Growth Des.* **13** 91–6
- [18] Kawaguchi K, Heurlin M, Lindgren D, Borgström M T, Ek M and Samuelson L 2011 *Appl. Phys. Lett.* **99** 131915
- [19] Ghalamestani S G, Heurlin M, Wernersson L-E, Lehmann S and Dick K A 2012 *Nanotechnology* **23** 285601
- [20] Algra R E, Hocevar M, Verheijen M A, Zardo I, Immink G W, van Enckevort W J P, Abstreiter G, Kouwenhoven L P, Vlieg E and Bakkers E P A M 2011 *Nano Lett.* **11** 1690–4
- [21] Wallentin J, Messing M E, Trygg E, Samuelson L, Deppert K and Borgström M T 2011 *J. Cryst. Growth* **331** 8–14
- [22] Lehmann S, Wallentin J, Jacobsson D, Deppert K and Dick K 2013 *Nano Lett.* doi:10.1021/nl401554w
- [23] Pankoke V, Kratzer P and Sakong S 2011 *Phys. Rev. B* **84** 075455

## Supplementary material

Morphological characterization on the grown GaAs/GaAs<sub>x</sub>Sb<sub>1-x</sub> core-shell nanowires show that at high Sb fluxes lowering the shell growth temperature results in the formation of rough side facets. The formation of these rough side facets could be due to the strain induced from the high lattice mismatch between the GaAs cores and the GaAs<sub>x</sub>Sb<sub>1-x</sub> shells, resulting in an island growth mode regime. HAADF STEM and HRTEM images of such a grown nanowire are shown in figure S1(a-c) where the contrast in (b) and (c) clearly shows the strain induced from the core-shell lattice mismatch.

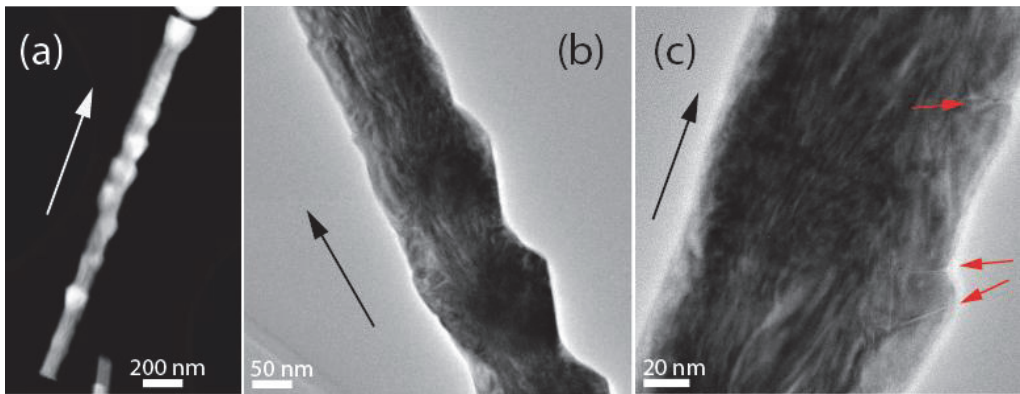


**Figure S1-** (a) HAADF STEM and (b-c) HRTEM images of a GaAs/GaAs<sub>x</sub>Sb<sub>1-x</sub> core-shell nanowire where the GaAs<sub>x</sub>Sb<sub>1-x</sub> shell was grown at high Sb flux of  $1.6 \times 10^{-6}$  Torr and low temperature of 470°C. The white and black arrows indicate the growth direction. The contrast in (b) and (c) is due to the strain induced from the high lattice mismatch between the GaAs core and GaAs<sub>x</sub>Sb<sub>1-x</sub> shell and the red arrows in (c) show strain-induced dislocation positions.

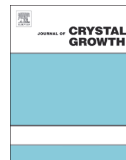


**6.5 Paper V: Comparison of Be-doped GaAs nanowires grown by Au- and Ga-assisted molecular beam epitaxy**

*Journal of Crystal Growth* **378** (2013) 532







## Comparison of Be-doped GaAs nanowires grown by Au- and Ga-assisted molecular beam epitaxy



D.L. Dheeraj<sup>a</sup>, A.M. Munshi<sup>a</sup>, O.M. Christoffersen<sup>a</sup>, D.C. Kim<sup>a</sup>, G. Signorello<sup>b</sup>, H. Riel<sup>b</sup>, A.T.J. van Helvoort<sup>c</sup>, H. Weman<sup>a</sup>, B.O. Fimland<sup>a,\*</sup>

<sup>a</sup> Department of Electronics and Telecommunications, Norwegian University of Science and Technology, NO-7491 Trondheim, Norway

<sup>b</sup> IBM Research – Zurich, Säumerstrasse 4, 8803 Rüschlikon, Switzerland

<sup>c</sup> Department of Physics, Norwegian University of Science and Technology, NO-7491 Trondheim, Norway

### ARTICLE INFO

Available online 5 January 2013

#### Keywords:

A1. Nanomaterials

A1. Doping

A3. Molecular beam epitaxy

B2. Semiconducting gallium arsenide

### ABSTRACT

We report on the growth, structural and electrical characterizations of Be-doped GaAs nanowires (NWs) grown by the Au- and Ga-assisted vapour–liquid–solid techniques using molecular beam epitaxy. The growth rate of Be-doped GaAs NWs grown by the Au-assisted technique is observed to be lower as compared to the growth rate of undoped GaAs NWs grown under identical conditions. However, no effect on either the growth rate or the morphology of NWs has been observed for Be-doped GaAs NWs grown by the Ga-assisted technique with the same Be flux as used for the Au-assisted technique. Electrical characterization reveals that the Ga-assisted grown NWs show more consistent, symmetric current–voltage ( $I$ – $V$ ) characteristics with higher electrical current than the Au-assisted grown NWs. Finally, we show that ohmic contacts to Be-doped Ga-assisted NWs can be achieved either by post-annealing the metal-contacted NW or increasing the doping concentration during the NW growth.

© 2013 Elsevier B.V. All rights reserved.

### 1. Introduction

Control of the doping in semiconductor nanowires (NWs) is essential for realizing a broad range of NW-based optoelectronic devices [1,2]. III–V NWs are usually grown by a Au-assisted vapour–liquid–solid (VLS) technique and have seen a huge progress during the last decade. For GaAs NWs, the Ga self-assisted VLS technique has recently attracted significant interest due to its potential advantages in the fabrication of core-shell structures and the reduced risk of deep levels by the exclusion of foreign metal-catalyst in the growth process [3,4]. Both techniques (Au- and Ga-assisted) have their own benefits and drawbacks, due to which understanding the dopant incorporation into the NWs grown by both the techniques is important.

Be has been the most commonly used p-type dopant in III–V thin films grown by molecular beam epitaxy (MBE). However, there have so far been very few systematic studies on Be doping of GaAs NWs grown by MBE [5,6]. The incorporation mechanisms of dopants in VLS grown NWs are quite different from those of thin films, mainly because of the intermediate liquid catalyst

particle that is assisting the growth of NWs [7]. In case of Au-assisted MBE growth of InP NWs, it has been shown that Si dopants incorporate efficiently on the sidewall of the NW by vapour–solid (VS) growth, rather than in the NW core grown by VLS technique [8]. In case of GaAs NWs grown by the Ga-assisted technique, it has been reported that high Be doping concentrations cause kinking and tapering of the NWs [5]. Hence, it is necessary to optimize the growth conditions that yield NWs with uniform morphology.

On the other hand, determining the dopant incorporation in NWs is a challenging task. Due to the tiny sizes and one-dimensional morphology of NWs, it is difficult to adapt the traditional “Hall effect” experiments commonly used to determine the carrier concentration in case of thin films. Several techniques have been explored to determine the dopant incorporation and carrier concentration in NWs, such as Raman spectroscopy, photoemission electron microscopy [9], atom probe tomography (APT) [10], and electrical characterization in a field-effect transistor (FET) configuration. However, each method has its own drawbacks: for example, APT is a slow technique probing small volumes, and Raman spectroscopy provides only qualitative information about doping from highly doped materials [11]. On the other hand, the FET characterizations are sensitive only at low doping levels enabling to observe any field effect [12]. In addition, it requires ohmic contacts to the source/drain electrodes

\* Corresponding author. Tel.: +47 73594424.

E-mail addresses: [dheeraj.dasa@ntnu.no](mailto:dheeraj.dasa@ntnu.no), [dheeraj.dasa@gmail.com](mailto:dheeraj.dasa@gmail.com) (D.L. Dheeraj), [bjorn.fimland@ntnu.no](mailto:bjorn.fimland@ntnu.no) (B.O. Fimland).

as well as a good interface between NW and gate insulator without significant charge trapping.

In this study, we investigate the p-type doping (using Be) of GaAs NWs grown by both Au- and Ga-assisted MBE techniques. The Be-doped GaAs NWs were grown at substrate temperatures between 500 and 580 °C in case of Au-assisted MBE, and at 630 °C when using Ga-assisted MBE. Electrical characterizations reveal that the Ga-assisted NWs have superior current–voltage ( $I$ – $V$ ) characteristics as compared to the Au-assisted NWs. For Ga-assisted NWs, we could obtain ohmic contacts to single NWs, resulting in linear  $I$ – $V$  curves. 4-probe measurements show the resistivity to be in the range of  $1.7$ – $5.9 \times 10^{-2} \Omega \text{ cm}$  for single Be-doped GaAs NWs grown by the Ga-assisted technique.

## 2. Experimental procedure

Be-doped GaAs NWs were grown by Au- and Ga-assisted VLS techniques in a Varian Gen II Modular MBE system equipped with a Ga dual-filament cell, Be effusion cell and an As valved cracker cell, allowing to fix the proportion of As dimers and tetramers. In the present study, the major species was  $\text{As}_4$ . The NW growth was carried out on p-type doped GaAs(111)B and Si(111) substrates for Au- and Ga-assisted techniques, respectively. In both cases, an  $\text{As}_4$  flux was kept at  $6 \times 10^{-6}$  Torr and the temperature of the Ga effusion cell was preset to yield a nominal planar GaAs growth rate of 0.7 ML/s ( $2.0 \text{ \AA/s}$ ) on a GaAs(001) surface. The temperature of the Be effusion cell was preset to yield a nominal Be concentration between  $4.3 \times 10^{18} \text{ cm}^{-3}$  and  $1.4 \times 10^{19} \text{ cm}^{-3}$  as measured in GaAs thin films grown at a growth rate of 0.7 ML/s on a GaAs(001) substrate.

For NWs grown by the Au-assisted VLS technique, the GaAs(111)B substrate surface was first deoxidized at 620 °C, as measured with a pyrometer, and then a 60 nm thick GaAs film was grown under growth conditions producing an atomically flat surface. The GaAs buffer layer was transferred to an electron-beam evaporation system for Au deposition. An approximately 6 Å thick Au film was deposited on the sample surface as measured by a quartz crystal thickness monitor. The sample was then loaded into the MBE system again for the NW growth. Under an  $\text{As}_4$  flux of  $6 \times 10^{-6}$  Torr, the substrate temperature was increased to a temperature suitable for GaAs NW growth, which was varied between 500 and 580 °C in this study. The sample grown at a substrate temperature of 510 °C will hereafter be called as Au1. At this stage, Au particles alloyed with the Ga from the substrate forming Au–Ga liquid particles. Growth of Be-doped GaAs NWs was initiated by opening the shutters of the Ga and Be effusion cells for the duration of 40 min. Growth of Be-doped GaAs NWs was always terminated by shutting down the Be, Ga and As fluxes simultaneously and immediately ramping down the substrate to room temperature.

For NWs grown by the Ga-assisted technique, the p-Si(111) substrates with native oxide were dipped in HF (5%) for 5 s, rinsed in deionized water for 1 min, dried by blowing nitrogen and then loaded inside the MBE chamber. The substrates were ramped up to the growth temperature of 630 °C, as measured by a pyrometer. The GaAs NW growth was initiated by opening the shutters of the Be, Ga and As cells (as well as the As valve) simultaneously. Shutters were kept open for the duration of 40 min. The temperature of the Be cell was chosen to yield a nominal Be concentration of  $4.3 \times 10^{18} \text{ cm}^{-3}$  for the first sample (hereafter called as Ga1) and  $1.4 \times 10^{19} \text{ cm}^{-3}$  for the second sample (hereafter called as Ga2). Growth of Be-doped GaAs NWs was always terminated by shutting down the Ga, As and Be fluxes simultaneously and immediately ramping down the substrate to room temperature.

Morphological characterization of the NWs was performed in a Zeiss Ultra field emission scanning electron microscope (SEM) operating at 5 kV. For characterization with transmission electron microscopy (TEM), the NWs were removed from the substrate by immersing a cleaved portion of the substrate in ethanol and sonicating them for 3 min. A small volume of the NW suspension was left to dry onto either a full or a lacey carbon film supported by a 300 mesh Cu TEM grid. The NWs were analyzed in a Philips CM30 operating at 200 kV.

2-probe and 4-probe contacted single NW devices were fabricated to measure the electrical properties. Standard e-beam lithography was used to pattern the electrodes. To remove the surface oxides, the NWs were etched in HCl solution before depositing the metal electrodes consisting of Pt (5 nm)/Ti (10 nm)/Pt (5 nm)/Au (150 nm) [13]. The electrical measurements on fabricated devices were performed with a Keithley 4200 semiconductor characterization system in air at room temperature.

## 3. Results and discussion

Figs. 1a and b show 45°-tilted view SEM images of Be-doped GaAs NWs grown by Au-assisted MBE at substrate temperatures of 540 °C and 510 °C, respectively. NWs grown at 540 °C (shown in Fig. 1a) are rod-shaped with diameters in the range of 30–50 nm, and with lengths in the range of 0.2–1.0 μm. We would like to emphasize that the average growth rate of these Be-doped NWs grown at 540 °C is significantly lower than that of the undoped GaAs NWs grown under identical conditions [14]. The NW growth ceased with further increase in substrate temperature to 580 °C, as is observed above approximately 630 °C in the case of undoped GaAs NWs [15]. The NWs grown at 510 °C (as shown in Fig. 1b) have a tapered morphology with NW diameters in the range of 40–70 nm measured at the half of their lengths, while the Au particle diameter was in the range of 30–50 nm, and the

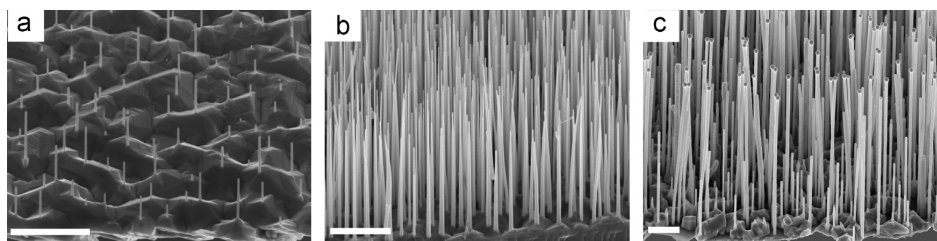


**Fig. 1.** 45° tilted view SEM image of Be-doped GaAs NWs grown by the Au-assisted technique at a substrate temperature of (a) 540 °C, and (b) 510 °C. (c) 45° tilted view SEM image of Be-doped GaAs NWs grown by the Ga-assisted technique at a substrate temperature of 630 °C. The nominal Be concentration for these NWs was  $\sim 4.3 \times 10^{18} \text{ cm}^{-3}$ . (All scale bars are 1 μm.)

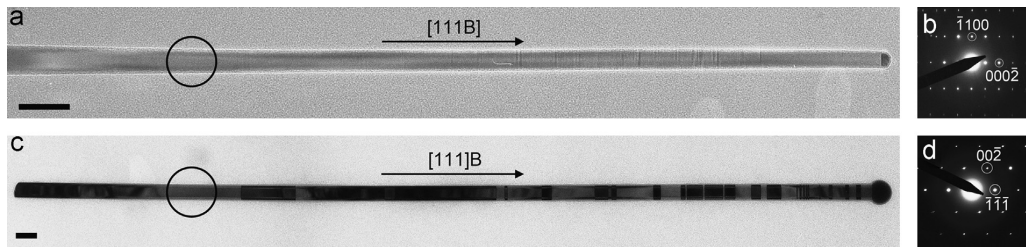
lengths of the NWs are in the range of 2–3.5  $\mu\text{m}$ . The NW diameter being larger than the diameter of Au particle, shown in Fig. 1b, can be attributed to radial deposition of GaAs on the NW sidewalls by VS growth [16]. Interestingly, and unlike for substrate temperatures of 540  $^{\circ}\text{C}$  and above, the growth rate for the Be-doped GaAs NWs grown at 510  $^{\circ}\text{C}$  is in the same range as for undoped GaAs NWs grown under identical growth conditions (not shown here).

Fig. 1c shows the 45 $^{\circ}$ -tilted view SEM image of Be-doped GaAs NWs grown by the Ga-assisted technique at a substrate temperature of 630  $^{\circ}\text{C}$ . The NWs are rod-shaped with the Ga droplet present at the tip of most of the NWs. The diameters and lengths of these NWs are in the range of 80–100 nm and 5–6  $\mu\text{m}$ , respectively. It is worth mentioning that within the investigated Be concentration, no significant difference in either growth rate or morphology is observed between these Be-doped and undoped GaAs NWs grown under identical conditions (not shown here).

Figs. 2a and c show the bright field (BF)-TEM images of Be-doped GaAs NWs grown by the Au- and Ga-assisted VLS techniques, respectively. Diffraction patterns of the NWs in Fig. 2a and c are shown in Fig. 2b and d, respectively. As can be seen from the selective area electron diffraction (SAED) patterns (Fig. 2b and d), the crystal structure of Be-doped GaAs NWs grown by the Au-assisted technique is predominantly wurtzite (WZ), with few stacking faults (Fig. 2a) whose density is different from one NW to another, whereas NWs grown by the Ga-assisted technique have predominantly zinc blende (ZB) crystal structure,

with few twin defects (Fig. 2c). In fact, this difference in crystal structure of NWs grown by the two different techniques was observed also during the growth of undoped GaAs NWs [17]. From these observations, we can conclude that the incorporation of Be in GaAs NWs (within the concentration range reported here) has no clear influence on their crystal structure.

Fig. 3a shows the representative  $I$ - $V$  curves of single Be-doped GaAs NWs grown by both Au- and Ga-assisted techniques. It is observed that Au-assisted (Au1) NWs generally show diode-like, non-symmetric  $I$ - $V$  characteristics with hysteresis, as shown in the inset of Fig. 3a. The measured electrical current also varies significantly from one NW to the other. It is worth mentioning here that no significant difference in the  $I$ - $V$  characteristics for Au-assisted NWs grown at different substrate temperatures has been observed. In contrast, Ga-assisted (Ga1) NWs show symmetric  $I$ - $V$  curves without any significant hysteresis, consistently in all measured NWs. Both Au1 and Ga1 NWs are grown with the same temperature of the Be effusion cell which would give the nominal Be concentration of  $\sim 4.3 \times 10^{18} \text{ cm}^{-3}$  in GaAs(001) thin film growth. This suggests that the incorporation of Be dopants would be more effective through the Ga-particle than through the Au-particle during the NW growth, or that lateral diffusion of Be dopants into the NW from the NW sidewalls is significant at 630  $^{\circ}\text{C}$ . Due to the relatively high growth temperature and low  $\text{As}_4/\text{Ga}$  flux ratio (beam equivalent pressure ratio of 15), lateral interstitial diffusion of Be [18,19] from the NW sidewalls into the NW could take place during the Ga-assisted growth at 630  $^{\circ}\text{C}$



**Fig. 2.** TEM images of Be-doped GaAs NWs grown by (a) the Au-assisted technique at a substrate temperature of 510  $^{\circ}\text{C}$ , and (c) the Ga-assisted VLS technique with the same nominal Be concentration as in Fig. 1. The diffraction patterns obtained from an area marked by a circle in (a) and (c) are shown in (b) and (d), respectively. The diffraction patterns confirm the predominant WZ and ZB crystal structure in NWs grown by the Au- and Ga-assisted techniques, respectively. (Scale bars are 100 nm.)

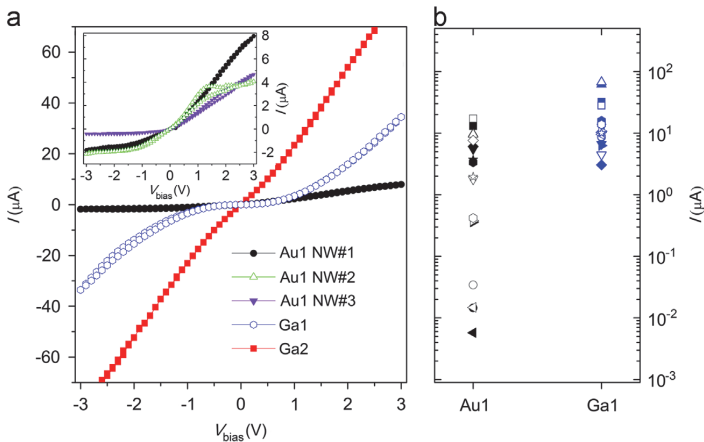


**Fig. 3.** (a) Typical  $I$ - $V$  curves of Be-doped GaAs NWs grown by the Au-assisted (Au1) and the Ga-assisted (Ga1, Ga2) MBE technique. The inset shows  $I$ - $V$  curves of Au1 GaAs NWs in a magnified view. (b) Statistical scatter plot of measured current at  $\pm 2 \text{ V}$  for multiple NWs (9 NWs each) from different growths (Au1 and Ga1). Filled symbols are currents measured at +2 V, whereas unfilled symbols are currents at -2 V.

dependent on the gradient of the Be concentration in the NW (i.e. dependent on the Be concentration at the sidewall and on how efficiently Be dopants are incorporated through the Ga particle). Further experiments are needed to clarify the mechanisms here. For better comparison, the electrical currents measured at  $\pm 2$  V in several NWs are plotted together in Fig. 3b. As can be seen, Ga-assisted NWs show far better  $I$ - $V$  characteristics with less dispersion than Au-assisted NWs. In the Ga-assisted NW case, an increase of the Be cell temperature leads to an increase of the current with an almost linear  $I$ - $V$  curve (Ga2 NW), which is as expected due to the higher doping concentration (nominal Be concentration of  $\sim 1.4 \times 10^{19} \text{ cm}^{-3}$ ) than in Ga1 NWs.

Further, we investigated the effect of heat treatment on the contacted NW devices. The non-linearity at low voltages ( $< 0.5$  V) observed in  $I$ - $V$  curves of Ga1 NWs can be removed by post-annealing the devices at  $400^\circ\text{C}$  for 30 s, as shown in Fig. 4. For Au-assisted NW (Au1) cases, no enhancement of linearity or current was observed after post-annealing. Hence, these results demonstrate that linear, ohmic  $I$ - $V$  characteristics can be achieved for doped Ga-assisted NWs by post-annealing without any change in the morphology after the annealing (inset of Fig. 4). It is already noted that a linear  $I$ - $V$  curve can be measured in more highly doped Ga2 NWs (Fig. 3a) without any annealing treatment. This indicates that higher Be-doping or post-annealing would enhance the ohmic contact by thinning the surface barrier or lowering it by forming an interface layer between NW and metal electrodes, effectively removing the Fermi-level pinning at the GaAs surface [20].

The 4-probe resistivity measurements were carried out on Ga1 NWs without any heat treatment, where 4 NWs were measured. The comparison between 2-probe and 4-probe resistance measurements revealed that the contact resistances accounts for 20–30% of the 2-probe resistance. The NW resistivity has been measured to vary between  $1.7 \times 10^{-2}$  and  $5.9 \times 10^{-2} \Omega \text{ cm}$ . If we regard the nominal carrier concentration in thin film growth as the carrier concentration of our NWs, the hole mobility of our Be-doped GaAs NWs could be estimated to be in the range of 24–84  $\text{cm}^2/\text{V}\cdot\text{s}$  with an average value of 49  $\text{cm}^2/\text{V}\cdot\text{s}$ . The estimated hole mobility of Be-doped GaAs NWs are lower than the hole mobility expected in bulk GaAs with the same doping concentration [21]. Here, the resistivity is calculated by assuming a cylindrical symmetry of the NW without any consideration of the surface depletion layer [22]. The inclusion of the surface

depletion layer as a dead layer for charge transport may increase the estimated hole mobility in the NWs. The observed variation of hole mobility might be due to the different levels of doping in different NWs during the MBE growth. In addition, the one-dimensional geometry of the NW itself and possible doping-related crystal defects in a NW would enhance the carrier scattering processes along the NW axis, which may result in the reduction of carrier mobility in doped NWs as compared to that of the doped semiconductor bulk [12].

The results presented here show that Be incorporates more efficiently in GaAs NWs grown by the Ga-assisted technique compared to the Au-assisted technique. This might be due to the differences in the composition of the catalyst particles as well as the growth conditions that are used in these techniques. Further study is needed to understand the exact reasons for the lower incorporation efficiency of Be in GaAs NWs grown by the Au-assisted technique.

#### 4. Conclusions

We have successfully demonstrated and compared the growth of Be-doped GaAs NWs grown by Au- and Ga-assisted VLS MBE techniques. The growth rate of the NWs grown by the Au-assisted technique is shown to be dependent on the substrate temperature during growth. Electrical characterization revealed that the incorporation of Be dopants in GaAs NWs is less efficient through the Au-assisted technique than through the Ga-assisted technique, and demands further optimization of the growth parameters for the Au-assisted technique. Be-doped GaAs NWs grown by the Ga-assisted method exhibit consistently symmetric  $I$ - $V$  curves in all measured NWs with higher electrical current than Au-assisted grown NWs. Further, we have shown that linear  $I$ - $V$  characteristics can be obtained for Be-doped GaAs NWs grown by the Ga-assisted technique by increasing the Be concentration or by post-annealing of NW-metal contacts.

#### Acknowledgments

This work was partially supported by the “RENERGI” program (Grant no. 190871) of the Research Council of Norway, and the NANORDSUN consortium (Grant no. 10048) funded from the “Top-level Research Initiative” of the Nordic Innovation Centre (NICE), Norway.

#### References

- [1] E.D. Minot, F. Kelkensberg, M. van Kouwen, J.A. van Dam, L.P. Kouwenhoven, V. Zwiller, M.T. Borgström, O. Wunnicke, M.A. Verheijen, E.P.A.M. Bakkers, *Nano Letters* 7 (2007) 367.
- [2] M.T. Björk, B.J. Ohlsson, C. Thelander, A.I. Persson, K. Deppert, L.R. Wallenberg, L. Samuelson, *Applied Physics Letters* 81 (2002) 4458.
- [3] C. Colombo, D. Spirkoska, M. Frimmer, G. Abstreiter, A. Fontcuberta i Morral, *Physical Review B* 77 (2008) 155326.
- [4] S. Plissard, K.A. Dick, X. Wallart, P. Caroff, *Applied Physics Letters* 96 (2010) 121901.
- [5] M. Hilsse, M. Ramsteiner, S. Breuer, L. Geelhaar, H. Riechert, *Applied Physics Letters* 96 (2010) 193104.
- [6] M. Piccin, G. Bais, V. Grillo, F. Jabeen, S. De Franceschi, E. Carlino, M. Lazzarino, F. Romanato, L. Businaro, S. Rubini, F. Martelli, A. Franciosi, *Physica E: Low-dimensional Systems and Nanostructures* 37 (2007) 134.
- [7] J. Dufouleur, C. Colombo, T. Garma, B. Ketterer, E. Uccelli, M. Nicotra, A. Fontcuberta i Morral, *Nano Letters* 10 (2010) 1734.
- [8] L. Rigutti, A. De Luna Bugallo, M. Tchernycheva, G. Jacopin, F.H. Julien, G. Cirlin, G. Patriarche, D. Lucot, L. Travers, J.-C. Harmand, *Journal of Nanomaterials* (2009) 2009.
- [9] M. Hjort, J. Wallentin, R. Timm, A.A. Zakharov, J.N. Andersen, L. Samuelson, M.T. Borgström, A. Miljkelsen, *Applied Physics Letters* 99 (2011) 233113.
- [10] D.E. Perea, E.R. Hemesath, E.J. Schwalbach, J.L. Lensch-Falk, P.W. Voorhees, L.J. Lauhon, *Nature Nanotechnology* 4 (2009) 315.

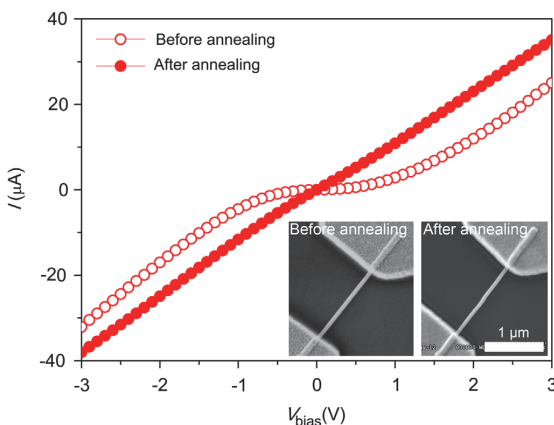


**Fig. 4.** 2-probe  $I$ - $V$  curves before and after annealing of contacted Be-doped GaAs NW grown by the Ga-assisted MBE technique (Ga1). Inset shows exemplary SEM images of contacted single NW (Ga1) before and after annealing. No noticeable change in either the morphology of the NW or at the NW/contact interface can be observed after the annealing.

- [11] J. Wagner, M. Maier, R. Murray, R.C. Newman, R.B. Beall, J.J. Harris, *Journal of Applied Physics* 69 (1991) 971.
- [12] J. Wallentin, M. Ek, L.R. Wallenberg, L. Samuelson, M.T. Borgström, *Nano Letters* 12 (2011) 151.
- [13] C. Gutsche, R. Niepelt, M. Gnauck, A. Lysov, W. Prost, C. Ronning, F.-J. Tegude, *Nano Letters* 12 (2012) 1453.
- [14] D.L. Dheeraj, G. Patriarche, H. Zhou, J.C. Harmand, H. Weman, B.O. Fimland, *Journal of Crystal Growth* 311 (2009) 1847.
- [15] C. Sartel, D.L. Dheeraj, F. Jabeen, J.C. Harmand, *Journal of Crystal Growth* 312 (2010) 2073.
- [16] H.L. Zhou, T.B. Hoang, D.L. Dheeraj, A.T.J. van Helvoort, L. Liu, J.C. Harmand, B.O. Fimland, H. Weman, *Nanotechnology* 20 (2009) 415701.
- [17] G.E. Cirlin, V.G. Dubrovskii, Y.B. Samsonenko, A.D. Bouravleuv, K. Durose, Y.Y. Proskuryakov, B. Mendes, L. Bowen, M.A. Kaliteevski, R.A. Abram, D. Zeze, *Physics Review B* 82 (2010) 035302.
- [18] R. Mosca, P. Bussei, S. Franchi, P. Frigeri, E. Gombia, A. Carnera, M. Peroni, *Journal of Applied Physics* 93 (2003) 9709.
- [19] H.-P. Komsa, E. Arola, J. Pakarinen, C.S. Peng, T.T. Rantala, *Physical Review B* 79 (2009) 115208.
- [20] M.J. Howes, D.V. Morgan, *Gallium Arsenide—Materials, Devices, and Circuits*, John Wiley & Sons Ltd., 1985.
- [21] J.S. Blakemore, *Journal of Applied Physics* 53 (1982) R123.
- [22] M.T. Björk, H. Schmid, J. Knoch, H. Riel, W. Riess, *Nature nanotechnology* 4 (2009) 103–107.



**6.6 Paper VI: Position-controlled uniform GaAs nanowires on silicon using nanoimprint lithography**

*Nano Letters* **14** (2014) 960





## Position-Controlled Uniform GaAs Nanowires on Silicon using Nanoimprint Lithography

A. M. Munshi,<sup>†</sup> D. L. Dheeraj,<sup>†</sup> V. T. Fauske,<sup>‡</sup> D. C. Kim,<sup>†,§</sup> J. Huh,<sup>†</sup> J. F. Reinertsen,<sup>†</sup> L. Ahtapodov,<sup>†</sup> K. D. Lee,<sup>||</sup> B. Heidari,<sup>||</sup> A. T. J. van Helvoort,<sup>‡</sup> B. O. Fimland,<sup>†</sup> and H. Weman<sup>\*,†</sup>

<sup>†</sup>Department of Electronics and Telecommunications, Norwegian University of Science and Technology (NTNU), NO-7491 Trondheim, Norway

<sup>‡</sup>Department of Physics, Norwegian University of Science and Technology (NTNU), NO-7491 Trondheim, Norway

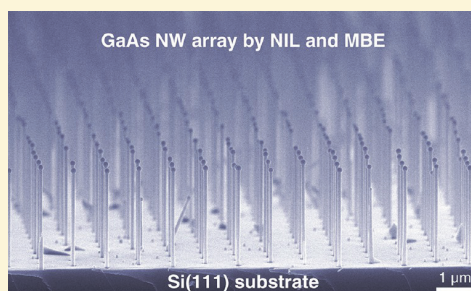
<sup>§</sup>CrayoNano AS, Otto Nielsens vei 12, NO-7052 Trondheim, Norway

<sup>||</sup>Obducat Technologies AB, Scheelevägen 2, SE-22363 Lund, Sweden

### Supporting Information

**ABSTRACT:** We report on the epitaxial growth of large-area position-controlled self-catalyzed GaAs nanowires (NWs) directly on Si by molecular beam epitaxy (MBE). Nanohole patterns are defined in a SiO<sub>2</sub> mask on 2 in. Si wafers using nanoimprint lithography (NIL) for the growth of positioned GaAs NWs. To optimize the yield of vertical NWs the MBE growth parameter space is tuned, including Ga predeposition time, Ga and As fluxes, growth temperature, and annealing treatment prior to NW growth. In addition, a non-negligible radial growth is observed with increasing growth time and is found to be independent of the As species (i.e., As<sub>2</sub> or As<sub>4</sub>) and the growth temperatures studied. Cross-sectional transmission electron microscopy analysis of the GaAs NW/Si substrate heterointerface reveals an epitaxial growth where NW base fills the oxide hole opening and eventually extends over the oxide mask. These findings have important implications for NW-based device designs with axial and radial p–n junctions. Finally, NIL positioned GaAs/AlGaAs core–shell heterostructured NWs are grown on Si to study the optical properties of the NWs. Room-temperature photoluminescence spectroscopy of ensembles of as-grown core–shell NWs reveals uniform and high optical quality, as required for the subsequent device applications. The combination of NIL and MBE thereby demonstrates the successful heterogeneous integration of highly uniform GaAs NWs on Si, important for fabricating high throughput, large-area position-controlled NW arrays for various optoelectronic device applications.

**KEYWORDS:** Self-catalyzed GaAs nanowires, silicon, nanoimprint lithography, molecular beam epitaxy, transmission electron microscopy, photoluminescence



Semiconductor nanowires (NWs) have received great interest in recent years for their potential usage as versatile building blocks in future electronic and optoelectronic devices.<sup>1–3</sup> In particular, direct band gap III–V NWs due to their superior carrier mobility and high absorption coefficient are of special interest for applications in high mobility transistors,<sup>4–6</sup> light emitting diodes (LEDs),<sup>7,8</sup> room temperature laser<sup>9,10</sup> as well as in solar cells with both radial<sup>11</sup> and axial<sup>12,13</sup> junctions. Moreover, when grown on lattice mismatched substrates due to the tiny diameter of the NWs, strain is expected to relieve in the radial direction of the NW without defect formation.<sup>14,15</sup> This unique property of NWs has resulted in the successful growth of vertical III–V NWs not only on flexible graphene<sup>16,17</sup> but also on low-cost Si substrates.<sup>18,19</sup> The most popular bottom-up approach to grow these NWs is based on the vapor–liquid–solid (VLS) mechanism using mainly Au as the catalyst.<sup>20</sup> However, Au

incorporation in the grown NWs as well as in the Si substrate is a concern that could hinder the integration of III–V NWs with the Si-based electronics.<sup>21</sup> One viable route to avoid this potential problem is to use the self-catalyzed technique<sup>22</sup> that recently has attracted a great attention.<sup>23</sup> In this technique, the group III element itself acts as the catalyst, eliminating any chances of contamination by a foreign catalyst. An additional advantage of the self-catalyzed growth technique is that one can realize core–shell heterostructured NWs without any VLS growth of the shell material in the axial direction. The Ga droplet, used in the case of GaAs NWs, can be solidified into the NW and a close to ideal conformal shell structure can be

**Received:** November 25, 2013

**Revised:** January 23, 2014

**Published:** January 27, 2014

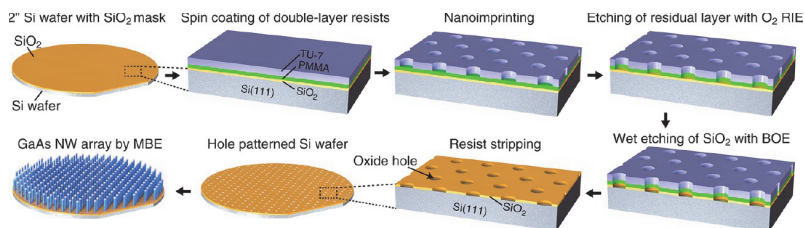


**Figure 1.** Schematic illustration of the NIL process used to pattern nanoholes on a SiO<sub>2</sub> covered 2 in. Si wafer for the growth of position-controlled self-catalyzed GaAs NWs.

growth around the core via vapor–solid (VS) growth on the NW side-facets.<sup>23</sup>

Usually, the self-catalyzed GaAs NWs are grown by a self-assembled mechanism where the Ga droplets are formed randomly in nanocraters of a native oxide covered Si substrate.<sup>24</sup> This self-assembled approach has already been successful in demonstrating vertical GaAs NWs with controlled crystal structure<sup>25–27</sup> and with good optical properties.<sup>23,28</sup> However, since the NWs are randomly positioned, each NW will have a different surrounding during growth, resulting in a variation in their morphological as well as structural and functional properties that could subsequently affect device performances. Therefore, in order to achieve uniform NWs that would afterward ensure a reliable device performance and design it is of paramount importance to have a precise control on their density and position. This can be achieved by patterning a mask with holes on top of the substrate before the NW growth. Patterning by electron-beam lithography (EBL) has been employed for such positioning of III–V NWs both on III–V<sup>29–31</sup> as well as on Si substrates.<sup>32–36</sup> However, EBL is considered to be a slow process, involves high-cost, and is unable to efficiently produce large-area patterning, and therefore cannot be used for wafer-scale production. Other techniques such as nanosphere lithography<sup>37,38</sup> and laser-interface lithography<sup>39</sup> have previously been used to create position-controlled NW arrays on large scales. However, these techniques are restricted to make only regular patterns and/or without control on in-plane size and spacing of the holes. An alternative method would be to use nanoimprint lithography (NIL) that is a simpler and relatively inexpensive technique and is capable of patterning masks on wafer-scale substrates with high throughput. Despite these advantages, there are so far only a few reports on NIL positioned III–V NWs using Au-assisted and catalyst-free techniques on III–V<sup>40–42</sup> and Si substrates.<sup>43</sup> Position-controlled growth of GaAs NWs on Si using NIL has not been explored in details by any NW growth techniques.

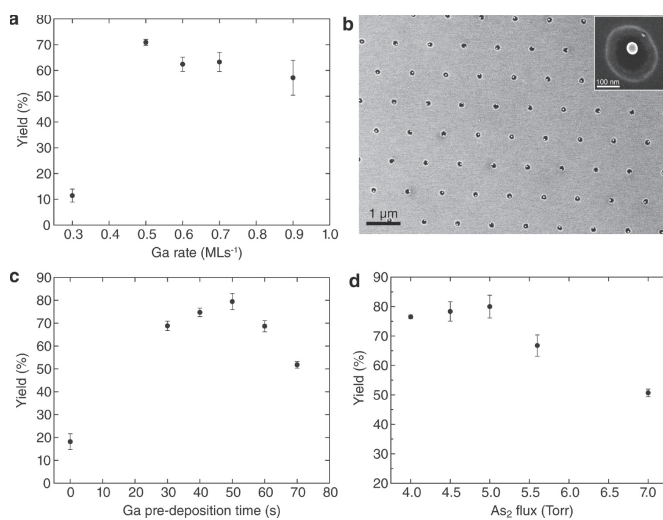
Here, we report the growth of large-area NIL patterned GaAs NWs directly on Si substrates using self-catalyzed molecular beam epitaxy (MBE). The MBE growth parameter space was tuned in order to maximize the yield of uniform vertical NWs. The GaAs NW/Si substrate interface was analyzed by cross-sectional transmission electron microscopy (TEM). The optical quality of these GaAs NWs, passivated by a radial AlGaAs shell, was assessed by photoluminescence (PL) spectroscopy.

Figure 1 shows a schematic illustration of the NIL process flow used in this study (see Supporting Information S1.1 for additional details). In short, thermal SiO<sub>2</sub> of ~40 nm thickness was grown on 2 in. p-type Si(111) substrates. A Si stamp with holes of diameter 75 nm, height 100 nm, and pitch 1 μm in a hexagonal pattern was used in this work. Using NIL and wet

etching process, the pattern was transferred to holes with average sizes ~100 nm in the SiO<sub>2</sub> layer on the Si substrates (Supporting Information Figure S1). Subsequently, the NIL patterned Si substrates were used for the MBE growth (see Supporting Information S1.2).

**Effect of Ga Flux.** First, the Ga flux was optimized in order to improve the yield of vertical GaAs NWs. The Ga flux was estimated using the growth rate of GaAs thin film measured on a GaAs(100) substrate in monolayers per second (ML s<sup>-1</sup>) by reflection high energy electron diffraction. The As flux was measured in terms of beam equivalent pressure by an ion gauge. The Ga rate was varied from 0.3–0.9 ML s<sup>-1</sup> under a constant As<sub>2</sub> flux of 5.0 × 10<sup>-6</sup> Torr and at a substrate temperature of 640 °C, as measured by a pyrometer. The variation of yield of vertical NWs on the Ga rate is plotted in Figure 2a. The yield was estimated by selecting different areas of a sample by scanning electron microscopy (SEM) and counting the total number of vertical NWs divided by the total number of successful nanoholes formed by the NIL process (Supporting Information Figure S1). At the lowest Ga rate (0.3 ML s<sup>-1</sup>), only very few NWs were found to grow in the holes and no other GaAs structures were observed on the substrate (Supporting Information S2). This is attributed to the high adatoms desorption from the oxide mask at the growth temperature of 640 °C,<sup>44</sup> resulting in a very low yield of about 10% at this low Ga rate. As the Ga rate was increased to 0.5 ML s<sup>-1</sup>, the yield of vertical NWs increased to about 70% and remained almost constant when the Ga rate was increased to 0.6 and 0.7 ML s<sup>-1</sup>. With further increase in the Ga rate to 0.9 ML s<sup>-1</sup>, the yield is reduced to about 60% and the number of two-dimensional (2D) GaAs crystals in the holes started to increase. From the above growth series, a Ga rate of 0.6 ML s<sup>-1</sup> was chosen for the optimization of the other growth parameters in the subsequent study. At this rate, the risks of Ga desorption as well as 2D crystal growth should be minimized. Here, it should be noted that the growth parameters are not independent from each other. For example, for each Ga rate there would be an optimum condition for the other parameters. It is suggested that a rate for which the Ga adatoms do not desorb completely from the substrate can be used for the NW growth.

**Effect of Growth Temperature.** The successful growth of a vertical NW is dependent on the initial nucleation stage. Here, the presence or absence of the Ga droplet in the oxide holes should be strongly linked to the success or the failure of the subsequent NW growth. To check the droplet formation, Ga predeposition experiments were carried out at two different substrate temperatures, 640 and 630 °C, without any NW growth step. It was noticed that at 640 °C, Ga droplets could not be found in every oxide holes (Supporting Information S3).



**Figure 2.** (a) Influence of Ga growth rate on the yield of vertical GaAs NWs grown with an As<sub>2</sub> flux of  $5.0 \times 10^{-6}$  Torr for 15 min at 640 °C. (b) SEM image of single Ga droplets in the holes on a SiO<sub>2</sub> covered Si substrate formed by predepositing Ga for 50 s with a rate of 0.6 ML s<sup>-1</sup> at a substrate temperature of 630 °C. Inset shows a magnified view of a single Ga droplet in a hole. (c) Influence of Ga predeposition time on the yield of vertical GaAs NWs grown with a Ga rate of 0.6 ML s<sup>-1</sup> and As<sub>2</sub> flux of  $5.0 \times 10^{-6}$  Torr for 15 min at 630 °C. (d) Influence of the As<sub>2</sub> flux on the yield of vertical GaAs NWs grown with a Ga rate of 0.6 ML s<sup>-1</sup> for 15 min at 630 °C. The error bars in the data points in panels a,c,d indicate the standard deviation from their mean values.

This is believed to be due to that growth at 640 °C is at the threshold above which substantial desorption of Ga adatoms takes place, resulting in an absence of Ga droplets in the holes. A small degree of inaccuracy in the temperature reading, from the thermoelement at the substrate holder or from the pyrometer during the MBE growth, and hence temperature control, could in turn result in a variation in the yield. By lowering the substrate temperature to 630 °C, a single Ga droplet is found to form successfully in the oxide holes as shown in Figure 2b for a sample with a 50 s Ga predeposition time and an average hole diameter of 100 nm. The size of the Ga droplets is found to be about 40 nm for this hole size (inset in Figure 2b). The growths at this temperature (630 °C) were found to be highly reproducible.

In addition, the formation of the Ga droplet in holes with larger sizes was examined (Supporting Information S4). The hole size was varied by etching the substrate in HF for longer durations before loading into the MBE. It was found that 2–3 Ga droplets formed for hole sizes  $\sim 140$  and  $\sim 150$  nm, respectively, indicating that the hole size used in this study ( $\sim 100$  nm) is optimum for obtaining a single droplet and subsequently a single NW per hole with the growth condition studied.

**Effect of Ga Predeposition Time.** To understand the effect of the Ga predeposition conditions on the yield of NWs, we carried out a NW growth series at 630 °C by varying the predeposition time from 0 to 70 s. The Ga rate and the As<sub>2</sub> flux chosen for this series were 0.6 ML s<sup>-1</sup> and  $5.0 \times 10^{-6}$  Torr, respectively. The influence of the Ga predeposition time on the yield of vertical NWs is plotted in Figure 2c. It can be seen that with a Ga predeposition time of 0 s, the yield of NWs was found to be very low ( $\sim 20\%$ ). Instead of NWs, mostly GaAs 2D crystals were grown in the holes in this case, as shown in Supporting Information S5. This is attributed to the fact that

without predeposition the Ga droplets could not form early enough to allow VLS growth, leading mainly to the growth of GaAs 2D crystals in the holes. With a predeposition time of 30 s, the yield drastically increases to about 70%. As the predeposition time increases further, the yield also increases and attains a maximum of about 80% for a predeposition time of 50 s. It is believed that the initial droplet size with this predeposition time shown in Figure 2b, favors the nucleation and growth of single vertical NWs leading to the highest yield. With further increase in the predeposition time to 70 s, the yield decreases and reaches about 50%. A longer predeposition time decreases the contact angle of the droplet possibly by forming an alloy or etching the Si substrate at the liquid-substrate interface, and favors 2D crystal growth. The formation of such 2D crystals can be seen in Supporting Information Figure S5f. A similar trend for the yield dependency of GaAs NWs on the Ga predeposition time was observed by Plissard et al. for EBL patterned Si substrates.<sup>33</sup> Interestingly, the optimum droplet size for the highest yield in the present study was also found to be in the same range as observed in ref 33, indicating the validity of our conclusion and the importance for an optimized predeposition time.

**Effect of As<sub>2</sub> flux.** The As<sub>2</sub> flux was optimized for a Ga rate of 0.6 ML s<sup>-1</sup> at a growth temperature of 630 °C. The As<sub>2</sub> flux was varied from  $4.0 \times 10^{-6}$  to  $7.0 \times 10^{-6}$  Torr (Supporting Information S6). A Ga predeposition time of 50 s was chosen for all these growths described below and the NW growths were carried out for duration of 15 min. The observed dependence of the yield on the As<sub>2</sub> flux is shown in Figure 2d. A maximum yield of about 80% was found for an As<sub>2</sub> flux of  $5.0 \times 10^{-6}$  Torr. For lower flux, the number of tilted NWs in the holes increases, resulting in a yield of vertical NWs of about 75% for an As<sub>2</sub> flux of  $4.0 \times 10^{-6}$  Torr. Whereas for higher flux, the number of 2D GaAs crystals in the holes increases which

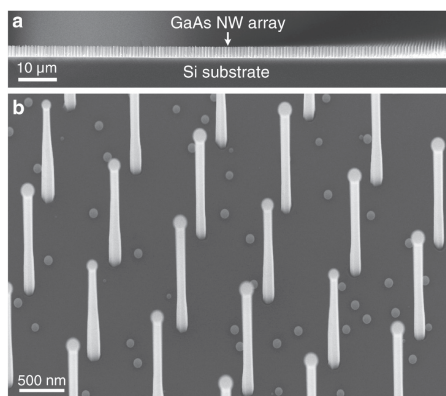


**Figure 3.** (a) Low-magnification side-view SEM image of vertical GaAs NW array on Si grown with 50 s of Ga predeposition, a Ga rate of  $0.6 \text{ ML s}^{-1}$  and an  $\text{As}_2$  flux of  $5.0 \times 10^{-6}$  Torr for 15 min at  $630^\circ\text{C}$ . (b) Magnified  $20^\circ$  tilted-view SEM image of the NW array shown in panel a.

results in a substantial reduction of yield to about 50% for an  $\text{As}_2$  flux of  $7.0 \times 10^{-6}$  Torr. The tilted NWs in the low flux regime are attributed to the formation of three-dimensional multiple-order twinning due to a low V/III ratio,<sup>45</sup> whereas the 2D crystals in the high flux regime are formed due to a local As-rich environment, hence hindering the VLS NW growth. These results demonstrate the importance of the right As flux for obtaining an optimized yield for a given Ga rate.

Figure 3a represents a side-view SEM image of the GaAs NW array grown with the optimized condition at  $630^\circ\text{C}$  for 15 min showing the uniformity over a large area. Figure 3b shows a magnified tilted-view SEM image of the NW array in Figure 3a, showing high uniformity in the length and diameter of the NWs. In addition to the vertically standing NWs, Ga droplets with sizes  $\sim 60$ – $90$  nm were formed on the oxide mask. The droplets started to form at an early stage of the growth and by increasing the growth duration their density and size increase. We believe that the formation of the droplets on the oxide mask is related to the roughness of the oxide surface.

In all the above-mentioned growths, the samples were annealed at  $690^\circ\text{C}$  for 5 min prior to the growth. We observed that the yield reduces to about 40% when growth was performed without the annealing step (Supporting Information S7). We suspect that the annealing at  $690^\circ\text{C}$  prior to the NW growth either helps in removing<sup>46</sup> the possibly formed thin regrown oxide in the holes during the substrate transfer and loading process into the MBE chamber and/or that it helps in cleaning the substrate by desorbing existing remnants in the holes, if any, from the earlier processes. The yield of the NWs could be further improved by improving the steps in the NIL process, for example, by further optimizing the  $\text{O}_2$  reactive ion etching step to get more uniform hole sizes in the double-layer resist or using a dry etching process as used by Plissard et al.,<sup>33</sup> instead of a wet chemical etching for the oxide holes.

**Effect of Growth Time.** In order to investigate the evolution of diameter and length of the GaAs NWs, a growth series with NW growth durations of 1, 5, 10, 15, and 30 min at  $630^\circ\text{C}$ , keeping all the other parameters constant, was carried out. Tilted-view SEM images of these NW arrays are shown in Supporting Information Figure S8.1. The length and diameter

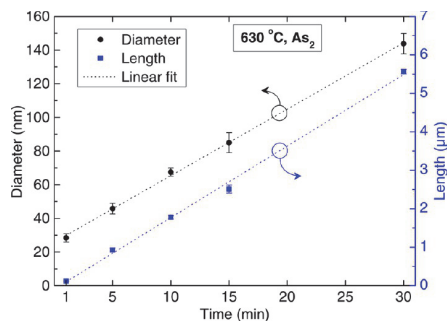


**Figure 4.** Plot of GaAs NW diameter and length versus growth time. The error bars in the data points indicate the standard deviation from their mean values. For all the samples, the diameter is measured at the middle of the NW.

of the NWs are measured from side-view SEM images for each sample and are plotted in Figure 4 as a function of growth time. It can be seen that both the diameter and the length of NWs increase linearly with time at a rate of  $\sim 4$  and  $185 \text{ nm/min}$ , respectively.<sup>47</sup> The monotonic increase in the diameter of the NWs represents a non-negligible radial growth that has to be considered in the NW-device design. The radial growth is also evident from the fact that the NW base starts to completely fill the oxide hole for longer growth durations (see e.g. Supporting Information Figure S8.1d–f). It can also be seen in Supporting Information Figure S8.2 that the diameter of the NWs at the bottom is slightly larger than the diameter at their tip, indicating that the NWs grown at  $630^\circ\text{C}$  are slightly tapered and the tapering increases with increasing the growth duration ( $\sim 1.4\%$  for 30 min, tapering  $\approx (\text{base diameter} - \text{tip diameter})/\text{length}$ ).

The same growth time series is also performed at  $640^\circ\text{C}$  as it was expected that the higher temperature would enhance the diffusion of adatoms on the NW sidewalls. A similar linear increase in the diameter and length with growth time was observed, implying that an increase in the growth temperature is unable to substantially reduce the radial growth (Supporting Information S9). The NWs grown at  $640^\circ\text{C}$  are found to have almost rodlike morphology ( $\sim 0.7\%$  for 30 min, Supporting Information Figure S9.2). The observed dependency of tapering with growth time and temperature can be ascribed to the higher radial growth at the NW base as it is exposed to the fluxes for a longer duration than the tip, and the temperature-dependent diffusion of Ga adatoms along the NW sidewalls from the base to the tip. Lastly, an effort to minimize the radial growth was also performed using a similar growth time series at  $640^\circ\text{C}$  but with  $\text{As}_4$  where the radial growth was again found to be similar to that with  $\text{As}_2$  (Supporting Information S10).<sup>48,49</sup>

For a NW-based device with an axial p–n junction, it is important that there is no radial growth taking place during the axial junction growth.<sup>12,13</sup> From the experiments reported here, at two different temperatures and with two different As species, it is suggested that radial growth should be considered in the device design with an axial p–n junction using the presented growth strategy. On the other hand, the growth strategy would be ideally suited for the growth of core–shell NW geometry with a radial p–n junction.

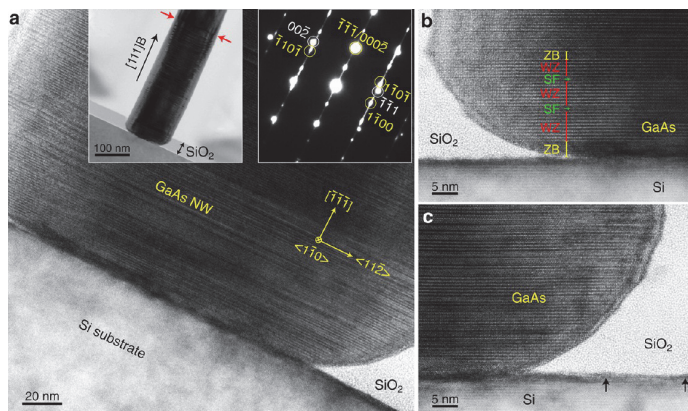


**Figure 5.** (a) Cross-sectional HRTEM image of the GaAs NW/Si substrate interface from the same sample shown in Figure 3. An overview bright-field TEM image of the same positioned GaAs NW on Si is shown in the left inset. The red arrows in the inset indicate the start of a predominantly ZB GaAs segment. Right inset shows a diffraction pattern taken from the NW/substrate interface confirming the epitaxial growth. Images were taken along  $\langle 110 \rangle$  zone axis. (b,c) Magnified HRTEM images from the left and right sides, respectively, of the NW/substrate interface in panel a. Some of the ZB and WZ sections and SFs are indicated in panel b. The GaAs NW is in contact with the Si substrate across the entire hole opening and extends over the  $\text{SiO}_2$  mask for a longer growth time. Black arrows in c indicate a slightly rough  $\text{SiO}_2$ /Si interface that is formed during the thermal oxide growth process.<sup>54</sup>

**Cross-Sectional TEM of GaAs NW/Si Substrate Interface.** The NW/substrate heterointerface was characterized by cross-sectional TEM using a JEOL 2100 TEM operated at 200 kV. The samples were prepared using a FEI Helios DualBeam focused ion beam (FIB) system with  $\text{Ga}^{2+}$  ions in the range 2–30 kV. Figure 5a shows a cross-sectional high-resolution (HR) TEM image of a vertically standing GaAs NW on a Si substrate grown for 15 min, corresponding to the NWs in Figure 3. An overview bright-field TEM image of the same NW is shown in the left inset in Figure 5a where the oxide mask on the Si substrate can be seen. A selected area electron diffraction pattern from the NW/substrate interface is shown in the right inset in Figure 5a, showing an epitaxial growth. Additional high-magnification HRTEM images of the left and right side of the NW/substrate interface are shown in Figure 5b,c. The bottom part of the NW consists of wurtzite (WZ) GaAs with stacking faults (SFs), and zinc blende (ZB) GaAs with rotational twins, as indicated in Figure 5b. The crystal phase becomes mainly ZB after 300–350 nm (above red arrows in the left inset in Figure 5a). The occurrence of the above-mentioned polytypes adjacent to the interface with the Si substrate is attributed to variations in the shape<sup>50</sup> and the supersaturation<sup>51</sup> of the Ga droplets during the initial NW growth stage and has been observed in the case of self-catalyzed GaAs NWs on Si as reported previously.<sup>52</sup> It can be seen in Figure 5 that the NW homogeneously covers the entire hole opening in the oxide mask on the Si substrate, confirming the radial growth GaAs NW as described above. Interestingly, the coverage of the oxide hole has turned out to be an important requirement for device design because it would prevent the formation of an additional p–n junction between the shell and the Si substrate during radial VS shell growth in the case of p–n core–shell NWs. The NW/substrate interface is found to be slightly rough, which could be due to the etching of the Si substrate by Ga during the predeposition step,<sup>53</sup> and/or to the thermal  $\text{SiO}_2$  growth process<sup>54</sup> as indicated by black arrows at the  $\text{SiO}_2$ /Si interface in Figure 5c. Obtaining an epitaxial interface with a continuous

contact area between the GaAs NW and the Si substrate would be critical for device performance.

**Positioned GaAs/AlGaAs Core–Shell NWs.** The NIL self-catalyzed MBE growth method allows for growing position-controlled radial heterostructured NW array as well, in the present case demonstrated by growing GaAs/AlGaAs core–shell NWs. Because of the high surface-to-volume ratio of the NWs, the surface states strongly degrade the PL intensity of these GaAs NWs.<sup>55</sup> It is therefore advantageous to use a higher band gap passivation layer to improve the PL efficiency as well as for further use of these GaAs NWs in device applications such as LEDs and solar cells. Because of the type-I band line-up and close lattice matching condition between GaAs and AlGaAs, an AlGaAs radial shell is most commonly used as the passivation layer. In the present study, an  $\text{Al}_{0.33}\text{Ga}_{0.67}\text{As}$  segment was grown after the GaAs NW core followed by the solidification of the droplet by supplying only an  $\text{As}_2$  flux of  $9.0 \times 10^{-6}$  Torr for 10 min. Subsequently, an  $\text{Al}_{0.33}\text{Ga}_{0.67}\text{As}$  radial shell of nominal thickness 25 nm was grown by the VS method on the sidewalls of the GaAs core. Finally, to prevent the oxidation of the AlGaAs shell, a 5 nm thick GaAs cap layer was grown. Figure 6a shows a tilted-view SEM image of the position-controlled GaAs/AlGaAs/GaAs core–shell-cap NW array grown at 630 °C. The final NWs have a length of  $\sim 5.5 \mu\text{m}$ , base diameter  $\sim 240$  nm, and tip diameter  $\sim 170$  nm, hence having slightly tapered ( $\sim 1.3\%$ ) morphology (Figure 6b). By taking into account the diameters at the base and tip of the GaAs core grown at 630 °C, this tapering morphology of the core–shell NWs is attributed to the tapered GaAs core, implying that the shell thickness is uniform over the whole length of the NWs.

**Photoluminescence Study of GaAs/AlGaAs Core–Shell NWs.** The optical properties of the GaAs/AlGaAs core–shell NWs were investigated by room-temperature (300 K) PL spectroscopy on ensembles of as-grown positioned NWs. Figure 6c shows a room-temperature PL spectrum taken from an ensemble of as-grown NWs. For the excitation, a

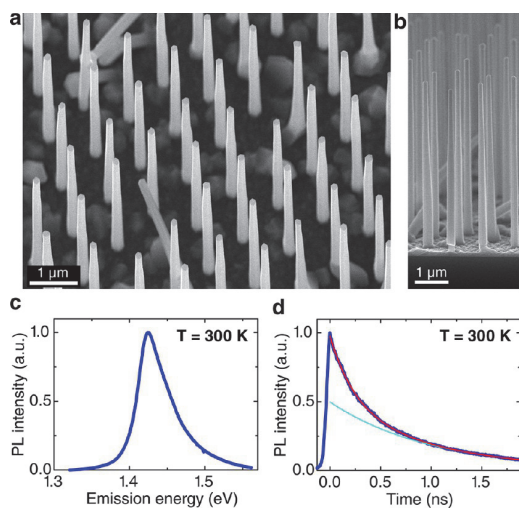


**Figure 6.** (a) The 20° tilted-view and (b) near side-view SEM images of NIL positioned GaAs/AlGaAs core-shell NWs encapsulated by a GaAs cap layer grown on a Si substrate by self-catalyzed MBE. (c) Room-temperature PL spectrum of an ensemble of positioned as-grown core-shell NWs. (d) Room-temperature time-resolved PL decay of the band-to-band transition of the as-grown NW ensemble. The decay of the PL intensity was fitted with a double exponential function (red line in d) with a fast (not shown) and a slowly decaying (cyan line in d) component. By evaluating the signal after the fast initial decay, the room temperature PL lifetime is found to be  $\sim 1.0$  ns.

continuous wave Spectra Physics Millennia Nd:YVO laser operating at 532 nm was used. An excitation power of 24  $\mu$ W was focused to a spot size ( $1/e^2$ ) of  $\sim 1.5$   $\mu$ m by a 50 $\times$ , 0.65 numerical aperture, infinity-corrected Mitutoyo microscope lens, exciting several NWs. The signal was collected by the same lens, dispersed with a Horiba Jobin-Yvon single grating spectrometer and detected with an Andor Newton Si charge coupled device (CCD) camera. The core-shell NWs show a strong PL peak centered at 1.424 eV (Figure 6c), attributed to the band-to-band transition within the ZB GaAs core. For time-resolved measurements, the as-grown NWs were excited by a pulsed Spectra Physics Tsunami Ti:sapphire laser operating at 750 nm with a pulse width of 120 fs. To obtain adequate signal, an excitation power of 1.5 mW was focused on the substrate as above. The signal was then dispersed with a Princeton Optics Acton SP2500 spectrometer and detected by an Optronis Optoscope SC-10 NIR enhanced streak camera. Figure 6d shows a room-temperature time-resolved PL decay from an ensemble of as-grown NWs obtained at the energy of band-to-band recombination (1.424 eV). By fitting to a double exponential function and evaluating the signal after the fast initial decay, the room-temperature PL lifetime is found to be  $\sim 1.0$  ns. The bright PL peak and the long radiative PL lifetime at room temperature are comparable to state-of-the-art GaAs NWs so far reported in the literature.<sup>28,56,57</sup>

In conclusion, NIL patterned self-catalyzed growth of vertical GaAs NWs on Si substrates by MBE is demonstrated. The influence of the growth parameters on the yield of vertical NWs was studied and discussed in details. The Ga predeposition time, As flux, and substrate annealing treatment before the growth are found to be critical for obtaining a high yield of

vertical GaAs NWs. With the optimized conditions, uniform GaAs NWs with a yield of about 80% was achieved. An unavoidable radial growth during the axial growth was observed, which has implication for device design. Cross-sectional TEM studies of the GaAs NW/Si substrate interface revealed that the contact area of the NW with the substrate extends across the entire oxide hole. This is important for device applications with radial p-n junctions grown in subsequent growth steps. Room-temperature PL spectroscopy analyses of as-grown NIL patterned GaAs/AlGaAs core-shell NW ensembles indicate a high quality material, as required for optoelectronic applications. The results are an important step forward toward the heterogeneous integration of III-V semiconductor NW arrays on wafer-scale Si substrates for various device applications. The technique can now be implemented to fabricate position-controlled radial p-n junction core-shell NW arrays directly on Si for applications such as solar cells and LEDs.

## ■ ASSOCIATED CONTENT

### Supporting Information

Additional information and figures. This material is available free of charge via the Internet at <http://pubs.acs.org>.

## ■ AUTHOR INFORMATION

### Corresponding Author

\*E-mail: helge.weman@ntnu.no.

### Author Contributions

A.M.M. and D.L.D. designed the experiment and carried out the NW growth. A.M.M. performed the SEM characterization, analyzed the data, and wrote the manuscript. V.T.F. did the FIB specimen preparation and TEM characterization. D.C.K. and J.H. did EBL hole patterning during the preliminary stage of the project. J.F.R. performed the PL characterization with some assistance from L.A. K.D.L. and B.H. prepared the NIL hole patterns. H.W. supervised the project. D.L.D., A.T.J.v.H., B.O.F. and H.W. contributed in interpretation and presentation of the results. All authors discussed the results and commented on the manuscript.

### Notes

The authors declare no competing financial interest.

## ■ ACKNOWLEDGMENTS

This work was supported by the RENNERGI (Grant 190871), FRINATEK (Grant 214235), and INFRASTRUKTUR (Grant 1974117 V30 (NorFab)) programs of the Research Council of Norway, and the NANORDSUN consortium (Grant 10048) funded from the "Top-level Research Initiative" of the Nordic Innovation Centre, Norway.

## ■ REFERENCES

- (1) Yan, R.; Gargas, D.; Yang, P. *Nat. Photonics* **2009**, *3*, 569–576.
- (2) Joyce, H. J.; Gao, Q.; Tan, H. H.; Jagadish, C.; Kim, Y.; Zou, J.; Smith, L. M.; Jackson, H. E.; Yarrison-Rice, J. M.; Parkinson, P.; Johnston, M. B. *Prog. Quantum Electron.* **2011**, *35*, 23–75.
- (3) Yang, P.; Yan, R.; Fardy, M. *Nano Lett.* **2010**, *10*, 1529–1536.
- (4) Thelander, C.; Fröberg, L. E.; Rehnstedt, C.; Samuelson, L.; Wernersson, L. E. *IEEE Electron Device Lett.* **2008**, *29*, 206–208.
- (5) Tomioka, K.; Yoshimura, M.; Fukui, T. *Nature* **2012**, *488*, 189–192.
- (6) Dayeh, S. A.; Aplin, D. P. R.; Zhou, X.; Yu, P. K. L.; Yu, E. T.; Wang, D. *Small* **2007**, *3*, 326–332.

- (7) Svensson, C. P. T.; Mårtensson, T.; Trägårdh, J.; Larsson, C.; Rask, M.; Hessman, D.; Samuelson, L.; Ohlsson, J. *Nanotechnology* **2008**, *19*, 305201.
- (8) Guo, W.; Zhang, M.; Banerjee, A.; Bhattacharya, P. *Nano Lett.* **2010**, *10*, 3355–3359.
- (9) Mayer, B.; Rudolph, D.; Schnell, J.; Morkötter, S.; Winnerl, J.; Treu, J.; Müller, K.; Bracher, G.; Abstreiter, G.; Koblmüller, G.; Finley, J. J. *Nat. Commun.* **2013**, DOI: 10.1038/ncomms3931.
- (10) Saxena, D.; Mokkalapati, S.; Parkinson, P.; Jiang, N.; Gao, Q.; Tan, H. H.; Jagadish, C. *Nat. Photonics* **2013**, *7*, 963–968.
- (11) Mariani, G.; Scofield, A. C.; Hung, C.-H.; Huffaker, D. L. *Nat. Commun.* **2013**, *4*, 1497.
- (12) Wallentin, J.; Anttu, N.; Asoli, D.; Huffman, M.; Åberg, I.; Magnusson, M. H.; Siefert, G.; Fuss-Kailuweit, P.; Dimroth, F.; Witzigmann, B.; Xu, H. Q.; Samuelson, L.; Deppert, K.; Borgström, M. T. *Science* **2013**, *339*, 1057–1060.
- (13) Cui, Y.; Wang, J.; Plissard, S. R.; Cavalli, A.; Vu, T. T. T.; van Veldhoven, R. P. J.; Gao, L.; Trainor, M.; Verheijen, M. A.; Haverkort, J. E. M.; Bakkers, E. P. A. M. *Nano Lett.* **2013**, *13*, 4113–4117.
- (14) Kavanagh, K. L. *Semicond. Sci. Technol.* **2010**, *25*, 024006.
- (15) Glas, F. *Phys. Rev. B* **2006**, *74*, 121302.
- (16) Hong, Y. J.; Fukui, T. *ACS Nano* **2011**, *5*, 7576–7584.
- (17) Munshi, A. M.; Dheeraj, D. L.; Fauske, V. T.; Kim, D.-C.; van Helvoort, A. T. J.; Fimland, B.-O.; Weman, H. *Nano Lett.* **2012**, *12*, 4570–4576.
- (18) Mårtensson, T.; Svensson, C. P. T.; Wacaser, B. A.; Larsson, M. W.; Seifert, W.; Deppert, K.; Gustafsson, A.; Wallenberg, L. R.; Samuelson, L. *Nano Lett.* **2004**, *4*, 1987–1990.
- (19) Bakkers, E. P. A. M.; van Dam, J. A.; De Franceschi, S.; Kouwenhoven, L. P.; Kaiser, M.; Verheijen, M.; Wondergem, H.; van der Sluis, P. *Nat. Mater.* **2004**, *3*, 769–773.
- (20) Wagner, R. S.; Ellis, W. C. *Appl. Phys. Lett.* **1964**, *4*, 89–90.
- (21) Bar-Sadan, M.; Barthel, J.; Shtrikman, H.; Houben, L. *Nano Lett.* **2012**, *12*, 2352–2356.
- (22) Ellis, W. C.; Frosch, C. J.; Zetterstrom, R. B. J. *Cryst. Growth* **1968**, *2*, 61–68.
- (23) Fontcuberta i Morral, A. *IEEE J. Sel. Top. Quantum Electron.* **2011**, *17*, 819–828.
- (24) Fontcuberta i Morral, A.; Colombo, C.; Abstreiter, G.; Arbiol, J.; Morante, J. R. *Appl. Phys. Lett.* **2008**, *92*, 063112–063113.
- (25) Krogstrup, P.; Popovitz-Biro, R.; Johnson, E.; Madsen, M. H.; Nygård, J.; Shtrikman, H. *Nano Lett.* **2010**, *10*, 4475–4482.
- (26) Munshi, A. M.; Dheeraj, D. L.; Todorovic, J.; van Helvoort, A. T. J.; Weman, H.; Fimland, B.-O. *J. Cryst. Growth* **2013**, *372*, 163–169.
- (27) Cirlin, G. E.; Dubrovskii, V. G.; Samsonenko, Y. B.; Bouravleuv, A. D.; Durose, K.; Proskuryakov, Y. Y.; Mendes, B.; Bowen, L.; Kaliteevski, M. A.; Abram, R. A.; Zeze, D. *Phys. Rev. B* **2010**, *82*, 035302.
- (28) Breuer, S.; Pfüller, C.; Flissikowski, T.; Brandt, O.; Grahn, H. T.; Geelhaar, L.; Riechert, H. *Nano Lett.* **2010**, *11*, 1276–1279.
- (29) Tomioka, K.; Mohan, P.; Noborisaka, J.; Hara, S.; Motohisa, J.; Fukui, T. *J. Cryst. Growth* **2007**, *298*, 644–647.
- (30) Bauer, B.; Rudolph, A.; Soda, M.; Fontcuberta i Morral, A.; Zweck, J.; Schuh, D.; Reiger, E. *Nanotechnology* **2010**, *21*, 435601.
- (31) Mårtensson, T.; Borgström, M.; Seifert, W.; Ohlsson, B. J.; Samuelson, L. *Nanotechnology* **2003**, *14*, 1255.
- (32) Plissard, S.; Dick, K. A.; Larrieu, G.; Godey, S.; Addad, A.; Wallart, X.; Caroff, P. *Nanotechnology* **2010**, *21*, 385602.
- (33) Plissard, S.; Larrieu, G.; Wallart, X.; Caroff, P. *Nanotechnology* **2011**, *22*, 275602.
- (34) Ghalamestani, S. G.; Johansson, S.; Borg, B. M.; Lind, E.; Dick, K. A.; Wernersson, L.-E. *Nanotechnology* **2012**, *23*, 015302.
- (35) Roest, A. L.; Verheijen, M. A.; Wunnicke, O.; Serafin, S.; Wondergem, H.; Bakkers, E. P. A. M. *Nanotechnology* **2006**, *17*, S271.
- (36) Tomioka, K.; Motohisa, J.; Hara, S.; Fukui, T. *Nano Lett.* **2008**, *8*, 3475–3480.
- (37) Fuhrmann, B.; Leipner, H. S.; Höche, H.-R.; Schubert, L.; Werner, P.; Gösele, U. *Nano Lett.* **2005**, *5*, 2524–2527.
- (38) Madaria, A. R.; Yao, M.; Chi, C.; Huang, N.; Lin, C.; Li, R.; Povinelli, M. L.; Dapkus, P. D.; Zhou, C. *Nano Lett.* **2012**, *12*, 2839–2845.
- (39) Kim, D. S.; Ji, R.; Fan, H. J.; Bertram, F.; Scholz, R.; Dadgar, A.; Nielsch, K.; Krost, A.; Christen, J.; Gösele, U.; Zacharias, M. *Small* **2007**, *3*, 76–80.
- (40) Mårtensson, T.; Carlberg, P.; Borgström, M.; Montelius, L.; Seifert, W.; Samuelson, L. *Nano Lett.* **2004**, *4*, 699–702.
- (41) Pierret, A.; Hocevar, M.; Diedenhofen, S. L.; Algra, R. E.; Vlieg, E.; Timmering, E. C.; Verschuuren, M. A.; Immink, G. W. G.; Verheijen, M. A.; Bakkers, E. P. A. M. *Nanotechnology* **2010**, *21*, 065305.
- (42) Haas, F.; Sladek, K.; Winden, A.; von der Ahe, M.; Weirich, T. E.; Rieger, T.; Lüth, H.; Grützmacher, D.; Schäfers, T.; Hardtdegen, H. *Nanotechnology* **2013**, *24*, 085603.
- (43) Hertenberger, S.; Funk, S.; Vizbaras, K.; Yadav, A.; Rudolph, D.; Becker, J.; Bolte, S.; Döblinger, M.; Bichler, M.; Scarpa, G.; Lugli, P.; Zardo, I.; Finley, J. J.; Amann, M.-C.; Abstreiter, G.; Koblmüller, G. *Appl. Phys. Lett.* **2012**, *101*, 043116.
- (44) Krogstrup, P.; Jørgensen, H. I.; Johnson, E.; Madsen, M. H.; Sørensen, C. B.; Fontcuberta i Morral, A.; Aagesen, M.; Nygård, J.; Glas, F. J. *Phys. D: Appl. Phys.* **2013**, *46*, 313001.
- (45) Uccelli, E.; Arbiol, J.; Magen, C.; Krogstrup, P.; Russo-Averchi, E.; Heiss, M.; Mugny, G.; Morier-Genoud, F. o.; Nygård, J.; Morante, J. R.; Fontcuberta i Morral, A. *Nano Lett.* **2011**, *11*, 3827–3832.
- (46) Xue, K.; Xu, J. B.; Ho, H. P. *Nanotechnology* **2007**, *18*, 485709.
- (47) Gibson, S.; LaPierre, R. *Phys. Status Solidi RRL* **2013**, *7*, 845–849.
- (48) Colombo, C.; Spirkoska, D.; Frimmer, M.; Abstreiter, G.; Fontcuberta i Morral, A. *Phys. Rev. B* **2008**, *77*, 155326.
- (49) Rieger, T.; Heiderich, S.; Lenk, S.; Lepsa, M. I.; Grützmacher, D. *J. Cryst. Growth* **2012**, *353*, 39–46.
- (50) Krogstrup, P.; Curiotto, S.; Johnson, E.; Aagesen, M.; Nygård, J.; Chatain, D. *Phys. Rev. Lett.* **2011**, *106*, 125505.
- (51) Glas, F.; Harmand, J.-C.; Patriarche, G. *Phys. Rev. Lett.* **2007**, *99*, 146101.
- (52) Biermanns, A.; Breuer, S.; Davydok, A.; Geelhaar, L.; Pietsch, U. *Phys. Status Solidi RRL* **2011**, *5*, 156–158.
- (53) Biermanns, A.; Breuer, S.; Trampert, A.; Davydok, A.; Geelhaar, L.; Pietsch, U. *Nanotechnology* **2012**, *23*, 305703.
- (54) Carim, A. H.; Bhattacharyya, A. *Appl. Phys. Lett.* **1985**, *46*, 872–874.
- (55) Titova, L. V.; Hoang, T. B.; Jackson, H. E.; Smith, L. M.; Yarrison-Rice, J. M.; Kim, Y.; Joyce, H. J.; Tan, H. H.; Jagadish, C. *Appl. Phys. Lett.* **2006**, *89*, 173126.
- (56) Jiang, N.; Gao, Q.; Parkinson, P.; Wong-Leung, J.; Mokkalapati, S.; Breuer, S.; Tan, H. H.; Zheng, C. L.; Etheridge, J.; Jagadish, C. *Nano Lett.* **2013**, *13*, 5135–5140.
- (57) Ahtapodov, L.; Todorovic, J.; Olk, P.; Mjåland, T.; Slättnes, P.; Dheeraj, D. L.; van Helvoort, A. T. J.; Fimland, B.-O.; Weman, H. *Nano Lett.* **2012**, *12*, 6090–6095.



# Position-Controlled Uniform GaAs Nanowires on Silicon using Nanoimprint Lithography

A. M. Munshi,<sup>†</sup> D. L. Dheeraj,<sup>†</sup> V. T. Fauske,<sup>‡</sup> D. C. Kim,<sup>†,⊥</sup> J. Huh,<sup>†</sup> J. F. Reinertsen,<sup>†</sup> L. Ahtapodov,<sup>†</sup>

K. D. Lee,<sup>§</sup> B. Heidari,<sup>§</sup> A. T. J. van Helvoort,<sup>‡</sup> B. O. Fimland,<sup>†</sup> and H. Weman<sup>†,\*</sup>

<sup>†</sup>*Department of Electronics and Telecommunications, Norwegian University of Science and  
Technology (NTNU), NO-7491 Trondheim, Norway*

<sup>‡</sup>*Department of Physics, Norwegian University of Science and Technology (NTNU), NO-7491  
Trondheim, Norway*

<sup>⊥</sup>*CrayoNano AS, Otto Nielsens vei 12, NO-7052 Trondheim, Norway*

<sup>§</sup>*Obducat Technologies AB, Scheelevägen 2, SE-22363 Lund, Sweden*

<sup>\*</sup>*Corresponding Author. E-mail: [helge.weman@ntnu.no](mailto:helge.weman@ntnu.no)*

## S1. Methods

### S1.1 Nanoimprint lithography

An Obducat Eitre 6 NanoImprinter with a thermal and UV module and anti-adhesion coated Si stamp was used in this study. The entire process flow to produce a nanohole array in a SiO<sub>2</sub> mask layer is schematically illustrated in Figure 1 in the Letter. First, the SiO<sub>2</sub>/Si wafer is spin-coated with a double-layer resist, consisting of polymethyl methacrylate (PMMA) and TU-7 imprint resist with an optimized thickness of 50 nm and 105 nm, respectively. The patterns of the Si stamp are first replicated onto the intermediate polymer stamp (IPS), and then the IPS is used to transfer the patterns to the TU-7 resist by simultaneous thermal and UV NIL process. Then O<sub>2</sub> reactive plasma etching (RIE) is used to etch out the hole pattern in the residual TU-7 and PMMA layers. Using a wet chemical etching with a buffered oxide etch (BOE), the SiO<sub>2</sub> is removed from the resist openings. Finally, the resist layers are stripped, resulting in a nanohole pattern on the SiO<sub>2</sub>/Si wafer as shown in Figure S1.

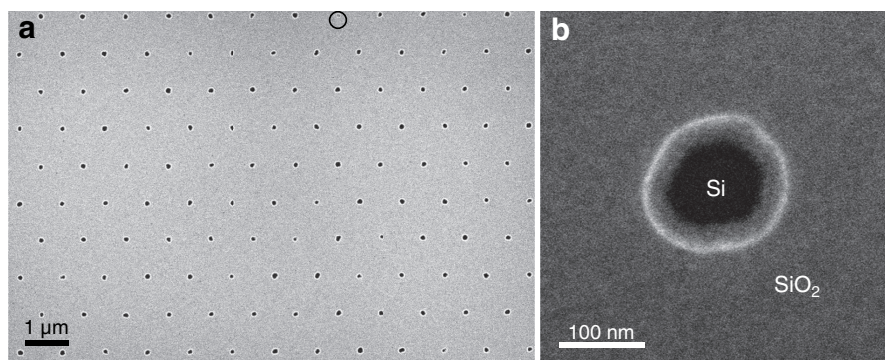


**Figure S1.** (a) SEM image of a NIL patterned nanohole array with hexagonal symmetry on a thermally grown SiO<sub>2</sub> covered Si substrate. Due to the limitations of the O<sub>2</sub> RIE step to remove the residual TU-7 and PMMA layers, the nanohole fabrication process is still sub-optimal. In some cases, this results in unsuccessful holes (black circle in **a**), or holes but with differences in their sizes. (b) Magnified view of a hole with a size of about 100 nm in a SiO<sub>2</sub> mask of thickness of about 40 nm. The Si and SiO<sub>2</sub> surfaces can be distinguished in the SEM due to differences in their contrast as indicated in **b**.

### S1.2 Nanowire growth

A solid-source Varian Gen II Modular MBE system equipped with a dual filament Ga cell and an As valved cracker cell was used for the growth of the NWs. The cracker of the As cell allowed the adjustment of the proportion of As dimers (As<sub>2</sub>) and tetramers (As<sub>4</sub>) as required in this study. After patterning the SiO<sub>2</sub>/Si substrates by NIL, a 20 s hydrofluoric (1% HF) acid treatment was used just before loading the substrates into the MBE. In order to optimize the yield of vertical NWs, several series of samples were grown by varying the Ga predeposition time, Ga flux, As<sub>2</sub> flux, growth temperature, and annealing treatment before the NW growth. In addition, a series of samples were

grown for different durations using both  $\text{As}_2$  and  $\text{As}_4$  at two different growth temperatures to investigate the evolution of NW length and diameter. The study was carried out by varying one of the parameters over a suitable range keeping all the other parameters constant. The same approach was then used with the next parameter after selecting the optimum values from the previous parameter study keeping other parameters constant. Finally, NIL positioned heterostructured GaAs/AlGaAs core-shell NWs were grown in order to address their optical properties.

## S2. Effect of Ga flux on the yield

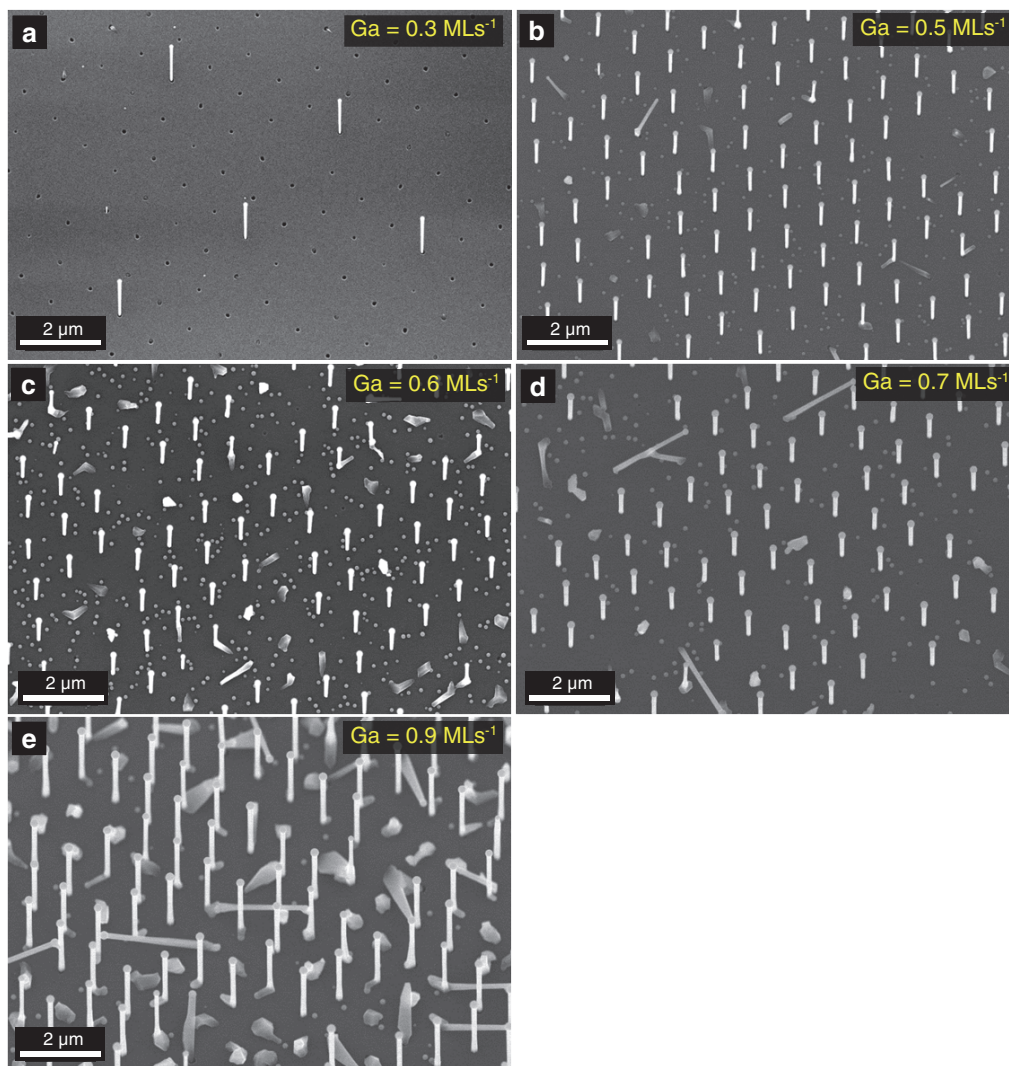


**Figure S2.** Tilted-view SEM images of GaAs NW arrays grown with Ga rate (a)  $0.3 \text{ MLs}^{-1}$ , (b)  $0.5 \text{ MLs}^{-1}$ , (c)  $0.6 \text{ MLs}^{-1}$ , (d)  $0.7 \text{ MLs}^{-1}$ , (e)  $0.9 \text{ MLs}^{-1}$  under a constant  $\text{As}_2$  flux of  $5.0 \times 10^{-6}$  Torr and at a substrate temperature of  $640 \text{ }^\circ\text{C}$ .

### S3. Ga predeposition at 640 °C

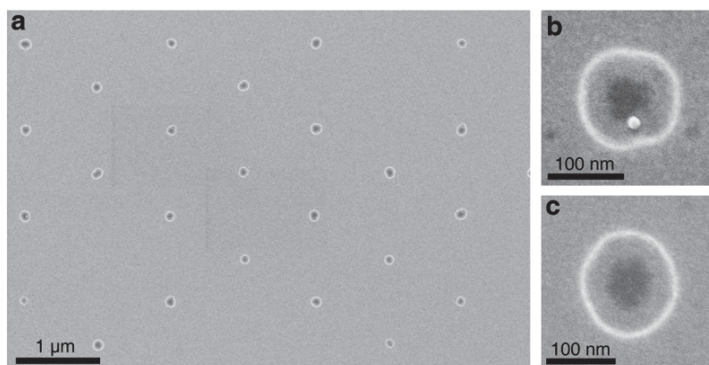


**Figure S3.** (a) SEM image after a Ga predeposition step at a temperature of 640 °C. (b,c) Magnified SEM images showing the (b) presence and (c) absence of a Ga droplet in the hole.

### S4. Ga predeposition at 630 °C - Effect of hole size

The hole size was varied by etching the substrate in hydrofluoric (1% HF) acid for 200 s before loading it into the molecular beam epitaxy (MBE) system.

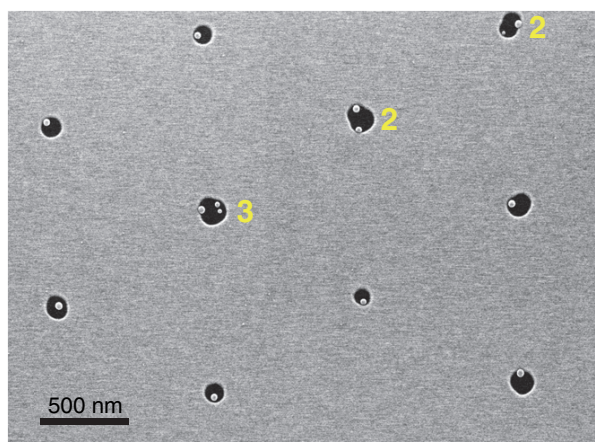


**Figure S4.** SEM image showing a varying number of Ga droplets formation in a hole when a longer HF etching step was applied. Here more than one droplet is indicated by “2” and “3”. Diameters of the holes are ~140 nm for double droplets and ~150 nm for triple droplets.

### S5. Effect of Ga predeposition time on the yield

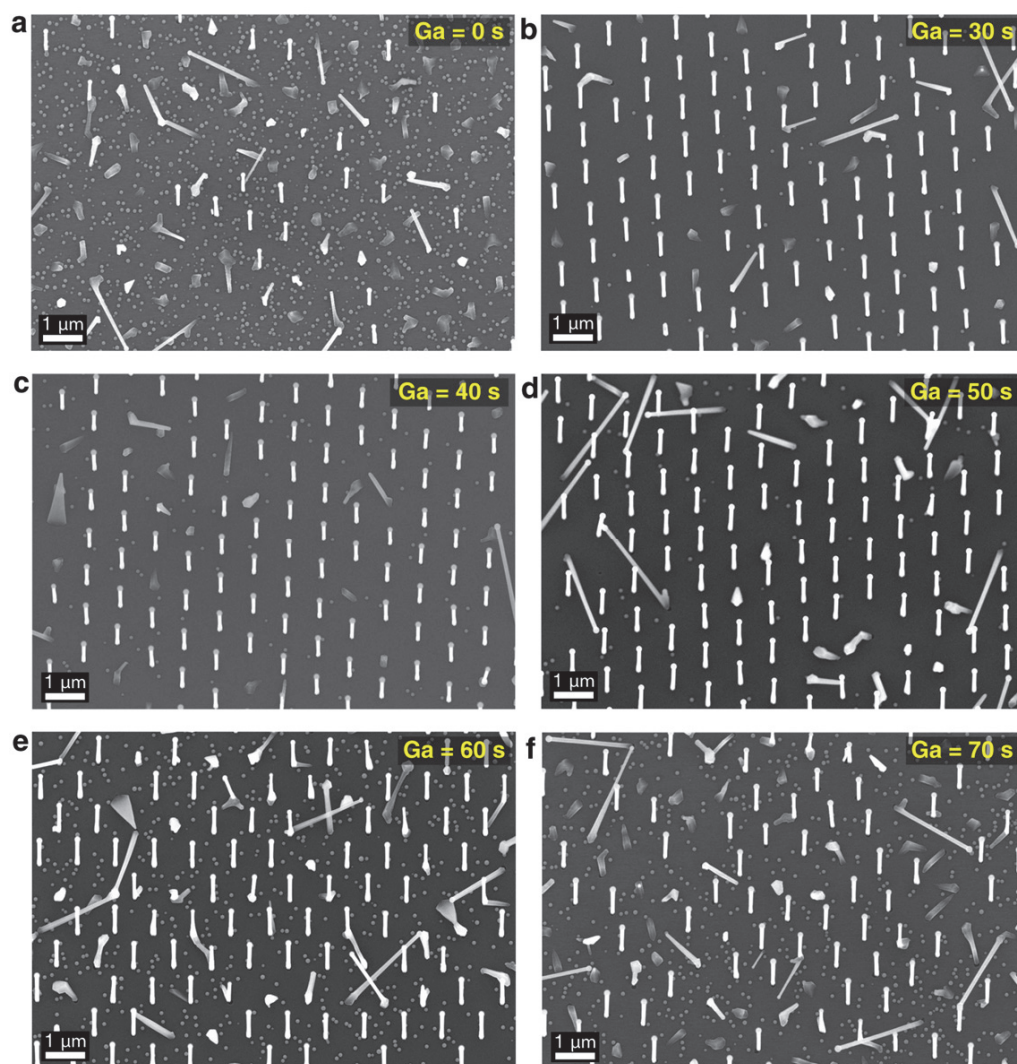


**Figure S5.** Tilted-view SEM images of GaAs NWs grown with Ga predeposition time (a) 0 s, (b) 30 s, (c) 40 s, (d) 50 s, (e) 60 s, (f) 70 s with a Ga rate of  $0.6 \text{ MLs}^{-1}$  and  $\text{As}_2$  flux of  $5.0 \times 10^{-6} \text{ Torr}$  for a growth temperature of  $630 \text{ }^\circ\text{C}$ .

S6. Effect of As<sub>2</sub> flux on the yield

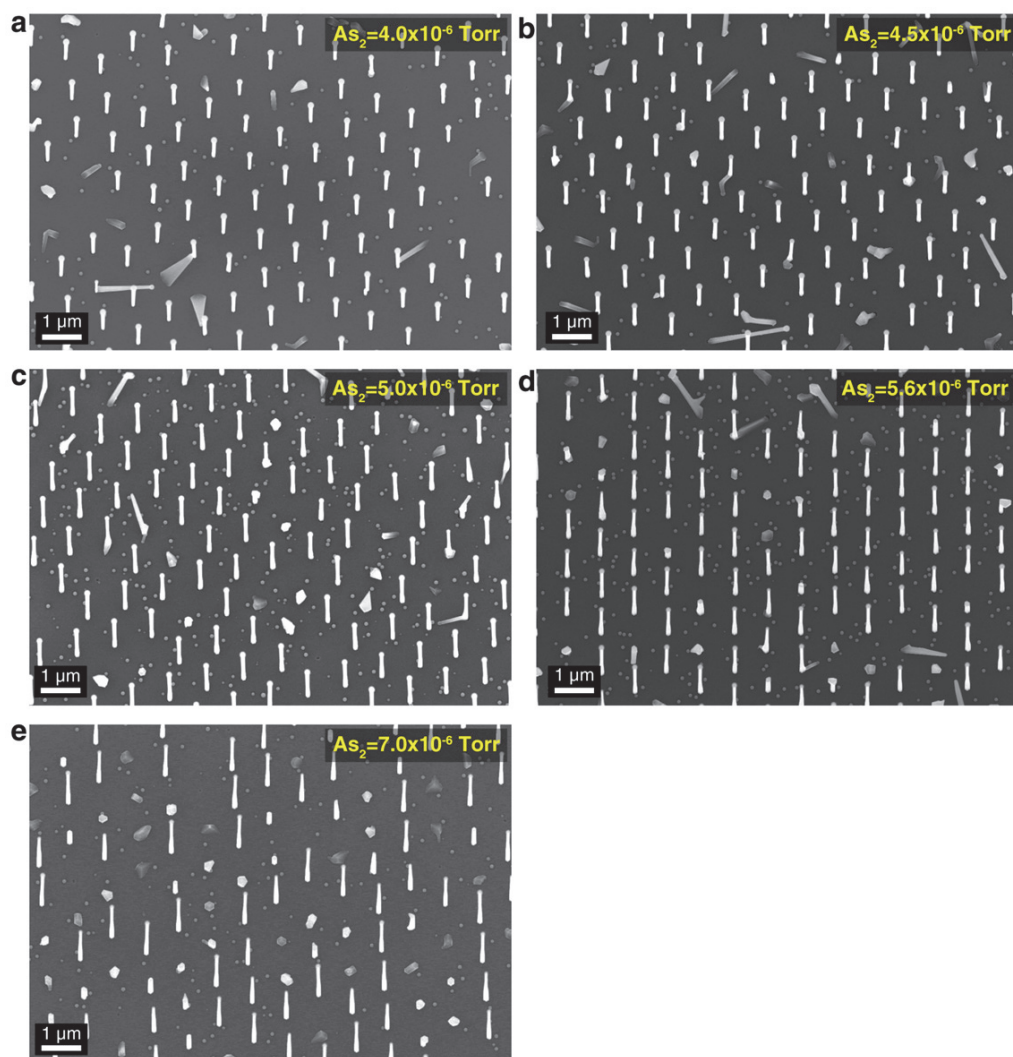


**Figure S6.** Tilted-view SEM images of GaAs NWs grown with an As<sub>2</sub> flux of (a) 4.0 × 10<sup>-6</sup> Torr, (b) 4.5 × 10<sup>-6</sup> Torr, (c) 5.0 × 10<sup>-6</sup> Torr, (d) 5.6 × 10<sup>-6</sup> Torr, and (e) 7.0 × 10<sup>-6</sup> Torr with a Ga rate of 0.6 MLs<sup>-1</sup>, 50 s predeposition at 630 °C.

### S7. Effect of not annealing Si substrate before growth



**Figure S7.** Tilted-view SEM image of GaAs NWs grown without an annealing step prior to the NW growth, showing a substantial reduction in the yield. Apart from the substrate annealing treatment, all other growth conditions were the same that result in a yield of  $\sim 80\%$ , i.e. Ga predeposition time of 50 s, Ga rate of  $0.6 \text{ MLs}^{-1}$  and  $\text{As}_2$  flux of  $5.0 \times 10^{-6} \text{ Torr}$  for at a growth temperature of  $630 \text{ }^\circ\text{C}$ .

S8. Time series at 630 °C with As<sub>2</sub>

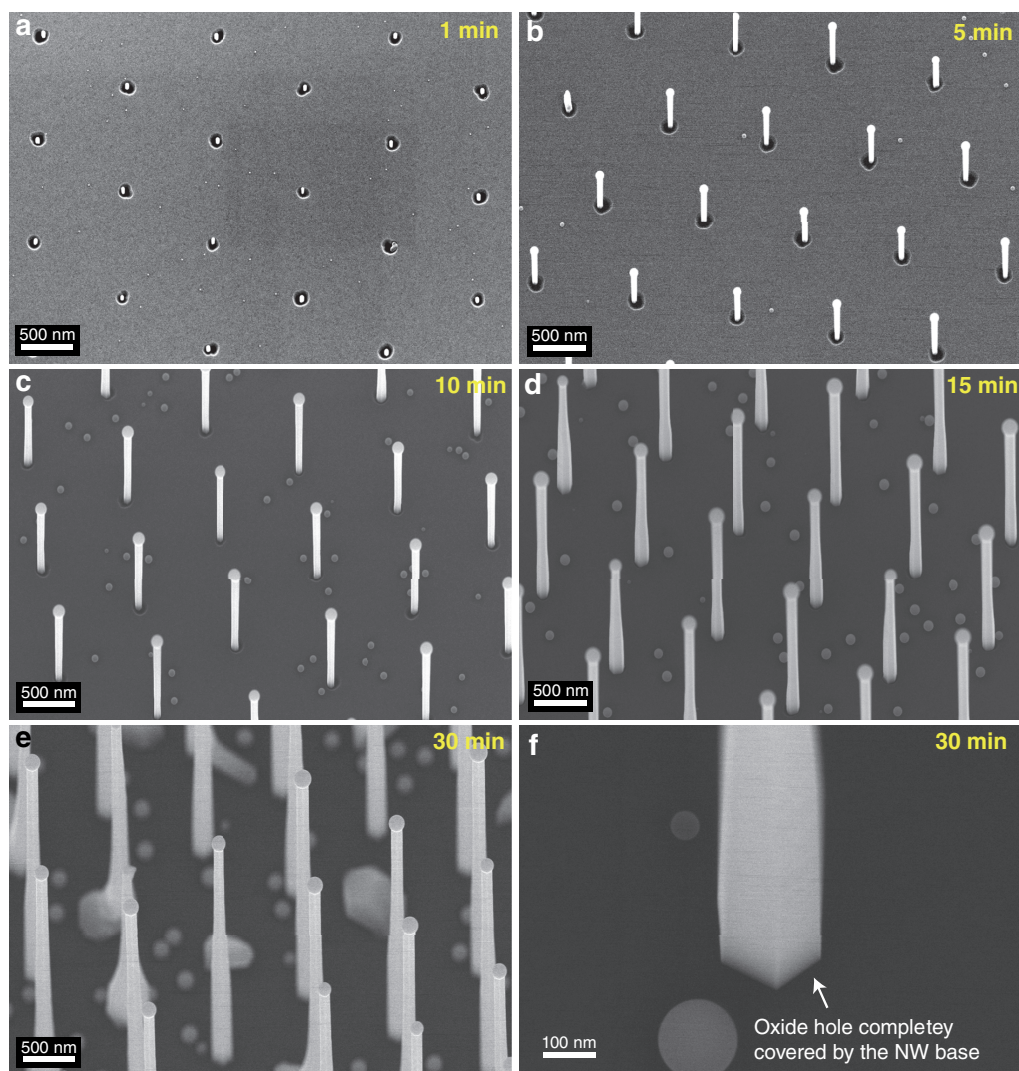


**Figure S8.1.** (a-e) SEM images (20° tilt angle) of GaAs NWs grown at 630 °C with As<sub>2</sub> for durations of (a) 1, (b) 5, (c) 10, (d) 15 (same as Figure 3b in the Letter) and (e) 30 min. (f) Magnified SEM image of the base of a GaAs NW from e, showing that the NW base fully covers the oxide hole and extends over the oxide mask.



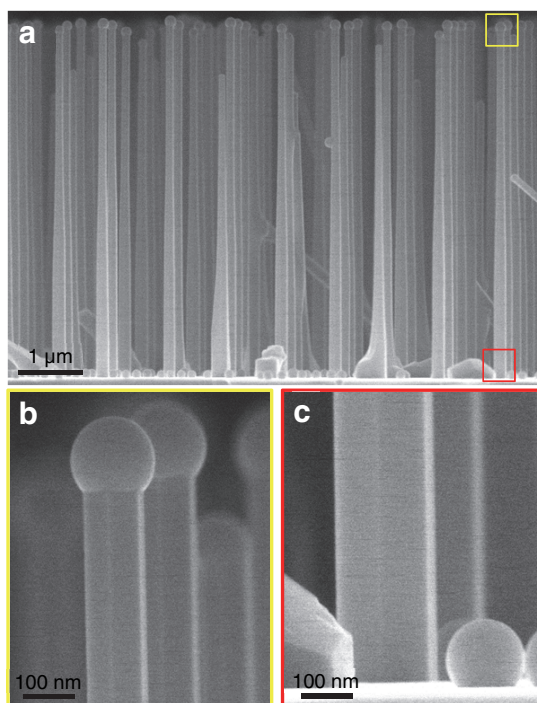


**Figure S8.2.** (a) Side-view SEM image of GaAs NWs grown for 30 min with  $\text{As}_2$  at a growth temperature of 630 °C. (b,c) Magnified-view of (b) the tip and (c) the base of the NW in **a** showing a tapered ( $\sim 1.4\%$ ) morphology.

### S9. Time series at 640 °C with $\text{As}_2$

GaAs NWs were grown for durations of 1, 5, 10, 15 and 30 min at 640 °C with  $\text{As}_2$  flux. This series should elucidate the effect of a higher growth temperature on the developments of diameter and length with time. The length and diameter of the NWs are measured from side-view SEM images for each sample and are plotted in Figure S10 as a function of growth duration. It can be seen that both diameter and length of the NWs are increasing linearly with growth time. It was noticed that the axial growth rate of the NWs grown at 640 °C ( $\sim 165$  nm/min) is slightly lower than that at 630 °C ( $\sim 185$  nm/min). This again indicates a higher material desorption at 640 °C.

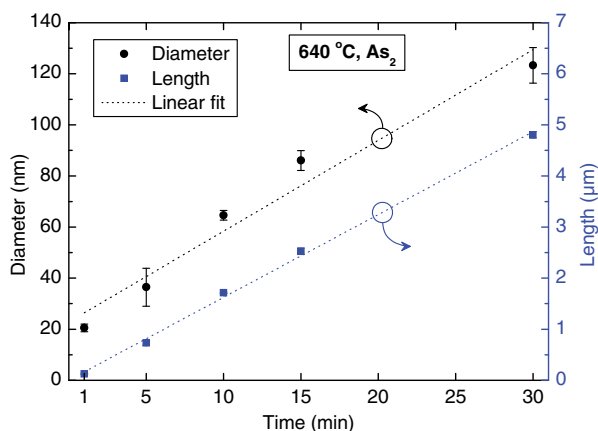


**Figure S9.1.** Plot of GaAs NW diameter and length with growth time at 640 °C using  $\text{As}_2$ . The increase in the NW diameter is found to be similar to that at 630 °C shown in Figure 7 in the Letter. The diameter was measured at the middle part of the NW. Error bars in the data represent standard deviation in the length and diameter from their mean values.

A side-view SEM image of a NW array grown for 30 min is shown in Figure 11a, revealing the uniformity in the length and diameter of the NWs. Figure 11b,c shows the magnified side-view SEM image of the top and bottom parts of the NWs in Figure 11a. For this growth duration, it is again evident that the radial growth at the bottom part of the NWs in Figure 11c has extended on top of the oxide without introducing any noticeable defects or change in morphology.

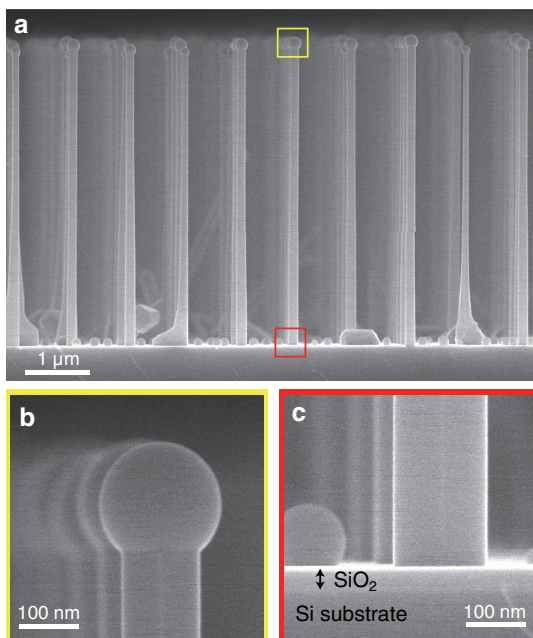


**Figure 9.2.** (a) Side-view SEM image of GaAs NWs grown for 30 min with  $\text{As}_2$  at a growth temperature of 640 °C. (b,c) Magnified-view of (b) the tip and (c) the base of the NW in (a) showing a slightly tapered ( $\sim 0.7\%$ ) morphology. The radial growth of the NWs has extended on top of the oxide.

### S10. Time series at 640 °C with As<sub>4</sub>

GaAs NWs were grown for durations of 1, 5, and 10 min at 640 °C with As<sub>4</sub> instead of As<sub>2</sub> by reducing the As cracker temperature from 900 °C to 600 °C. It is believed that the diffusion length of Ga is shorter under As<sub>2</sub> than under As<sub>4</sub>, resulting in an increased radial growth in the former case and an increased axial growth in the latter, as was observed in GaAs NWs grown by Au-assisted MBE.<sup>1</sup>

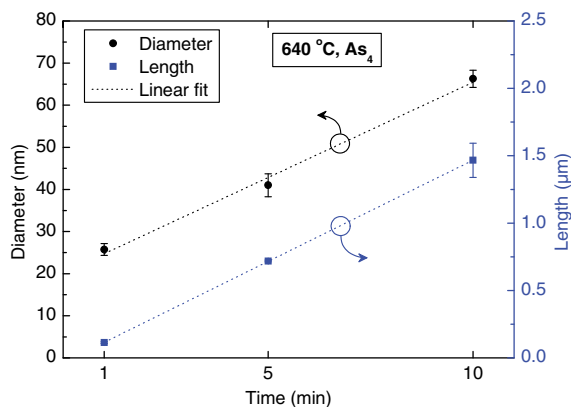


**Figure S10.** Plot of NW diameter and length with growth time at 640 °C with As<sub>4</sub>. The increase in the NW diameter is found to be similar to that with As<sub>2</sub> (Figure S10). Error bars in the data represent standard deviation in the length and diameter from their mean values.

### Supporting references

- (1) Sartel, C.; Dheeraj, D. L.; Jabeen, F.; Harmand, J. C. *J. Cryst. Growth* **2010**, *312*, 2073-2077.

## 7 References

- [1] D. M. Chapin, C. S. Fuller, G. L. Pearson, A new silicon p-n junction photocell for converting solar radiation into electrical power. *J. Appl. Phys.* **25**, 676 (1954).
- [2] S. W. Glunz, R. Preu, D. Biro, 1.16 - Crystalline silicon solar cells: state-of-the-art and future developments. *Comprehensive Renewable Energy* **1**, 353 (2012).
- [3] Y. Hamakawa, Thin-film solar cells: Next generation photovoltaics and its applications. *Springer Series in Photonics, Vol. 13*, (2004).
- [4] A. Morales-Acevedo, G. Casados-Cruz, Forecasting the development of different solar cell technologies. *International J. Photoenergy* **2013**, 1 (2013).
- [5] M. Green, Third generation photovoltaics: Advanced solar energy conversion. *Springer Series in Photonics, Vol. 12*, (2003).
- [6] World record solar cell with 44.7% efficiency. *Press Release, Sept 23, 2013* [http://www.ise.fraunhofer.de/en/press-and-media/press-releases/presseinformationen-2013/world-record-solar-cell-with-44.7-efficiency?set\\_language=en](http://www.ise.fraunhofer.de/en/press-and-media/press-releases/presseinformationen-2013/world-record-solar-cell-with-44.7-efficiency?set_language=en).
- [7] A. Luque, A. Martí, Increasing the Efficiency of Ideal Solar Cells by Photon Induced Transitions at Intermediate Levels. *Phys. Rev. Lett.* **78**, 5014 (1997).
- [8] A. Luque, A. Marti, C. Stanley, Understanding intermediate-band solar cells. *Nature Photon.* **6**, 146 (2012).
- [9] A. J. Nozik, Quantum dot solar cells. *Physica E* **14**, 115 (2002).
- [10] R. T. Ross, A. J. Nozik, Efficiency of hot-carrier solar energy converters. *J. Appl. Phys.* **53**, 3813 (1982).
- [11] T. Trupke, M. A. Green, P. Würfel, Improving solar cell efficiencies by up-conversion of sub-band-gap light. *J. Appl. Phys.* **92**, 4117 (2002).
- [12] T. Trupke, M. A. Green, P. Würfel, Improving solar cell efficiencies by down-conversion of high-energy photons. *J. Appl. Phys.* **92**, 1668 (2002).
- [13] G. F. Brown, J. Wu, Third generation photovoltaics. *Laser & Photon. Rev.* **3**, 394 (2009).
- [14] R. Yu, Q. Lin, S.-F. Leung, Z. Fan, Nanomaterials and nanostructures for efficient light absorption and photovoltaics. *Nano Energy* **1**, 57 (2012).
- [15] T. J. Kempa, R. W. Day, S.-K. Kim, H.-G. Park, C. M. Lieber, Semiconductor nanowires: a platform for exploring limits and concepts for nano-enabled solar cells. *Energy Environ. Sci.* **6**, 719 (2013).
- [16] E. C. Garnett, M. L. Brongersma, Y. Cui, M. D. McGehee, Nanowire solar cells. *Annu. Rev. Mater. Res.* **41**, 269 (2011).

- [17] S. Ke, A. Kargar, P. Namsoek, K. N. Madsen, P. W. Naughton, T. Bright, Y. Jing, D. Wang, Compound semiconductor nanowire solar cells. *IEEE J. Sel. Top. Quantum Electron.* **17**, 1033 (2011).
- [18] R. Yan, D. Gargas, P. Yang, Nanowire photonics. *Nature Photon.* **3**, 569 (2009).
- [19] P. Yang, R. Yan, M. Fardy, Semiconductor nanowire: what's next? *Nano Lett.* **10**, 1529 (2010).
- [20] H. J. Joyce, Q. Gao, H. H. Tan, C. Jagadish, Y. Kim, J. Zou, L. M. Smith, H. E. Jackson, J. M. Yarrison-Rice, P. Parkinson, M. B. Johnston, III–V semiconductor nanowires for optoelectronic device applications. *Prog. Quantum Electron.* **35**, 23 (2011).
- [21] J. K. Hyun, S. Zhang, L. J. Lauhon, Nanowire heterostructures. *Annu. Rev. Mater. Res.* **43**, 451 (2013).
- [22] F. Glas, Critical dimensions for the plastic relaxation of strained axial heterostructures in free-standing nanowires. *Phys. Rev. B* **74**, 121302 (2006).
- [23] K. L. Kavanagh, Misfit dislocations in nanowire heterostructures. *Semicond. Sci. Technol.* **25**, 024006 (2010).
- [24] S. L. Diedenhofen, O. T. A. Janssen, G. Grzela, E. P. A. M. Bakkers, J. Gómez Rivas, Strong geometrical dependence of the absorption of light in arrays of semiconductor nanowires. *ACS Nano* **5**, 2316 (2011).
- [25] K. Seo, M. Wober, P. Steinvurzel, E. Schonbrun, Y. Dan, T. Ellenbogen, K. B. Crozier, Multicolored vertical silicon nanowires. *Nano Lett.* **11**, 1851 (2011).
- [26] L. Cao, J.-S. Park, P. Fan, B. Clemens, M. L. Brongersma, Resonant germanium nanoantenna photodetectors. *Nano Lett.* **10**, 1229 (2010).
- [27] O. L. Muskens, J. G. Rivas, R. E. Algra, E. P. A. M. Bakkers, A. Lagendijk, Design of light scattering in nanowire materials for photovoltaic applications. *Nano Lett.* **8**, 2638 (2008).
- [28] E. D. Kosten, E. L. Warren, H. A. Atwater, Ray optical light trapping in silicon microwires: Exceeding the  $2n^2$  intensity limit. *Opt. Express* **19**, 3316 (2011).
- [29] P. Krogstrup, H. I. Jorgensen, M. Heiss, O. Demichel, J. V. Holm, M. Aagesen, J. Nygård, A. Fontcuberta i Morral, Single-nanowire solar cells beyond the Shockley-Queisser limit. *Nature Photon.* **7**, 306 (2013).
- [30] B. M. Kayes, H. A. Atwater, N. S. Lewis, Comparison of the device physics principles of planar and radial p-n junction nanorod solar cells. *J. Appl. Phys.* **97**, (2005).
- [31] M. T. Borgström, J. Wallentin, M. Heurlin, S. Fält, P. Wickert, J. Leene, M. H. Magnusson, K. Deppert, L. Samuelson, Nanowires with promise for photovoltaics. *IEEE J. Sel. Top. Quantum Electron.* **17**, 1050 (2011).

- [32] G. Mariani, A. C. Scofield, C.-H. Hung, D. L. Huffaker, GaAs nanopillar-array solar cells employing in situ surface passivation. *Nature Commun.* **4**, 1497 (2013).
- [33] J. Wallentin, N. Anttu, D. Asoli, M. Huffman, I. Åberg, M. H. Magnusson, G. Siefer, P. Fuss-Kailuweit, F. Dimroth, B. Witzigmann, H. Q. Xu, L. Samuelson, K. Deppert, M. T. Borgström, InP nanowire array solar cells achieving 13.8% efficiency by exceeding the ray optics limit. *Science* **339**, 1057 (2013).
- [34] D. E. Perea, J. E. Allen, S. J. May, B. W. Wessels, D. N. Seidman, L. J. Lauhon, Three-dimensional nanoscale composition mapping of semiconductor nanowires. *Nano Lett.* **6**, 181 (2006).
- [35] M. Bar-Sadan, J. Barthel, H. Shtrikman, L. Houben, Direct imaging of single Au atoms within GaAs nanowires. *Nano Lett.* **12**, 2352 (2012).
- [36] J. E. Allen, E. R. Hemesath, D. E. Perea, J. L. Lensch-Falk, LiZ.Y, F. Yin, M. H. Gass, P. Wang, A. L. Bleloch, R. E. Palmer, L. J. Lauhon, High-resolution detection of Au catalyst atoms in Si nanowires. *Nature Nanotech.* **3**, 168 (2008).
- [37] A. Fontcuberta i Morral, C. Colombo, G. Abstreiter, J. Arbiol, J. R. Morante, Nucleation mechanism of gallium-assisted molecular beam epitaxy growth of gallium arsenide nanowires. *Appl. Phys. Lett.* **92**, 063112 (2008).
- [38] J. H. Paek, T. Nishiwaki, M. Yamaguchi, N. Sawaki, Catalyst free MBE-VLS growth of GaAs nanowires on (111)Si substrate. *Phys. Status Solidi C* **6**, 1436 (2009).
- [39] S. Plissard, K. A. Dick, X. Wallart, P. Caroff, Gold-free GaAs/GaAsSb heterostructure nanowires grown on silicon. *Appl. Phys. Lett.* **96**, 121901 (2010).
- [40] M. Murayama, T. Nakayama, Chemical trend of band offsets at wurtzite/zincblende heterocrystalline semiconductor interfaces. *Phys. Rev B* **49**, 4710 (1994).
- [41] A. De, C. E. Pryor, Predicted band structures of III-V semiconductors in the wurtzite phase. *Phys. Rev B* **81**, 155210 (2010).
- [42] T. Akiyama, T. Yamashita, K. Nakamura, T. Ito, Band alignment tuning in twin-plane superlattices of semiconductor nanowires. *Nano Lett.* **10**, 4614 (2010).
- [43] J. Wallentin, M. Ek, L. R. Wallenberg, L. Samuelson, M. T. Borgström, Electron trapping in InP nanowire FETs with stacking faults. *Nano Lett.* **12**, 151 (2011).
- [44] C. Thelander, P. Caroff, S. b. Plissard, A. W. Dey, K. A. Dick, Effects of crystal phase mixing on the electrical properties of InAs nanowires. *Nano Lett.* **11**, 2424 (2011).

- [45] P. Parkinson, H. J. Joyce, Q. Gao, H. H. Tan, X. Zhang, J. Zou, C. Jagadish, L. M. Herz, M. B. Johnston, Carrier lifetime and mobility enhancement in nearly defect-free core-shell nanowires measured using time-resolved terahertz spectroscopy. *Nano Lett.* **9**, 3349 (2009).
- [46] M. D. Schroer, J. R. Petta, Correlating the nanostructure and electronic properties of InAs nanowires. *Nano Lett.* **10**, 1618 (2010).
- [47] A. K. Geim, Graphene: status and prospects. *Science* **324**, 1530 (2009).
- [48] K. S. Novoselov, V. I. Falko, L. Colombo, P. R. Gellert, M. G. Schwab, K. Kim, A roadmap for graphene. *Nature* **490**, 192 (2012).
- [49] W. I. Park, C.-H. Lee, J. M. Lee, N.-J. Kim, G.-C. Yi, Inorganic nanostructures grown on graphene layers. *Nanoscale* **3**, 3522 (2011).
- [50] H. Park, S. Chang, J. Jean, J. J. Cheng, P. T. Araujo, M. Wang, M. G. Bawendi, M. S. Dresselhaus, V. Bulović, J. Kong, S. Gradečak, Graphene cathode-based ZnO nanowire hybrid solar cells. *Nano Lett.* **13**, 233 (2013).
- [51] P. K. Mohseni, A. Behnam, J. D. Wood, X. Zhao, K. J. Yu, N. C. Wang, A. Rockett, J. A. Rogers, J. W. Lyding, E. Pop, X. Li, Monolithic III-V nanowire solar cells on graphene via direct van der Waals epitaxy. *Adv. Mater.*, DOI: 10.1002/adma.201305909 (2014).
- [52] D. L. Dheeraj, G. Patriarche, H. Zhou, T. B. Hoang, A. F. Moses, S. Grønsberg, A. T. J. van Helvoort, B.-O. Fimland, H. Weman, Growth and characterization of wurtzite GaAs nanowires with defect-free zinc blende GaAsSb inserts. *Nano Lett.* **8**, 4459 (2008).
- [53] C. Yiyang, W. Zhiming, N. Jianchao, A. B. Waseem, L. Jing, L. Shuping, H. Kai, K. Junyong, Type-II core/shell nanowire heterostructures and their photovoltaic applications. *Nano-Micro Lett.* **4**, 135 (2012).
- [54] M. E. Pistol, C. E. Pryor, Band structure of segmented semiconductor nanowires. *Phys. Rev B* **80**, 035316 (2009).
- [55] E. Dimakis, M. Ramsteiner, A. Tahraoui, H. Riechert, L. Geelhaar, Shell-doping of GaAs nanowires with Si for n-type conductivity. *Nano Res.* **5**, 796 (2012).
- [56] S. Breuer, C. Pfüller, T. Flissikowski, O. Brandt, H. T. Grahn, L. Geelhaar, H. Riechert, Suitability of Au- and self-assisted GaAs nanowires for optoelectronic applications. *Nano Lett.* **11**, 1276 (2010).
- [57] Y. A. Du, S. Sakong, P. Kratzer, As vacancies, Ga antisites, and Au impurities in zinc blende and wurtzite GaAs nanowire segments from first principles. *Phys. Rev. B* **87**, 075308 (2013).
- [58] R. S. Wagner, W. C. Ellis, Vapor-liquid-solid mechanism of single crystal growth. *Appl. Phys. Lett.* **4**, 89 (1964).
- [59] N. Holonyak Jr., C. M. Wolfe, J. S. Moore, Vapor-liquid-solid growth of gallium phosphide. *Appl. Phys. Lett.* **6**, 64 (1965).

- [60] K. Hiruma, T. Katsuyama, K. Ogawa, M. Koguchi, H. Kakibayashi, G. P. Morgan, Quantum size microcrystals grown using organometallic vapor phase epitaxy. *Appl. Phys. Lett.* **59**, 431 (1991).
- [61] M. Yazawa, M. Koguchi, K. Hiruma, Heteroepitaxial ultrafine wire-like growth of InAs on GaAs substrates. *Appl. Phys. Lett.* **58**, 1080 (1991).
- [62] M. Koguchi, H. Kakibayashi, M. Yazawa, K. Hiruma, T. Katsuyama, Crystal structure change of GaAs and InAs whiskers from zinc-blende to wurtzite type. *Jpn. J. Appl. Phys.* **31**, 2061 (1992).
- [63] Z. H. Wu, X. Y. Mei, D. Kim, M. Blumin, H. E. Ruda, Growth of Au-catalyzed ordered GaAs nanowire arrays by molecular-beam epitaxy. *Appl. Phys. Lett.* **81**, 5177 (2002).
- [64] J. C. Harmand, G. Patriarche, N. Péré-Laperne, M.-N. Mérat-Combes, L. Travers, F. Glas, Analysis of vapor-liquid-solid mechanism in Au-assisted GaAs nanowire growth. *Appl. Phys. Lett.* **87**, 203101 (2005).
- [65] B. J. Ohlsson, M. T. Björk, M. H. Magnusson, K. Deppert, L. Samuelson, L. R. Wallenberg, Size-, shape-, and position-controlled GaAs nano-whiskers. *Appl. Phys. Lett.* **79**, 3335 (2001).
- [66] B. J. Ohlsson, M. T. Björk, A. I. Persson, C. Thelander, L. R. Wallenberg, M. H. Magnusson, K. Deppert, L. Samuelson, Growth and characterization of GaAs and InAs nano-whiskers and InAs/GaAs heterostructures. *Physica E* **13**, 1126 (2002).
- [67] W. C. Ellis, C. J. Frosch, R. B. Zetterstrom, Morphology of gallium phosphide crystals grown by VLS mechanism with gallium as liquid-forming agent. *J. Cryst. Growth* **2**, 61 (1968).
- [68] E. Alarcón-Lladó, S. Conesa-Boj, X. Wallart, P. Caroff, A. Fontcuberta i Morral, Raman spectroscopy of self-catalyzed GaAs<sub>1-x</sub>Sb<sub>x</sub> nanowires grown on silicon. *Nanotechnology* **24**, 405707 (2013).
- [69] S. Conesa-Boj, D. Kriegner, X.-L. Han, S. Plissard, X. Wallart, J. Stangl, A. Fontcuberta i Morral, P. Caroff, Gold-free ternary III-V antimonide nanowire arrays on silicon: Twin-free down to the first bilayer. *Nano Lett.* **14**, 326 (2013).
- [70] T. Rieger, M. I. Lepsa, T. Schäpers, D. Grützmacher, Controlled wurtzite inclusions in self-catalyzed zinc blende III-V semiconductor nanowires. *J. Cryst. Growth* **378**, 506 (2013).
- [71] X. Tao, A. D. Kimberly, P. Sébastien, N. Thanh Hai, M. Younes, B. Maxime, N. Jean-Philippe, W. Xavier, G. Bruno, C. Philippe, Faceting, composition and crystal phase evolution in III-V antimonide nanowire heterostructures revealed by combining microscopy techniques. *Nanotechnology* **23**, 095702 (2012).



- [72] C. García Núñez, A. F. Braña, J. L. Pau, D. Ghita, B. J. García, G. Shen, D. S. Wilbert, S. M. Kim, P. Kung, Pure zincblende GaAs nanowires grown by Ga-assisted chemical beam epitaxy. *J. Cryst. Growth* **372**, 205 (2013).
- [73] M. Heiß, A. Gustafsson, S. Conesa-Boj, F. Peiró, J. R. Morante, G. Abstreiter, J. Arbiol, L. Samuelson, A. Fontcuberta i Morral, Catalyst-free nanowires with axial  $\text{In}_x\text{Ga}_{1-x}\text{As}/\text{GaAs}$  heterostructures. *Nanotechnology* **20**, 075603 (2009).
- [74] A. T. Vogel, J. de Boor, J. V. Wittemann, S. L. Mensah, P. Werner, V. Schmidt, Fabrication of high-quality InSb nanowire arrays by chemical beam epitaxy. *Cryst. Growth Des.* **11**, 1896 (2011).
- [75] S. Ermez, S. Gradecak, Self-assisted GaAs Nanowire Growth by MOCVD <http://www-mtl.mit.edu/wpmu/ar2013/self-assisted-gaas-nanowire-growth-by-mocvd/>. *MTL Annual Research Report 2013*.
- [76] S. Breuer, F. Karouta, H. H. Tan, C. Jagadish, MOCVD growth of GaAs nanowires using Ga droplets. *Conference on Optoelectronic and Microelectronic Materials & Devices (COMMAD)*, 39 (2012).
- [77] Y. Zhang, M. Aagesen, J. V. Holm, H. I. Jørgensen, J. Wu, H. Liu, Self-catalyzed GaAsP nanowires grown on silicon substrates by solid-source molecular beam epitaxy. *Nano Lett.* **13**, 3897 (2013).
- [78] G. Zhang, K. Tateno, H. Gotoh, T. Sogawa, Vertically aligned InP nanowires grown via the self-assisted vapor-liquid-solid mode. *Appl. Phys. Exp.* **5**, 055201 (2012).
- [79] M. Pozuelo, S. V. Prikhodko, R. Grantab, H. Zhou, L. Gao, S. D. Sitzman, V. Gambin, V. B. Shenoy, R. F. Hicks, S. Kodambaka, Zincblende to wurtzite transition during the self-catalyzed growth of InP nanostructures. *J. Cryst. Growth* **312**, 2305 (2010).
- [80] H. Zhou, M. Pozuelo, R. F. Hicks, S. Kodambaka, Self-catalyzed vapor-liquid-solid growth of  $\text{InP}_{1-x}\text{Sb}_x$  nanostructures. *J. Cryst. Growth* **319**, 25 (2011).
- [81] B. Mandl, K. A. Dick, D. Kriegner, M. Keplinger, G. Bauer, J. Stangl, K. Deppert, Crystal structure control in Au-free self-seeded InSb wire growth. *Nanotechnology* **22**, 145603 (2011).
- [82] K. Tomioka, K. Ikejiri, T. Tanaka, J. Motohisa, S. Hara, K. Hiruma, T. Fukui, Selective-area growth of III-V nanowires and their applications. *J. Mater. Res.* **26**, 2127 (2011).
- [83] D. Rudolph, S. Hertenberger, S. Bolte, W. Paosangthong, D. e. Spirkoska, M. Döblinger, M. Bichler, J. J. Finley, G. Abstreiter, G. Koblmüller, Direct observation of a noncatalytic growth regime for GaAs nanowires. *Nano Lett.* **11**, 3848 (2011).
- [84] S. Hertenberger, D. Rudolph, S. Bolte, M. Döblinger, M. Bichler, D. Spirkoska, J. J. Finley, G. Abstreiter, G. Koblmüller, Absence of vapor-liquid-

- solid growth during molecular beam epitaxy of self-induced InAs nanowires on Si. *Appl. Phys. Lett.* **98**, (2011).
- [85] E. Dimakis, J. Lähnemann, U. Jahn, S. Breuer, M. Hilde, L. Geelhaar, H. Riechert, Self-assisted nucleation and vapor-solid growth of InAs nanowires on bare Si(111). *Cryst. Growth Des.* **11**, 4001 (2011).
- [86] S. Hertenberger, D. Rudolph, M. Bichler, J. J. Finley, G. Abstreiter, G. Koblmüller, Growth kinetics in position-controlled and catalyst-free InAs nanowire arrays on Si(111) grown by selective area molecular beam epitaxy. *J. Appl. Phys.* **108**, (2010).
- [87] G. Koblmüller, S. Hertenberger, K. Vizbaras, M. Bichler, F. Bao, J. P. Zhang, G. Abstreiter, Self-induced growth of vertical free-standing InAs nanowires on Si(111) by molecular beam epitaxy. *Nanotechnology* **21**, 365602 (2010).
- [88] S. Hertenberger, S. Funk, K. Vizbaras, A. Yadav, D. Rudolph, J. Becker, S. Bolte, M. Döblinger, M. Bichler, G. Scarpa, P. Lugli, I. Zardo, J. J. Finley, M.-C. Amann, G. Abstreiter, G. Koblmüller, High compositional homogeneity in In-rich InGaAs nanowire arrays on nanoimprinted SiO<sub>2</sub>/Si (111). *Appl. Phys. Lett.* **101**, (2012).
- [89] G. Koblmüller, G. Abstreiter, Growth and properties of InGaAs nanowires on silicon. *Phys. Status Solidi RRL* **8**, 11 (2014).
- [90] I. Isakov, M. Panfilova, M. J. L. Sourribes, V. Tileli, A. E. Porter, P. A. Warburton, InAs<sub>1-x</sub>P<sub>x</sub> nanowires grown by catalyst-free molecular-beam epitaxy. *Nanotechnology* **24**, 085707 (2013).
- [91] A. I. Persson, M. W. Larsson, S. Stenstrom, B. J. Ohlsson, L. Samuelson, L. R. Wallenberg, Solid-phase diffusion mechanism for GaAs nanowire growth. *Nature Mater.* **3**, 677 (2004).
- [92] B. A. Wacaser, K. A. Dick, J. Johansson, M. T. Borgström, K. Deppert, L. Samuelson, Preferential interface nucleation: an expansion of the VLS growth mechanism for nanowires. *Adv. Mater.* **21**, 153 (2009).
- [93] M. T. Björk, B. J. Ohlsson, T. Sass, A. I. Persson, C. Thelander, M. H. Magnusson, K. Deppert, L. R. Wallenberg, L. Samuelson, One-dimensional heterostructures in semiconductor nanowhiskers. *Appl. Phys. Lett.* **80**, 1058 (2002).
- [94] T. Mårtensson, M. Borgström, W. Seifert, B. J. Ohlsson, L. Samuelson, Fabrication of individually seeded nanowire arrays by vapour-liquid-solid growth. *Nanotechnology* **14**, 1255 (2003).
- [95] V. G. Dubrovskii, G. E. Cirlin, I. P. Soshnikov, A. A. Tonkikh, N. V. Sibirev, Y. B. Samsonenko, V. M. Ustinov, Diffusion-induced growth of GaAs nanowhiskers during molecular beam epitaxy: Theory and experiment. *Phys. Rev. B* **71**, 205325 (2005).

- [96] V. G. Dubrovskii, N. V. Sibirev, General form of the dependences of nanowire growth rate on the nanowire radius. *J. Cryst. Growth* **304**, 504 (2007).
- [97] F. Glas, J.-C. Harmand, G. Patriarche, Why does wurtzite form in nanowires of III-V zinc blende semiconductors? *Phys. Rev. Lett.* **99**, 146101 (2007).
- [98] V. G. Dubrovskii, N. V. Sibirev, J. C. Harmand, F. Glas, Growth kinetics and crystal structure of semiconductor nanowires. *Phys. Rev. B* **78**, 235301 (2008).
- [99] D. E. Perea, J. E. Allen, S. J. May, B. W. Wessels, D. N. Seidman, L. J. Lauhon, Three-dimensional nanoscale composition mapping of semiconductor nanowires. *Nano Lett.* **6**, 181 (2005).
- [100] M. Ohring, *Materials Science of Thin Films*. Academic Press, 2nd Edition, (2001).
- [101] E. Russo-Averchi, M. Heiss, L. Michelet, P. Krogstrup, J. Nygard, C. Magen, J. R. Morante, E. Uccelli, J. Arbiol, A. Fontcuberta i Morral, Suppression of three dimensional twinning for a 100% yield of vertical GaAs nanowires on silicon. *Nanoscale* **4**, 1486 (2012).
- [102] N. V. Sibirev, M. Tchernycheva, M. A. Timofeeva, J.-C. Harmand, G. E. Cirlin, V. G. Dubrovskii, Influence of shadow effect on the growth and shape of InAs nanowires. *J. Appl. Phys.* **111**, 104317 (2012).
- [103] M. Morita, T. Ohmi, E. Hasegawa, M. Kawakami, K. Suma, Control factor of native oxide growth on silicon in air or in ultrapure water. *Appl. Phys. Lett.* **55**, 562 (1989).
- [104] P. Krogstrup, R. Popovitz-Biro, E. Johnson, M. H. Madsen, J. Nygård, H. Shtrikman, Structural phase control in self-catalyzed growth of GaAs nanowires on silicon (111). *Nano Lett.* **10**, 4475 (2010).
- [105] A. Biermanns, S. Breuer, A. Trampert, A. Davydok, L. Geelhaar, U. Pietsch, Strain accommodation in Ga-assisted GaAs nanowires grown on silicon (111). *Nanotechnology* **23**, 305703 (2012).
- [106] P. Caroff, J. Bolinsson, J. Johansson, Crystal phases in III-V nanowires: from random toward engineered polytypism. *IEEE J. Sel. Top. Quantum Electron.* **17**, 829 (2011).
- [107] I. P. Soshnikov, G. É. Cirlin, A. A. Tonkikh, Y. B. Samsonenko, V. G. Dubrovskii, V. M. Ustinov, O. M. Gorbenko, D. Litvinov, D. Gerthsen, Atomic structure of MBE-grown GaAs nanowhiskers. *Phys. Solid State* **47**, 2213 (2005).
- [108] G. E. Cirlin, V. G. Dubrovskii, Y. B. Samsonenko, A. D. Bouravleuv, K. Durose, Y. Y. Proskuryakov, B. Mendes, L. Bowen, M. A. Kaliteevski, R. A. Abram, D. Zeze, Self-catalyzed, pure zincblende GaAs nanowires grown on Si(111) by molecular beam epitaxy. *Phys. Rev. B* **82**, 035302 (2010).
- [109] D. Spirkoska, J. Arbiol, A. Gustafsson, S. Conesa-Boj, F. Glas, I. Zardo, M. Heigoldt, M. H. Gass, A. L. Bleloch, S. Estrade, M. Kaniber, J. Rossler, F.

- Peiro, J. R. Morante, G. Abstreiter, L. Samuelson, A. Fontcuberta i Morral, Structural and optical properties of high quality zinc-blende/wurtzite GaAs nanowire heterostructures. *Phys. Rev. B* **80**, 245325 (2009).
- [110] F. Jabeen, V. Grillo, S. Rubini, F. Martelli, Self-catalyzed growth of GaAs nanowires on cleaved Si by molecular beam epitaxy. *Nanotechnology* **19**, 275711 (2008).
- [111] T. B. Hoang, A. F. Moses, H. L. Zhou, D. L. Dheeraj, B. O. Fimland, H. Weman, Observation of free exciton photoluminescence emission from single wurtzite GaAs nanowires. *Appl. Phys. Lett.* **94**, (2009).
- [112] M. Heiss, S. Conesa-Boj, J. Ren, H.-H. Tseng, A. Gali, A. Rudolph, E. Uccelli, F. Peiró, J. R. Morante, D. Schuh, E. Reiger, E. Kaxiras, J. Arbiol, A. Fontcuberta i Morral, Direct correlation of crystal structure and optical properties in wurtzite/zinc-blende GaAs nanowire heterostructures. *Phys. Rev B* **83**, 045303 (2011).
- [113] P. Kusch, S. Breuer, M. Ramsteiner, L. Geelhaar, H. Riechert, S. Reich, Band gap of wurtzite GaAs: A resonant Raman study. *Phys. Rev B* **86**, 075317 (2012).
- [114] M. Mattila, T. Hakkarainen, M. Mulot, H. Lipsanen, Crystal-structure-dependent photoluminescence from InP nanowires. *Nanotechnology* **17**, 1580 (2006).
- [115] J. Trägårdh, A. I. Persson, J. B. Wagner, D. Hessman, L. Samuelson, Measurements of the band gap of wurtzite  $\text{InAs}_{1-x}\text{P}_x$  nanowires using photocurrent spectroscopy. *J. Appl. Phys.* **101**, (2007).
- [116] M. Moewe, L. C. Chuang, S. Crankshaw, C. Chase, C. Chang-Hasnain, Atomically sharp catalyst-free wurtzite GaAs/AlGaAs nanoneedles grown on silicon. *Appl. Phys. Lett.* **93**, 023116 (2008).
- [117] B. Ketterer, M. Heiss, M. J. Livrozet, A. Rudolph, E. Reiger, A. Fontcuberta i Morral, Determination of the band gap and the split-off band in wurtzite GaAs using Raman and photoluminescence excitation spectroscopy. *Phys. Rev B* **83**, 125307 (2011).
- [118] A. Mishra, L. V. Titova, T. B. Hoang, H. E. Jackson, L. M. Smith, J. M. Yarrison-Rice, Y. Kim, H. J. Joyce, Q. Gao, H. H. Tan, C. Jagadish, Polarization and temperature dependence of photoluminescence from zincblende and wurtzite InP nanowires. *Appl. Phys. Lett.* **91**, (2007).
- [119] T. Ba Hoang, A. F. Moses, L. Ahtapodov, H. Zhou, D. L. Dheeraj, A. T. J. van Helvoort, B.-O. Fimland, H. Weman, Engineering parallel and perpendicular polarized photoluminescence from a single semiconductor nanowire by crystal phase control. *Nano Lett.* **10**, 2927 (2010).
- [120] C.-Y. Yeh, Z. W. Lu, S. Froyen, A. Zunger, Zinc-blende–wurtzite polytypism in semiconductors. *Phys. Rev B* **46**, 10086 (1992).

- [121] H. J. Joyce, J. Wong-Leung, Q. Gao, H. H. Tan, C. Jagadish, Phase perfection in zinc blende and wurtzite III–V nanowires using basic growth parameters. *Nano Lett.* **10**, 908 (2010).
- [122] K. Pemasiri, M. Montazeri, R. Gass, L. M. Smith, H. E. Jackson, J. Yarrison-Rice, S. Paiman, Q. Gao, H. H. Tan, C. Jagadish, X. Zhang, J. Zou, Carrier dynamics and quantum confinement in type II ZB-WZ InP nanowire homostructures. *Nano Lett.* **9**, 648 (2009).
- [123] J. Johansson, L. S. Karlsson, K. A. Dick, J. Bolinsson, B. A. Wacaser, K. Deppert, L. Samuelson, Effects of supersaturation on the crystal structure of gold seeded III–V nanowires. *Cryst. Growth Des.* **9**, 766 (2009).
- [124] V. G. Dubrovskii, N. V. Sibirev, J. C. Harmand, F. Glas, Growth kinetics and crystal structure of semiconductor nanowires. *Phys. Rev B* **78**, 235301 (2008).
- [125] M. Soda, A. Rudolph, D. Schuh, J. Zweck, D. Bougeard, E. Reiger, Transition from Au to pseudo-Ga catalyzed growth mode observed in GaAs nanowires grown by molecular beam epitaxy. *Phys. Rev B* **85**, 245450 (2012).
- [126] P. Krogstrup, S. Curiotto, E. Johnson, M. Aagesen, J. Nygård, D. Chatain, Impact of the liquid phase shape on the structure of III-V nanowires. *Phys. Rev. Lett.* **106**, 125505 (2011).
- [127] V. G. Dubrovskii, G. E. Cirlin, N. V. Sibirev, F. Jabeen, J. C. Harmand, P. Werner, New mode of vapor–liquid–solid nanowire growth. *Nano Lett.* **11**, 1247 (2011).
- [128] X. Yu, H. Wang, J. Lu, J. Zhao, J. Misuraca, P. Xiong, S. von Molnár, Evidence for structural phase transitions induced by the triple phase line shift in self-catalyzed GaAs nanowires. *Nano Lett.* **12**, 5436 (2012).
- [129] P. Krogstrup, M. H. Madsen, W. Hu, M. Kozu, Y. Nakata, J. Nygard, M. Takahashi, R. Feidenhans'l, In-situ x-ray characterization of wurtzite formation in GaAs nanowires. *Appl. Phys. Lett.* **100**, 093103 (2012).
- [130] P. Avouris, Graphene: electronic and photonic properties and devices. *Nano Lett.* **10**, 4285 (2010).
- [131] A. A. Balandin, S. Ghosh, W. Bao, I. Calizo, D. Teweldebrhan, F. Miao, C. N. Lau, Superior thermal conductivity of single-layer graphene. *Nano Lett.* **8**, 902 (2008).
- [132] R. R. Nair, P. Blake, A. N. Grigorenko, K. S. Novoselov, T. J. Booth, T. Stauber, N. M. R. Peres, A. K. Geim, Fine structure constant defines visual transparency of graphene. *Science* **320**, 1308 (2008).
- [133] C. Lee, X. Wei, J. W. Kysar, J. Hone, Measurement of the elastic properties and intrinsic strength of monolayer graphene. *Science* **321**, 385 (2008).
- [134] S.-H. Bae, O. Kahya, B. K. Sharma, J. Kwon, H. J. Cho, B. Özyilmaz, J.-H. Ahn, Graphene-P(VDF-TrFE) multilayer film for flexible applications. *ACS Nano*, (2013).

- [135] C. Sire, F. Ardiaca, S. Lepilliet, J.-W. T. Seo, M. C. Hersam, G. Dambrine, H. Happy, V. Derycke, Flexible gigahertz transistors derived from solution-based single-layer graphene. *Nano Lett.* **12**, 1184 (2012).
- [136] K. S. Kim, Y. Zhao, H. Jang, S. Y. Lee, J. M. Kim, K. S. Kim, J.-H. Ahn, P. Kim, J.-Y. Choi, B. H. Hong, Large-scale pattern growth of graphene films for stretchable transparent electrodes. *Nature* **457**, 706 (2009).
- [137] X. Li, W. Cai, J. An, S. Kim, J. Nah, D. Yang, R. Piner, A. Velamakanni, I. Jung, E. Tutuc, S. K. Banerjee, L. Colombo, R. S. Ruoff, Large-area synthesis of high-quality and uniform graphene films on copper foils. *Science* **324**, 1312 (2009).
- [138] L. Gao, J. R. Guest, N. P. Guisinger, Epitaxial graphene on Cu(111). *Nano Lett.* **10**, 3512 (2010).
- [139] Z. Yan, J. Lin, Z. Peng, Z. Sun, Y. Zhu, L. Li, C. Xiang, E. L. Samuel, C. Kittrell, J. M. Tour, Toward the synthesis of wafer-scale single-crystal graphene on copper foils. *ACS Nano* **6**, 9110 (2012).
- [140] R. Hawaldar, P. Merino, M. R. Correia, I. Bdikin, J. Grácio, J. Méndez, J. A. Martín-Gago, M. K. Singh, Large-area high-throughput synthesis of monolayer graphene sheet by Hot Filament Thermal Chemical Vapor Deposition. *Sci. Rep.* **2**, (2012).
- [141] S. J. Chae, F. Güneş, K. K. Kim, E. S. Kim, G. H. Han, S. M. Kim, H.-J. Shin, S.-M. Yoon, J.-Y. Choi, M. H. Park, C. W. Yang, D. Pribat, Y. H. Lee, Synthesis of large-area graphene layers on poly-nickel substrate by chemical vapor deposition: wrinkle formation. *Adv. Mater.* **21**, 2328 (2009).
- [142] A. Reina, S. Thiele, X. Jia, S. Bhaviripudi, M. Dresselhaus, J. Schaefer, J. Kong, Growth of large-area single- and bi-layer graphene by controlled carbon precipitation on polycrystalline Ni surfaces. *Nano Res.* **2**, 509 (2009).
- [143] Y. Zhang, T. Gao, S. Xie, B. Dai, L. Fu, Y. Gao, Y. Chen, M. Liu, Z. Liu, Different growth behaviors of ambient pressure chemical vapor deposition graphene on Ni(111) and Ni films: A scanning tunneling microscopy study. *Nano Res.* **5**, 402 (2012).
- [144] L. Gao, W. Ren, H. Xu, L. Jin, Z. Wang, T. Ma, L.-P. Ma, Z. Zhang, Q. Fu, L.-M. Peng, X. Bao, H.-M. Cheng, Repeated growth and bubbling transfer of graphene with millimetre-size single-crystal grains using platinum. *Nature Commun.* **3**, 699 (2012).
- [145] P. Sutter, J. T. Sadowski, E. Sutter, Graphene on Pt(111): growth and substrate interaction. *Phys. Rev. B* **80**, 245411 (2009).
- [146] K. V. Emtsev, A. Bostwick, K. Horn, J. Jobst, G. L. Kellogg, L. Ley, J. L. McChesney, T. Ohta, S. A. Reshanov, J. Rohrl, E. Rotenberg, A. K. Schmid, D. Waldmann, H. B. Weber, T. Seyller, Towards wafer-size graphene layers

- by atmospheric pressure graphitization of silicon carbide. *Nature Mater.* **8**, 203 (2009).
- [147] C. Berger, Z. Song, T. Li, X. Li, A. Y. Ogbazghi, R. Feng, Z. Dai, A. N. Marchenkov, E. H. Conrad, P. N. First, W. A. de Heer, Ultrathin epitaxial graphite: 2D electron gas properties and a route toward graphene-based nanoelectronics. *J. Phys. Chem. B* **108**, 19912 (2004).
- [148] M. Sprinkle, P. Soukiassian, W. A. de Heer, C. Berger, E. H. Conrad, Epitaxial graphene: the material for graphene electronics. *Phys. Status Solidi RRL* **3**, A91 (2009).
- [149] C. Virojanadara, R. Yakimova, A. A. Zakharov, L. I. Johansson, Large homogeneous mono-/bi-layer graphene on 6H-SiC(0001) and buffer layer elimination. *J. Phys. D: Appl. Phys.* **43**, 374010 (2010).
- [150] S. Bae, H. Kim, Y. Lee, X. Xu, J.-S. Park, Y. Zheng, J. Balakrishnan, T. Lei, H. Ri Kim, Y. I. Song, Y.-J. Kim, K. S. Kim, B. Ozyilmaz, J.-H. Ahn, B. H. Hong, S. Iijima, Roll-to-roll production of 30-inch graphene films for transparent electrodes. *Nature Nanotech.* **5**, 574 (2010).
- [151] T. Hesjedal, Continuous roll-to-roll growth of graphene films by chemical vapor deposition. *Appl. Phys. Lett.* **98**, 133106 (2011).
- [152] Y. Hao, M. S. Bharathi, L. Wang, Y. Liu, H. Chen, S. Nie, X. Wang, H. Chou, C. Tan, B. Fallahazad, H. Ramanarayan, C. W. Magnuson, E. Tutuc, B. I. Yakobson, K. F. McCarty, Y.-W. Zhang, P. Kim, J. Hone, L. Colombo, R. S. Ruoff, The role of surface oxygen in the growth of large single-crystal graphene on copper. *Science* **342**, 720 (2013).
- [153] A. Reina, H. Son, L. Jiao, B. Fan, M. S. Dresselhaus, Z. Liu, J. Kong, Transferring and Identification of Single- and Few-Layer Graphene on Arbitrary Substrates. *J. Phys. Chem. C* **112**, 17741 (2008).
- [154] X. Liang, B. A. Sperling, I. Calizo, G. Cheng, C. A. Hacker, Q. Zhang, Y. Obeng, K. Yan, H. Peng, Q. Li, X. Zhu, H. Yuan, A. R. Hight Walker, Z. Liu, L.-m. Peng, C. A. Richter, Toward clean and crackless transfer of graphene. *ACS Nano* **5**, 9144 (2011).
- [155] J. Kang, D. Shin, S. Bae, B. H. Hong, Graphene transfer: key for applications. *Nanoscale* **4**, 5527 (2012).
- [156] Y. Zhu, Z. Sun, Z. Yan, Z. Jin, J. M. Tour, Rational design of hybrid graphene films for high-performance transparent electrodes. *ACS Nano* **5**, 6472 (2011).
- [157] D. Anna, On display with transparent conducting films. *Nanotechnology* **23**, 110201 (2012).
- [158] K. Tae-il, K. Rak-Hwan, J. A. Rogers, Microscale inorganic light-emitting diodes on flexible and stretchable substrates. *IEEE Photonics Journal* **4**, 607 (2012).

- [159] M. He, J. Jung, F. Qiu, Z. Lin, Graphene-based transparent flexible electrodes for polymer solar cells. *J. Mater. Chem.* **22**, 24254 (2012).
- [160] L. Gomez De Arco, Y. Zhang, C. W. Schlenker, K. Ryu, M. E. Thompson, C. Zhou, Continuous, highly flexible, and transparent graphene films by chemical vapor deposition for organic photovoltaics. *ACS Nano* **4**, 2865 (2010).
- [161] Z. Liu, J. Li, Z.-H. Sun, G. Tai, S.-P. Lau, F. Yan, The application of highly doped single-layer graphene as the top electrodes of semitransparent organic solar cells. *ACS Nano* **6**, 810 (2011).
- [162] A. K. Geim, K. S. Novoselov, The rise of graphene. *Nature Mater.* **6**, 183 (2007).
- [163] A. K. Geim, A. H. MacDonald, Graphene: exploring carbon flatland. *Phys. Today* **60**, 35 (2007).
- [164] A. Koma, Van der Waals epitaxy for highly lattice-mismatched systems. *J. Cryst. Growth* **201-202**, 236 (1999).
- [165] K. Nakada, A. Ishii, DFT calculation for adatom adsorption on graphene, Graphene Simulation, J. R. Gong (Ed.), ISBN: 978-953-307-556-3, DOI: 10.5772/20477. *InTech*, (2011).
- [166] K. Nakada, A. Ishii, Migration of adatom adsorption on graphene using DFT calculation. *Solid State Commun.* **151**, 13 (2011).
- [167] Y. J. Hong, T. Fukui, Controlled van der Waals heteroepitaxy of InAs nanowires on carbon honeycomb lattices. *ACS Nano* **5**, 7576 (2011).
- [168] Y. J. Hong, W. H. Lee, Y. Wu, R. S. Ruoff, T. Fukui, van der Waals epitaxy of InAs nanowires vertically aligned on single-layer graphene. *Nano Lett.* **12**, 1431 (2012).
- [169] P. K. Mohseni, A. Behnam, J. D. Wood, C. D. English, J. W. Lyding, E. Pop, X. Li, In<sub>x</sub>Ga<sub>1-x</sub>As nanowire growth on graphene: van der Waals epitaxy induced phase segregation. *Nano Lett.* **13**, 1153 (2013).
- [170] G. Priante, S. Ambrosini, V. G. Dubrovskii, A. Franciosi, S. Rubini, Stopping and resuming at will the growth of GaAs nanowires. *Cryst. Growth Des.* **13**, 3976 (2013).
- [171] V. Pankoke, P. Kratzer, S. Sakong, Calculation of the diameter-dependent polytypism in GaAs nanowires from an atomic motif expansion of the formation energy. *Phys. Rev. B* **84**, 075455 (2011).
- [172] M. Hilde, M. Ramsteiner, S. Breuer, L. Geelhaar, H. Riechert, Incorporation of the dopants Si and Be into GaAs nanowires. *Appl. Phys. Lett.* **96**, (2010).
- [173] A. Casadei, P. Krogstrup, M. Heiss, J. A. Röhr, C. Colombo, T. Ruelle, S. Upadhyay, C. B. Sørensen, J. Nygård, A. Fontcuberta i Morral, Doping incorporation paths in catalyst-free Be-doped GaAs nanowires. *Appl. Phys. Lett.* **102**, (2013).



- [174] C. Colombo, M. Hei $\beta$ , M. Grätzel, A. Fontcuberta i Morral, Gallium arsenide p-i-n radial structures for photovoltaic applications. *Appl. Phys. Lett.* **94**, (2009).
- [175] A. Y. Cho, J. R. Arthur, Molecular beam epitaxy. *Prog. Solid State Chem.* **10**, 157 (1975).
- [176] J. De-Sheng, Y. Makita, K. Ploog, H. J. Queisser, Electrical properties and photoluminescence of Te-doped GaAs grown by molecular beam epitaxy. *J. Appl. Phys.* **53**, 999 (1982).
- [177] H. Kauko, C. L. Zheng, Y. Zhu, S. Glanvill, C. Dwyer, A. M. Munshi, B. O. Fimland, A. T. J. van Helvoort, J. Etheridge, Compositional analysis of GaAs/AlGaAs heterostructures using quantitative scanning transmission electron microscopy. *Appl. Phys. Lett.* **103**, (2013).
- [178] M. Fickenscher, T. Shi, H. E. Jackson, L. M. Smith, J. M. Yarrison-Rice, C. Zheng, P. Miller, J. Etheridge, B. M. Wong, Q. Gao, S. Deshpande, H. H. Tan, C. Jagadish, Optical, structural, and numerical investigations of GaAs/AlGaAs core-multishell nanowire quantum well tubes. *Nano Lett.* **13**, 1016 (2013).
- [179] C. Zheng, J. Wong-Leung, Q. Gao, H. H. Tan, C. Jagadish, J. Etheridge, Polarity-driven 3-fold symmetry of GaAs/AlGaAs core multishell nanowires. *Nano Lett.* **13**, 3742 (2013).
- [180] N. Jiang, Q. Gao, P. Parkinson, J. Wong-Leung, S. Mokkapati, S. Breuer, H. H. Tan, C. L. Zheng, J. Etheridge, C. Jagadish, Enhanced Minority Carrier Lifetimes in GaAs/AlGaAs Core-Shell Nanowires through Shell Growth Optimization. *Nano Lett.* **13**, 5135 (2013).
- [181] V. Dhaka, J. Oksanen, H. Jiang, T. Haggren, A. Nykänen, R. Sanatinia, J.-P. Kakko, T. Huutio, M. Mattila, J. Ruokolainen, S. Anand, E. Kauppinen, H. Lipsanen, Aluminum-induced photoluminescence red shifts in core-shell GaAs/Al<sub>x</sub>Ga<sub>1-x</sub>As nanowires. *Nano Lett.* **13**, 3581 (2013).
- [182] M. Heiss, Y. Fontana, A. Gustafsson, G. Wüst, C. Magen, D. D. O'Regan, J. W. Luo, B. Ketterer, S. Conesa-Boj, A. V. Kuhlmann, J. Houel, E. Russo-Averchi, J. R. Morante, M. Cantoni, N. Marzari, J. Arbiol, A. Zunger, R. J. Warburton, A. Fontcuberta i Morral, Self-assembled quantum dots in a nanowire system for quantum photonics. *Nature Mater.* **12**, 439 (2013).
- [183] D. Rudolph, S. Funk, M. Döblinger, S. Morkötter, S. Hertenberger, L. Schweickert, J. Becker, S. Matich, M. Bichler, D. Spirkoska, I. Zardo, J. J. Finley, G. Abstreiter, G. Koblmüller, Spontaneous alloy composition ordering in GaAs-AlGaAs core-shell nanowires. *Nano Lett.* **13**, 1522 (2013).
- [184] N. Sköld, J. B. Wagner, G. Karlsson, T. Hernán, W. Seifert, M.-E. Pistol, L. Samuelson, Phase segregation in AlInP shells on GaAs nanowires. *Nano Lett.* **6**, 2743 (2006).

- [185] J. B. Wagner, N. Sköld, L. Reine Wallenberg, L. Samuelson, Growth and segregation of GaAs–Al<sub>x</sub>In<sub>1-x</sub>P core-shell nanowires. *J. Cryst. Growth* **312**, 1755 (2010).
- [186] G. Biasiol, E. Kapon, Mechanisms of self-ordering of quantum nanostructures grown on nonplanar surfaces. *Phys. Rev. Lett.* **81**, 2962 (1998).
- [187] G. Biasiol, K. Leifer, E. Kapon, Formation of semiconductor vertical quantum barriers by epitaxial growth on corrugated surfaces. *Phys. Rev. B* **61**, 7223 (2000).
- [188] G. Biasiol, A. Gustafsson, K. Leifer, E. Kapon, Mechanisms of self-ordering in nonplanar epitaxy of semiconductor nanostructures. *Phys. Rev. B* **65**, 205306 (2002).
- [189] J. Todorovic, A. F. Moses, T. Karlberg, P. Olk, D. L. Dheeraj, B. O. Fimland, H. Weman, A. T. J. van Helvoort, Correlated micro-photoluminescence and electron microscopy studies of the same individual heterostructured semiconductor nanowires. *Nanotechnology* **22**, 325707 (2011).
- [190] D. Spirkoska, G. Abstreiter, A. Fontcuberta i Morral GaAs nanowires and related prismatic heterostructures. *Semicond. Sci. Technol.* **24**, 113001 (2009).
- [191] M.-H. Bae, B.-K. Kim, D.-H. Ha, S. J. Lee, R. Sharma, K. J. Choi, J.-J. Kim, W. J. Choi, J. C. Shin, Non-lithographic growth of core-shell GaAs nanowires on Si for optoelectronic applications. *Cryst. Growth Des.*, DOI: 10.1021/cg401520q (2014).
- [192] K. Tomioka, J. Motohisa, S. Hara, K. Hiruma, T. Fukui, GaAs/AlGaAs core multishell nanowire-based light-emitting diodes on Si. *Nano Lett.* **10**, 1639 (2010).
- [193] C. P. T. Svensson, M. Thomas, T. Johanna, L. Christina, R. Michael, H. Dan, S. Lars, O. Jonas, Monolithic GaAs/InGaP nanowire light emitting diodes on silicon. *Nanotechnology* **19**, 305201 (2008).
- [194] D. Saxena, S. Mokkapatil, P. Parkinson, N. Jiang, Q. Gao, H. H. Tan, C. Jagadish, Optically pumped room-temperature GaAs nanowire lasers. *Nature Photon.* **7**, 963 (2013).
- [195] B. Mayer, D. Rudolph, J. Schnell, S. Morkötter, J. Winnerl, J. Treu, K. Müller, G. Bracher, G. Abstreiter, G. Koblmüller, J. J. Finley, Lasing from individual GaAs-AlGaAs core-shell nanowires up to room temperature. *Nature Commun.* **4**, (2013).
- [196] V. Dhaka, J. Oksanen, H. Jiang, T. Haggren, A. Nykänen, R. Sanatinia, J.-P. Kakko, T. Huhtio, M. Mattila, J. Ruokolainen, S. Anand, E. Kauppinen, H. Lipsanen, Aluminum-induced photoluminescence red shifts in core-shell GaAs/Al<sub>x</sub>Ga<sub>1-x</sub>As nanowires. *Nano Lett.* **13**, 3581 (2013).
- [197] M. Hocevar, L. T. Thanh Giang, R. Songmuang, M. den Hertog, L. Besombes, J. Bleuse, Y.-M. Niquet, N. T. Pelekanos, Residual strain and piezoelectric

- effects in passivated GaAs/AlGaAs core-shell nanowires. *Appl. Phys. Lett.* **102**, (2013).
- [198] F. Banhart, J. Kotakoski, A. V. Krasheninnikov, Structural defects in graphene. *ACS Nano* **5**, 26 (2011).
- [199] M. Heigoldt, J. Arbiol, D. Spirkoska, J. M. Rebled, S. Conesa-Boj, G. Abstreiter, F. Peiro, J. R. Morante, A. Fontcuberta i Morral, Long range epitaxial growth of prismatic heterostructures on the facets of catalyst-free GaAs nanowires. *J. Mater. Chem.* **19**, 840 (2009).
- [200] J. V. Holm, H. I. Jørgensen, P. Krogstrup, J. Nygård, H. Liu, M. Aagesen, Surface-passivated GaAsP single-nanowire solar cells exceeding 10% efficiency grown on silicon. *Nature Commun.* **4**, 1498 (2013).